

UNIVERSIDAD DE COSTA RICA  
SISTEMA DE ESTUDIOS DE POSGRADO

EFFECTO DE LA LIBERACIÓN CONTROLADA DE MOLÉCULAS  
CARGADAS SOBRE LA DIFERENCIACIÓN DE LAS CÉLULAS  
MADRE MESENQUIMALES HUMANAS A OSTEÓBLASTOS

Tesis sometida a la consideración de la Comisión del Programa de  
Estudios de Posgrado en Microbiología, Parasitología, Química  
Clínica e Inmunología para optar al grado y título de Maestría  
Académica en Microbiología

KARLA SOFÍA RAMÍREZ SÁNCHEZ

Ciudad Universitaria Rodrigo Facio, Costa Rica

2022

## **Dedication**

I dedicate this thesis to God; in whose hands I commend my work. He is my refuge and my strength in difficult times, as well as the source of all wisdom.

I would like to express my deepest gratitude to my boyfriend, the moon of my life, thanks for your emotional support during these years and for being such a great friend.

To my loving family, whose support has been vital in getting me to where I am today. Mom, dad, brother, and sister, thank you all.

To my grandfather and grandmother, who are my source of happiness, the foundations on which my life is built. I owe a lot of who I am to them.

## **Acknowledgements**

I would like to publicly express my gratitude to all the people who in one way or another helped me to achieve success on this project thesis:

I am extremely grateful to Ph.D Ricardo Starbird for all his teachings, as well as for his friendship during all these years.

I could also not have undertaken this journey without Ph.D Mónica Prado, who has been the best tutor I could have hoped for.

Words cannot express my gratitude to Ph.D Inés Ardao Palacios and Ph.D Carlos A. García González for all the coordination and teachings during my stay in Santiago de Compostela.

Special thanks to Ph.D Esteban Avendaño and Ph.D Víctor Santos Rosales for all the support provided during my work.

I would be remiss in not mentioning my work peers at Tecnológico de Costa Rica, specially to M.Sc. Silvia Castro Piedra, M.Sc. Fernando Alvarado Hidalgo, Eng. Laria Rodríguez Quesada, Eng Sebastián León Carvajal, and Eng. María Paula Palma, for all the support and pleasant moments.

Lastly, I would like to mention all the people at the Pharmacy Department from the University of Santiago de Compostela, for giving me their friendship and for sharing memorable moments.

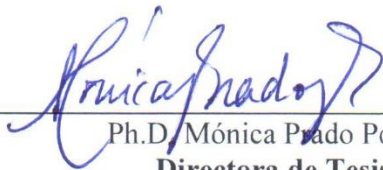
To all of you, thanks.

“Esta Tesis fue aceptada por la Comisión del Programa de Estudios de Posgrado en Microbiología, Parasitología, Química Clínica e Inmunología de la Universidad de Costa Rica, como requisito parcial para optar al grado y título de Maestría Académica en Microbiología”



---

Ph.D. Carlos Chacón Díaz  
**Representante de la Decana  
Sistema de Estudios de Posgrado**



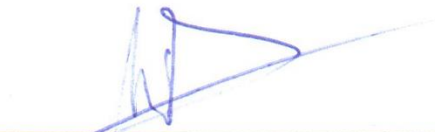
---

Ph.D. Mónica Prado Porras  
**Directora de Tesis**



---

Ph.D. Ricardo Starbird Pérez  
**Asesor**



---

Ph.D. Inés Ardao Palacios  
**Asesora**



---

Ph.D. Rodrigo Mora Rodríguez  
**Representante del Director del Programa de Posgrado en  
Microbiología, Parasitología, Química Clínica e Inmunología**



---

Karla Sofía Ramírez Sánchez  
**Sustentante**

## 1 List of contents

Hoja de aprobación .....	¡Error! Marcador no definido.
1 List of contents .....	v
2 RESUMEN .....	viii
3 ABSTRACT .....	ix
4 List of Tables .....	x
5 List of Figures .....	xi
6 List of abbreviations .....	xiii
7 List of Annexes .....	xv
8 List of Equations .....	xvi
9 Introduction .....	1
10 Theoretical framework .....	5
10.1 Mesenchymal stem cells in tissue engineering applications for bone repair therapies.....	5
10.1.1 Bone diseases as consequence of aging progressive.....	5
10.1.2 Characteristics of mesenchymal stem cells. ....	6
10.1.3 MSCs isolation sources.....	7
10.1.4 Mesenchymal stem cells surface markers. ....	9
10.1.5 Multilineage differentiation of mesenchymal stem cells.....	10
10.1.6 Importance of the mesenchymal stem cells in tissue engineering and bone defects.....	14
10.2 Dexamethasone and glycosaminoglycans as osteoblast differentiation factors during <i>in vitro</i> MSCs culture. ....	15
10.2.1 Effect of dexamethasone on MSCs differentiation. ....	15
10.2.2 Glycosaminoglycans and their potential use as differentiation factor on MSCs.....	17
10.3 Porous and non-porous materials as drug delivery systems.....	18
10.3.1 PEDOT as conductive polymer for drug immobilization.....	19
10.3.2 Controlled drug release by electrical stimulation employing nonporous conductive materials. ....	20
10.3.3 Polysaccharide-based porous materials as drug-delivery systems.....	22
10.3.4 Diffusive phenomena on the controlled release of drugs on polysaccharide-based porous materials. ....	23

10.3.5	Future perspective: innovative polysaccharide-based porous materials as extracellular matrices for tissue regeneration.....	24
11	Justification.....	27
12	Hypothesis.....	28
13	Objectives.....	29
13.1	General objective:.....	29
13.2	Specific objectives:.....	29
14	Materials and methods .....	30
14.1	Materials. ....	30
14.2	Deposition of the gold electrode.....	31
14.3	Modification of the gold electrode with a coating of PEDOT/ $\kappa$ C/Dex. ....	32
14.4	Evaluation of the stability and size of the dispersion systems.....	32
14.5	Analysis of the Topography and Composition of PEDOT/ $\kappa$ C/Dex Coating by Profilometry and $\mu$ -Raman Spectroscopy Methods. ....	33
14.6	Dexamethasone-21 phosphate release experiments from the PEDOT/ $\kappa$ C/Dex film.....	34
14.7	Preparation of three-dimensional scaffolds based on polysaccharides and dexamethasone-21 phosphate. ....	36
14.8	Physical characterization of polysaccharide/Dex-based cryogels.....	36
14.9	Dexamethasone-21 phosphate release experiments from the polysaccharide-based cryogels.....	38
14.10	Osteogenic differentiation of human mesenchymal stem cells. ....	39
14.11	Biocompatibility test for the electrodes and cryogels system.....	39
14.12	Effect of high molecular weight heparin on hMSCs differentiation to osteoblast.....	40
14.13	Alkaline phosphatase enzymatic activity measurement.....	41
14.14	Qualitative analysis of osteogenesis by immunofluorescence analysis of osteoblast cell markers.....	42
14.15	RNA isolation from hMSCs. ....	43
14.16	Quantitative analysis of osteoblast differentiation by qPCR.....	43
14.17	hMSCs differentiation using dexamethasone 21-phosphate controlled released systems.....	45
15	Results and discusi3n .....	46
15.1	Evaluation of the stability and size of the dispersion systems.....	46

<b>15.2</b>	<b>Analysis of the topography and composition of PEDOT/<math>\kappa</math>C/Dex coating by <math>\mu</math>-Raman spectroscopy and profilometry methods.....</b>	<b>48</b>
<b>15.3</b>	<b>Dexamethasone-21 phosphate release experiments from the PEDOT/<math>\kappa</math>C/Dex coating.....</b>	<b>51</b>
<b>15.4</b>	<b>Physical characterization of starch based cryogels.....</b>	<b>56</b>
<b>15.5</b>	<b>Analysis of polysaccharide-based scaffolds microstructure. ....</b>	<b>57</b>
<b>15.6</b>	<b>Cryogels swelling ratio test.....</b>	<b>58</b>
<b>15.7</b>	<b>Cryogels erosion studies.....</b>	<b>60</b>
<b>15.8</b>	<b>Drug release experiments from the polysaccharide-based cryogels.....</b>	<b>61</b>
<b>15.9</b>	<b>PEDOT/<math>\kappa</math>C/Dex electrodes and polysaccharide-based cryogels biocompatibility analysis. ....</b>	<b>64</b>
<b>15.10</b>	<b>Effects of dexamethasone 21-phosphate and high molecular weight heparin on MSCs differentiation to osteoblast. ....</b>	<b>65</b>
<b>15.11</b>	<b>hMSCs differentiation using dexamethasone 21-phosphate controlled released systems.....</b>	<b>75</b>
<b>16</b>	<b>Conclusions.....</b>	<b>81</b>
<b>17</b>	<b>References.....</b>	<b>83</b>
<b>18</b>	<b>Annexes.....</b>	<b>98</b>

## 2 RESUMEN

La creciente incidencia de trastornos y enfermedades óseas causadas por el envejecimiento progresivo y el aumento de la esperanza de vida constituyen un problema importante para las sociedades modernas, lo que genera la necesidad de desarrollar estrategias para la regeneración y síntesis de tejido óseo artificial. En particular, los materiales conductores inteligentes para la administración de fármacos se han convertido en una herramienta importante para la medicina regenerativa para promover la liberación controlada de agentes bioactivos osteogénicos. En este trabajo, el agente de diferenciación de osteoblastos, dexametasona 21-fosfato (Dex), se incorporó durante la polimerización de un material conductor en un electrodo de oro, y posteriormente se indujo su liberación controlada a través de estimulación eléctrica de bajo voltaje. La cantidad de fármaco liberado se determinó mediante voltamperometría cíclica y espectrometría de masas de alta resolución. El sistema conductor de liberación controlada de Dex se aplicó durante el cultivo de células madre mesenquimales humanas (hMSC) para inducir su diferenciación a osteoblastos. La actividad enzimática de ALPL, análisis de marcaje con anticuerpos fluorescentes y análisis moleculares de qPCR se utilizaron para estudiar los principales marcadores de osteoblastos expresados durante la diferenciación celular, lo que demostró que la liberación controlada de Dex desde la película conductora indujo la osteogénesis de las hMSCs. Además, se preparó un material poroso a base de polisacáridos y se utilizó también para la inmovilización y posterior liberación de Dex desencadenada principalmente por difusión. Asimismo, el sistema poroso también se utilizó durante el cultivo de hMSC, demostrando tener efecto durante la diferenciación a osteoblastos. Los resultados obtenidos son de gran valor para el desarrollo de diversas estrategias y sistemas de implantes en la reparación del tejido óseo y la medicina regenerativa.



### **3 ABSTRACT**

The increasing incidence of bone disorders and diseases caused by progressing aging and the increase in life expectancies constitute a major problem for modern societies, triggering a need to develop strategies for the regeneration and synthesis of artificial bone tissue. Particularly, smart conductive materials for drug delivery have become an important strategy for regenerative medicine to promote the controlled release of osteogenic bioactive agents. In this work, the osteoblast differentiation agent, dexamethasone 21-phosphate (Dex) was added during the polymerization of a conductive material on a gold electrode, consequently, controlled drug release was accomplished during low voltage electrical stimulation. The amount of released drug was determined using cyclic voltammetry and high-resolution mass spectrometry. Dex conductive controlled released system was applied during human mesenchymal stem cells (hMSCs) culture to induce their differentiation to osteoblast. ALPL enzymatic activity, immunofluorescence analysis and qPCR molecular studies were used to analyze the main osteoblast markers expressed during cells differentiation, demonstrating that controlled release of Dex from a conductive layer induced osteogenesis from hMSCs. Additionally, a porous material based on polysaccharides was prepared and used for Dex immobilization, where drug release was triggered mainly by diffusion. The system was used during hMSCs culture, demonstrating exceptional effect during osteoblast differentiation. Results are useful in the development of diverse strategies and implant systems in bone tissue repair and regenerative medicine field.

## 4 List of Tables

<b>Table 1.</b> Human mesenchymal stem cells (hMSCs) surface markers according with the body isolation source. ....	9
<b>Table 2.</b> Gradient elution method for the mobile phase using during dexamethasone-21 phosphate analysis. Solvents were H <sub>2</sub> O:0.05% formic acid (A) and methanol:0.05% formic acid (B).....	35
<b>Table 3.</b> Polysaccharide-based cryogels notation regarding the initial content of the polymers (expressed in weight percentage of initial blend solution for the cryogel formation). ....	36
<b>Table 4.</b> Culture media composition used during osteoblast differentiation of hMSCs.....	41
<b>Table 5.</b> qPCR reaction components using for the analysis of osteoblast markers.....	44
<b>Table 6.</b> Primers/probes used for real-time polymerase chain reaction during the osteoblast differentiation of hMSCs.....	44
<b>Table 7.</b> $\zeta$ -potential values of dispersions used in the fixation of the drug on the electrode.....	46
<b>Table 8.</b> Textural and physical properties of the polysaccharide-based cryogels. ....	57

## 5 List of Figures

<b>Figure 1.</b> Schematic representation of the functions and chemical/cellular composition of bones. From Zhang X, et al. 2021 (32). .....	5
<b>Figure 2.</b> Human mesenchymal stem cells sources and their differentiation capacity: osteoblasts, chondrocytes, myotubes, stromal cells, fibroblasts, and adipocytes. From James AW. 2013 (81).....	11
<b>Figure 3.</b> Flowchart depicting the biogenesis of osteoblasts after RunX2 transcriptional factor expression. From Thiagarajan L, Abu-Awwad HADM, Dixon JE. 2017 (93). .....	12
<b>Figure 4.</b> Dexamethasone signaling pathways during mesenchymal stem cells differentiation to osteoblast lineage. From Langenbach F, Handschel J. 2013 (10).....	17
<b>Figure 5.</b> Molecular structure of the EDOT monomer (left) and the PEDOT polymer (right).....	19
<b>Figure 6.</b> Deposited PEDOT/ $\kappa$ C/Dex film on a passivated electrode after 160 cycles of electrical oxidation (left) and gold electrode without passivation as reference (right). From Ramírez-Sánchez, et al. 2020 (12). .....	31
<b>Figure 7.</b> Schematic representation of the polymethylmethacrylate (PMMA) continuous flow cell used in electrochemical stimulation of PEDOT/ $\kappa$ C/Dex modified electrode. Designed by Eng. Jorge Sandoval. ....	34
<b>Figure 8.</b> Schematic representation of a gold electrode (left) and a stainless steel homemade trans well containing a Dex-based cryogel (right) adjusted to a well of a 48-wells culture plate. Designed by Eng. Sebastián León-Carvajal. ....	40
<b>Figure 9.</b> Size distribution (d.nm) of a. $\kappa$ C; b. $\kappa$ C/Dex and c. EDOT/ $\kappa$ C/Dex dispersions, measured by dynamic light scattering (DLS) method. ....	48
<b>Figure 10.</b> Profilometry images obtained for PEDOT/ $\kappa$ C/Dex films (a.) before and (b.) after 160 cycles of Cyclic Voltammetry in a 0.10 M ammonium acetate solution.....	49
<b>Figure 11.</b> 2D confocal Raman map of the 1430 $\text{cm}^{-1}$ band a. before release process and b. after 160 release cycles. Raman mapping of the 1625 $\text{cm}^{-1}$ band intensity c. before release process and d. after 160 release cycles at 0.5 $\mu\text{m}$ depth inside the conductive layer.....	50
<b>Figure 12.</b> Cyclic voltammograms for the PEDOT/ $\kappa$ C/Dex recorded at 25 $\text{mV}\cdot\text{s}^{-1}$ after 10, 60 and 160 cycles of electrical stimulation in ammonium acetate 0.10 M. ....	52
<b>Figure 13.</b> a. The passive release profile of Dex as a function of square root of time, over 300 minutes from unstimulated electrodes. The active electrically controlled delivery process by stimulation events (columns) compared to the passive release profile (line).....	53
<b>Figure 14.</b> Dexamethasone 21-phosphate release profile from PEDOT/ $\kappa$ C/Dex electrodes after electrical stimulation events. Arrows shown the events where the desirable Dex concentration was released. 56	
<b>Figure 15.</b> SEM images of the textural appearance of a. Starch, b. Starch/ $\kappa$ C, c. Starch/ $\kappa$ C/Dex 0.00002% wt., and d. Starch/ $\kappa$ C/Dex 0.0018 % wt. ....	58
<b>Figure 16.</b> Swelling ratio of St, St/ $\kappa$ C, St/ $\kappa$ Ca/Dex 0.00005% and St/ $\kappa$ C/Dex 0.0018% based .....	59
<b>Figure 17:</b> Erosion profiles of St, St/ $\kappa$ C, St/ $\kappa$ Ca/Dex 0.00005% and St/ $\kappa$ C/Dex 0.0018% based cryogels after 6 days of water exposure at 37°C.....	61
<b>Figure 18:</b> Dexamethasone release profiles from St/ $\kappa$ C/Dex porous materials containing 0.00005 wt.% to 0.0018 % of dexamethasone-21 phosphate in ammonium acetate 0.1 M, pH 7.2 at 37 °C and 100 rpm for 24 hours. ....	62

- Figure 19:** 2D micro-FTIR map of the  $1625\text{ cm}^{-1}$  signal before (a-d) and after (e-h) 24 hours of Dex release from the polysaccharide-based cryogel using 0.0002% wt. (a; e); 0.0004%wt. (b; f); 0.0010% wt. (c; g), and 0.0018% wt. (d; h) of drug in the initial formulation. .... 63
- Figure 20.** Biocompatibility analysis of starch-based cryogels and PEDOT/ $\kappa$ C/Dex modified electrode using the CCK-8 assay on hMSCs culture. .... 65
- Figure 21.** ALPL enzymatic activity $\cdot\text{min}^{-1}\cdot\text{ug}^{-1}$  total protein of hMSCs at 3, 7 and 14 days of analysis. C-: Basal media; Dx: Basal media + Dx 100 nM; Dex-21 ph: Basal media + Dex 100 nM. \*\*Significant differences ( $p < 0.05$ ), letters are grouping statistically equal treatments. .... 66
- Figure 22.** ALPL enzymatic activity $\cdot\text{min}^{-1}\cdot\text{ug}^{-1}$  total protein of hMSCs culture on culture media containing different concentrations of hep at 3, 7 and 14 days of analysis. Negative control: Basal media, Dex-21ph: Basal media + Dex 100 nM, Dex-21ph + Hep 0.025: Basal media + Dex 100 nM + Hep 0.025 UI $\cdot\text{mL}^{-1}$ ; Dex-21ph + Hep 0.25: Basal media + Dex 100 nM + Hep 0.25 UI $\cdot\text{mL}^{-1}$ , Dex-21ph + Hep 0.5: Basal media + Dex 100 nM + Hep 0.5 UI $\cdot\text{mL}^{-1}$ ; Dex-21ph + Hep 2.5: Basal media + Dex 100 nM + Hep 2.5 UI $\cdot\text{mL}^{-1}$ ; Dex-21ph + Hep 25: Basal media + Dex 100 nM + Hep 25 UI $\cdot\text{mL}^{-1}$ . \*\* Significant differences ( $p < 0.05$ ), letters are grouping statistically equal treatments. .... 68
- Figure 23.** ALPL enzymatic activity $\cdot\text{min}^{-1}\cdot\text{ug}^{-1}$  total protein of hMSCs culture at 3, 7 and 14 days of analysis. Negative Control: Basal media, Dex-21ph: Basal media + Dex 100 nM + ascorbic acid +  $\beta$ -Glycerophosphate, Hep 0.5 UI $\cdot\text{mL}^{-1}$ : basal media + ascorbic acid +  $\beta$ -Glycerophosphate + Hep 0.5 UI $\cdot\text{mL}^{-1}$ . \*\* Significant differences ( $p < 0.05$ ), letters are grouping statistically equal treatments. .... 69
- Figure 24.** Comparisons of gene expressions of ALPL, OPN, and RunX2 among Dex-21ph 100 nM and Dex base 100 nM treatments after 7 and 14 days of analysis. \*\* Significant differences ( $p < 0.05$ ), letters are grouping statistically equal treatments..... 71
- Figure 25.** Immunofluorescence analysis of hMSCs using anti-ALPL antibody during hMSCs osteoblast differentiation induced by dexamethasone 21-phosphate and heparin: a. Negative control, b. Dex 100 nM, and c. Dex 100 nM + Hep 0.5 UI $\cdot\text{mL}^{-1}$ . .... 73
- Figure 26:**Immunofluorescence analysis of hMSCs using anti-Col I antibody during hMSCs osteoblast differentiation induced by dexamethasone 21-phosphate and heparin: a) Negative control, b) Dex 100 nM and c) Dex 100 nM + Hep 0.5 UI $\cdot\text{mL}^{-1}$ . .... 74
- Figure 27.** ALPL enzymatic activity $\cdot\text{min}^{-1}\cdot\text{ug}^{-1}$  total protein of hMSCs culture on culture media containing at 7 and 14 days of analysis. Negative : Basal media, Dex-21ph: Basal media + Dex 100 nM + Hep 0.5 UI $\cdot\text{mL}^{-1}$ , Cryogel 0.00005%: Basal media + Hep 0.5 UI $\cdot\text{mL}^{-1}$  + 25 mg Dex 0.00005% cryogel; Electrode: Basal media + Hep 0.5 UI $\cdot\text{mL}^{-1}$  + Electrode. \*\* Significant differences ( $p < 0.05$ ), letters are grouping statistically equal treatments..... 76
- Figure 28.** Comparisons of gene expressions of ALPL, OPN, and RunX2 among Dex-21ph 100 nM and Dex-21ph controlled released treatments after 7 and 14 days of analysis. \*\* Significant differences ( $p < 0.05$ ), letters are grouping statistically equal treatments..... 78
- Figure 29.** Immunofluorescence analysis of hMSCs using anti-OPN antibody after biochemical stimulation induced by dexamethasone 21-phosphate and heparin: a. Negative control, b. Dex 100 nM + Hep 0.5 UI $\cdot\text{mL}^{-1}$ , c. 25 mg Dex 0.00005% cryogel + Hep 0.5 UI $\cdot\text{mL}^{-1}$ , and d. electrode + Hep 0.5 UI $\cdot\text{mL}^{-1}$ ..... 80

## **6 List of abbreviations**

ALPL: Alkaline phosphatase

Ang1: Angiopoietin 1

BMPs: Bone morphogenetic proteins

BSP: Bone sialoprotein

C/EBP $\alpha$ : Enhancer binding protein  $\alpha$

sFRPs: Secreted frizzled-related proteins

Col1A1: Type I collagen gene

CS: Chondroitin sulfate

CXCL12: CXC ligand 12

Dex: Dexamethasone 21-phosphate disodium salt

DS: Dermatan sulfate

Dx: Dexamethasone base

ECM: Extracellular matrix

EDOT: 3,4-ethylenedioxythiophene

FBS: Fetal bovine serum

FGF: Fibroblast growth factor

GAGs: Glycosaminoglycans

GlcA: D-glucuronic acid

GlcN: D-glucosamine residues

HA: Hyaluronan

Hep: Heparin

HS: Heparan sulfate (HS)

HSCs: Hematopoietic stem cells

IdoA: L-iduronic acid

IPA: Isopropyl-alcohol

KCl: Potassium chloride

KS: Keratan sulfate

MSCs: Mesenchymal stem cells  
hMSCs: Human mesenchymal stem cells  
 $\text{NH}_4\text{CH}_3\text{CO}_2$ : Ammonium acetate  
NMTS: Nuclear matrix targeting signal  
OCN: Osteocalcin  
OPN: Osteopontin  
OSE2: Osteoblast-specific cis-acting element  
OSX: Osterix  
Pax3: Paired box 3  
PCL: Poly( $\epsilon$ -Caprolactone)  
PEDOT: poly (3,4 ethylenedioxythiophene)  
SCF: Stem cell factor  
SEM: Scanning electron microscopy  
TGF- $\beta$ : Transforming growth factor- $\beta$   
 $\kappa$ C:  $\kappa$ -Carrageenan  
 $\beta$ -Gly:  $\beta$ -Glycerophosphate  
AA: Ascorbic acid

## 7 List of Annexes

<b>Annex 1.</b> Code used for the configuration of the electrode stimulator .....	98
<b>Annex 2.</b> Galvanostatic curve of the electro-polymerization process from an EDOT/ $\kappa$ C:Dx dispersion onto a bare gold electrode.....	100
<b>Annex 3.</b> Raman spectra of the PEDOT/ $\kappa$ C:Dx coating.....	101
<b>Annex 4.</b> $\mu$ -Raman spectral measurement of the dexamethasone 21-phosphate disodium salt. ....	102
<b>Annex 5.</b> RNA concentration values.....	103
<b>Annex 6.</b> Immunofluorescence analysis of hMSCs using anti-ALPL antibody after biochemical stimulation induced by dexamethasone 21-phosphate and heparin: a) Negative control, b) Dex 100 nM + Hep 0.5 UI·mL <sup>-1</sup> , c) 25 mg Dex 0.00005% cryogel + Hep 0.5 UI·mL <sup>-1</sup> , and d) electrode + Hep 0.5 UI·mL <sup>-1</sup> ..	104
<b>Annex 7.</b> Paper 1. Design and simulation of flexible thin-film electrodes for cell culture stimulation .....	105
<b>Annex 8.</b> Paper 2. Polysaccharide $\kappa$ -Carrageenan as Doping Agent in Conductive Coatings for Electrochemical Controlled Release of Dexamethasone at Therapeutic Doses.....	106
<b>Annex 9.</b> Paper 3. Smart Porous Multi-Stimulus Polysaccharide-Based Biomaterials for Tissue Engineering.....	111

## 8 List of Equations

$\varepsilon = 1 - \rho_{bulk} \rho_{skel} \times 100$ (Equation 1) .....	37
$V_p = 1 \rho_{bulk} - 1 \rho_{skel}$ (Equation 2).....	37
$S_r = W_s - W_i W_i \times 100$ (Equation 3) .....	37
$DD = (W_i - W_f) W_i \times 100$ (Equation 4).....	37





UNIVERSIDAD DE  
COSTA RICA

SEP Sistema de  
Estudios de Posgrado

**Autorización para digitalización y comunicación pública de Trabajos Finales de Graduación del Sistema de Estudios de Posgrado en el Repositorio Institucional de la Universidad de Costa Rica.**

Yo, Karla Sofía Ramírez Sánchez, con cédula de identidad 304920710, en mi condición de autor del TFG titulado \_\_\_\_\_

EFFECTO DE LA LIBERACIÓN CONTROLADA DE MOLÉCULAS CARGADAS  
SOBRE LA DIFERENCIACIÓN DE LAS CÉLULAS MADRE MESENQUIMALES HUMANAS A OSTEÓBLASTOS

Autorizo a la Universidad de Costa Rica para digitalizar y hacer divulgación pública de forma gratuita de dicho TFG a través del Repositorio Institucional u otro medio electrónico, para ser puesto a disposición del público según lo que establezca el Sistema de Estudios de Posgrado. SI  NO \*

\*En caso de la negativa favor indicar el tiempo de restricción: \_\_\_\_\_ año (s).

Este Trabajo Final de Graduación será publicado en formato PDF, o en el formato que en el momento se establezca, de tal forma que el acceso al mismo sea libre, con el fin de permitir la consulta e impresión, pero no su modificación.

Manifiesto que mi Trabajo Final de Graduación fue debidamente subido al sistema digital Kerwá y su contenido corresponde al documento original que sirvió para la obtención de mi título, y que su información no infringe ni violenta ningún derecho a terceros. El TFG además cuenta con el visto bueno de mi Director (a) de Tesis o Tutor (a) y cumplió con lo establecido en la revisión del Formato por parte del Sistema de Estudios de Posgrado.

**INFORMACIÓN DEL ESTUDIANTE:**

Nombre Completo: Karla Sofía Ramírez Sánchez

Número de Carné: B99393 Número de cédula: 304920710

Correo Electrónico: karla.ramirezsanchez@ucr.ac.cr

Fecha: 02 de enero 2023 Número de teléfono: 7265-4137

Nombre del Director (a) de Tesis o Tutor (a): Mónica Prado Porras

**FIRMA ESTUDIANTE**

Nota: El presente documento constituye una declaración jurada, cuyos alcances aseguran a la Universidad, que su contenido sea tomado como cierto. Su importancia radica en que permite abreviar procedimientos administrativos, y al mismo tiempo genera una responsabilidad legal para que quien declare contrario a la verdad de lo que manifiesta, puede como consecuencia, enfrentar un proceso penal por delito de perjurio, tipificado en el artículo 318 de nuestro Código Penal. Lo anterior implica que el estudiante se vea forzado a realizar su mayor esfuerzo para que no sólo incluya información veraz en la Licencia de Publicación, sino que también realice diligentemente la gestión de subir el documento correcto en la plataforma digital Kerwá.

## 9 Introduction

The increasing incidence of bone disorders and diseases imply a need to develop strategies for the regeneration and synthesis of artificial bone tissue that can be applied *in vivo* (1). Specifically, tissue engineering applications during tissue regeneration have become a potential tool to be applied in bone repair therapies and orthopedic diseases.

Regenerative medicine and tissue engineering aim to repair damaged tissues using cells or synthetic/natural cellular components to initialize the natural regeneration process (2). The basic tissue engineering strategy involves the use of biomaterials and scaffolds with growth factors that, in combination with specific cell types, restore the damage and functionality of the affected tissue (3, 4).

The development of devices for the activation of osteogenic differentiation on precursory cells to provide approaches for the reduction of inflammation and subsequent infections is currently being studied, mainly because the release of pharmacological molecules incorporated on the systems provide better control over their supply and improve the specificity of drug targeting (1, 4, 5).

Progress in the study and synthesis of relevant biomedical applications have focused on the use of pluripotent stem cells; particularly since certain stem cells offer promising results for the formation of osteoblasts and their application in tissue repair therapies (6).

Mesenchymal stem cells (MSCs) have been for many years an interesting field of research as suitable candidates for many therapeutic applications, including tissue regeneration and cell therapy (2, 7). The importance is reinforced by the multipotentiality of MSCs to differentiate in several cell lineages, where the main application is focus in improving healing of large bone defects (7, 8). Current research in tissue engineering often involve the combination of MSCs with novel-

synthesized bioactive biomaterials with physical, chemical, and structural similarities to physiological MSCs-niche (2, 7, 8).

Dexamethasone base (Dx) is one of the most prescribed corticosteroids worldwide due to its effect on the negative regulation of the expression of inflammatory cytokines, chemokines, and metalloproteases (9). Moreover, it is one of the most important drugs used during the MSCs culture, specifically, this synthetic glucocorticoid in combination with other growth factors and therapeutic drugs is recognized for its *in vitro* effect to induce and enhance the differentiation of MSCs to osteoblasts (5, 10–12).

GAGs are a family of polydisperse, sulfated, anionic, linear polysaccharides that have been employed on MSCs culture (13) and are responsible for several critical biological functions (14–16). Preliminarily, it is well known that the negative charges of these molecules may interact with cell receptors associated with numerous biological processes (17). On the contrary, other authors have reported undesirable GAGs effects on cells culture, because of that, its use as additive on culture media has been a controversial issue (18).

Several multidisciplinary studies and research involving the field of biochemistry and cell culture engineering have been developed to generate novel strategies for stem cell differentiation, a well-known example is the controlled release of drugs (19, 20). Dexamethasone 21-phosphate disodium salt (Dex) immobilization and delivery from polysaccharide-based porous and non-porous conductive materials have been confirmed by collaborators (5, 12), to create synthetic appropriate scaffolds for osteo-induction of MSCs.

Drug release methods may be described by two main approaches: mechanical systems related to those that work through pump-type mechanisms, which have miniaturized technology to be implanted *in vivo* (21, 22); and by the use of polymeric materials, which include diffusional release, chemical release, and more recently, electrochemical release methods (19, 20). Many of these systems are implanted *in vivo* and drug release is controlled according to the drug carrier

system used (22). Particularly, the diffusion-controlled release from aerogels has been studied, so that they ultimately function as scaffolds for *in vivo* tissue regeneration studies (5, 23).

Additionally, using electrochemical mechanisms, the release of drugs from a matrix constituted for the conductive polymer poly (3,4 ethylenedioxythiophene) (PEDOT) was studied in 2019, from which the drug dissociates according to an electrical stimulus (12, 24). Polysaccharide-based porous materials and PEDOT-polysaccharides systems have been proposed as carriers for bioactive compounds immobilization and their subsequently controlled or non-controlled delivery (12).

Finally,  $\kappa$ -Carrageenan ( $\kappa$ C) in combination with other polysaccharides is the focus of study during the synthesis of scaffolds that may function as an extracellular matrix (ECM). ECM is a dynamic three-dimensional structure which provides structural support for cells (25). The diversity of ECM components and their interaction with cells receptors makes possible the regulation of cellular behavior (26, 27). Certain porous materials based on polysaccharides have been proposed as ECMs and as drug-delivery systems (28, 29), mainly because they offer a highly porosity, three-dimensional structure, and controllable-mechanical properties (25, 30). Porous systems can act as a carrier for drugs, showing high loading capacity, enhanced stability upon storage, and accelerated drug release (i.e. Dx and Dex), if required (31), because of that, tissue engineering applications have also studied these type of systems as potent stimulators of MSCs differentiation to bone cells.

In this work,  $\kappa$ C/PEDOT-conductive materials and polysaccharides-based porous systems containing Dex were prepared. Self-made gold electrodes were used for PEDOT films synthesis. Cryogels and electrodes were used as Dex-delivery scaffolds obtaining the drug at therapeutic concentrations and, both systems were applied during MSCs culture to study their potential influence during osteoblast differentiation of cells. Finally, the potential effect of the heparin (Hep), which is

the most negatively charged GAG, during MSCs differentiation to osteoblast was also confirmed.

## 10 Theoretical framework

### 10.1 Mesenchymal stem cells in tissue engineering applications for bone repair therapies.

#### 10.1.1 Bone diseases as consequence of aging progressive.

The bone is a high-density and complex calcified tissue, chemically built up as a mineralized matrix which comprises organic matrices, water, lipidic contents, collagen, and a small amount of non-collagenous proteins (32–34). Bone tissue exerts vital functions: protects internal organs, is a support for the body, facilitates the movement, produces blood and progenitor lymphoid cells, regulates blood pH, and stores and releases fats and minerals. A summary of the bone composition and functions is showed in Figure 1:

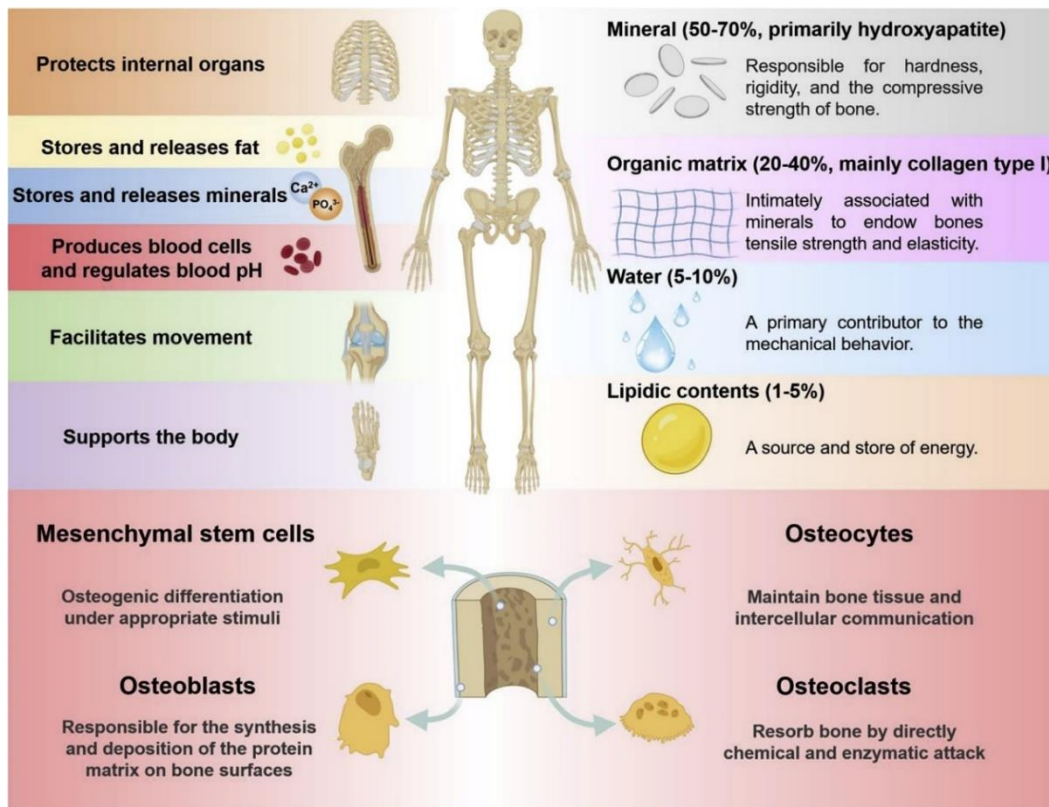


**Figure 1.** Schematic representation of the functions and chemical/cellular composition of bones. From Zhang X, *et al.* 2021 (32).

As progressing aging and the increase in life expectancies, the impact of bone-related diseases such as bone cancer (e.g., osteosarcoma, bone metastasis), bone infection, osteoporosis, and osteoarthritis (OA) also increased (35). In fact, several reports have demonstrated that these bone defects have increased in the last years, constituting a major issue for modern societies, affecting more than 50 million people in the United States, threatening public health (35, 36).

Bone autografts and allografts are the most traditional strategies for the treatment of these diseases and bone reconstruction, nevertheless, some of these treatments may present several drawbacks. Because of that, numerous strategies employing organic and inorganic porous and non-porous scaffolds for the *in vitro* or *in vivo* colonization of MSCs have been extensively studied, mainly controlling the physical and mechanical properties of the scaffolds, and approaching the properties of multipotentiality of MSCs (37–39), as will be discussed in the following chapters.

### **10.1.2 Characteristics of mesenchymal stem cells.**

The human body houses several cell types with capacity to give to daughter cells restricted potential. Some examples of such cells are the embryonic stem cells, the hematopoietic stem cells, and the MSCs (40).

Specifically, MSCs represent a rare population of multipotent progenitors, described as adherent and non-hematopoietic stromal cells. These cells were initially described in bone marrow (BM) by Friedenstein in 1966 (41). However, their isolation has been carried out from other adult connective tissues (40, 42, 43).

MSCs are described as a fibroblastic cell type with high replicative capacity that can produce clonal cells. Because their multipotentiality, their use has been very explored in tissue engineering studies and for clinic uses. MSCs are capable to induce multilineage differentiation from a single cell, and it is known their ability to

differentiate into osteoblasts, chondrocytes, adipocytes, myocytes, tenocytes, and neural cells (40, 44).

Even though of the importance of MSCs differentiation abilities for tissue repair, the main mechanism of MSCs therapeutic effects is related to their paracrine effects (45). According with Pounos (40), after a tissular damage event, these cells are activated by several signals including injury, inflammation, and necrosis, triggered their paracrine effects including angiogenesis, preventing apoptosis, and modulating extracellular matrix dynamics. Equally, MSCs are related with the modulation of the activation or suppression of the immune system, to control the whole-tissue regeneration process.

Therefore, it is important to know that although the *in vitro* expansion of MSCs constitutes a marked and sustained increase in proliferation, MSCs are affected by their replicative senescence, and the slowly replication will increase over time, while the multipotentiality will gradually decline. This phenomenon affects the downstream applications including the *ex vivo* MSC expansion before reimplantation to home to sites of injury and inflammation (43).

### **10.1.3 MSCs isolation sources.**

Several sources in the human body have been employed for stem cells isolation. The selection of the organ or tissue depends on the logistical and practical isolation method and of the stem cells *in vitro* desirable characteristics, also, is important to define the differentiation potential of cells (46, 47).

Although MSCs are obtained from almost any tissue on the human body, the most common sources are bone marrow (BM) and adipose tissue (AT). Nevertheless, there are some practical limitations during isolation method depending on the difficulty and invasiveness of the process (46, 48).

MSCs were first discovered in the bone marrow, where these cells constitute an element of stromal cells in the tissue. However, only a small percentage of the



total number of bone marrow populating cells are MSCs, some researchers have reported the isolation of only 0.01% to 0.001% of these mononuclear and plastic adherent fibroblasts like cells colonies and their isolation depend on the patient status and the volume of aspirates. In bone marrow, MSCs are in close association with the resident hematopoietic stem cells (HSCs), near of the sinusoidal endothelium. These cells participate as osteogenic progenitors but also in the production of signals for the modulation of the maturation of HSCs through the secretion of tropic factors such as angiopoietin 1 (Ang1), stem cell factor (SCF), and CXC ligand 12 (CXCL12) (42, 48, 49).

Although cells isolated from BM are the most employed during bone tissue therapies, BM isolation is a highly invasive and painful procedure implying general anesthesia and many days for hospital care, making the isolation more problematic in comparison with peripheral blood, AT, or birth-derived tissues. Because of that some researchers have searched alternative sources for MSCs isolation (48). One example are the AT-derived MSCs, which can be isolated from subcutaneous lipoaspirates resulted as a product of cosmetic and therapeutic surgical interventions, peritoneal and inguinal fat pads (47, 50).

According with some authors, AT allows the isolation of a large number of high activity cell, in fact, it is reported that the percentage of MSCs are nearly of 2% of stromal vascular fraction on AT and sometimes nearing 30%, reported as the greatest one in all tissues (47, 50, 51). One important thing is that approximately the 98–100% of the cells obtained from AT are viable and could be expanded effectively *in vitro* conserving their stability in long-term cell cultures (50).

In comparison with BM-MSCs, AT-MSCs present very similar characteristics in terms of morphology, phenotype, functions, and multilineage differentiation potential. The isolation methods are easier and less painful than BM-MSCs, nevertheless, depending on the donor characteristics (e.g. age and sex), the expansion and differentiation could be affected (50).

On the other hand, MSCs populations could be also found in dental tissues (52, 53), which not only display self-renewal and multi-differentiation potential but also present immunomodulatory mechanisms and potent tissue regenerative properties. Umbilical derived-MSCs present similar surface phenotype, multipotency and plastic adherence properties of those MSCs found in other sources, they are also important in regenerative medicine (54, 55). Other sources for MSCs isolation include endometrial derived MSCs (56), synovium and synovial fluid derived MSCs (57), placental derived MSCs (58), peripheral blood (59), and others.

#### 10.1.4 Mesenchymal stem cells surface markers.

Once MSCs isolation is completed, the characterization of cell markers should be carried out. According to some authors, hMSCs expresses a specific set of cell surface markers that make it different for the other cells. HMSCs are positive for CD73, CD90, CD105 whereas are negative for the expression of CD14, CD34, and HLA-DR. The main MSCs markers according with the body source are reported in Table 1.

**Table 1.** Human mesenchymal stem cells (hMSCs) surface markers according with the body isolation source.

MSCs type	Cell markers	Reference
BM-hMSCs	CD105 CD73 CD90 CD271 CD146, CD13, CD45, SSEA-3 Stro-4	(60–64)
AT-hMSCs	CD90, CD44, CD105, CD73, CD166, CD13, CD146	(65–68)
Dental tissue-hMSCs	CD73, CD90, CD105, CD146, CD29, CD44, CD105	(69–71)
Umbilical-hMSCs	CD44, CD29, CD105, CD73, HLA-ABC, CD90, CD70, CD166	(69–71)

Endometrial-hMSCs	CD105, CD90, CD73, CD44, CD29, PDGFR $\beta$	(72–74)
Placental-hMSCs	CD166, CD105, CD90, CD73, CD49e, CD44, CD29, CD13, HLA-ABC, CD146, CD49a/VLA-1, STRO-1, CD106	(75–79)

### 10.1.5 Multilineage differentiation of mesenchymal stem cells.

One of the most important characteristics of MSCs is their capability to differentiate into a diverse set of mesoderm-type cells, including osteoblasts, adipocytes, and chondrocytes (Figure 2). This property of MSCs opens therapeutic opportunities for the treatment of lesions in mesenchymal tissues, focusing mainly on bone and cartilage defects, for the tissue regeneration therapies. In general, the differentiation into different cell lineages is determined by different factors and signaling pathways. Collectively, canonical and noncanonical  $\beta$ -catenin-dependent Wnt signaling has demonstrated both pro-osteogenic and anti-adipogenic activities (80, 81).

Wnt/ $\beta$ -catenin signaling pathway maintains preadipocytes in an undifferentiated state through inhibition of the adipogenic transcription factors: the enhancer binding protein  $\alpha$  (C/EBP $\alpha$ ) and peroxisome proliferator-activated receptor  $\gamma$  (PPAR $\gamma$ ), because of that, several studies have demonstrated that the inhibition of Wnt/ $\beta$ -catenin signaling positively regulates adipogenesis (81).

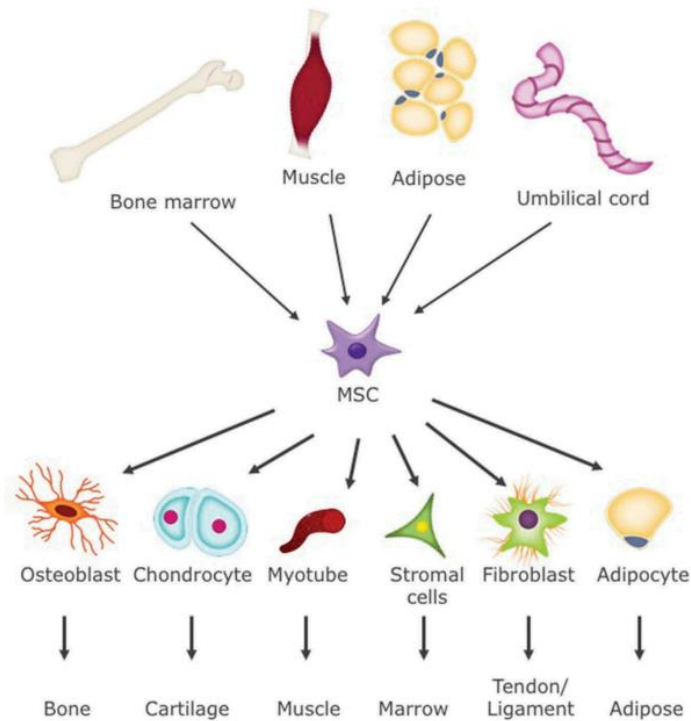


**Figure 2.** Human mesenchymal stem cells sources and their differentiation capacity: osteoblasts, chondrocytes, myotubes, stromal cells, fibroblasts, and adipocytes. From James AW. 2013 (81).

According with Figure 3, PPAR $\gamma$  is considered the master regulator of adipogenesis as well as RunX family transcription factor 2 (RunX2) is reported as the master regulator of osteogenesis. PPAR $\gamma$  not only is an adipogenic regulator, but also is implicated as an anti-osteoblastogenic molecule.

PPAR $\gamma$  and RunX2 act together to mediate the effects of various cytokines in determination of adipogenesis versus osteogenesis during MSC differentiation, the expression of a transcriptional factor is related with the down regulation of the other. Particularly, secreted frizzled-related proteins (sFRPs) are induced during adipogenesis, the overexpression of sFRP1 promotes adipogenic differentiation through inhibition of canonical Wnt signaling. Nevertheless, currently, it is lack of the fully mechanism through which Wnt/ $\beta$ -catenin signaling is regulated in controlling the fate of MSCs is known (80, 81, 83, 84).

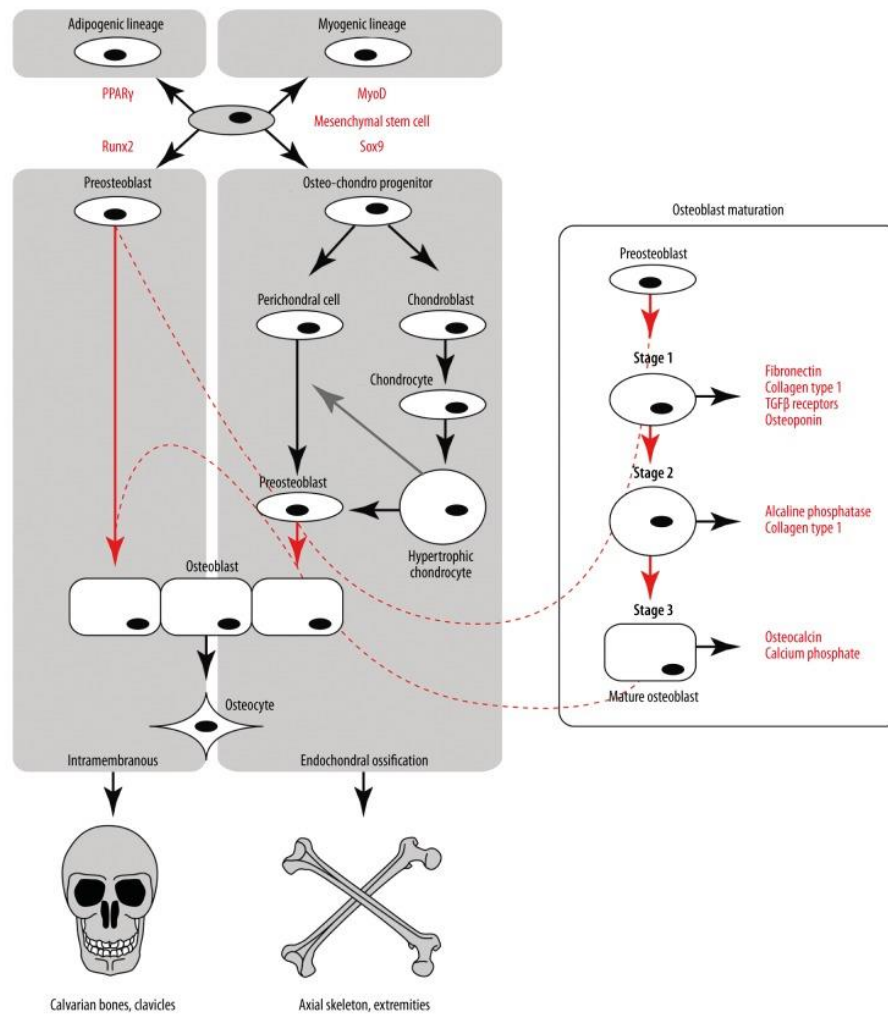


**Figure 3.** Flowchart depicting the biogenesis of osteoblasts after RunX2 transcriptional factor expression. From Thiagarajan L, Abu-Awwad HADM, Dixon JE. 2017 (93).

On the other hand, myogenic differentiation of MSCs understands the activation of some specific myogenic transcription factors, including paired box 3 (Pax3), MyoD, and Myf-5, which are required for the differentiation of MSCs on skeletal myogenic lineages, whereas myogenin and MRF4 are thought to regulate cell fusion and terminal differentiation. MyoD is considered the master regulator on MSCs differentiation to myoblast. Pax3 also has a great influence during myoblast differentiation. Some studies have reported that Pax3 overexpression promotes the myogenic differentiation and blocks the adipogenic, osteogenic, and

chondrogenic differentiation of MSCs. In addition, MyoD overexpression was found to inhibit Twist-1 (an antagonist of myogenesis), resulting in an increase in muscle cell differentiation (85–90).

Figure 2 also shows that MSCs are recognized as the common ancestor for osteoblast. According with Hang, *et al.* (91), these cells participate during the endochondral and intramembranous ossification. Firstly, the transcriptional factor RunX2 is expressed to limit the potential of stem cells to differentiate to osteoblast. In fact, this transcriptional factor is the most essential for osteoblast commitment, differentiation, matrix production, and mineralization during bone formation. Rutkovskiy, *et al.* (92) reported that the ectopic expression of RunX2 in non-osteoblastic cells leads to the expression of genes that determine the osteoblast phenotype and controls the expression of osteogenic marker genes such as *ALPL* (Alkaline phosphatase), *OPN* (Osteopontin), *OSX* (Osterix), *Col1A1* (type-I collagen), *BSP* (Bone sialoprotein), and *OCN* (Osteocalcin) (93).

There is a nuclear matrix targeting signal (NMTS) in the C terminal of RunX2. These NMTS can localize RunX2 in the osteoblast-specific cis-acting element (OSE2) in the nucleus, Runx2 binds OSE2 in the promoter to initiate osteogenesis. During the first step, the expression of osteoblast differentiation markers including the fibronectin, Col1A1 and OPN is completed. After that, the maturation of extracellular matrix is carried out by expression and activation of ALPL enzyme, and finally, matrix mineralization is enriched by OCN, which promotes the calcium deposition in the matrix (Figure 3) (93–97).

Bones of the axial skeleton are formed by a film of cartilage intermediate, formed in the process of endochondral ossification. During this process, MSCs begin to differentiate along a pathway that leads the differentiation of chondrocytes, which is required for skeletogenesis. Chondrogenesis starts when MSCs are stimulated to express Sox9, which is require only at the onset of chondrogenesis. Sox9 is the main transcription factor essential for chondrocyte differentiation, their expression is followed by deposition of cartilage matrix containing collagen I, IX and XI as well as aggrecan.

The expression of the SOX protein is controlled by fibroblast growth factor (FGF), transforming growth factor- $\beta$  (TGF- $\beta$ ), bone morphogenetic proteins (BMPs) and Wnt families. Specifically, BMPs control the expression of Sox9 via the BMP receptors BMP1RA and BMP1RB, FGF has an important role for the proliferation and survival of cranial neural crest derived cells, and the Wnt signalling molecules initiates chondrogenesis activating  $\beta$ -catenin into canonical Wnts and noncanonical Wnts.

Members of the TGF- $\beta$  family also have been shown to play a major role in bone and cartilage development. Particularly, TGF- $\beta$  promotes proteoglycan deposition, because of that, TGF- $\beta$  is a standard media additive used during chondrogenesis differentiation of MSCs (82, 98–102).

#### **10.1.6 Importance of the mesenchymal stem cells in tissue engineering and bone defects.**

After orthopedic surgeries caused by bone defects, most people experience trauma, inflammation, or remnant tumors. Because of that, tissue engineering has provided diverse strategies for repairing such tissue defects, nevertheless, their clinical application or scaleup has given suboptimal results, been still limited (103, 104).

Different types of bone grafts have been used: autografts, allografts, and synthetic grafts. The autograft in comparison with the others is considered the best strategy to treat bone defects, mainly considering the osteoinductive and osteoconductive properties, and the histocompatibility of the biological scaffold employed (105). Nevertheless, diverse studies have evidenced that a MSCs-based therapy in combination with allogenic grafts could be a viable alternative to autologous bone transplants, specifically, taking advantage of the MSCs multipotentiality, the possibility of being easily isolated from tissue aspirates, and their high *ex vivo* expansion potential. The above is accompanied by the release of growth factors,

and the stimulation of these progenitor cells to be finally injected in the damaged tissue (105–107).

An example of MSCs-based therapies consisted in the culture of cells on a three-dimensional scaffold. According with some authors (108), MSCs have been seeded on ceramic biomaterials, the local implantation at the defect resulted in complete fusion at 5–7 months post-surgery, showing good integration with the affected tissue and causing repair.

Currently, some other scaffolds based on natural and synthetic materials are available, an example is the use of hydroxyapatite (HA) scaffolds for *in vitro* MSCs culture, which has been used in several animal models, showing a great potential in promoting bone union and repair. One of the most important properties of these materials is the open porosity which make possible the vascularization, the blood vessels are closely involved in osteogenesis, the osteoblast cells produce osteoid tissues, which differentiate to osteocytes, and finally form healthy bone (106, 107). Nevertheless, several strategies for enhancing vascularization including the modification of the scaffold design, the release of angiogenic factors, and *in vivo* and *in vitro* pre-vascularization are currently under study, which will be reviewed in upcoming chapters.

## **10.2 Dexamethasone and glycosaminoglycans as osteoblast differentiation factors during *in vitro* MSCs culture.**

### **10.2.1 Effect of dexamethasone on MSCs differentiation.**

Differentiation of hMSCs is influenced by changes in the biochemical agents of the culture medium that contains them under *in vitro* conditions, such as the drug Dx.

Dx is a synthetic glucocorticoid that reduces inflammation in the central nervous system, acting through glucocorticoid receptors found in most neurons and glial cells (5, 10, 23, 109–111). In addition, is one of the most prescribed



corticosteroids worldwide as a treatment for eye diseases, rheumatoid arthritis and to reduce inflammation due to its effect on the negative regulation of the expression of inflammatory cytokines (IL-1, IL-6, IFN- $\gamma$  and TNF- $\alpha$ ), chemokines (CXCL10 and CCL-5), and metalloproteases (9).

Dx along with other growth factors and therapeutic drugs is recognized for its *in vitro* effect to induce and enhance the differentiation of hMSCs to osteoblasts (10, 11). Due to being locally delivered, the specificity and efficiency of Dx means that only small amounts of the drug are required (5, 10, 23, 109–111). In this case, the optimal Dx concentration used to drive differentiation of MSCs is in the range of 10 to 100 nM. An interesting point to consider is that concentrations greater than 1000 nM can have a toxic effect on cells and have even been related to the development of osteoporosis and bone density loss (4, 10).

MSC differentiation into osteoblasts is strictly regulated by diverse factors that persist in intracellular signaling pathways such as Notch/Hedgehog, ERK, and  $\beta$ -catenin. The activation of these signaling pathways leads to the initial expression and subsequent regulation of the *RunX2* gene, this process induces to the transcription of the *RunX2*, which as was mentioned, is the main transcriptional factor for osteoblast differentiation. After *RunX2*, the expression of other important markers of osteoblast is carried out, including the *ALPL* gene that codes for alkaline phosphatase, and the *Col1A1*, followed by the mineralization of the extracellular matrix (112, 113).

The role of Dx in MSC and its influence on osteoblast differentiation is explained by the expression of *RunX2* by various mechanisms. The first one, through the transcriptional activation of the gene mediated by FHL2 (upregulated in presence of Dx) protein which activates the WNT/ $\beta$ -catenin signaling-dependent *RunX2* expression. Dx binds to the corticosteroid-binding site of the response element in the FHL2 promoter, inducing protein synthesis. FHL2 is bound to  $\beta$ -catenin in the presence of WNT3a (an activator of the WNT signaling pathway), this leads to the release of  $\beta$ -catenin to the nucleus and enhances the *RunX2* transcription.

The second mechanism explains that the regulation of *RunX2* is mediated by the activity of a TAZ molecule (a transcriptional coactivator) type  $\beta$ -catenin. In this case, TAZ is responsible for the recruitment of components of the transcriptional machinery for *RunX2* while repressing *PPAR $\gamma$*  gene transcription, to avoid adipogenic differentiation. Finally, the third mechanism of osteogenesis induction by Dx is through the activation of MKP-1 (ERK2). For the latter case, Dx increases the transcription of the ERK2 gene, once transcribed, it phosphorylates the RunX2 factor at serine 125, which leads to greater activity and expression of osteogenic genes (10, 112, 114) (Figure 4).

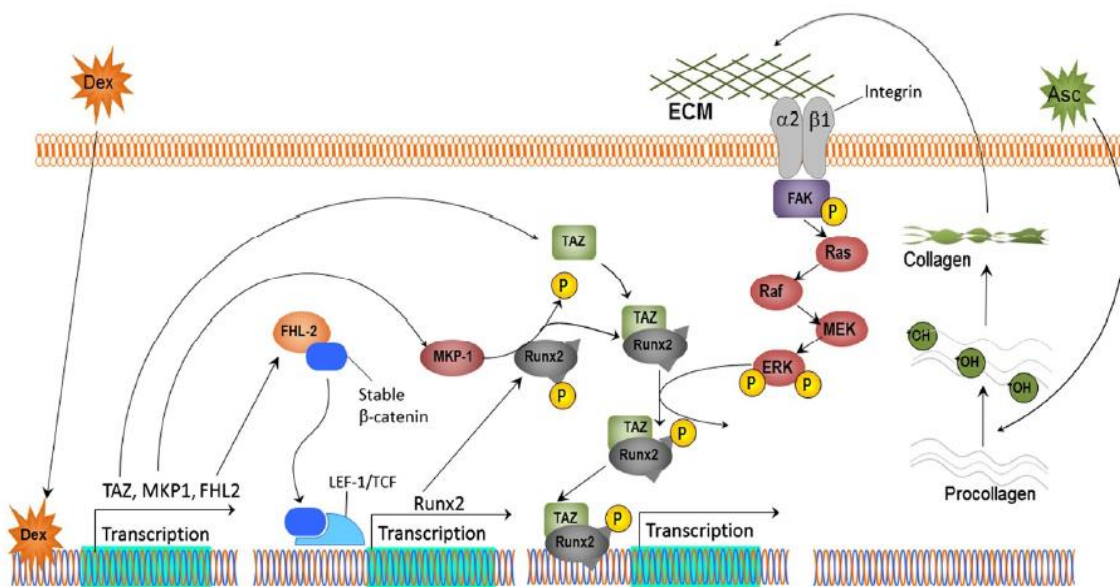


**Figure 4.** Dexamethasone signaling pathways during mesenchymal stem cells differentiation to osteoblast lineage. From Langenbach F, Handschel J. 2013 (10).

### 10.2.2 Glycosaminoglycans and their potential use as differentiation factor on MSCs.

GAGs are a family of polydisperse, sulfated, anionic, and linear polysaccharides responsible for a great number of critical biological functions. In general, GAGs

consist of repeating disaccharide units composed of uronic acid and amino sugars. There are 4 main types of glycosaminoglycans: Hep and heparan sulfate (HS), chondroitin sulfate (CS) and dermatan sulfate (DS), hyaluronan (HA), and finally, keratan sulfate (KS) (14–16).

In 2015 (17), it was reported that Hep is associated with numerous biological processes, including osteogenesis from MSCs through the interaction with extracellular components as growth factors, cytokines, lipoproteins, and ECM proteins, a process that could be closely related to the concentration of the drug added to the culture medium (18).

Regarding their structure, Hep and HS are the most complex existing GAGs. They are composed of 20 to 40 repeating disaccharide units linked by 1,4-glycosidic bonds, including uronic acid (D-glucuronic acid (GlcA) or L-iduronic acid (IdoA)), commonly linked to sulfate groups; and by D-glucosamine residues (GlcN, a hexosamine) with N-sulfate, N-acetyl, or free amino groups. In contrast to HS, in the Hep molecule, L-iduronic acid predominates by 90% compared to D-glucuronic acid and has more sulphate groups (14, 15).

Hep and HS are synthesized in the Golgi complex and exported to the outside of the cell, where they are predominantly found in the ECM or on the cell surface bound to core proteins, where they form particular complexes called proteoglycans (14, 16). Hep is a highly important GAG that is frequently used in the pharmaceutical field as an anticoagulant to treat high-risk thrombotic disorders, since it binds with high affinity to antithrombin III (ATIII), which deactivates various enzymes of the coagulation cascade (115, 116).

### **10.3 Porous and non-porous materials as drug delivery systems.**

Sections 10.3.2 - 10.3.4 were published by the thesis author in 2020 as it is reported in Annexes section (117).

### 10.3.1 PEDOT as conductive polymer for drug immobilization.

The conductive polymer PEDOT is synthesized from EDOT (Figure 5). It has been extensively studied for its high transparency, its easy processing in aqueous solution with surfactants, and its applicability for flexible devices (118). The controlled synthesis of PEDOT from EDOT is possible through electropolymerization or electrodeposition (119).

PEDOT is categorized as a biocompatible conductive polymer (109). However, in cases where organic molecules or whole cells are involved, it is recommended to evaluate the combination with biopolymers, to improve the biocompatibility of the matrix (120). Previously,, the cytotoxicity of a PEDOT porous matrix in combination with the biopolymer κC was confirmed in a human neuroblastoma cell line (SH-SY5Y) (109). The high surface-volume ratio, high porosity, the high degree of interconnection of pores, and an appropriate pore size are some of the properties that this type of scaffold must have to improve the biological and electrical properties of the interface (121).

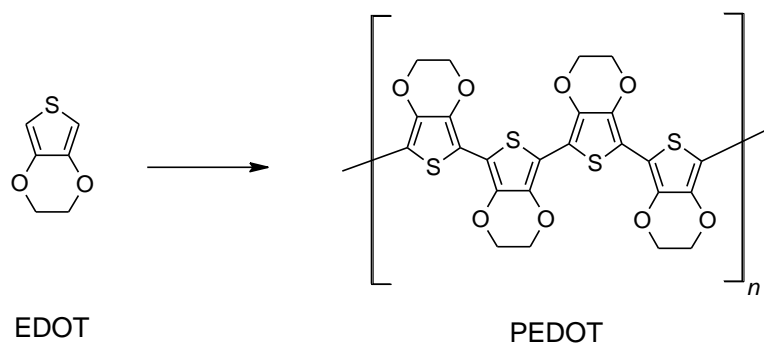


**Figure 5.** Molecular structure of the EDOT monomer (left) and the PEDOT polymer (right).

The electrochemical properties of PEDOT and its simple processability can be exploited in a wide range of applications, including biomedicine and biotechnology (122). This polymer has been described as a promising material for the local release of drugs (specifically charged molecules), since it allows the incorporation of these anionic molecules by electrostatic mechanisms during electropolymerization in thin films and their subsequent release by charge transfer

through of the interface during an electrical stimulation event (24, 123). In addition, the controlled release of Hep and HS from conductive polymeric matrices has also been investigated, although not extensively (124). However, it constitutes a potential method for the future generation of a scaffold for bone tissue regeneration.

The application of external electrical stimuli on MSCs was studied on 2013, as result, authors confirmed that cells were not negatively affected by low alternating current stimuli even in periods of 6 hours of stimulation (6), which strengthens that the drug fixation and subsequent release from PEDOT matrices could be applied.

The electrodeposition of the PEDOT/ $\kappa$ C polymeric matrix can be carried out on different types of materials such as gold (Au), platinum (Pt) or indium tin oxide (ITO) (109, 118, 123). However, given its biocompatibility and in accordance with previously research (109, 123), the gold electrodes system is the best to stimulate the matrix and to induce drug release.

### **10.3.2 Controlled drug release by electrical stimulation employing nonporous conductive materials.**

In order to prevent the negative effects resulting from exposure to high dosages of drugs, local electronically controlled release of pharmaceutical compounds from implantable devices appears as a promising option (125). Drugs anchored inside the conductive materials have been reported using supercritical technology and electropolymerization (126, 127).

Electrochemical methods involve the use of conductive polymers, which are electrochemically oxidized during the polymerization processes, generating charge carriers, and, thus, allowing ionic drugs' impregnation based on electrostatic interactions (128). There are two main electrochemical methods to induce the immobilization of drugs. In the first one, an ionic drug (preferably anionic) acts as a doping agent and its anchoring proceeds simultaneously with the process of matrix formation, commonly named one-step immobilization or *in*

*situ* immobilization (126, 129). Drug fixation is the result of the ion-exchange processes during polymer oxidation. Ionic drugs can serve as counter-ions for the positively charged centers in the growing polymer chain (130). Anti-cancer drugs, anti-inflammatory compounds, and hormones have been fixed on conductive materials using one-step immobilization, mainly for the development of neural devices (24, 131, 132).

The second method corresponds to the two-step or *ex situ* immobilization. The incorporation of the drug is carried out after the synthesis of the matrix, through ion exchange processes taking place at their surface. First, the polymer film is synthesized from a solution consisting of the monomer and a small ionic molecule as doping agent, without the drug. The obtained film is later reduced and oxidized by an electrical stimulus (126, 129). Reduction induces the removal of the dopant from the film; meanwhile, the drug, which acts as the second doping agent, is incorporated during the process of matrix oxidation (130). This approach allows to prevent the interference of drugs during the growth of polymer matrix and their subsequent release does not have much impact on their physicochemical properties (126, 129).

Different strategies of drug fixation on conductive polymers using two different doping agents have been reported (12, 130). The anti-inflammatory drugs Dex and the polysaccharide  $\kappa$ -carrageenan were included simultaneously during PEDOT film formation, using *in situ* immobilization. After film oxidation,  $\kappa$ C was maintained on the matrix, granting the film greater stability and integrity even after drug release (12).

Drug delivery is caused by electrochemical stimulation of the conductive matrix, which induces the oxidation and/or reduction of the film. By applying a negative potential, the polymeric matrix is reduced, and the cationic charge of the polymer backbone is neutralized, causing the release of the anionic drug by electrostatic mechanisms (129). In a similar procedure, applying negative and positive cyclic potentials induces the reduction and oxidation of the polymeric film, respectively; meanwhile, the matrix experiments expansion and contraction, which force the

release of the drug. Although cyclic stimulation allows a greater amount of drug release in comparison with other methods, some authors have reported that the application of the stimulus may cause delamination, cracks, and breakdowns of the matrix, mainly in one-step immobilization systems (133–135).

The controlled release of drugs using electrical stimulation from conductive polymer films (12, 24, 127) opens the door for a different approach regarding the application of polysaccharide aerogels on drug delivery. Since these materials can be coated with an electrically conductive material while incorporating active compounds, those composites may be used in the controlled release of bioactive molecules by electrical stimulation (136, 137). These biochemical release systems are the focus of several research groups and further investigations should follow this path to promote smart porous scaffolds that merge mechanical, electrical, and biochemical stimulation processes, mimicking the *in vivo* ECM conditions.

### **10.3.3 Polysaccharide-based porous materials as drug-delivery systems.**

One of the main approaches and most relevant applications of biopolymer-based porous materials is their use as drug-delivery systems (28, 29). The application of these materials as controlled drug-release matrices has gained interest in the last years due to their properties, such as its high surface area, high porosity, and biocompatibility (29). Porous materials can act as carriers for bioactive compounds, showing high loading capacity, enhanced stability upon storage, and accelerated drug release, if required (138). Along with the high loading capacity, biopolymer-based porous materials also show an improved dissolution rate of poorly water-soluble drugs (29).

The biocompatibility of natural polymers along with the outstanding performance of porous matrices as carriers for active compounds, such as drugs, have promoted the systems as scaffolds in body implants to accelerate tissue formation by providing a suitable porous structure that promotes cell colonization (5, 139).

Diverse authors have also studied the incorporation of drugs and growth factors to promote the attachment, proliferation, and differentiation of cells, in order to provide both substitutes for damaged tissues and therapeutic schemes that reduce post-implantation inflammation and infections (1, 4, 5).

Controllable drug-release systems may be categorized as mechanical methods, which are mainly *in vivo* implantable pump delivery systems built from biocompatible nanomaterials (21, 22), and as polymeric drug delivery systems. The last one makes use of biopolymers, in which the delivery of drugs is mainly dominated via diffusion and by electrochemical methods as was recently reported (22). Hence, the incorporation of drugs within these kinds of porous scaffolds has been studied previously for osteogenic differentiation, bone repair activity, and the stimulation of neural tissues (5, 127).

#### **10.3.4 Diffusive phenomena on the controlled release of drugs on polysaccharide-based porous materials.**

Different methods for drug impregnation can be found in literature regarding porous materials from polysaccharides. Supercritical technology employing  $scCO_2$  has been defined as the most innovative technique for producing polymer/drug composite systems for pharmaceutical applications (140). By means of supercritical fluid technology, the impregnation of scaffolds with drugs such as ketoprofen was achieved (139). This process consists of placing aerogel particles and ketoprofen in a closed autoclave under agitation; the ketoprofen is dissolved in  $scCO_2$  and adsorbed in the aerogel matrix. The same procedure was reproduced for obtaining poly( $\epsilon$ -Caprolactone) (PCL) scaffolds loaded with ketoprofen (141) and for alginate-based aerogel microparticles for mucosal drug-delivery (29).

Three steps are considered for the diffusion model: first, the film diffusion; the second step is the slowest, thus controlling the kinetics of the phenomenon, and it is called intraparticle diffusion; finally, the last step is the adsorbate release on



adsorbent active sites (142). Several works have been published regarding the release of drugs by means of diffusion phenomena (23, 29, 138, 139, 143, 144). The first mechanism when a drug-loaded polymeric material meets an aqueous solution is the filling of the pores near the surface; then, drug diffusion is initiated by the dissolution of the solute in the water-filled pores and the continuous diffusion in water (145). Through time, the polymeric network starts swelling, inducing several structural changes that are affected by the cross-linking density and the degree of crystallinity of the 3D network. From the swelling of the polymer, a new diffusion starts through the swelled polymer structure (145). By analyzing the release profile of drugs, conclusions can be obtained on whether the kinetics follow a Fickian or non-Fickian diffusion profile (139).

Innovative drug delivery systems are not only studied to improve cellular responses in different tissues but as a strategy that develops platforms and nano-scale devices for selective delivery of therapeutic small drug molecules to the cells or tissues of interest, for the maintenance of appropriate doses, and to improve individual therapy. To meet this demand, many drugs have been reformulated in new drug delivery systems to provide enhanced efficiency and more beneficial therapies (21, 22).

#### **10.3.5 Future perspective: innovative polysaccharide-based porous materials as extracellular matrices for tissue regeneration.**

In recent years, tissue engineering and regenerative medicine studies has been based on the combination of specific types of cells and three-dimensional (3D) porous scaffolds to induce a successful *in vitro* generation of diverse tissues (146–148). The main efforts on engineered ECMs in the biomedical field have been focused on the use and stimulation of pluripotent stem cells.

An ECM is an organized network composed by a mixture of cellular and non-cellular components. It plays an important role in tissue and organ morphogenesis, cell function, and structure maintenance. The biochemical and

mechanical stimulus that cells receive from the matrix influences their growth, migration, differentiation, survival, and homeostasis (149).

Aerogels are porous three-dimensional matrices, which possess a nanostructure that it is able to mimic the extracellular matrix of the natural tissue, providing a favorable environment for the regeneration of tissues and organs (28). Coupled with high porosity, low densities, and high inner surface areas, porous materials can provide appropriate morphology engineering, opening the possibility for their application as synthetic scaffolds for tissue engineering (121).

Specifically, the scaffold acts as a template for new tissue formation (150) and its three-dimensional structure guides the proliferation and colonization of cells, promoting tissue growth (151). An ideal synthetic ECM should exhibit a highly open and uniform porosity, over 80%, with micro-and mesopores that enable cell infiltration and macropores for proper vascularization (152). The configuration of the scaffold topology is critical in controlling cellular function, it should match the endogenous topology of the cell membrane in order to enhance signaling and function.

Nowadays, regenerative medicine is focused on the evaluation of novel skeletal muscle regeneration strategies, which involve the prefabrication of muscle tissues *in vitro* by differentiation and maturing of muscle precursor cells on a scaffold, providing the required environment for myogenic differentiation of the cultured cells (153). Researchers are studying the incorporation of products obtained from cellular metabolism in synthetic ECMs. These materials are mainly constituted of glycosaminoglycans, a group of polysaccharides that can modulate cell activity by mimicking aspects of the *in vivo* extracellular environment, providing important roles in cell signaling, proliferation, and orientation through their ability to interact with ECM proteins and growth factors (14–16, 154). Hyaluronic acid, heparan sulfate, and heparin are the most used glycosaminoglycans in synthetic ECMs, mainly to direct the culture of MSCs (155, 156).

On the other hand, the synthesis of alginate hydrogels for platelet-rich plasma encapsulation as a coating for polylactic acid porous devices is another strategy used to improve cellular responses on synthetic ECM, the hydrogel system allows for better cellular integration and influences the vascularization into the membrane after skin implantation of the device, and the access to nutrients and growth factors was also improved with the engineered hydrogel. Platelet-rich plasma hydrogels could also support oxygenation of cells, avoiding hypoxia immediately post-transplantation (157, 158). In a similar study, calcium peroxide (CPO) was used during the synthesis of a gelatin methacryloyl bioprinted scaffold to achieve improved cellular oxygenation and increase fibroblast viability under hypoxia conditions (159).

The spatial arrangement, porosity, biocompatibility, and proper scale of the ECM are some of the most important features that must be adjusted for use in nervous tissue, skin, bone, and muscle (153). Nevertheless, several other factors, such as mechanical properties and chemical modification of scaffolds, significantly influence cellular behavior and are also considered during synthetic ECM (160, 161).

Current and future studied strategies are based in the use of these type of scaffolds which could be employed and modified for drug immobilization and as conductive systems for MSCs stimulation focused on cell stimulation for the synthesis of in vitro bone tissue for regeneration.

## 11 Justification

Degenerative conditions causing by aging, defects on bone tissue, and the needed for organ transplant have gained interest in the control of hMSCs differentiation making use of scaffolds designed with bioactive materials to facilitate the formation of functional tissues.

HMSCs differentiation into different lineages can be induced by incorporating biochemical agents into the culture medium, and it has also been studied that some glycosaminoglycans can favor the response time in the differentiation to osteoblasts.

Given that, the study of the *in vitro* role of the controlled release of at least one bioactive agent in the proliferation and differentiation of cells to the osteogenic lineage, may be a promising approach for future design and development of scaffolds that allow cell establishment and differentiation, favoring a normal tissue regeneration process.

In this case, the faradic mechanism of a conductive polymer on a gold electrode allowed the fixation and subsequent release of Dex in a cell culture medium. This system permitted a more precise control of the quantity and concentration of drug released, reducing the possible diffusion events; so that it could be a better candidate in future therapy strategies for various injuries or chronic diseases. In parallel, a three-dimensional porous system for Dex incorporation was prepared and applied during hMSCs culture.

## **12 Hypothesis**

The controlled release induced by electrical stimulation of at least one charge molecule from gold electrodes coated by conductive polymeric matrices promotes the differentiation of hMSCs into osteoblasts.

## **13 Objectives**

### **13.1 General objective:**

To study the *in vitro* effect of the controlled release of charged molecules from porous and non-porous conductive materials, on the proliferation and differentiation of human mesenchymal stem cells.

### **13.2 Specific objectives:**

1. To synthesize conductive materials for the controlled release of a charged molecule for the study of the proliferation and differentiation of human mesenchymal stem cells.
2. To establish the concentration profile of at least one charged molecule for the differentiation of human mesenchymal stem cells to osteoblasts.
3. To analyze the expression of osteoblasts characteristic markers to confirm the differentiation of mesenchymal stem cells after suffering biochemical stimulation.
4. To evaluate the *in vitro* effect of the controlled release of at least one charged molecule from conductive matrices on the proliferation and differentiation of human mesenchymal stem cells, for its prior study as tissue regeneration therapy.

## 14 Materials and methods

This work was carried out at School of Chemistry and Biotechnology Research Center (CIB) from Tecnológico de Costa Rica, Cartago, Costa Rica. Characterization of materials were carried out at Materials Science and Engineering Research Center (CICIMA) and Tropical Diseases Research Center (CIET) from Universidad de Costa Rica. Finally, the cellular and molecular analyses were studied at Pharmaceutic Technology Laboratory from Pharmacy Faculty and at Molecular medicine and Chronic Diseases Research Center (CiMUS) from Universidad de Santiago de Compostela, Santiago de Compostela, Spain.

### 14.1 Materials.

$\kappa$ Ca from red algae (quality level 200), isopropyl-alcohol (IPA, gradient grade, for LC-GC), potassium chloride (KCl, >99.0% purity), ammonium acetate ( $\text{NH}_4\text{CH}_3\text{CO}_2$ , purity 98%), dexamethasone 21-phosphate disodium salt (Dex, 98.0% purity), fetal bovine serum (FBS), dexamethasone base (Dx), 3,4-ethylenedioxythiophene (EDOT, 97.0% purity), ultrapure water MS quality, MS methanol, and ALPL enzymatic activity kit (AP100) were obtained from Sigma Aldrich (San José, Costa Rica). Anti-human ALPL ABfinity™ Rabbit monoclonal antibody (7H11L3), rabbit anti-human osteopontin polyclonal antibody (PA5-34579), prolong with DAPI, and  $\alpha$ -MEM no nucleosides culture medium were purchase from ThermoFisher Scientific. Goat anti-rabbit (IgG) secondary antibody preadsorbed with Alexa Fluor® 594 (ab150084), and anti-Col-I (ab280968), was purchased from Abcam, starch from corn (St, N-460, 52% amylose) was adquired from Roquette (Lestrem, France). All chemical reagents were used without further purification. Distilled and deionized water was used in all experiment.

## 14.2 Deposition of the gold electrode.

Gold electrodes (Au, 99.99 % pure, Goodfellow Corporation, Coraopolis, PA 15108-9302, USA) fabrication was extensively studied by the author and others in earlier researches (162–164). In general, electrodes preparation for drug immobilization was carried out by the deposition of gold on a polyimide substrate using a high vacuum chamber. A coating thickness of  $42.0 \pm 0.4$  nm of gold was deposited by means of electron beam evaporation with a base pressure of the order of  $2.2 \times 10^{-6}$  Torr, deposition rates of  $0.38 \pm 0.03$  nm·s<sup>-1</sup> were used. After that, electrodes were passivated using a shadow mask to leave a specific exposed area ( $20.49 \pm 0.02$  mm<sup>2</sup>, Figure 6). In parallel, gold electrodes to be used during cell culture analyses were prepared using the same method, nevertheless, the dimensions of the system were corrected to adjust it to a 24-well dish (exposed area of  $132.52 \pm 0.02$  mm<sup>2</sup>).

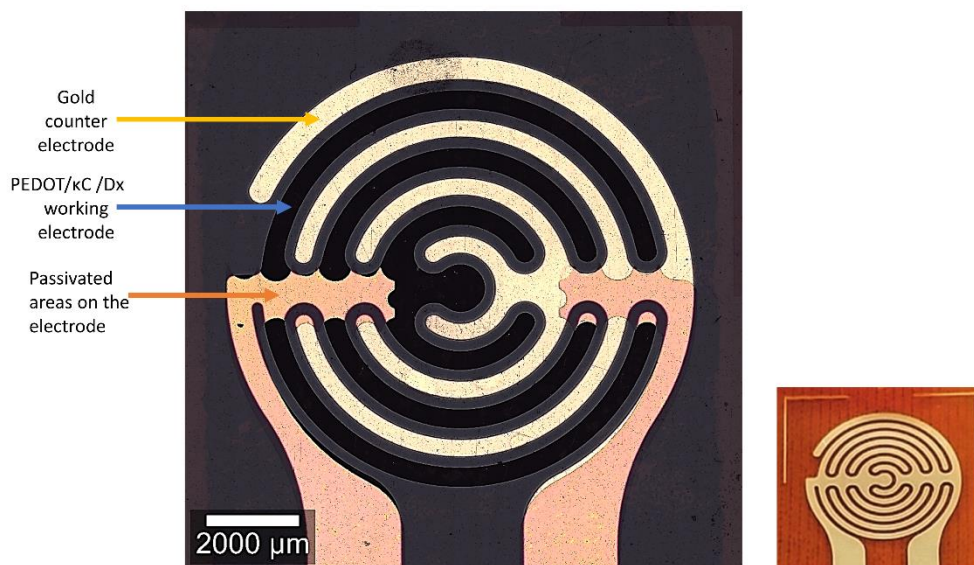


**Figure 6.** Deposited PEDOT/κC/Dex film on a passivated electrode after 160 cycles of electrical oxidation (left) and gold electrode without passivation as reference (right). From Ramírez-Sánchez, *et al.* 2020 (12).

Prior to the drug deposition, electrodes were electrochemically cleaned with KCl 0.2 M (165) applying cyclic voltammetry (CV) sweeps from a range of -600 to 900



mV with  $100 \text{ mV}\cdot\text{s}^{-1}$  scan rate, using an Autolab Potentiostat supplied by Metrohm (PGSTAT-302N, AUTOLAB, Utrecht, The Netherlands).

Finally, the functionality of the electrode system was confirmed by physics modelation (162) using the COMSOL® (COMSOL Inc., Burlington, Massachusetts, USA) multiphysics package. The simulations were performed using the Secondary Current Distribution physics and considered the gold (Au) electrode structure in KCl 0.2M (Annex 7)

### **14.3 Modification of the gold electrode with a coating of PEDOT/ $\kappa$ C/Dex.**

Firstly, the surfactant dispersion was prepared according to a previous work (123), briefly:  $\kappa$ C at micellar critical concentration (0.2% wt.) and KCl electrolyte (0.2 M) were added to deionized water previously heated at  $50 \text{ }^\circ\text{C}$  and magnetically stirring at 150 rpm for 1 hour. After that, the samples were sonicated using 140 Joules in a Sonifier QSonica (Q700, Ultrasonic Corporation, Danbury, CT, USA), before and after adding the monomer EDOT (10 mM) and Dex at three different concentrations: 1 mM, 5 mM, and 10 mM.

Once the dispersion system was established, the solution was electropolymerized on the electrode surface under galvanostatic conditions using an Autolab Potentiostat. The gold electrode (Figure 6) was used as a working electrode, a platinum sheet as counter electrode, and Ag|AgCl (KCl 3.0 M) worked as reference electrode. The electrical polymerization was carried out by a potentiometry method, applying a constant current of  $102.45 \text{ }\mu\text{A}$  (current density:  $0.5 \text{ mA}\cdot\text{cm}^{-2}$ ), a potential limit on a range of 1400 mV to 1700 mV during 360 s (ca.  $180 \text{ mC}\cdot\text{cm}^{-2}$  of charge density). Next, the electrodes were intensively rinsed with deionized water and stored at  $4 \text{ }^\circ\text{C}$  before their use (1 week maximum).

### **14.4 Evaluation of the stability and size of the dispersion systems.**

The characterization of the particle size and  $\zeta$ -potential was performed using triplicates of six dispersions, prepared in deionized water, namely: (1)  $\kappa$ C 0.2%

wt.; (2) Dex 10 mM; (3) EDOT 10 mM/ $\kappa$ C 0.2% wt.; (4) EDOT 10 mM/Dex 10 mM; (5)  $\kappa$ C 0.2% wt./Dex 10 mM; and (6) EDOT 10 mM/ $\kappa$ C 0.2% wt.:Dx 10 mM. Measurements were performed in a Zetasizer instrument (Nano ZS, Malvern Panalytical Ltd., Worcestershire, UK) at 25 °C and 173° angle. Finally, dispersions were sonicated using a high-power ultrasonic bath (Branson<sup>®</sup>, Merck corporation, San José, Costa Rica) for 6 min to promote their homogenization. Two additional formulations of EDOT/ $\kappa$ C/Dex were prepared to reach lower dexamethasone concentrations into the conductive layer.

#### **14.5 Analysis of the Topography and Composition of PEDOT/ $\kappa$ C/Dex Coating by Profilometry and $\mu$ -Raman Spectroscopy Methods.**

Electrode topography was studied by profilometry analysis (Bruker, model: Dektak TX Advance, AZ, USA). The arithmetical mean roughness of the surface ( $S_a$ ) was calculated to describe the topography of the materials by using a 2  $\mu$ m tip radius and a force of 1 mg in a 300  $\times$  300  $\mu$ m<sup>2</sup> and a scan area rate of 2.5  $\mu$ m $\cdot$ s<sup>-1</sup>.

To analyze the coating composition, Raman spectroscopy analysis was carried out using a confocal  $\mu$ -Raman microscope (Alpha300 R WITec, GmbH, Ulm, Germany) with a 532 nm excitation laser, using an exposure time of 0.5 s, and 105 accumulations. The Raman stack scan was obtained using an integration time of 4 s in 4  $\mu$ m<sup>2</sup> of area, a total of 200 measurements per line were recorded, reached 20 lines in each stack. Oversampling was used to improve the image quality, which was done in case of the cross-sectional scan. The scan depth was fixed at 5  $\mu$ m and a total of 10 stack scans were achieved. The intensity of the relative wavenumber at 1435 cm<sup>-1</sup> and 1625 cm<sup>-1</sup> were extracted from each acquired spectrum, corresponding to PEDOT (163) and Dex/ $\kappa$ C (135, 165), respectively and plotted as 2D image. The intensity counts are related to the presence of the functional group, and it is presented as bright yellow areas.

#### 14.6 Dexamethasone-21 phosphate release experiments from the PEDOT/ $\kappa$ C/Dex film.

The drug release from the modified electrode was carried out in a continuous flow cell (Figure 7) using cyclic voltammetry (CV) sweeps with a three electrodes system (PEDOT/ $\kappa$ C/Dex, Ag|AgCl, and a gold film as working, reference, and counter electrodes, respectively). The buffer solution was injected with a constant flow of  $250 \mu\text{L}\cdot\text{min}^{-1}$  using a syringe pump (New era pump systems, NE-1002X). The active release of the drug was performed in 1 mL of fresh ammonium acetate solution (0.10 M) pH 7.2 (166), by scanning of CV from  $-600$  to  $1000$  mV with a  $25 \text{ mV}\cdot\text{s}^{-1}$  scan rate, over a period of 300 min (5 samples total) at room temperature.

In order to analyze the amount of drug released by diffusion events, the same procedure but, without electrical stimulation, was performed. For the experiment, 1.0 mL of 0.10 M ammonium acetate was injected through the cell containing the electrodes, a total of five samples were collected during 300 min of analysis.

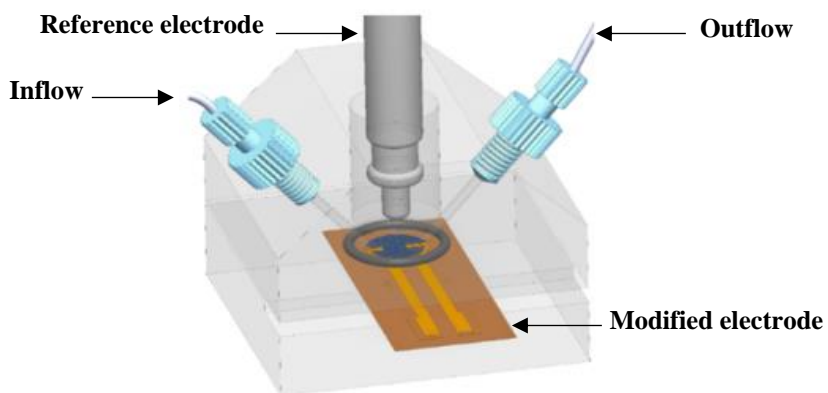


**Figure 7.** Schematic representation of the polymethylmethacrylate (PMMA) continuous flow cell used in electrochemical stimulation of PEDOT/ $\kappa$ C/Dex modified electrode. Designed by Eng. Jorge Sandoval.

Finally, Dex containing samples were filtered using a nitrocellulose  $0.2 \mu\text{m}$  filter. The concentration of drug for the active and passive release events, was determined using a Xevo G2-XS quadrupole time of flight (Q-tof) mass spectrometer (Waters Corporation, Wilmslow, UK) coupled with an Acquity UPLC

H-Class. For the analysis, a 10- $\mu$ L injection of the sample was separated with an Acquity UPLC<sup>®</sup> C18 column (2.1 mm $\cdot$ 50.0 mm). The mobile phase consisted of a solution of water:formic acid 0.05% and methanol:formic acid 0.05% and they were supplied under not isocratic conditions with a constant flow of 0.3 mL $\cdot$ min<sup>-1</sup> (Table 2).

**Table 2.** Gradient elution method for the mobile phase using during dexamethasone-21 phosphate analysis. Solvents were H<sub>2</sub>O:0.05% formic acid (A) and methanol:0.05% formic acid (B).

Time (min)	Flow (mL $\cdot$ min <sup>-1</sup> )	% A	% B
0	0.3	95	5
1	0.3	95	5
2	0.3	5	95
10	0.3	5	95
12	0	50	50
15	0.3	50	50
16	0.3	50	50

Configuration of the mass spectrometer was set according to the parameters in a previous work (167), with the following modifications: Capillary voltage of 2 kV, 40 V sampling cone and a source offset of 80 V. Source temperatures were established at 130°C and 280°C for the desolvation temperature. The cone gas flow was set at 9 L $\cdot$ h<sup>-1</sup> and 792 L $\cdot$ h<sup>-1</sup> for the desolvation gas. Finally, for the identification of the Dx, MS mode under negative polarity was used with a mass range from 50 to 500 m $\cdot$ z<sup>-1</sup>. Quantification was carried out using Multiple Reaction Monitoring (MRM) acquisition method with the optimized transition of 471.1584 m $\cdot$ z<sup>-1</sup> for the precursor ion and 78.9585 m $\cdot$ z<sup>-1</sup> for the product ion, with a collision energy of 35 eV. Concentration in each sample was calculated using the Software MassLynx<sup>™</sup> (V4.1, Waters Corporation, Wilmslow, UK) and an external calibration curve between 0.5 ppb to 1000 ppb of Dex ( $R^2 = 0.9965$ ).

### 14.7 Preparation of three-dimensional scaffolds based on polysaccharides and dexamethasone-21 phosphate.

Aqueous solutions containing starch,  $\kappa$ Ca and Dex were prepared using continuous magnetic stirring for 2 hours or until no appreciable lumps were observed. The concentration of each component is showed in Table 2.

**Table 3.** Polysaccharide-based cryogels notation regarding the initial content of the polymers (expressed in weight percentage of initial blend solution for the cryogel formation).

Sample	Starch (wt. %)	$\kappa$ -Carrageenan (wt. %)	Dexamethasone (wt. %)
St	9	0	0
St/ $\kappa$ Ca	9	0.5	0
Dex 0.00005 %	9	0.5	0.00005
Dex 0.0002 %	9	0.5	0.0002
Dex 0.0004 %	9	0.5	0.0004
Dex 0.0010 %	9	0.5	0.001
Dex 0.0018 %	9	0.5	0.0018

Each dispersion was autoclaved at 121°C and 1.1 bar for 7 minutes used an autoclave Raypa AES-12 (Spain). Then, the autoclave was quickly depressurized until atmospheric pressure was reached (at 95°C). Immediately, the resulting viscous solution were poured into  $12.9 \pm 0.2$  mm diameter cylindrical molds and were subsequently stored at 4°C during 48 hours for starch retrogradation. After that, the resulting hydrogels were frozen at -80°C overnight and finally, the frozen samples were freeze-dried for 24 hours using a freeze-dryer (Telstar, LyoQuest Plus -85/ECO, Spain) at -65° and 0.025 mbar. The resulted cryogels were then UV-irradiated for 2 hours to induce sterilization.

### 14.8 Physical characterization of polysaccharide/Dex-based cryogels.

Skeletal density of polysaccharide-based cryogels ( $\rho_{skel}$ ) was determined using a He pycnometer (Quanta-Chrome MPY-2, Spain) set at room temperature and 15 psi. A total of 5 replicates were used for each measurement. Cryogels bulk density ( $\rho_{bulk}$ ) was calculated by weighing and measuring individual cryogels

dimensions. Finally, equation 1 and equation 2 were used to calculate cryogels overall percentage porosity ( $\varepsilon$ ) and total pore volume ( $V_p$ ), respectively (168).

$$\varepsilon = 1 - \frac{\rho_{bulk}}{\rho_{skel}} \times 100 \quad (\text{Equation 1})$$

$$V_p = \frac{1}{\rho_{bulk}} - \frac{1}{\rho_{skel}} \quad (\text{Equation 2})$$

On the other hand, mass gain analysis after water exposure was adopted to monitor the swelling behavior of the synthesized cryogels according with a previous work (169). Swelling ratio were calculated by triplicate using equation 3. Firstly, the initial mass of the dried composites was determined, after that, the samples were immersed in 3 mL of deionized water, and were incubated at 37°C. Later, samples were taken out and then, the weight of the swollen samples were immediately recorded. The swelling kinetics were determined based on the mass changes at 24 hours of analysis.

The data analysis was carried out by one-way analysis of variance (ANOVA) method with a confidence level of 95% using IBM SPSS software.

$$S_r = \frac{W_s - W_i}{W_i} \times 100 \quad (\text{Equation 3})$$

Where  $S_r$  is swollen ratio,  $W_s$  is the weight of the swollen sample and  $W_i$  is the weight of the dried samples.

Degradation ratio of cryogels was determinate by their weight loss after phosphate saline buffer (PBS 0.1 M, pH 7.1) exposure according to equation 4. For the analysis, the weight of dried scaffolds was recorded. After that, samples were transferred to 1.5 mL tubes containing 1 mL of PBS and incubated at 37 °C at 60 rpm for a maximum of 7 days. Finally, samples were washed three times using distilled water, frozen at -80 °C and dried at -62 °C under vacuum conditions and weighed at regular time points.

$$DD = \frac{(W_i - W_f)}{W_i} \times 100 \quad (\text{Equation 4})$$

Where, DD is degradation degree,  $W_i$  is the weight of the dried cryogel and  $W_f$  is the weight of the cryogel after water exposure.

Finally, micrographs of the prepared cryogels were recorded by scanning electron microscopy (SEM, Zeiss FESEM ULTRA PLUS, Oberkochen, Germany). Samples were gold-sputtered prior to imaging to minimize charging and to improve the contrast of the images.

#### **14.9 Dexamethasone-21 phosphate release experiments from the polysaccharide-based cryogels.**

Dex at diverse concentrations (Table 3) were added during the synthesis of cryogels to induce their subsequent release from the samples. Scaffolds pieces of 100 mg were immersed in 24-well dishes containing 4.5 mL of ammonium acetate solution (0.1 M, pH 7.2). The plates were placed in a thermoblock (Echotherm™, Torrey Pines Scientific Inc) at 100 rpm and 37°C during a period of 96 hours. For the analysis, aliquots of 0.3 mL were sampled at selected times, and the withdrawn volumes were replaced with fresh medium. All samples were centrifuged during 10 minutes at 14000 rpm to avoid interferences in the drug quantification analysis due to the presence of scaffolds debris. Finally, the amount of Dex released from the scaffolds was determined using mass spectrometry method, according with method described previously.

A second analysis using micro infrared spectroscopy was carried out to monitoring the presence of the drug before and after the release events. Firstly, a group of dry scaffolds were triturated to collapse the structure, in parallel, another cryogels samples were immersed in ammonium acetate buffer during 24 hours at 37°C and 100 rpm, after that time, samples were dried at 40°C under vacuum conditions and finally, them were triturated. Micro-FTIR spectroscopy measurements were performed using a Spotlight 400 FTIR Imaging System. The analyses were performed individually, measurements were obtained for a range of 4000-750  $\text{cm}^{-1}$  with a resolution of 16  $\text{cm}^{-1}$  and studying the intensity of the

relative signal at  $1625\text{ cm}^{-1}$  (130, 170, 171). Molecular micrographs were obtained for randomly selected areas of  $50\text{-}100\text{ }\mu\text{m}^2$  on the sample surface, using  $128\text{ scans}\cdot\text{pixel}^{-1}$  and was plotted as 2D image. The absorbance intensity was related to the presence of the drug.

#### **14.10 Osteogenic differentiation of human mesenchymal stem cells.**

hMSCs were purchased by ATCC. Firstly, cells at density of  $5000\text{ cells}\cdot\text{cm}^2$  were cultured in a  $T75\text{ cm}^2$  flask, removing non-adherent cells after 24 h of incubation. Cells were expanded *in vitro* using basal medium (BM), constituted by non-nucleosides  $\alpha$ -Minimum Essential Media ( $\alpha$ -MEM) with L-Glutamine, and supplemented with 10% fetal bovine serum (FBS) and 1% of penicillin ( $10\ 000\text{ UI}\cdot\text{mL}^{-1}$ ) and streptomycin ( $10\ 000\text{ UI}\cdot\text{mL}^{-1}$ ), and maintained at  $37^\circ\text{C}$  in a humidified atmosphere of 5%  $\text{CO}_2$ . Passage 4 and passage 5 were used.

#### **14.11 Biocompatibility test for the electrodes and cryogels system.**

Biocompatibility test for the electrodes and cryogels was performed according to the International Standards Organization (ISO 10993-5:2009). hMSCs (passage 5) were seeded in 48-well plates using  $\alpha$ -MEM culture media in a density of  $14000\text{ cells}\cdot\text{cm}^2$ . After 24 hours of culture, a monolayer of adherent cells was obtained, and the culture media was replaced by fresh media. In parallel, prior to seeding, materials were sterilized by UV-light for 120 minutes. After that time, polymerized electrodes were placed around the well and the cryogels pieces of 13 mg and 1 mg containing dexamethasone 0.0005% wt. and 0.018% wt. respectively, were placed in self-made stainless steel trans-wells and transferred to the culture plate (Figure 8). A culture of cells without the scaffolds and other of cells with the trans wells were maintained as negative controls. All analysis were carried out by triplicate and maintained at  $37\text{ }^\circ\text{C}$  and 5% of  $\text{CO}_2$ .

Finally, biocompatibility determination was performed by cell proliferation analysis after 24 h and 48 h, using Cell Counting Kit-8 (CCK-8, Roche, Basel, Switzerland),



according with manufacture's protocol: test compounds were removed and replaced by 180  $\mu\text{L}$  of fresh culture medium containing 20  $\mu\text{L}$  of a solution of water-soluble tetrazolium salt (WST-8). The plate was protected from the light and incubate for 2 hours at 37°C, after that time, absorbance was determined at 450 nm using a plate reader. Statistical analysis was carried out using SPSS software.

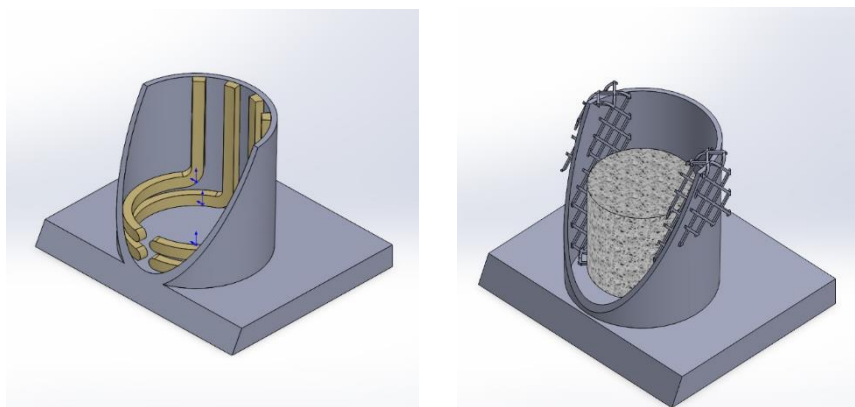


**Figure 8.** Schematic representation of a gold electrode (left) and a stainless steel homemade trans well containing a Dex-based cryogel (right) adjusted to a well of a 48-wells culture plate. Designed by Eng. Sebastián León-Carvajal.

#### 14.12 Effect of high molecular weight heparin on hMSCs differentiation to osteoblast.

HMSCs (passage 5) were culture in 96-well plates in a density of 14000 cells·cm<sup>-2</sup>, after 24 hours, cells were exposed during 14 days to osteoblastic differentiation conditions. Cells were exposed to culture medium consisted in BM containing  $\beta$ -Glycerophosphate (10 mM), ascorbic acid (50  $\mu\text{g}\cdot\text{mL}^{-1}$ ), Dex 100 nM, and Hep at several concentrations (0.025 UI·mL<sup>-1</sup> to 25 UI·mL<sup>-1</sup>) (Table 4), the same culture medium without heparin was used as positive control. Cells in basal media were used as negative control. and lastly, a control containing basal media containing  $\beta$ -Glycerophosphate (10 mM), ascorbic acid (50  $\mu\text{g}\cdot\text{mL}^{-1}$ ), and Hep 0.5 UI·mL<sup>-1</sup> was used. Finally, in order to evaluate the differences between the type of dexamethasone used, a comparison between Dx and Dex containing culture medium was carried out. The culture medium was changed every 3 days. Samples were analyzed at 3, 7 and 14 days.

**Table 4.** Culture media composition used during osteoblast differentiation of hMSCs.

Culture medium	Culture medium composition
Negative control	Basal medium ( $\alpha$ MEM + SFB + antibiotics)
Dx	BM + $\beta$ -Gly + AA + Dex 100 nM
Dex	BM + $\beta$ -Gly + AA + Dex 100 nM
Dx + Hep 0.025 U·mL <sup>-1</sup>	BM + $\beta$ -Gly + AA + Dex 100 nM + Hep 0.025 U·mL <sup>-1</sup>
Dx + Hep 0.25 U·mL <sup>-1</sup>	BM + $\beta$ -Gly + AA + Dex 100 nM + Hep 0.25 U·mL <sup>-1</sup>
Dx 21-ph + Hep 0.5 U·mL <sup>-1</sup>	BM + $\beta$ -Gly + AA + Dex 100 nM + Hep 0.5 U·mL <sup>-1</sup>
Dx 21-ph + Hep 2.5 U·mL <sup>-1</sup>	BM + $\beta$ -Gly + AA + Dex 100 nM + Hep 2.5 U·mL <sup>-1</sup>
Dx 21-ph + Hep 25 U·mL <sup>-1</sup>	BM + $\beta$ -Gly + AA + Dex 100 nM + Hep 25 U·mL <sup>-1</sup>
Hep 0.5 U·mL <sup>-1</sup>	BM + $\beta$ -Gly + AA + Hep 0.5 U·mL <sup>-1</sup>

#### 14.13 Alkaline phosphatase enzymatic activity measurement.

Differentiation potential to osteoblast of hMSCs using Dex and Hep was quantitative evaluated by the enzymatic activity of ALPL (172, 173). Prior analysis, a standard calibration curve of the enzymatic activity product, *p*-nitrophenol, in the range of (0 to 25 nmol per well) was analyzed.

After 3, 7, and 14 days of analysis, culture medium was removed from culture plates, and 200  $\mu$ L of distilled water was added to each well. After that, cells were exposed to three continuous freeze-thawed cycles (120 minutes at -80°C and 120 minutes at room temperature) to induce their lysis and the subsequent protein release (174, 175). Immediately, cell lysates were added in a culture plate and finally, the enzymatic substrate *p*-nitrophenyl phosphate 5 mM dissolved in diethanolamine buffer (pH 9.3) was added. Enzymatic reaction was carried out at 37°C, and the reaction product *p*-nitrophenol was quantified in a plate reader (Synergy HTX multi-mode reader, Biotek) using a wavelength of 412 nm every 5 minutes until 60 minutes. The enzymatic activity was calculated according to the product formation in comparison with the standard curve.

Finally, ALPL activity assay was normalized by the whole protein content, determined with the bicinchoninic acid (BCA) assay at 562 nm using

BCA Protein Assay Kit (Pierce™, ThermoFisher Scientific), according with manufacturer's protocol, with some modifications: 25  $\mu\text{L}$  of each standard protein concentration (0 to 250  $\mu\text{g}\cdot\text{mL}^{-1}$ ) or each sample replicate were added into a 96-wells microplate well, after that, 200  $\mu\text{L}$  of the working reagent were added to each well and the plate was mixed thoroughly on a plate shaker for 30 seconds. The plate was incubated at 37°C in a dark chamber and was cooled to room temperature before each measure. Measurements of the absorbance were carried out at 562 nm on a plate reader. The incubation time was extended to 1.5 hours for all samples. Finally, whole protein concentration was calculated in comparison with the standard curve, and ALPL activity content was normalized with the whole total protein content data.

#### **14.14 Qualitative analysis of osteogenesis by immunofluorescence analysis of osteoblast cell markers.**

HMSCs (passage 5) were seeded in Nunc™ Lab-Tek™ culture plates in a density of 14000 cells·cm<sup>-2</sup>. After 24 hours, cells were exposed to differentiation medium, containing Dex 100 nM and Hep 0.5 UI·mL<sup>-1</sup>. Cells in basal medium were used as negative control and differentiation medium without heparin as positive control. After 7 and 14 days of differentiation, culture medium was removed and cells were fixed with 4% paraformaldehyde for 10 minutes and then, permeabilized for 10 minutes using 0.1 % Triton-X100 in PBS (PBST) at room temperature. Bovine serum albumin 1% wt. in PBST was used as blocking buffer, where cells were exposed at room temperature for 30 minutes. ALPL expression was determined with ALPL recombinant rabbit monoclonal antibody 1:200 working solution (BSA 1% wt. in PBS) for 60 minutes at 37°C, after that, cells were washed three times 5 minutes each with PBS and lastly, cells were stained with goat Anti-Rabbit IgG (Alexa Fluor® 594) secondary antibody 1:400 working solution at room temperature for 60 minutes and washed 3 more times using PBS. To finish, the same samples were incubated with recombinant Alexa Fluor® 647 Anti-Collagen I antibody 1:200 working solution at room temperature during 60

minutes in a dark chamber, washed 3 times with PBS and finally, nucleus were stained using 1 drop of mounting medium with DAPI and then, observed under a confocal microscope.

A second immunofluorescent analysis using anti-OPN and anti-ALPL antibodies was carried out for samples containing cryogels and electrodes.

#### **14.15 RNA isolation from hMSCs.**

HMSCs (passage 5) were culture in 24-well plates, with a cell density of 14000 cells·cm<sup>-2</sup>. Culture media consisting in BM, β-glycerophosphate, ascorbic acid, Dex 100 mM, and Hep 0.5 UI·mL<sup>-1</sup> was changed every three days, all the controls were included in the analysis. RNeasy mini kit (Qiagen) was used during RNA isolation, according with manufacture's protocol: cells were detached from the culture plate using TrypLE and centrifuged at 6000 rpm for 10 minutes to obtain a pellet. After that, 350 μL RLT buffer (lysis buffer) was added to the pellet and vortex 1 minute, immediately, 350 μL of 70 % v/v ethanol was added to the lysate and mixed by pipetting.

Sample was transferred to a RNeasy Mini spin column, placed in a 2 mL collection tube, and centrifuged for 15 seconds at 8 000 RCF. Subsequently, 700 μl of Buffer RW1 were added to the RNeasy spin column (centrifugation 15 seconds·8000 RCF<sup>-1</sup>), after that, 500 μl of buffer RPE was added to the RNeasy spin column (centrifugation 2 min·8000 RCF<sup>-1</sup>). The column was placed in a new 1.5 mL collection tube and finally, 30 μL of RNase-free water was added directly to the spin column membrane and centrifuged for 1 minute at 8000 RCF to elude the RNA. Total RNA concentration was determined by spectrophotometric quantification and finally stored at -80°C before their use.

#### **14.16 Quantitative analysis of osteoblast differentiation by qPCR.**

Total RNA (80 ng) was reverse transcribed into cDNA using Power SYBR™ Green RNA-to-CT™ 1-Step Kit (Applied Biosystems) according with

manufacture's protocol (Table 5). cDNA was immediately analyzed in the same reaction, using the primers to amplify the following genes: *RunX2*, *ALPL*, and *OPN*. Thermocycling reactions were carried out at 48°C during 30 minutes for reverse transcription, and at 95°C for 10 minutes for DNA polymerase activation. Finally, reaction was followed by several cycles at 95°C for 15 seconds (denaturation) and 54°C for 60 seconds (annealing). Glyceraldehyde 3-phosphate dehydrogenase (*GAPDH*) was employed as housekeeping gene. The  $\Delta C_t$  values were calculated for each sample by subtracting the threshold cycle value ( $C_t$ ) of *GAPDH* from the  $C_t$  value of gene of interest. Lower  $C_t$  and  $\Delta C_t$  values indicate higher gene abundance. Finally, data were normalized to obtain  $\Delta\Delta C_t$  values, which was directly related with the percentage of gene expression.

**Table 5.** qPCR reaction components using for the analysis of osteoblast markers.

Master mix component	Volume/concentration
Power SYBR® Green RT-PCR Mix (2×)	10 $\mu$ L
Forward primer final concentration	200 nM
Reverse primer concentration	200 nM
Enzyme Mix (125×)	0.16 $\mu$ L
RNA template	80 ng
RNase-free H <sub>2</sub> O	to complete 10 $\mu$ L

All primer sequences and qPCR temperatures are reported in Table 6.

**Table 6.** Primers/probes used for real-time polymerase chain reaction during the osteoblast differentiation of hMSCs.

Gene	Primer sequence (forward/reverse)	T annealing (°C)	Cycles	Product size	Reference
<i>GAPDH</i>	5'GAGTCAACGGATTTGGTCGT'3 5'CATTGATGACAAGCTTCCCG'3	54	50	192	(176)
<i>ALPL</i>	5'ACACTGAAATATGCCCTGGA'3 5'GAAGGGGAACTTGTCCATCT'3	54	50	177	(176)
<i>OPN</i>	5'CATGAGAATTGCAGTGATTTGCT'3 5'CTTGAAGGGTCTGTGGGG'3	54	50	186	(177)
<i>RunX2</i>	5'AAGCAGTATTACAACAGAGGGTACAAG'3 5'GGTGCTCGGATCCCAAAA'3	54	50	124	(178)

#### **14.17 hMSCs differentiation using dexamethasone 21-phosphate controlled released systems.**

HMSCs (passage 5) were culture in 24-well plates, in a cellular density of 14000 cells·cm<sup>-2</sup>. Culture media consisted in BM for negative control, BM, β-glycerophosphate, ascorbic acid, Dex 100 nM, and Hep 0.5 UI·mL<sup>-1</sup> for positive control. On the other hand, culture medium containing BM, β-glycerophosphate, ascorbic acid, and Hep 0.5 UI·mL<sup>-1</sup> were used for the test, where Dex was added from the electrodes and cryogels delivery systems.

For the experiment, a PEDOT/κC:Dx electrode specifically designed to be adjusted to 24-wells plates and previously sterilized by UV-radiation, was put into a well and was immediately electro-stimulated during 6 minutes, using an electronic device to generate custom waveforms for stimulation. The device consisted in a 12-bit Digital-to-Analog (DAC) converter from Visgence, Inc (USA), adjusted to a potential range from -0.6 V to 1.0 V. Finally, the electrode was removed from the well. Four replicates were used during the analysis.

For the cryogels test, a total of 25 mg of Dx 0.00005 % scaffold was used. Cryogels were put on a homemade stainless steel trans well into the well, and 2 mL of culture media was used. Cryogels were replaced every three days, four replicates were used during the test.

To confirm the effect of the Dex controlled-delivery systems on hMSCs, ALPL enzymatic activity, immunofluorescence analysis of ALPL and OPN proteins, and qPCR test were carried out as was described previously.

## 15 Results and discusión

### 15.1 Evaluation of the stability and size of the dispersion systems.

The dispersions used to electrodeposit the monomer and the Dex on the electrode were evaluated by their  $\zeta$ -potential values and particle size distribution in order to determine its stability in aqueous medium.  $\zeta$ -potential data was obtained for the six prepared dispersions, and they are shown in Table 7. It is possible to observe that EDOT/ $\kappa$ C/Dex system has an appropriate stability (-48.70 mV), which is dominated for the  $\kappa$ C micellar system (-43.30 mV). Values of  $\zeta$ -potential over -30 mV are considered stable assuming that an electrostatic charge is the main stabilization mechanism, and the colloidal system is in the range of hundreds (179, 180). The anionic nature of the  $\kappa$ C and Dex avoids aggregation due to the negative values obtained in the  $\zeta$ -potential analysis, which are comparable with previously reported results for these molecules (123, 181, 182). A stable dispersion prevents aggregation or deposition of the particles that carried the monomer during the electrochemical deposition. Additionally, the stable system may allow a homogeneous dispersion of  $\kappa$ C and Dex in the electrodeposited film as seen by Raman spectroscopy.

**Table 7.**  $\zeta$ -potential values of dispersions used in the fixation of the drug on the electrode.

System	$\zeta$ -potential (mV)	SD (mV)
Dex	-69.40	1.14
$\kappa$ C	-43.30	3.31
$\kappa$ C/Dex	-42.63	1.67
EDOT/Dex	-70.83	1.09
$\kappa$ C:EDOT	-48.46	1.70
EDOT/ $\kappa$ C/Dex	-48.70	1.21

Particle size measurements of the main three dispersions were performed to determine the dimension of their aggregates after the sonication process. Figure 9a shows the size distribution for the  $\kappa$ C 0.2% wt. solution, it is possible to observe a single population for the surfactant. Some authors have reported previously that

$\kappa$ C solutions are polydisperse (two or more populations), because it increases the gel behavior due to its polysaccharide nature (183, 184). Nevertheless, they emphasized that the main signal for the  $\kappa$ C aggregates has an average size in the range of 800 to 1000 nm (184), which agrees with our results. The intensive sonication process before the measure and the low concentration of  $\kappa$ C used in the analysis may explain why only one population were observed in Figure 9a, similar to a previous report (123).

On the other hand, once the Dex was added to the dispersion, a polydisperse behavior was found in the  $\kappa$ C/Dex system and two populations were detected (Figure 9b). Dex solutions are characterized by a single population with a particle size average of 100 nm (185), which is consistent with our result. Eventually, it is possible to observe that the stability of the system has remained when the monomer was added (Figure 9c). The stability of the dispersions depends mainly on the used surfactant, and it has an important influence in the physical and electrochemical properties of the electrodeposited films (186).



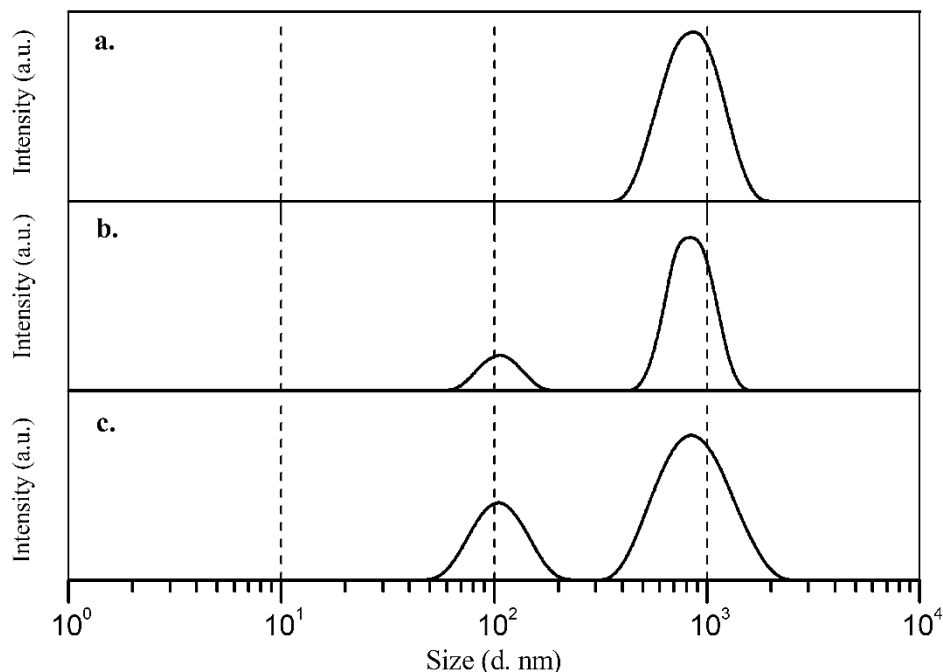


**Figure 9.** Size distribution (d.nm) of a.  $\kappa\text{C}$ ; b.  $\kappa\text{C}/\text{Dex}$  and c.  $\text{EDOT}/\kappa\text{C}/\text{Dex}$  dispersions, measured by dynamic light scattering (DLS) method.

## 15.2 Analysis of the topography and composition of $\text{PEDOT}/\kappa\text{C}/\text{Dex}$ coating by $\mu\text{-Raman}$ spectroscopy and profilometry methods.

The  $\text{PEDOT}/\kappa\text{C}/\text{Dex}$  composite was obtained from an  $\text{EDOT}/\kappa\text{C}/\text{Dex}$  dispersion by electrochemical deposition under galvanostatic conditions (Annex 2), as it was established in a previous work (123, 163). Then, the topography of the  $\text{PEDOT}/\kappa\text{C}/\text{Dex}$  coating was characterized before ( $S_a$ :  $0.270 \pm 0.005 \mu\text{m}$ , Surface area:  $1361 \text{ mm}^2$ , Negative volume  $0.1562 \text{ mm}^3$  and Volume  $1.695 \text{ mm}^3$ ) and after ( $S_a$ :  $0.250 \pm 0.005 \mu\text{m}$ , Surface area:  $1337 \text{ mm}^2$ , Negative volume  $0.1707 \text{ mm}^3$  and Volume  $1.690 \text{ mm}^3$ ) releasing the Dex from the conductive coating. The roughness data of both surfaces did not show significantly differences between them (see Figure 10a and 10b). The volume ratio between peaks and valleys describes the symmetry in the surface topography. A negative value is indicative of more distinct valleys and positive is more distinct peaks about the average plane. Our samples were dominated by peaks and low negative volume (around ten times) and those values are consistent with a previous report

for PEDOT/ $\kappa$ C coatings (123). It is suggested that rough surfaces in comparison with smooth surfaces improve cell attachment due to the formation of specific surface-cell contacts by increasing the expression of different integrins subunits (187, 188). Although, diverse authors have reported that surface roughness values higher than 0.5  $\mu\text{m}$  are desirable to ensure the maximum attachment and proliferation of cells, large rough surface also stimulates more anti-inflammatory responses because the activation of M2 macrophages and the subsequent release of anti-inflammatory cytokines (124). The PEDOT/ $\kappa$ C/Dex surface roughness value and the lack of their significant variation during the delivery of Dex may indicate the reliability of electroactive composite for cell culture studies, since no additional mechanism may be seemed due to the topography changes.

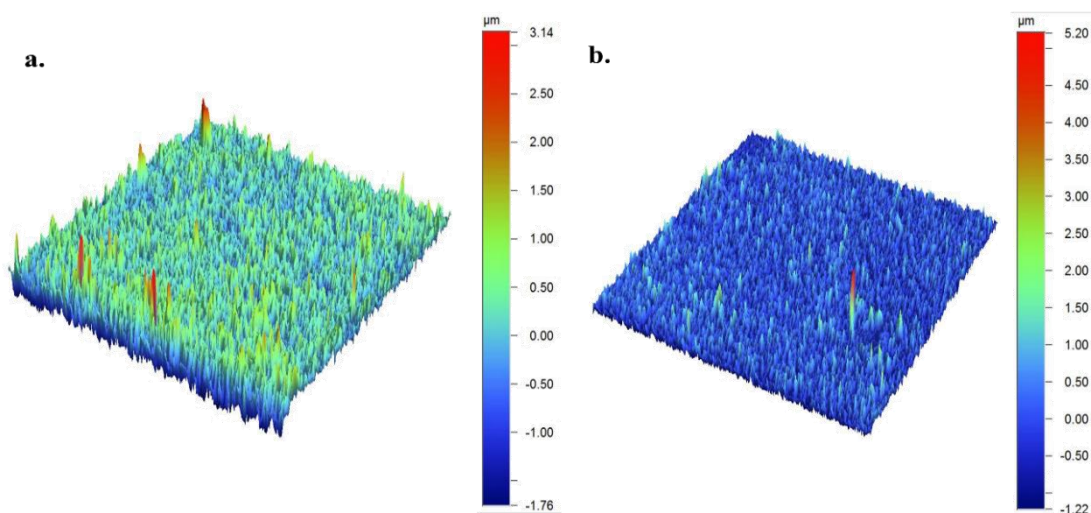


**Figure 10.** Profilometry images obtained for PEDOT/ $\kappa$ C/Dex films (a.) before and (b.) after 160 cycles of Cyclic Voltammetry in a 0.10 M ammonium acetate solution.

The qualitative composition of the conductive film was determined using Confocal  $\mu$ -Raman spectroscopy before (Figure 11a and 11c) and after (Figure 11b and 11d) 160 sweeps of electrical stimulation in a 4  $\mu\text{m}^2$  area and 5  $\mu\text{m}$  depth inside the composite. The analysis was performed to determine the presence of PEDOT, Dex and  $\kappa$ C inside the electroactive composite. The signal was obtained and

plotted in a 2D image that allows the association of the signal (counts) to the presence of the corresponding functional groups for each component.

PEDOT shows a strong signal in the spectral range of  $1421\text{--}1442\text{ cm}^{-1}$ , associated to the thiophene symmetric  $C_{\alpha}=C_{\beta}$  stretching (123, 163, 189) and its oxidation state. The corresponding signal was obtained from the composite (Annex 3) before and after 160 cycles of electrical stimulation and it was mapped at  $1430 \pm 25\text{ cm}^{-1}$  (Figure 11a and 11b), where bright yellow dots corresponded to presence of PEDOT. A homogeneous distribution of the conductive polymer was detected in both samples.

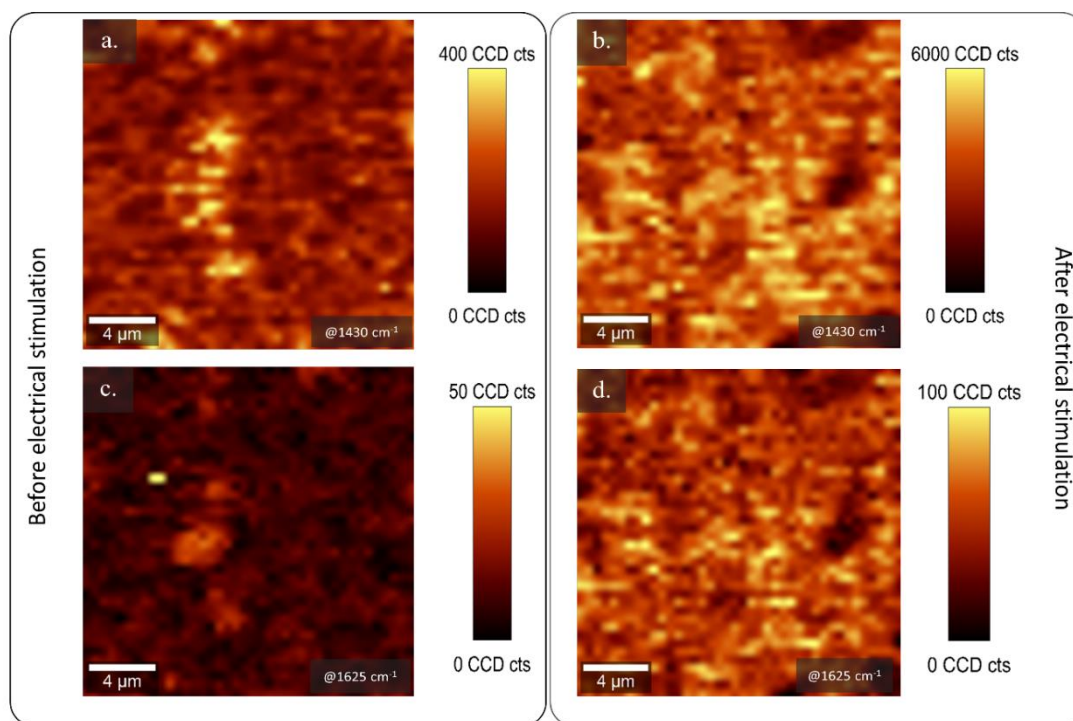


**Figure 11.** 2D confocal Raman map of the  $1430\text{ cm}^{-1}$  band a. before release process and b. after 160 release cycles. Raman mapping of the  $1625\text{ cm}^{-1}$  band intensity c. before release process and d. after 160 release cycles at  $0.5\text{ }\mu\text{m}$  depth inside the conductive layer.

Additionally, a relative intense band at  $1625 \pm 30\text{ cm}^{-1}$  was detected, corroborating the qualitative existence of Dex and  $\kappa\text{C}$  in the conductive film (Figure 11c and 11d). This signal is distributed through the conductive matrix. The result is similar to previous studies (111, 190), which reported the characteristic spectral signals

of Dex in the ranges of 3200-3500  $\text{cm}^{-1}$ , 2850-3000  $\text{cm}^{-1}$  and near to 1650  $\text{cm}^{-1}$ , as is verified in Annex 4, corresponding to hydroxyl, methyl and carbonyl groups, respectively. Dex and  $\kappa\text{C}$  act as doping agents, so, there is a consistent association of the respective signal for both molecules and the PEDOT band. The identification of the band at 1625  $\text{cm}^{-1}$  overlapping with PEDOT signal, confirmed the presence of the doping agent before and even after electrochemical stimulation, as is shown in Annex 3a and Annex 3b, respectively. Adding  $\kappa\text{C}$  in the formulation provides a proper doping agent during the release of the Dex, reducing the degradation by overoxidation and eventually delamination as is shown in Figure 6 (123).

### **15.3 Dexamethasone-21 phosphate release experiments from the PEDOT/ $\kappa\text{C}$ /Dex coating.**

Drug loading into the conducting polymers films is based on the fact that this kind of polymers are electrically oxidized during the polymerization processes, generating charge carriers (134, 135, 164). The doping agent (e.g. Dex and  $\kappa\text{C}$ ) is incorporated to the oxidized polymer to maintain charge neutrality (128). In this work, Dex and  $\kappa\text{C}$  are used as doping agents, the presence of sulfate and phosphate groups imparts negative charges in the polysaccharide and the drug, respectively.

The electrochemical controlled release studies from PEDOT/ $\kappa\text{C}$ /Dex coating were performed within a potential range of -600 to 1000 mV to evaluate intrinsic redox processes of the film (111, 134, 182). Figure 12 shows the characteristic oxidation and reduction potential signal ranges at 0 to 500 mV and -100 to -400 mV respectively, after different number of voltammetry scans. According to some authors, the voltammetric behavior of dexamethasone shows a reduction signal at the potential of -350 mV (111, 134), which indicates the release of the drug from a stimulated electrode. The corresponding CV signals are shown in Figure 12, this signal decreased gradually according to the sweep number, disappearing completely after 160 cycles of electrical stimulation. Electrochemical reduction of a conducting polymer results in the migration of small doping molecules from the

conducting composite to maintain the electro neutrality of the matrix (128, 135). Thus, the application of alternating positive and negative potentials during cyclic voltammetry analysis caused the release of the Dex from the PEDOT coating. Spontaneous release of the dopant from the PEDOT structure is an instant process, but the Dex release is slow since it is driven by diffusion from the inner film to the surface.  $\kappa\text{C}$  is a large molecule, this type of dopant is more attached into the polymer coating and it is not leached out during the electrical stimulation, granting to the polymer greater electrochemical stability (111, 128, 191), as was confirmed by raman spectroscopy.

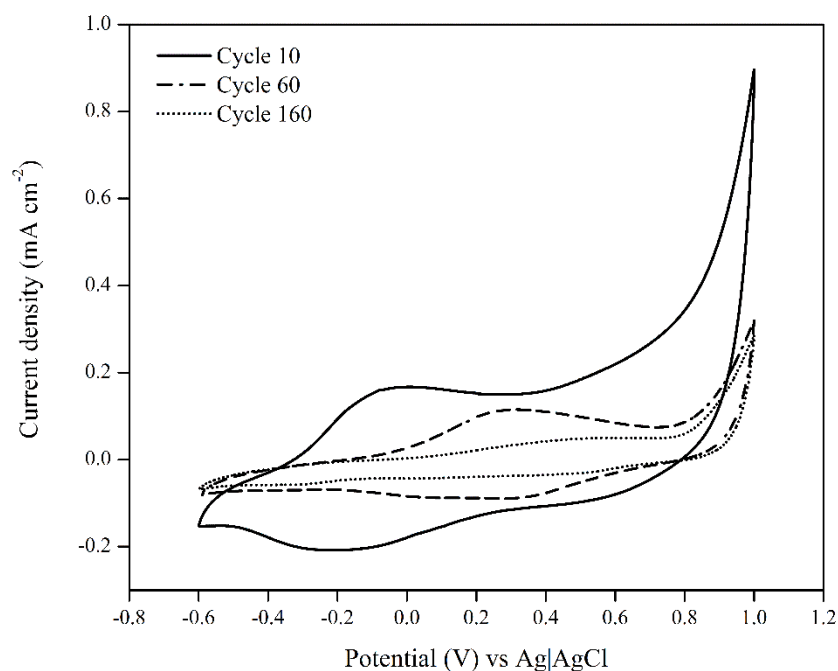


**Figure 12.** Cyclic voltammograms for the PEDOT/ $\kappa\text{C}$ /Dex recorded at  $25 \text{ mV}\cdot\text{s}^{-1}$  after 10, 60 and 160 cycles of electrical stimulation in ammonium acetate 0.10 M.

The release profile of the Dex was investigated under passive conditions (unstimulated) and under active electrical stimulation using an ammonium acetate 0.10 M solution as supporting electrolyte. The surface area of the electrode is associated to promote larger amounts of passive drug release

according to the second Fick's law of diffusion (192, 193), yet, in our case, the electrode surface and total area are maintained virtually constant. The quantification of Dex from the PEDOT/ $\kappa$ C/Dex modified electrodes was achieved using HR-mass spectroscopy (Figure 13).

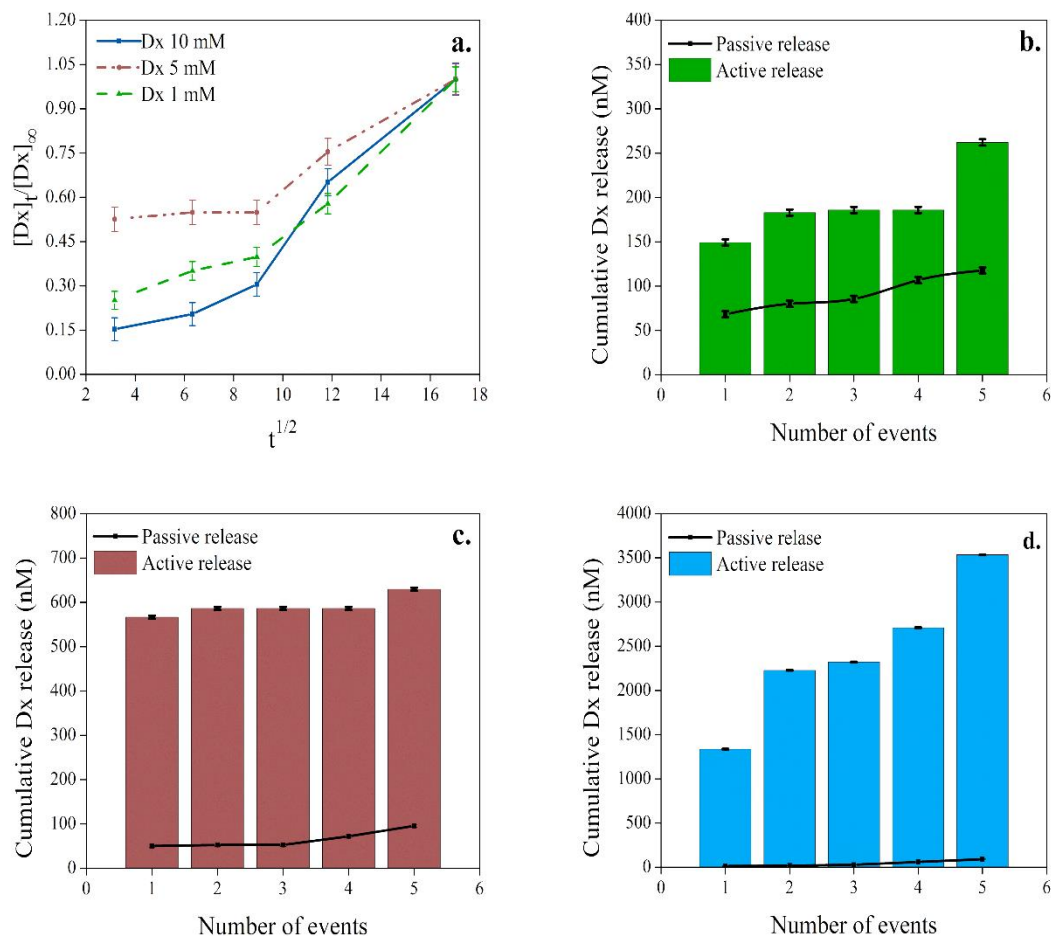


**Figure 13.** a. The passive release profile of Dex as a function of square root of time, over 300 minutes from unstimulated electrodes. The active electrically controlled delivery process by stimulation events (columns) compared to the passive release profile (line).

The active release profile was performed with a total of 76 CV sweeps in five release events, taking around 300 minutes to be completed. Accordingly, the passive release profile from unstimulated electrodes were evaluated over the same period.

Figure 13.a shows the passive release profile of Dex as a function of square root of time according to the Higuchi model for the drug release from a polymer film (5, 194), where pure Fickian diffusion is the dominant phenomena (192). The low diffusion value, in the beginning of the process, may depend on the slow penetration of supportive electrolyte into the polymeric film (193). The pattern changed after 80 minutes, and a higher diffusion value reflects the diffusivity of the passive Dex release process. The three systems (1 mM, 5 mM and 10 mM) showed analogous Fickian diffusion behavior.

On the other hand, the Figure 13.b, 13.c and 13.d showed a remarkable dependency of the released Dex concentration during the electrical stimulated events (bars) compared to a passive unstimulated electrode (line). Some authors have studied controlled drug release systems using conductive polymers such as polypyrrole and PEDOT, where the anionic molecule is used as doping agent and their subsequent release is mainly determined via diffusion (24, 111, 133–135). Nevertheless, for a controllable release system, it is desirable to have a high active release and low diffusion relationship (24, 127), as shown by our system (see Figure 13). For instance, the initial concentration of 10 mM released in the passive process ca. 2% of the delivered Dex in stimulated process. This is probably associated with the use of  $\kappa\text{C}$  as second doping in the matrix, which granting the film stability and integrity during stimulation cycles (123, 128).

The therapeutic dosages of dexamethasone in mesenchymal stem cells cultures are effective at levels of 100-1000 nM to promote their differentiation to osteoblast or in order to be used during anti-inflammatory treatment (17, 114, 195). In this work, the accumulative concentration of the released Dex using 1 mM and 5 mM initial formulations (Figure 13.b and 13.c) were 300 nM ( $0.66 \mu\text{g}\cdot\text{cm}^{-2}$ ) and 600 nM ( $1.60 \mu\text{g}\cdot\text{cm}^{-2}$ ), respectively. Even though, these values are at therapeutically relevant levels, they are in part determined by the Dex amount released via diffusion.

Instead, when 10 mM of drug was poured in the initial formulation, a total of 3700 nM ( $8.89 \mu\text{g}\cdot\text{cm}^{-2}$ ) of cumulative Dex was detected. This concentration range far

in excess of the quantity of Dex released from similar systems using an identical initial concentration of drug for the coating preparation, for which values are even lower than  $5.03 \mu\text{g}\cdot\text{cm}^{-2}$  (24, 127, 133). Such concentrations surpass the amount of drug needed in cell cultures and it is not recommended to apply in biological systems. Nonetheless, using a specific electrochemical stimulation profile may be allowed to provide an adequate quantity of drug to different biological applications.

Finally, based on the previous characterization, the quantity of initial drug to be immobilized on the electrodes designed for 24-well plates was adjusted to 250000 nM. It was because the electrodes used during cell culture presented a total area approximately 3.5 times bigger than electrodes in Figure 6. After that, the number of stimulation cycles were also studied to determine the amount of electrical stimulation events needed to release the adequate drug concentration in the cell culture.

According with the above, electrode was stimulated six times in total, the first two events of stimulation released an excess of drug in the well, after, it was obtaining the desirable concentration of drug (approximately 110 ng in each event) in the next four events. Because of that, during cell culture, once the electrode was prepared, it was cycling 2 times to release the excess of drug and finally, electrode was applied in the cell culture plate, where it was stimulated 4 more times (1 event per well). The obtained results are shown in Figure 14, arrows indicate the cycles of stimulation where the electrode was applied into the culture well.



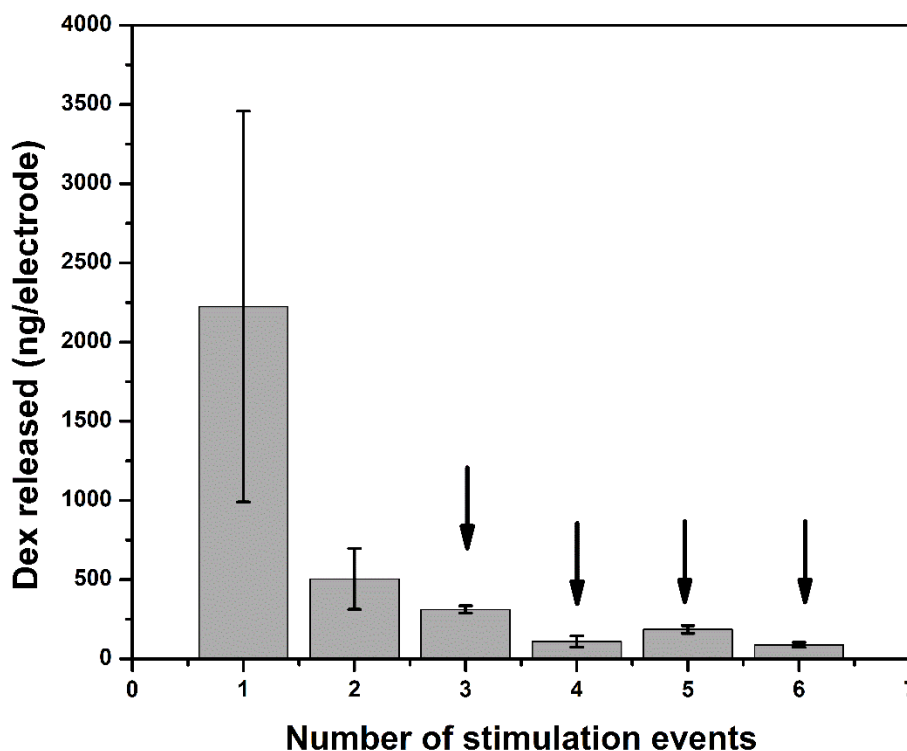


**Figure 14.** Dexamethasone 21-phosphate release profile from PEDOT/ $\kappa$ C/Dex electrodes after electrical stimulation events. Arrows shown the events where the desirable Dex concentration was released.

#### 15.4 Physical characterization of starch based cryogels.

Cryogels were obtained in a cylindrical shape, and had a whitish color, regardless polysaccharide content used. Data from physical and textural characterization of cryogels are shown in Table 8. The volume rate before and after samples lyophilization is reported as shrinkage percentage and was directly obtained from geometric measurements of the samples before and after drying.

In general, the volume shrinkage was lower than 40% for all cryogel samples and is in accordance with those informed for starch-based aerogels with similar amylose content (139). Hydrogels drying method may affect the final gel structure due to the liquid-gas surface tension and liquid-solid adhesive forces. Furthermore, shrinkage of porous structures based on starch and other polysaccharides is very common due to their hydrophilic nature (196).

Furthermore, all samples presented very low bulk densities ( $\rho_{bulk}$ ) and there were not apparently differences between samples according to initial formulation ( $p < 0.05$ ), the obtained values are comparable with previous reports using a similar concentration of corn starch (139). Similarly, not significant differences were determinate between skeletal density sample values, which were in the range of native starch ( $1.50 \text{ g}\cdot\text{cm}^{-3}$ ) (197), see Table 8.

Finally, porosity was determined using equation 1, which is directly related to the geometrical scaffold density. The obtaining values were higher than 90 %, which represent high porosity and compiles the requirements for synthetic scaffolds to be used for tissue engineering applications (151).

**Table 8.** Textural and physical properties of the polysaccharide-based cryogels.

Sample	Shrinkage (%)	$\rho_{bulk}$ ( $\text{g}\cdot\text{cm}^{-3}$ )	$\rho_{skel}$ ( $\text{g}\cdot\text{cm}^{-3}$ )	$\epsilon$ (%)	Vp ( $\text{cm}^3$ )
St	$39.94 \pm 4.01$	$0.14 \pm 0.01$	$1.47 \pm 0.01$	$90.22 \pm 0.01$	$6.26 \pm 0.01$
St/kCa	$33.58 \pm 8.12$	$0.13 \pm 0.01$	$1.46 \pm 0.01$	$91.08 \pm 0.01$	$6.95 \pm 0.01$
Dx 0.00005	$28.79 \pm 4.84$	$0.13 \pm 0.01$	$1.45 \pm 0.02$	$91.02 \pm 0.01$	$6.58 \pm 0.01$
Dx 0.0018	$36.43 \pm 8.38$	$0.13 \pm 0.01$	$1.48 \pm 0.02$	$90.51 \pm 0.01$	$6.82 \pm 0.01$

### 15.5 Analysis of polysaccharide-based scaffolds microstructure.

Scanning electron microscopy (SEM) was used to analyze the microstructure of all the cryogels samples (Figure 15). As result, SEM images revealed a three-dimensional porous structure with interconnected pores, showing an attractive porosity for tissue engineering applications. Similarly, pores presented a diameter in a range of approximately 50 to 100 nm for all cryogels formulations, this pore size is in the range to be used for hMSCs culture applications (198, 199). Besides, according with (200), this type of porous structure facilitates their usage as drug delivery systems due to the water circulation efficiency.

Generally, the presence of  $\kappa$ C and Dex in the cryogel formulations did not show a significant impact on the porous morphology and pores size in the fibrous network, demonstrating that the main contribution in the scaffold structural organization is attributed to the starch presence.

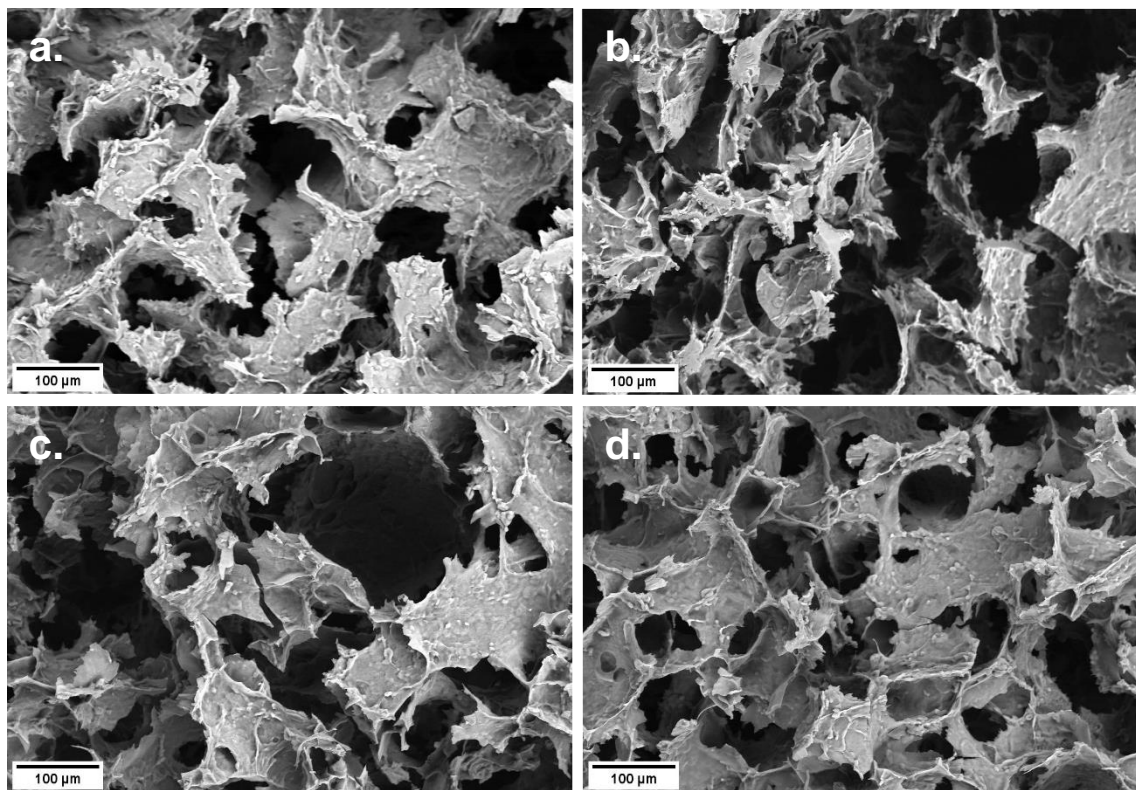


**Figure 15.** SEM images of the textural appearance of a. Starch, b. Starch/ $\kappa$ C, c. Starch/ $\kappa$ C/Dex 0.00002% wt., and d. Starch/ $\kappa$ C/Dex 0.0018 % wt.

### 15.6 Cryogels swelling ratio test.

Swelling kinetic studies were performed for all the different cryogel samples, determination of swelling percentage gives indication about the porosity and stability of scaffolds (201, 202). The profiles of the swelling kinetics presented on Figure 16 indicate that the water uptake capacity for all samples increased quickly at the first 15 minutes at 37°C. The fast water uptake is a characteristic behavior of cryogels, while hydrogels swelling is lower (203).

Additionally, as it was presented in the same figure, the maximum swelling ratio was observed for the pure St/ $\kappa$ Ca/Dex cryogels, nevertheless, there were not significant differences in comparison with St/ $\kappa$ Ca and St samples.

According with (203), a porous structure containing high starch percentage leads to an increment in the hydrophilicity of the scaffold, increases water absorption, and favors the water transport through the porous matrix, as was perceived on the analysis of structural organization of the scaffold (Figure 16).

Finally, it is of our best interest that Dex-based cryogels showed a quickly maximum swelling ratio above 900%, this result is similar to some research, which confirm that an elevated swelling ratio may allow a fast transport of solute molecules, nutrients and waste products on the cryogels structure, favoring their use as drug release system and for biomedical applications, as will be explained in the next section (169).

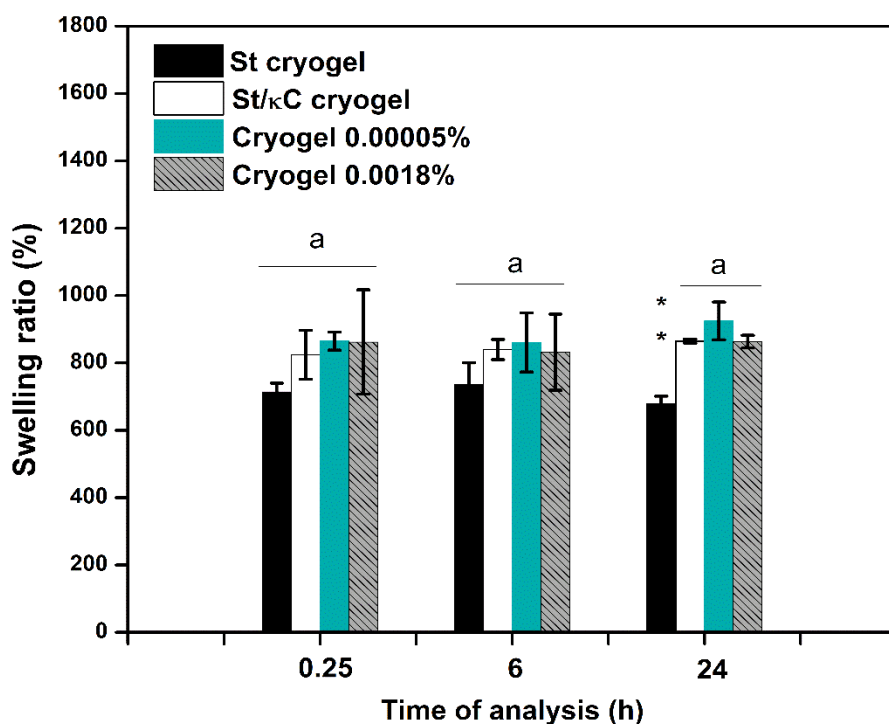


**Figure 16.** Swelling ratio of St, St/ $\kappa$ C, St/ $\kappa$ Ca/Dex 0.00005% and St/ $\kappa$ C/Dex 0.0018% based cryogels after 120 minutes of water exposure at 37°C. \*\* Significant differences ( $p < 0.05$ ), letters are grouping statistically equal treatments.

### 15.7 Cryogels erosion studies.

The erosion test of scaffolds was carried out to study the removal of the cryogels surface layers due to the polymer-solvent interactions to determinate if it is depended on the chemical composition of the surface.

A kinetic analysis of the weight loss after saline buffer immersion at 37°C was used to obtain the erosion percentage after 7 days. Figure 17 shows the comparative degradation profiles of St, St/ $\kappa$ Ca, and St/ $\kappa$ Ca/Dex based cryogels. All the samples showed the maximum degradation at third day of analysis (except for St), where the weight loss was determined between 12% and 25%, this is also related with the hydrophilicity of the starch based-cryogel. Not significant differences were detected between treatments.

Some authors have report that erosion test promotes information about the possible *in vivo* degradability of the matrix, this is important because could be correlated the kinetics of drug release (202, 204). In fact, drug delivery systems can be described such as diffusion-controlled, swelling-controlled, erosion-controlled, and stimulus-controlled, some of these properties make polymeric biomaterials adequate to deliver drugs to human body. In general, kinetic studies have shown that the general drug release behavior of cryogels is controlled by diffusion, swelling, and erosion control (205). These properties confirms that the formulated polysaccharide-based cryogels could be employed as Dex delivery systems.

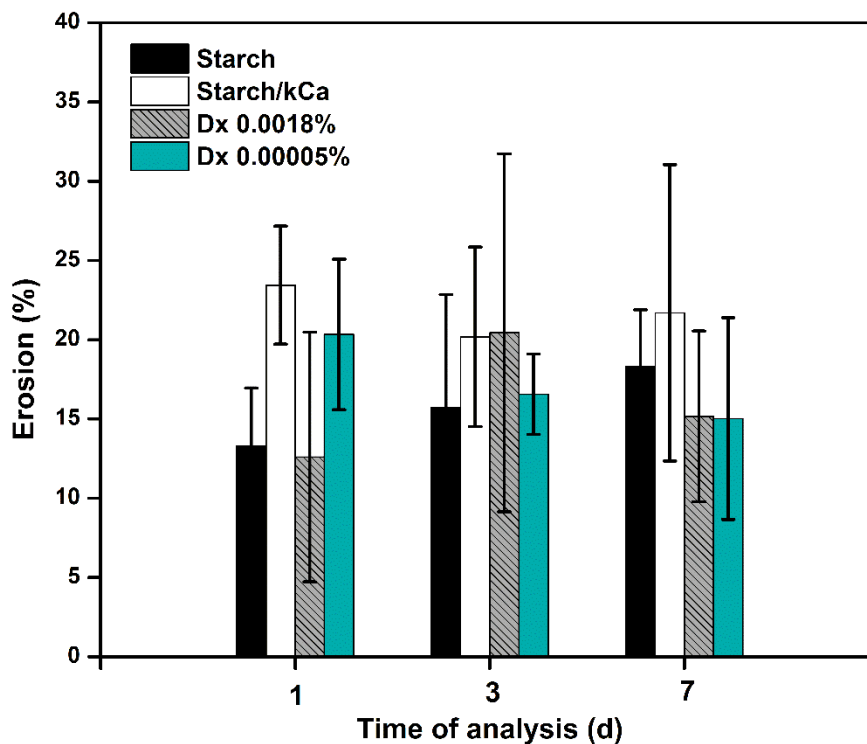


**Figure 17:** Erosion profiles of St, St/kC, St/kCa/Dex 0.00005% and St/kC/Dex 0.0018% based cryogels after 6 days of water exposure at 37°C.

### 15.8 Drug release experiments from the polysaccharide-based cryogels.

Results obtained for the *in vitro* release of Dex from the polysaccharide-based cryogels produced by the freeze-drying method are shown in Figure 18. Generally, all Dex cryogel formulations achieved accelerated drug release rates during the first six hours of analysis, followed by a sustained release in the following 24 hours, releasing an approximate of 28% to 35% of the total drug after 4 days.

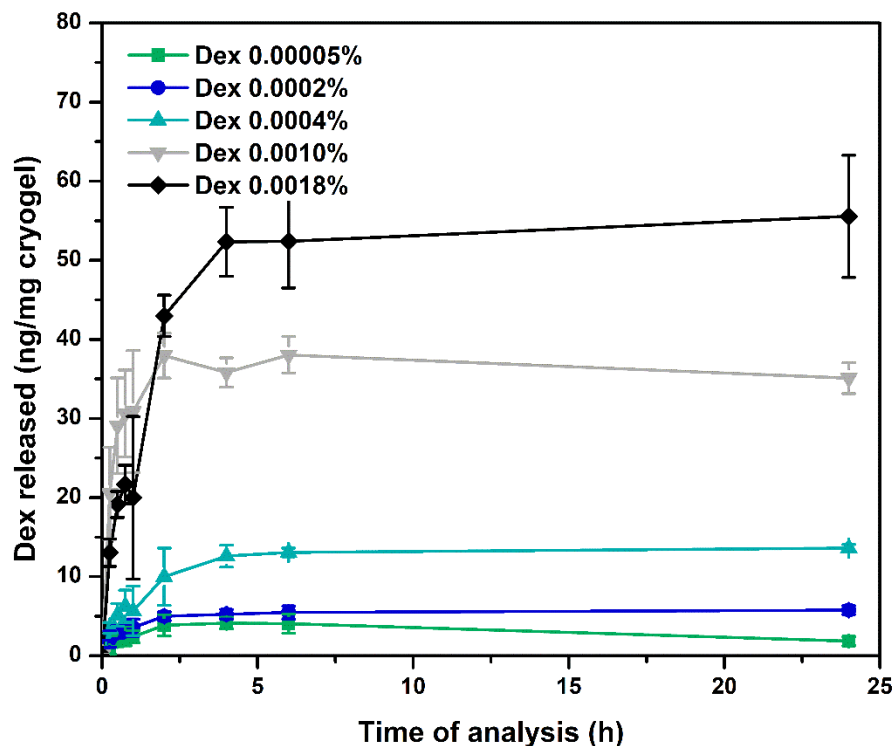


**Figure 18:** Dexamethasone release profiles from St/ $\kappa$ C/Dex porous materials containing 0.00005 wt.% to 0.0018 % of dexamethasone-21 phosphate in ammonium acetate 0.1 M, pH 7.2 at 37 °C and 100 rpm for 24 hours.

As it was previously reported, the dosages of Dex to promote the differentiation of mesenchymal stem cells to osteoblast during *in vitro* culture are effective at levels of 100–1000 nM (206, 207). In this work, the amount of released drug for the cryogel containing Dex 0.00005 wt. % were of  $1.85 \pm 0.55$  ng of drug·mg<sup>-1</sup> of porous scaffold, so that, approximately  $\geq 25$  mg of cryogel is necessary to release cells appropriate concentrations (100 nM) of drug in 24-well culture plates.

Similarly, when 0.0018% of Dex was used in the initial formulation, a total of  $55.55 \pm 7.21$  ng of drug·mg<sup>-1</sup> of scaffold was released. Diverse authors report that this amount of drug may be used during human *in vivo* Dex administration in order to obtain an anti-inflammatory potential response (208, 209). Consequently, the cryogel system containing Dex at high dosages may be useful as drug delivery

scaffolds for biological applications or could be used as a potential model to design strategies for *in vivo* drug administration through diverse routes (210).

On the other hand, the composition of the cryogels was determined using micro-FTIR spectroscopy before and after 24 hours of Dex delivery to monitoring qualitatively the drug released. Dex presence was confirmed by the analysis of the signal at  $1625\text{ cm}^{-1}$  (12), corresponding to the presence of the carbonyl functional group on the drug and represented as light-blue and green zones in the 2D graphic. As is showed by Figure 19, the signal is distributed through the matrix confirming the presence of the drug before and even after 24 hours of delivery, nevertheless, it is potentially reduced after delivery process in all Dex formulations.

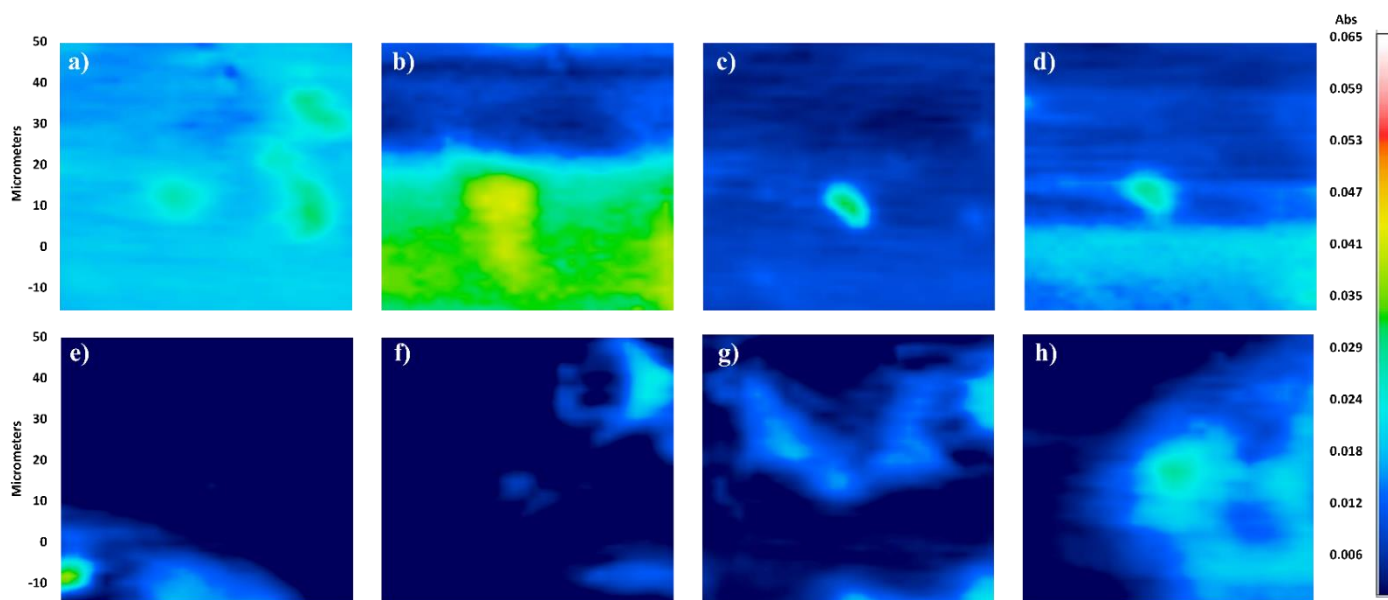


**Figure 19:** 2D micro-FTIR map of the  $1625\text{ cm}^{-1}$  signal before (a-d) and after (e-h) 24 hours of Dex release from the polysaccharide-based cryogel using 0.0002% wt. (a; e); 0.0004%wt. (b; f); 0.0010% wt. (c; g), and 0.0018% wt. (d; h) of drug in the initial formulation.



### **15.9 PEDOT/ $\kappa$ C/Dex electrodes and polysaccharide-based cryogels biocompatibility analysis.**

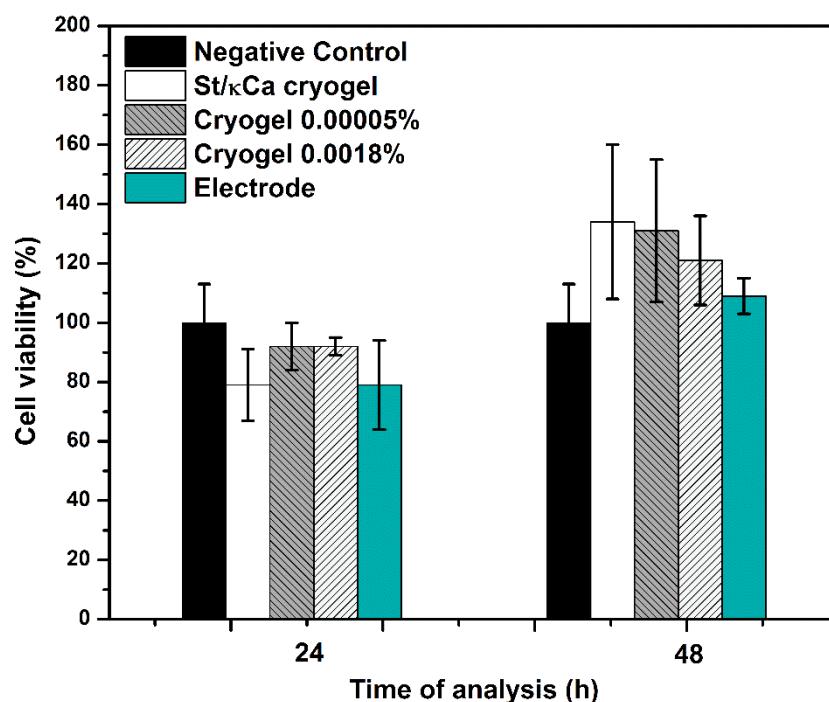
Cytotoxicity and biocompatibility assays are extremely important during biomedical applications, because of that, viability assays were carried out using Cell Counting Kit-8 to study the ability of cells to survive in the presence of the PEDOT/ $\kappa$ C/Dex films and polysaccharide-based cryogels.

Figure 20 shows the results for all the samples after 24 and 48 h of incubation, not significant differences on cell viability between control and samples were detected. It is well known that according to ISO 10993-5:2009 a material is considered biocompatible when the standard cell viability is  $\geq 70\%$ , which is in accordance with our results, confirming the biocompatibility of the scaffolds and films (211–213).

Biocompatibility of starch and  $\kappa$ C based porous structures at several concentrations has been extensively demonstrated in previous studies (214–219). Biocompatibility, in addition to excellent mechanical and physical properties, and versatility for modification with other polymers make those cryogels promising candidates in recent and future studies as carriers for drug delivery, implantable tissue systems, and as extracellular matrices for cell colonization (28, 117, 121).

The low rate of decrease in cell viability for cryogels samples at 24 h (85.0 % of viability compared with the control group), could be attributed to the cryogel degradation at 24 h (section 15.7), it is important to mention that those cryogels were partially dissolved during the first 24 h of culture, degradation of polysaccharides samples could trigger the increase of the culture medium osmolarity and viscosity, as it was demonstrated in previous studies (170). Hypertonic conditions generate variations in cell metabolism, causing a decrease in their proliferation rate (220, 221), nevertheless, not cell viability effects were detectable at 48 h of incubation.

Finally, biocompatibility of PEDOT nanostructures has been demonstrated with SH-SY5Y human neuroblastoma cell line (109) and C3H10 mouse embryonic fibroblasts (222). Porous and non-porous electrical systems polymerized with PEDOT are proposed as potential structures during electrical stimulation of cells for tissue regeneration and as drug delivery systems (222–224), making this one excellent conductive polymer to be incorporated in MSC cultures to induce their differentiation to osteoblast.



**Figure 20.** Biocompatibility analysis of starch-based cryogels and PEDOT/ $\kappa$ C/Dex modified electrode using the CCK-8 assay on hMSCs culture.

### 15.10 Effects of dexamethasone 21-phosphate and high molecular weight heparin on MSCs differentiation to osteoblast.

Differentiation process of hMSCs to osteoblast was monitoring by ALPL enzymatic activity, immunofluorescence analysis and real time PCR.

As was previously explained, the negative charges of the phosphate groups in Dex make possible their incorporation in the PEDOT conducting film and their subsequent release by electrical stimulation, nevertheless, traditionally, the *in vitro* process of MSCs differentiation has been controlled using media containing specific biomolecules (e.g., Dx, ascorbic acid, and  $\beta$ -gly) (225), because of that, the study of the effect of dexamethasone 21-phosphate on MSCs culture in comparison with dexamethasone base was carried out.

Figure 21 shows the obtained results, confirming that not significant differences ( $p > 0.05$ ) according with ALPL activity·min<sup>-1</sup> were determinate between treatments, namely, Dex in comparison with Dx influences in a similar way the differentiation of hMSCs to osteoblast.

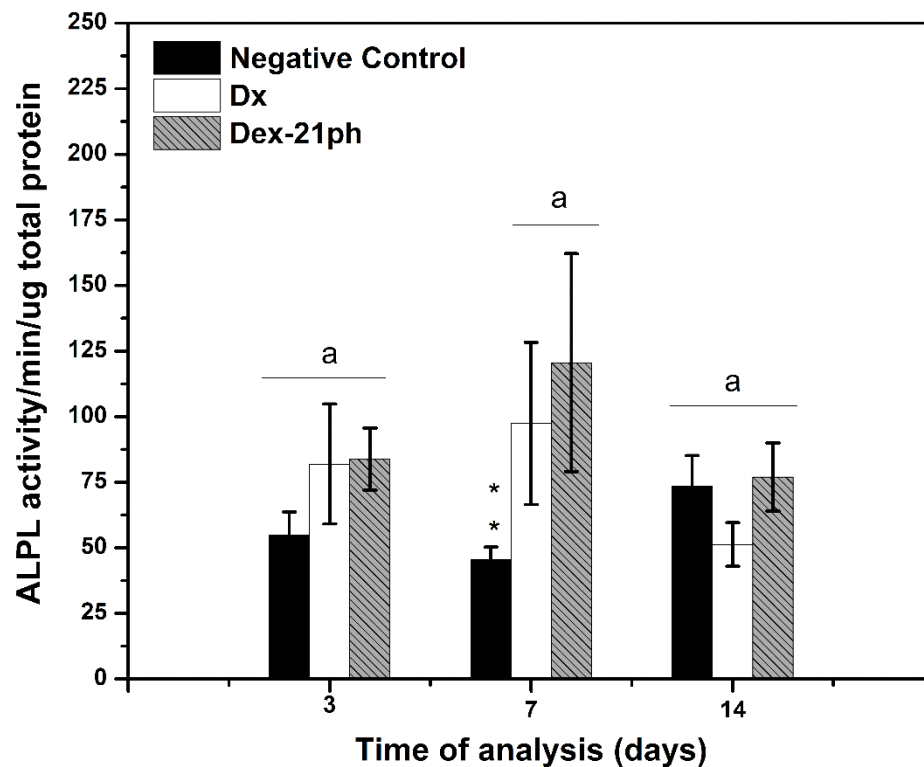


**Figure 21.** ALPL enzymatic activity·min<sup>-1</sup>·ug<sup>-1</sup> total protein of hMSCs at 3, 7 and 14 days of analysis. C-: Basal media; Dx: Basal media + Dx 100 nM; Dex-21 ph: Basal media + Dex 100 nM. \*\*Significant differences ( $p < 0.05$ ), letters are grouping statistically equal treatments.

Since it was demonstrated that Dex is entrapped in human erythrocytes to be dephosphorylated to diffusible Dx (226–228), most scientific reports have limited the use of this drug during *in vivo* studies (229), and Dx as the *in vitro* differentiation factor on MSCs, nevertheless, as it was mentioned, not differences between drugs were identified in this study, which is in accordance with some recent reports (225, 230, 231). The obtained results are important because confirms that the developed controlled released system of Dex could be employed during MSCs *in vitro* applications, the same conclusion was obtained for some researchers in the controlled released systems field (225, 232–235).

As was mentioned, Dx is bind to the nucleus corticosteroid receptor and acts through Notch/Hedgehog, ERK, and  $\beta$ -catenin signaling pathways, inducing *RunX2* expression which upregulates *ALPL* gene, inducing differentiation (112, 113). In general, several studies have demonstrated that Dx induces an increase in the global metabolic hyperactivity of MSCs at day 7, increasing levels of glutamine, cholesterol, glycerolipid precursors, and osteoblastic markers, some of which are subsequently reduced at day 14, and continuing to be reduced until day 21 (114, 236, 237), which is in accordance with the results obtained in Figure 21.

On the other hand, Hep has been used in many biological applications due to its specific affinity to a wide variety of cellular important signals (238–240), because of that, in a similar manner, Hep concentration in response to hMSCs osteoblast differentiation was established in accordance with *ALPL* enzymatic activity normalized with the total protein content at day 3, 7, and 14 (Figure 22).

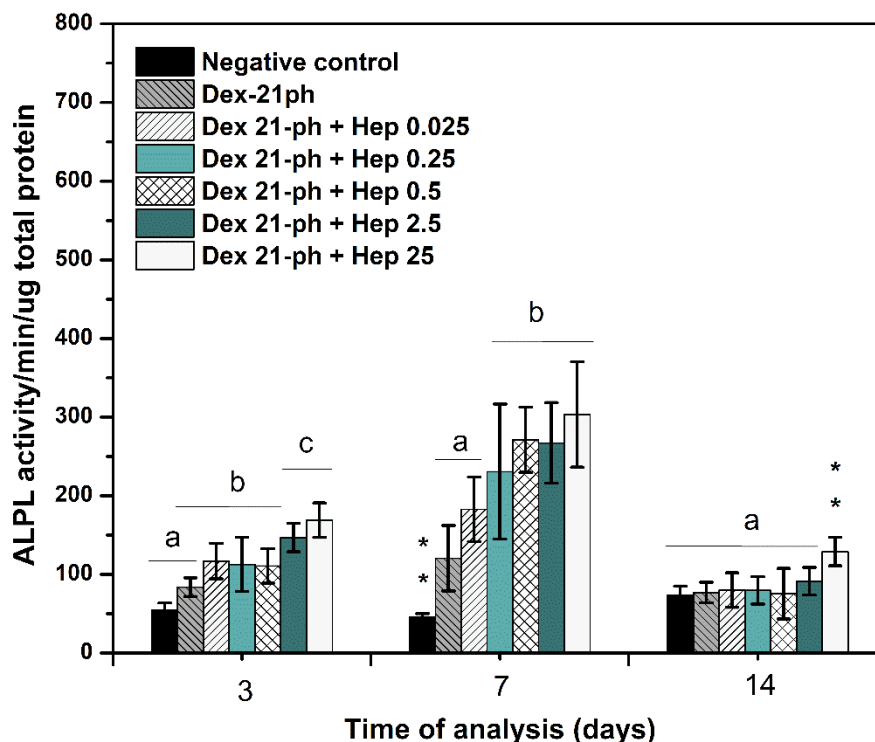


**Figure 22.** ALPL enzymatic activity·min<sup>-1</sup>·ug<sup>-1</sup> total protein of hMSCs culture on culture media containing different concentrations of hep at 3, 7 and 14 days of analysis. Negative control: Basal media, Dex-21ph: Basal media + Dex 100 nM, Dex-21ph + Hep 0.025: Basal media + Dex 100 nM + Hep 0.025 UI·mL<sup>-1</sup>; Dex-21ph + Hep 0.25: Basal media + Dex 100 nM + Hep 0.25 UI·mL<sup>-1</sup>, Dex-21ph + Hep 0.5: Basal media + Dex 100 nM + Hep 0.5 UI·mL<sup>-1</sup>; Dex-21ph + Hep 2.5: Basal media + Dex 100 nM + Hep 2.5 UI·mL<sup>-1</sup>; Dex-21ph + Hep 25: Basal media + Dex 100 nM + Hep 25 UI·mL<sup>-1</sup>. \*\* Significant differences ( $p < 0.05$ ), letters are grouping statistically equal treatments.

Results demonstrated that Hep in combination with Dex promotes osteogenic differentiation of hMSCs, which is dependent of drug concentration. ALPL enzymatic activity increased at the third day of stimulation at concentration of 2.5 UI·mL<sup>-1</sup>, nevertheless, the most remarkable difference was obtained at seventh day, where only 0.5 UI·mL<sup>-1</sup> of Hep were enough to induce a significant difference between Dex containing culture medium and treatment. On contrary, significant differences were detected for the assay containing only heparin in comparison with Dex treatment (Figure 23), which confirms that the Hep has an effect only when is added on dexamethasone containing culture medium, which is in accordance with previous reports (241, 242).

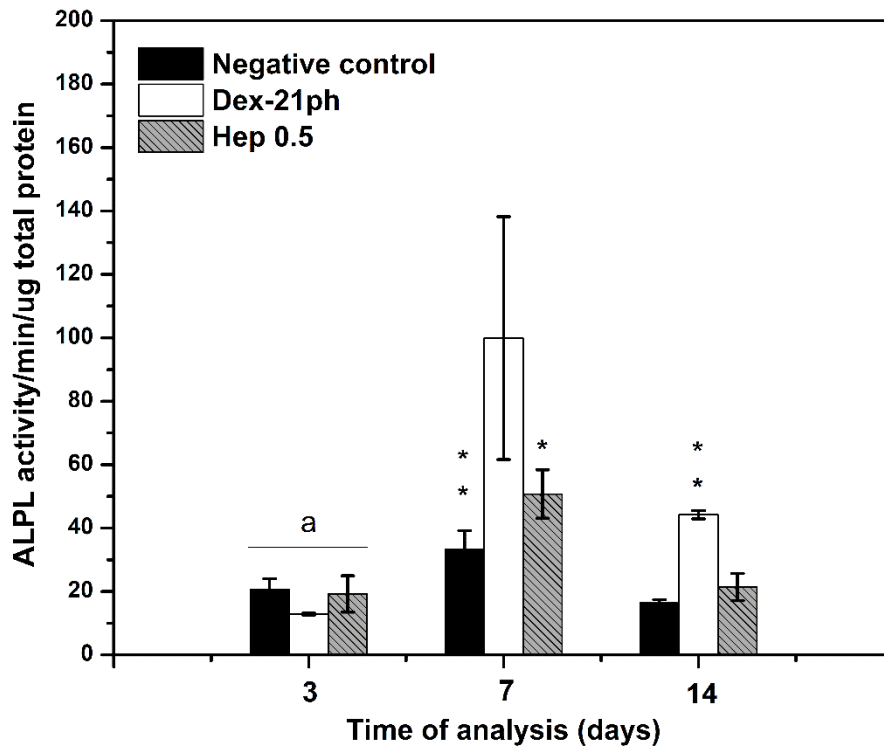


**Figure 23.** ALPL enzymatic activity·min<sup>-1</sup>·ug<sup>-1</sup> total protein of hMSCs culture at 3, 7 and 14 days of analysis. Negative Control: Basal media, Dex-21ph: Basal media + Dex 100 nM + ascorbic acid + β-Glycerophosphate, Hep 0.5 UI·mL<sup>-1</sup>: basal media + ascorbic acid + β-Glycerophosphate + Hep 0.5 UI·mL<sup>-1</sup>. \*\* Significant differences (p < 0.05), letters are grouping statistically equal treatments.

In this work, although a concentration of 25 UI·mL<sup>-1</sup> of Hep caused hMSCs differentiation at the third day of stimulation, the concentration of 0.5 UI·mL<sup>-1</sup> was selected for the subsequent experiments. This selection was based on previously reports (18). Some researchers determined that low doses of Hep (0.03 UI·mL<sup>-1</sup>) modestly could change hMSCs behavior in terms of proliferation, whereas cell culture for long periods under high drug concentrations (18 UI·mL<sup>-1</sup>) cause the expression of senescence markers, and result in significantly larger cells and nuclei, which are morphological features consistent with a senescent cellular state (18, 243).

Several scientists have analyzed the changes in gene expression profile of hMSCs upon Hep treatment and concluded that this drug alters expression of genes related with cell cycle control, specifically, *CDKN1B* (p27) and *CCNG2* (cyclin G2) are upregulated at high Hep concentrations, these genes are associated with cell growth inhibition, thus, high doses of drug could be prejudicial for hMSCs viability in long term cultures (18). Therefore, as was demonstrate in this work, drug concentration is an important factor to consider.

On the other hand, researchers revealed that Hep could stimulates expression of several cell surface proteins and nuclear effectors, due to its biochemical activity as a multivalent co-ligand, in fact, the most striking effect is the major induction of members of the TGF $\beta$ /BMP superfamily and Wnt and FGF, precisely, these factors and biochemical pathways are the most important on osteoblast differentiation of hMSCs, which justifies the results obtained in this work (18, 244, 245).

Finally, the study of the Hep effect on stem cells culture are important in the field of tissue engineering and regenerative medicine, specifically for the study and the development of functionalized scaffolds with cell signaling epitopes, such as proteins, drugs, and growth factors that could influence outside-in signaling, in order to elicit specific biological responses such as differentiation (156).

Hep is a protein-binding GAG, because of that is an attractive drug to modify scaffolds for regenerative medicine and cell culture applications, some similar studies were carried out for some researchers previously, obtaining interesting results in terms of colonization and differentiation of cells into the scaffold (246–248).

Equally, once Hep was added, the effect of Dex in comparison with Dx was confirmed through the analysis of *ALPL*, *OPN*, and *RunX2* genes by real time PCR. As was mentioned, these genes are the main markers during hMSCs differentiation to osteoblast. Figure 24 shows the obtained results at 7 and 14 days of analysis. *ALPL* gene presented the maximum expression at day 7 of

biochemical stimulation, decreasing significantly at day 14 for both treatments, confirming the results obtaining in Figure 21. Nonetheless, unlike the ALPL enzymatic activity analysis, relative *ALPL* gene expression was higher for treatments containing Dx in comparison with Dex, suggesting that there could be some differences in stimulation pattern according with the type of drug used.

To confirm that, *OPN* gene expression was also analyzed, in that case, not significant differences were determined between treatments, although a little increasement at day 7 in Dx treatment was identified, demonstrating that possibly this treatment experiments a shorter differentiation time in comparison with cells exposed to Dex, which explains that *OPN* gene were expressed until day 14 in Dex containing treatments. The same result was obtained for the *RunX2* gene, both treatments expressed the marker at 7 days of analysis, nevertheless a higher expression percentage was identified for Dx treatments, decreasing at day 14. On contrary, *RunX2* gene expression in Dex exposed cells continued to be identified until day 14, as is part of the common differentiation process of hMSCs to osteoblast.

Despite the obtained results related with the type of drug used, it was confirmed that Dex treatments induced the differentiation of hMSCs, which supports that this drug could be used in drug delivery systems to be applied in hMSCs cultures.

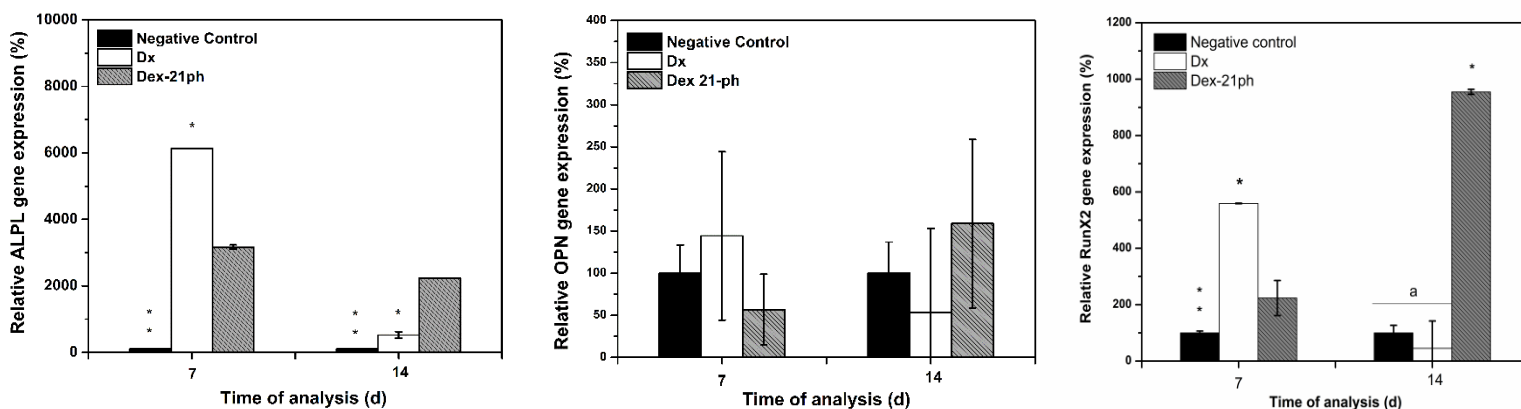


**Figure 24.** Comparisons of gene expressions of ALPL, OPN, and RunX2 among Dex-21ph 100 nM and Dx base 100 nM treatments after 7 and 14 days of analysis. \*\* Significant differences ( $p < 0.05$ ), letters are grouping statistically equal treatments.



Lastly, the osteogenic proteins ALPL and type I collagen (Col-I) were qualitative studied by immunofluorescent staining at day 7 and 14, specifically, Col-I is the most abundant extracellular protein in bone and is expressed during all stages of osteoblast development, while ALPL is commonly found to precede the bone matrix mineralization (249).

Figure 25 and Figure 26 shown the results obtained at day 7 corresponding to ALPL and Col-I analysis respectively. In that figures it is possible to observe that the expression of ALPL were higher in heparin containing culture media in comparison with positive control, which confirms the results obtained previously, contrary, Col-I is expressed in all treatments and not apparently differences were determined between Dex and Dex + Hep treatments. Additionally, ALPL is also expressed in negative control assay, which is in accordance with the result obtained during ALPL enzymatic activity. Researchers have determined that this protein is always expressed in hMSCs at basal levels and are upregulated after biochemical stimulus in osteogenic culture media (250).

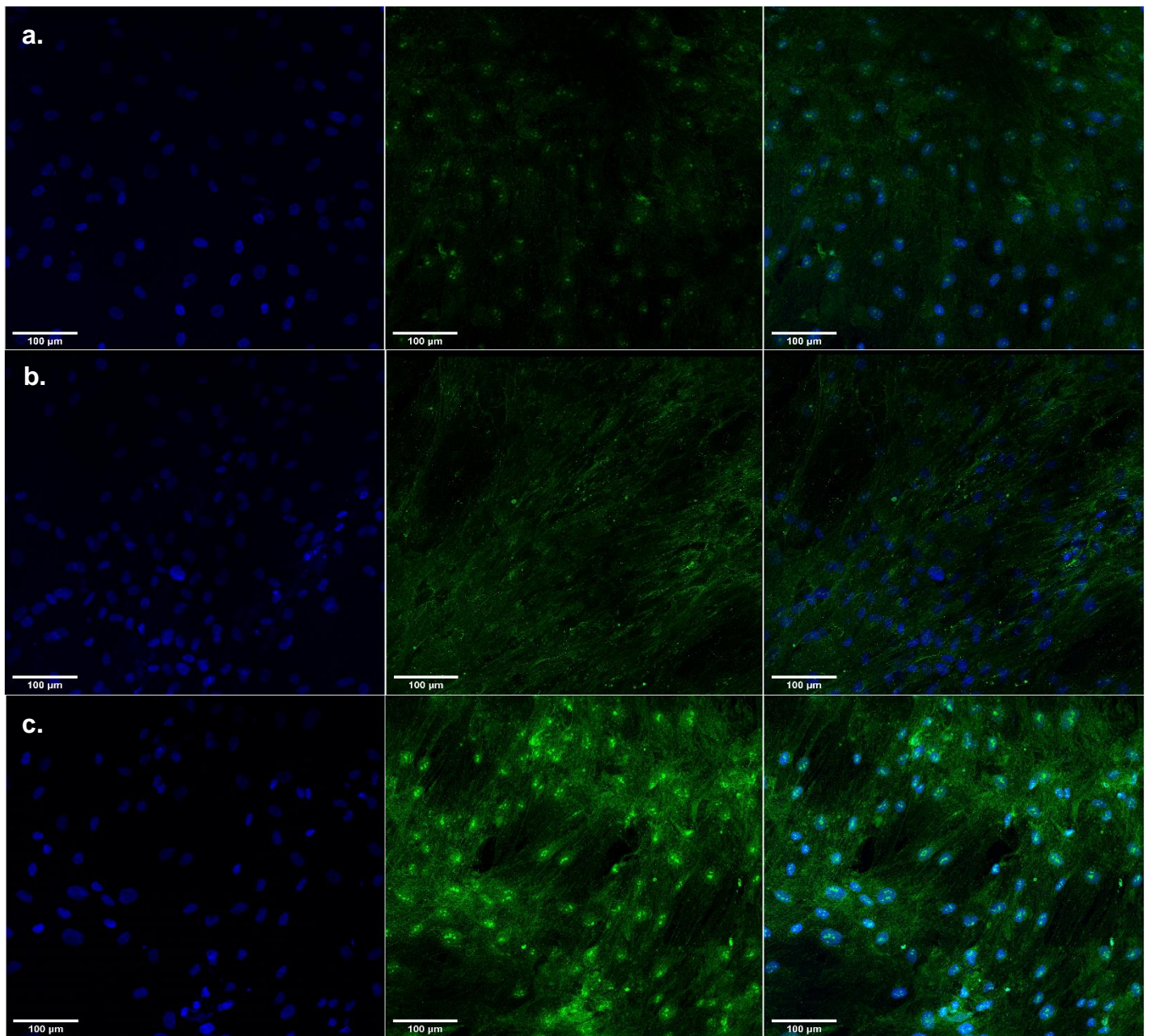


**Figure 25.** Immunofluorescence analysis of hMSCs using anti-ALPL antibody during hMSCs osteoblast differentiation induced by dexamethasone 21-phosphate and heparin: a. Negative control, b. Dex 100 nM, and c. Dex 100 nM + Hep 0.5 UI·mL<sup>-1</sup>.

Similarly, some researchers have described that Col-I and ALPL expression is higher between the first and the seventh day of analysis, nevertheless, their presence was also appreciable by IF assays at day 14. Both proteins are primarily involved in the early stages of osteogenic differentiation, after that time, proteins

are downregulated, and cells continue with the mineralization of ECM and OCN expression. In fact, OCN is regarded as the hallmark in the final stages of differentiation and maturation of stem cells into osteoblasts, nevertheless it was not tested in this assay (250).

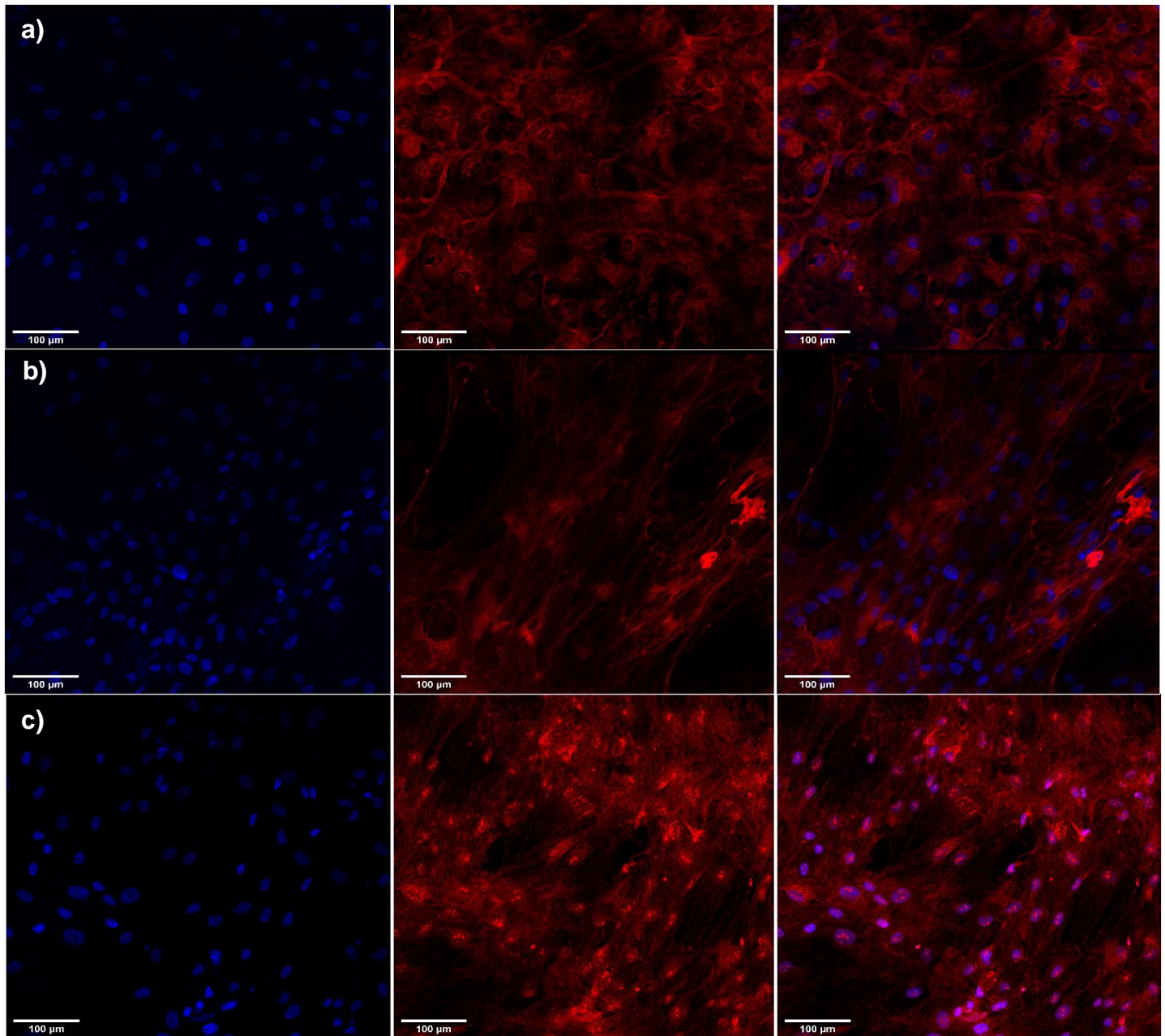


**Figure 26:**Immunofluorescence analysis of hMSCs using anti-Col I antibody during hMSCs osteoblast differentiation induced by dexamethasone 21-phosphate and heparin: a) Negative control, b) Dex 100 nM and c) Dex 100 nM + Hep 0.5 UI·mL<sup>-1</sup>.

Sun and collaborators (251) carried out research to determine the collagen deposition by pre-osteoblastic cells. It is well known that Col-I is a typical component of ECM, because of that, deposition of this protein is a natural process of homeostatic metabolism of cells, nevertheless, during osteoblastic differentiation cells are stimulated to produce large amounts of Col-I, these collagen fibrils are densely banded, causing the cells assemble in an aligned orientation, continuing with extracellular matrix biomineralization, and ending in a matrix with compositionally and morphologically similar features to the *in vivo* bone tissue microenvironment, this explains the results obtained for Col-I staining, which was deposited in the ECM of all treatments.

#### **15.11 hMSCs differentiation using dexamethasone 21-phosphate controlled released systems.**

ALPL enzymatic activity was used to test the released drug capability caused by electrical stimulation and from porous systems on the differentiation of hMSCs to osteoblast. Recently, the application of systems to deliver proteins, growth factors, and other therapeutic agents to induce stem cells stimulation has attracted much attention (225, 229, 230, 232, 233, 235, 252–257).

Based on the analysis of ALPL enzymatic activity (Figure 27), it is possible to conclude that the controlled release of drugs from both systems induced osteoblast differentiation of cells. In fact, not significant differences were obtained between positive control and treatments, which signifies that the systems are efficient to be applied during hMSCs culture.

For the electrodes system, Dex was released after electrical stimulus on the cell culture well, after that, the electrode was removed. The same method was carried out every three days, during two complete weeks. It is well known that traditional drug release systems are based on diffusional events from three-dimensional scaffolds, nevertheless, currently the use of electrical systems to trigger certain biological responses has drawn attention (258, 259).

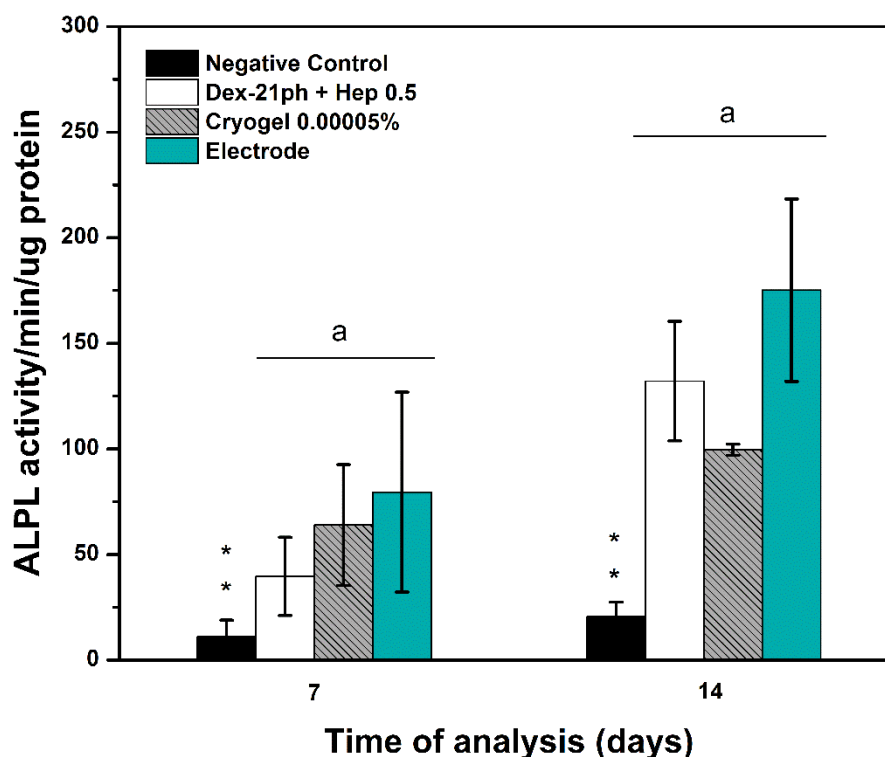


**Figure 27.** ALPL enzymatic activity·min<sup>-1</sup>·ug<sup>-1</sup> total protein of hMSCs culture on culture media containing at 7 and 14 days of analysis. Negative : Basal media, Dex-21ph: Basal media + Dex 100 nM + Hep 0.5 UI·mL<sup>-1</sup>, Cryogel 0.00005%: Basal media + Hep 0.5 UI·mL<sup>-1</sup> + 25 mg Dex 0.00005% cryogel; Electrode: Basal media + Hep 0.5 UI·mL<sup>-1</sup> + Electrode. \*\* Significant differences (p < 0.05), letters are grouping statistically equal treatments.

In 2013, researchers designed a conductive system using graphene-conductive materials containing a drug to be applied to induce cell differentiation (260). Additionally, researchers mentioned that is possible to control the differentiation of hMSCs using only the electrical stimulation, nevertheless, the stimulation cycles must be at high frequencies, using high voltages and should be continuous during all the experiment (258, 259, 261), because of that, the effect of the electrical stimulus caused during Dex released in this work is negligible.

Similarly, St/kC cryogels were proposed as Dex delivery systems to induce hMSCs biochemical stimulation, as was mentioned, the release profile of drug from scaffolds resulted in an initial burst release due to the hydrophilicity nature of drug and starch, completing the total release of drug after 24 hours.

Researchers have proposed the use of this type of three-dimensional scaffolds based on biomaterials to be employed as ECM to cause mechanical stimulation of cells, more recently, the use of these systems have drawn attention as vehicles for drug delivery, which is important for tissue engineering applications, to be used as implantable systems to induce tissue regeneration.

In conclusion, the controlled released of Dex obtained from both systems were useful for differentiation of hMSCs and provided valuable information for the preparation of innovative Dex loaded systems for bone regeneration, focused on the strategy on preparation of three-dimensional matrices with conductive materials to create smart systems for controlled drug delivery.

Additionally, a real time PCR analysis to study the expression levels of *ALPL*, *OPN* and *RunX2* genes after Dex controlled released was carried out. Figure 28 shows the obtained results for electrode system, nevertheless, it was not possible to determinate the effect of cryogels system at molecular level, it is possible that cryogels erosion cause a contamination of the RNA, as was determinate for the relation 260/230 and 260/280 obtained by the UV-analysis reported in Annex 5.

The obtained results in Figure 28 are in accordance with the obtained for Figure 27. *ALPL* gene presented the maximum expression at 7 days for both treatments, decreasing at day 14, as the normal osteoblast differentiation process of hMSCs reported previously. Nonetheless, the most important results are shown for *OPN* and *RunX2* genes, unlike the *ALPL*, these genes were expressed at 7 days in the treatments containing the electrode system for controlled Dex release in comparison with the positive control, which experimented the higher gene expression at 14 days.

As was mentioned, the differentiation of hMSCs by the effect of electrical stimulation, needs several stimulation cycles during a long time applied at high frequencies, and under high voltages, because of that, the observed effect related to the earliest differentiation in cells exposed to electrode could be not attributed to the electrical stimulus. Nevertheless, as it was observed in Figure 14, there are

some variations in relation with the drug released between stimulation events. These variations cause differences on the amount of drug in each well, some researchers reported that hMSCs differentiation profile depends on the Dex concentration, little variations could affect the cycle of differentiation, causing an earliest or later expression of osteoblast differentiation (253, 262, 263), which could justify the obtained results. Therefore, a good strategy to consider is to increase the number of samples in the qPCR analyzes for future tests.

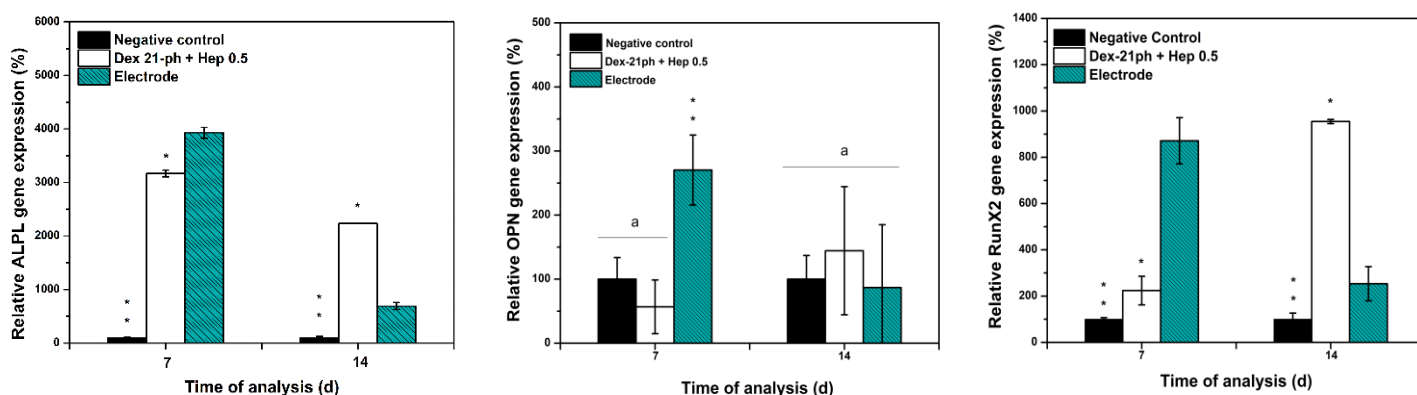


**Figure 28.** Comparisons of gene expressions of ALPL, OPN, and RunX2 among Dex-21ph 100 nM and Dex-21ph controlled released treatments after 7 and 14 days of analysis. \*\* Significant differences ( $p < 0.05$ ), letters are grouping statistically equal treatments.

Immunofluorescence analysis was carried out to confirm the results obtained in Figure 27 and Figure 28 in accordance with hMSCs differentiation caused from Dex released. In this case, the osteogenic proteins ALPL and OPN were qualitatively studied by immunofluorescent staining at day 7 and 14. As was expected, ALPL enzyme was detected in all samples during all times, which is in accordance with the results represented on Figure 25, where the protein was expressed in all samples, including the negative control, related with the protein basal levels, the results may be consulted in Annex 6.

OPN protein, which is a soluble extracellular matrix-associated glycoprotein, was studied by immunofluorescent staining to confirm differentiation of hMSCs to osteoblast caused in treatments containing the cryogels and electrodes (Figure 29). Some authors (264) reported that OPN is mainly secreted by osteoblasts

and by osteogenesis progenitor cells, such as hMSCs. In fact, OPN is secreted once cells undergoing changes behavior such as differentiation (265), to aid their biological activities and functions. Once hMSCs secrete OPN, their proliferation and migration are increased, causing *in vivo* bone resorption (264). At molecular level, OPN activates the FAK/ERK signaling, which are related with the complete process of osteogenesis, as was described previously (264, 265).

Results in Figure 29 showed that OPN was expressed in all samples under Dex stimulation at day 14, including the negative control, confirming osteoblast differentiation, which is in accordance with qPCR obtained results. This assay makes possible conclude that like electrodes, cryogels influence differentiation of hMSCs, increasing the expression of master osteoblastic regulation markers as the OPN protein.



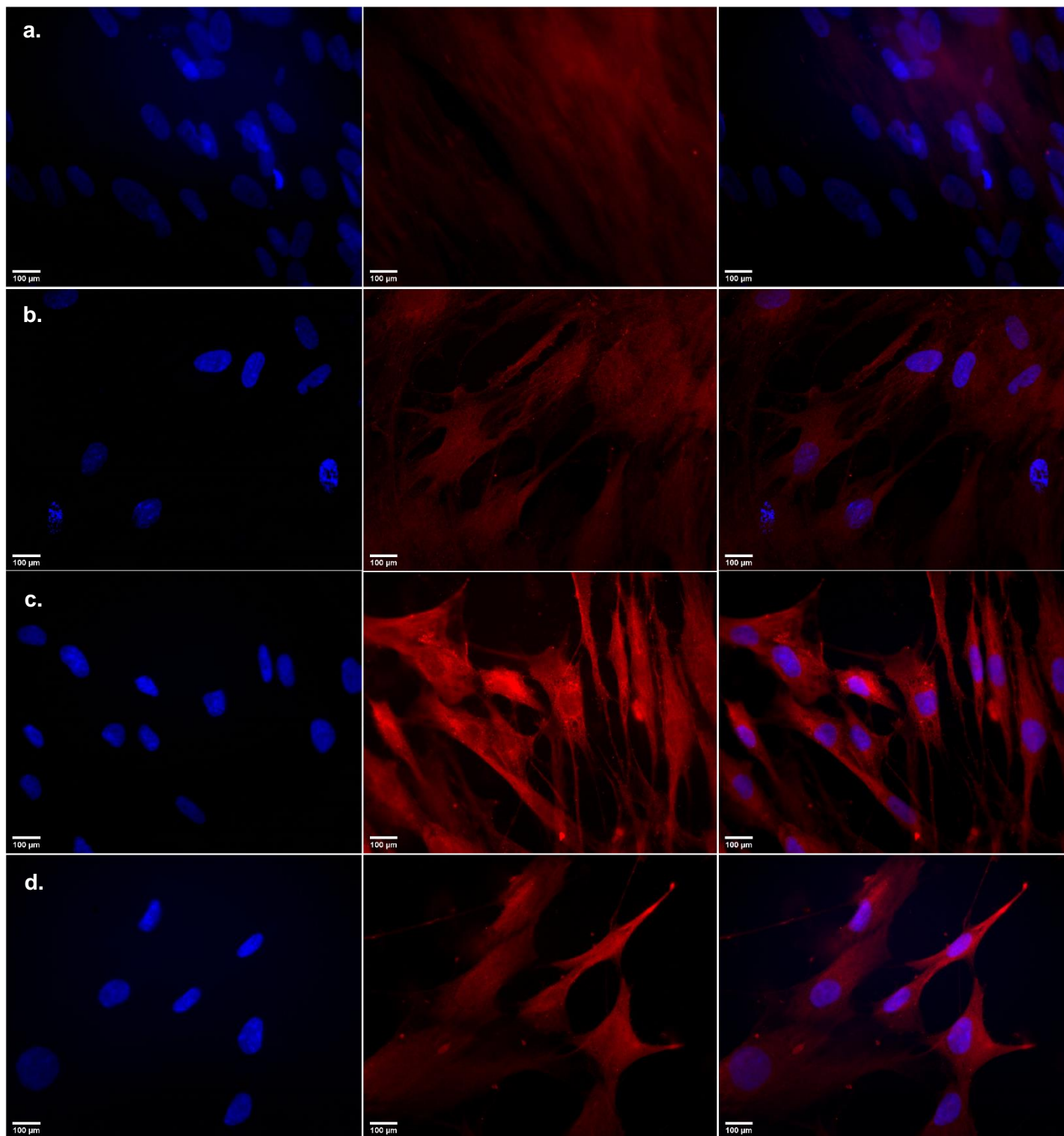


**Figure 29.** Immunofluorescence analysis of hMSCs using anti-OPN antibody after biochemical stimulation induced by dexamethasone 21-phosphate and heparin: a. Negative control, b. Dex 100 nM + Hep 0.5 UI·mL<sup>-1</sup>, c. 25 mg Dex 0.00005% cryogel + Hep 0.5 UI·mL<sup>-1</sup>, and d. electrode + Hep 0.5 UI·mL<sup>-1</sup>.

## 16 Conclusions

- Dex was successfully included into a polymer formulation and subsequently released at therapeutic doses by electrically-controlled triggering and diffusion from a gold-PEDOT electrode system. The total released drug was achieved controlling the initial amount of Dex and the electrical stimulation events. The chemical composition inside the conductive film was confirmed by 2D Raman and electrochemical cyclic voltammetry analysis. Concentrations of drug obtained are recommended ideal to be applied during mesenchymal stem cells culture to induce their differentiation.
- Cryogels formulation and preparation protocol allowed Dex impregnation, showed adequate physical properties in terms of porosity, porous size, degradation, and swelling kinetics to be used as controlled drug release systems to be applied *in vitro* and *in vivo* and as three-dimensional extracellular matrices for cell culture.
- The porous and conductive non-porous systems used for Dex immobilization showed excellent biological compatibility during hMSCs culture, confirming their potential use as drug release systems during *in vitro* MSCs culture.
- ALPL enzymatic activity, qPCR, and immunofluorescence analysis confirmed that Hep in combination with Dex is critical to cause an earliest osteoblast differentiation on human mesenchymal stem cells, showing significant differences between treatments and controls even at 3 days of analysis. Concentrations in the range of  $0.5 \text{ UI} \cdot \text{mL}^{-1}$  to  $25 \text{ UI} \cdot \text{mL}^{-1}$  may be used during MSCs differentiation protocols; this is of relevance in clinical trials and cell therapy to accelerate hMSC differentiation and in tissue engineering applications during three-dimensional scaffolds preparation.
- Diffusive and electrically controlled release of Dex using porous and conductive non-porous scaffolds respectively, induced MSCs differentiation to osteoblast in basal culture media combined with Hep as was confirmed by ALPL enzymatic activity, immunofluorescence, and

qPCR analysis. These results have potential for future applications that use these types of scaffolds during tissue engineering and clinical trials.

## 17 References

1. Paun IA, Zamfirescu M, Luculescu CR, Acasandrei AM, Mustaciosu CC, Mihailescu M, Dinescu M. 2017. Electrically responsive microreservoirs for controllable delivery of dexamethasone in bone tissue engineering. *Appl Surf Sci* 392:321–331.
2. Polini A, Pisignano D, Parodi M, Quarto R, Scaglione S. 2011. Osteoinduction of human mesenchymal stem cells by bioactive composite scaffolds without supplemental osteogenic growth factors. *PLoS One* 6.
3. Liu Q, Cen L, Zhou H, Yin S, Liu G, Liu W, Cao Y, Cui L. 2009. The Role of the Extracellular Signal-Related Kinase Signaling Pathway in Osteogenic Differentiation of Human Adipose-Derived Stem Cells and in Adipogenic Transition Initiated by Dexamethasone. *Tissue Eng Part A* 15:3487–3497.
4. Costa PF, Puga AM, Díaz-Gomez L, Concheiro A, Busch DH, Alvarez-Lorenzo C. 2015. Additive manufacturing of scaffolds with dexamethasone controlled release for enhanced bone regeneration. *Int J Pharm* 496:541–550.
5. Goimil L, Santos-Rosales V, Delgado A, Évora C, Reyes R, Lozano-Pérez AA, Aznar-Cervantes SD, Cenis JL, Gómez-Amoza JL, Concheiro A, Alvarez-Lorenzo C, García-González CA. 2019. ScCO<sub>2</sub>-foamed silk fibroin aerogel/poly( $\epsilon$ -caprolactone) scaffolds containing dexamethasone for bone regeneration. *J CO<sub>2</sub> Util* 31:51–64.
6. Creecy CM, O'Neill CF, Arulanandam BP, Sylvia VL, Navara CS, Bizios R. 2013. Mesenchymal Stem Cell Osteodifferentiation in Response to Alternating Electric Current. *Tissue Eng Part A* 19:467–474.
7. Bloise N, Petecchia L, Ceccarelli G, Fassina L, Usai C, Bertoglio F, Balli M, Vassalli M, De Angelis MGC, Gavazzo P, Imbriani M, Visai L. 2019. The effect of pulsed electromagnetic field exposure on osteoinduction of human mesenchymal stem cells cultured on nano-TiO<sub>2</sub> surfaces. *PLoS One* 13.
8. Kaivosoja E, Sariola V, Chen Y, Kontinen YT. 2015. The effect of pulsed electromagnetic fields and dehydroepiandrosterone on viability and osteo-induction of human mesenchymal stem cells. *J Tissue Eng Regen Med* 9:31–40.
9. Rodríguez Villanueva J, Rodríguez Villanueva L, Guzmán Navarro M. 2017. Pharmaceutical technology can turn a traditional drug, dexamethasone into a first-line ocular medicine. A global perspective and future trends. *Int J Pharm* 516:342–351.
10. Langenbach F, Handschel J. Effects of dexamethasone, ascorbic acid and  $\beta$ -glycerophosphate on the osteogenic differentiation of stem cells in vitro.
11. Zhou X, Feng W, Qiu K, Chen L, Wang W, Nie W, Mo X, He C. 2015. BMP-2 Derived Peptide and Dexamethasone Incorporated Mesoporous Silica Nanoparticles for Enhanced Osteogenic Differentiation of Bone Mesenchymal Stem Cells. *ACS Appl Mater Interfaces* 7:15777–15789.
12. Ramírez-Sánchez KR, Ledezma-Espinoza A, Sánchez-Kopper A, Avendaño-Soto E, Prado M, Perez RS. 2020. Polysaccharide  $\kappa$ -carrageenan as doping agent in conductive coatings for electrochemical controlled release of dexamethasone at therapeutic doses. *Molecules* 25.
13. Li B, Lin Z, Mitsi M, Zhang Y, Vogel V. 2015. Heparin-induced conformational changes of fibronectin within the extracellular matrix promote hMSC osteogenic differentiation. *Biomater Sci* 3:73–84.
14. Solakyildirim K. 2019. Recent advances in glycosaminoglycan analysis by various mass spectrometry techniques. *Anal Bioanal Chem* 411:3731–3741.
15. Sun X, Lin L, Liu X, Zhang F, Chi L, Xia Q, Linhardt RJ. 2016. Capillary Electrophoresis–Mass Spectrometry for the Analysis of Heparin Oligosaccharides and Low Molecular Weight Heparin. *Anal Chem* 88:1937–1943.
16. Lech M, Capila I, Kaundinya G V. 2015. Mass Spectrometric Methods for the Analysis of Heparin and Heparan Sulfate, p. 119–128. *In* .
17. Simann M, Schneider V, Le Blanc S, Dotterweich J, Zehe V, Krug M, Jakob F, Schilling T, Schütze N. 2015. Heparin affects human bone marrow stromal cell fate: Promoting osteogenic and reducing adipogenic differentiation and conversion. *Bone* 78:102–113.

18. Ling L, Camilleri ET, Helledie T, Samsonraj RM, Titmarsh DM, Chua RJ, Dreesen O, Dombrowski C, Rider DA, Galindo M, Lee I, Hong W, Hui JH, Nurcombe V, van Wijnen AJ, Cool SM. 2016. Effect of heparin on the biological properties and molecular signature of human mesenchymal stem cells. *Gene* 576:292–303.
19. Shen K, Tang Q, Fang X, Zhang C, Zhu Z, Hou Y, Lai M. 2020. The sustained release of dexamethasone from TiO<sub>2</sub> nanotubes reinforced by chitosan to enhance osteoblast function and anti-inflammation activity. *Mater Sci Eng C* 116.
20. Bae SE, Choi DH, Han DK, Park K. 2010. Effect of temporally controlled release of dexamethasone on in vivo chondrogenic differentiation of mesenchymal stromal cells. *J Control Release* 143:23–30.
21. Danckwerts M, Fassihi A. 1991. Implantable Controlled Release Drug Delivery Systems: A Review. *Drug Dev Ind Pharm* 17:1465–1502.
22. Ding C, Li Z. 2017. A review of drug release mechanisms from nanocarrier systems. *Mater Sci Eng C* 76:1440–1453.
23. Goimil L, Jaeger P, Ardao I, Gómez-Amoza JL, Concheiro A, Alvarez-Lorenzo C, García-González CA. 2018. Preparation and stability of dexamethasone-loaded polymeric scaffolds for bone regeneration processed by compressed CO<sub>2</sub> foaming. *J CO<sub>2</sub> Util* 24:89–98.
24. Boehler C, Oberueber F, Asplund M. 2019. Tuning drug delivery from conducting polymer films for accurately controlled release of charged molecules. *J Control Release* 304:173–180.
25. Hixon KR, Lu T, Sell SA. 2017. A comprehensive review of cryogels and their roles in tissue engineering applications. *Acta Biomater. Acta Materialia Inc* <https://doi.org/10.1016/j.actbio.2017.08.033>.
26. Kechagia JZ, Ivaska J, Roca-Cusachs P. 2019. Integrins as biomechanical sensors of the microenvironment. *Nat Rev Mol Cell Biol. Nature Publishing Group* <https://doi.org/10.1038/s41580-019-0134-2>.
27. Du J, Chen X, Liang X, Zhang G, Xu J, He L, Zhan Q, Feng XQ, Chien S, Yang C. 2011. Integrin activation and internalization on soft ECM as a mechanism of induction of stem cell differentiation by ECM elasticity. *Proc Natl Acad Sci U S A* 108:9466–9471.
28. García-González CA, Budtova T, Durães L, Erkey C, Del Gaudio P, Gurikov P, Koebel M, Liebner F, Neagu M, Smirnova I. 2019. An opinion paper on aerogels for biomedical and environmental applications. *Molecules. MDPI AG* <https://doi.org/10.3390/molecules24091815>.
29. Gonçalves VSS, Gurikov P, Poejo J, Matias AA, Heinrich S, Duarte CMM, Smirnova I. 2016. Alginate-based hybrid aerogel microparticles for mucosal drug delivery. *Eur J Pharm Biopharm* 107:160–170.
30. Mirtaghavi A, Luo J, Muthuraj R. 2020. Recent advances in porous 3d cellulose aerogels for tissue engineering applications: A review. *J Compos Sci. MDPI AG* <https://doi.org/10.3390/jcs4040152>.
31. Baldino L, Cardea S, Scognamiglio M, Reverchon E. 2019. A new tool to produce alginate-based aerogels for medical applications, by supercritical gel drying. *J Supercrit Fluids* 146:152–158.
32. Zhang X, Koo S, Kim JH, Huang X, Kong N, Zhang L, Zhou J, Xue J, Harris MB, Tao W, Kim JS. 2021. Nanoscale materials-based platforms for the treatment of bone-related diseases. *Matter. Cell Press* <https://doi.org/10.1016/j.matt.2021.05.019>.
33. Nanci A. 1999. Content and Distribution of Noncollagenous Matrix Proteins in Bone and Cementum: Relationship to Speed of Formation and Collagen Packing Density.
34. J Aerssens, J Dequeker, J M Mbuyi-Muamba. 1994. Bone tissue composition: biochemical anatomy of bone. *Clin Rheumatol* 1:54–62.
35. Sarafrazi N, Wambogo EA, Shepherd JA. 2017. Osteoporosis or Low Bone Mass in Older Adults: United States, 2017-2018 Key findings.
36. Kettler M, Block GA, Evenepoel P, Fukagawa M, Herzog CA, McCann L, Moe SM, Shroff R, Tonelli MA, Toussaint ND, Vervloet MG, Leonard MB. 2018. Diagnosis, evaluation, prevention, and treatment of chronic kidney disease-mineral and bone disorder: Synopsis of the kidney disease: Improving global outcomes 2017 clinical practice guideline update.

- Ann Intern Med. American College of Physicians <https://doi.org/10.7326/M17-2640>.
37. Pan P, Yue Q, Li J, Gao M, Yang X, Ren Y, Cheng X, Cui P, Deng Y. 2021. Smart Cargo Delivery System based on Mesoporous Nanoparticles for Bone Disease Diagnosis and Treatment. *Adv Sci*. John Wiley and Sons Inc <https://doi.org/10.1002/advs.202004586>.
  38. Berrio ME, Oñate A, Salas A, Fernández K, Meléndrez MF. 2021. Synthesis and applications of graphene oxide aerogels in bone tissue regeneration: a review. *Mater Today Chem*. Elsevier Ltd <https://doi.org/10.1016/j.mtchem.2021.100422>.
  39. Gisbert-Garzarán M, Manzano M, Vallet-Regí M. 2020. Mesoporous silica nanoparticles for the treatment of complex bone diseases: Bone cancer, bone infection and osteoporosis. *Pharmaceutics* 12.
  40. Ippokratis Pountosa, Diane Corscaddenb, Paul Emeryb, Peter V. Giannoudis. 2007. Mesenchymal stem cell tissue engineering: Techniques for isolation, expansion and application. *Injury* 3854:523–533.
  41. Friedenstein AJ, Piatetzky-Shapiro I, Petrakova & K V. 1966. Osteogenesis in transplants of bone marrow cells. *Embryol. exp. Morph.*
  42. Fitzsimmons REB, Mazurek MS, Soos A, Simmons CA. 2018. Mesenchymal stromal/stem cells in regenerative medicine and tissue engineering. *Stem Cells Int*. Hindawi Limited <https://doi.org/10.1155/2018/8031718>.
  43. Stewart MC, Stewart AA. 2011. Mesenchymal Stem Cells: Characteristics, Sources, and Mechanisms of Action. *Vet Clin North Am - Equine Pract* <https://doi.org/10.1016/j.cveq.2011.06.004>.
  44. Azouna N, Jenhani F, Regaya Z, Berraeis L, Othman T, Ducrocq E, Domenech J. 2012. Phenotypical and functional characteristics of mesenchymal stem cells from bone marrow: Comparison of culture using different media supplemented with human platelet lysate or fetal bovine serum. *Stem Cell Res Ther* 3.
  45. Jiang W, Xu J. 2020. Immune modulation by mesenchymal stem cells. *Cell Prolif*. Blackwell Publishing Ltd <https://doi.org/10.1111/cpr.12712>.
  46. Li X, Wang M, Jing X, Guo W, Hao C, Zhang Y, Gao S, Chen M, Zhang Z, Zhang X, Shen S, Zhang B, Xian H, Wang Z, Wang Y, Sui X, Wang A, Peng J, Lu S, Liu S, Guo Q. 2018. Bone Marrow-and Adipose Tissue-Derived Mesenchymal Stem Cells: Characterization, Differentiation, and Applications in Cartilage Tissue Engineering. *Critical Reviews™ in Eukaryotic Gene Expression*.
  47. Maqsood M, Kang M, Wu X, Chen J, Teng L, Qiu L. 2020. Adult mesenchymal stem cells and their exosomes: Sources, characteristics, and application in regenerative medicine. *Life Sci*. Elsevier Inc. <https://doi.org/10.1016/j.lfs.2020.118002>.
  48. Mazini L, Rochette L, Amine M, Malka G. 2019. Regenerative capacity of adipose derived stem cells (ADSCs), comparison with mesenchymal stem cells (MSCs). *Int J Mol Sci*. MDPI AG <https://doi.org/10.3390/ijms20102523>.
  49. Andrzejewska A, Lukomska B, Janowski M. 2019. Concise Review: Mesenchymal Stem Cells: From Roots to Boost. *Stem Cells*. Wiley-Blackwell <https://doi.org/10.1002/stem.3016>.
  50. Berebichez-Fridman R, Montero-Olvera PR. 2018. Sources and clinical applications of mesenchymal stem cells state-of-the-art review. *Sultan Qaboos Univ Med J* 18:e264–e277.
  51. Lelek J, Zuba-Surma EK. 2020. Perspectives for future use of extracellular vesicles from umbilical cord-and adipose tissue-derived mesenchymal stem/stromal cells in regenerative therapies—synthetic review. *Int J Mol Sci*. MDPI AG <https://doi.org/10.3390/ijms21030799>.
  52. Andrukhov O, Behm C, Blufstein A, Rausch-Fan X. 2019. Immunomodulatory properties of dental tissue-derived mesenchymal stem cells: Implication in disease and tissue regeneration. *World J Stem Cells*. Baishideng Publishing Group Co <https://doi.org/10.4252/wjsc.v11.i9.604>.
  53. Liu J, Yu F, Sun Y, Jiang B, Zhang W, Yang J, Xu GT, Liang A, Liu S. 2015. Concise reviews: Characteristics and potential applications of human dental tissue-derived mesenchymal stem cells. *Stem Cells*. Wiley-Blackwell <https://doi.org/10.1002/stem.1909>.
  54. Nagamura-Inoue T. 2014. Umbilical cord-derived mesenchymal stem cells: Their advantages and potential clinical utility. *World J Stem Cells* 6:195.

55. Chen Y, Shen H, Ding Y, Yu Y, Shao L, Shen Z. 2021. The application of umbilical cord-derived MSCs in cardiovascular diseases. *J Cell Mol Med*. John Wiley and Sons Inc <https://doi.org/10.1111/jcmm.16830>.
56. Rungsiwiwut R, Virutamasen P, Pruksananonda K. 2021. Mesenchymal stem cells for restoring endometrial function: An infertility perspective. *Reprod Med Biol*. John Wiley and Sons Ltd <https://doi.org/10.1002/rmb2.12339>.
57. Endo K, Horiuchi K, Katano H, Ozeki N, Sakamaki Y, Koga H, Sekiya I. 2015. Intra-articular Injection of PDGF-BB Explored in a Novel in Vitro Model Mobilizes Mesenchymal Stem Cells From the Synovium Into Synovial Fluid in Rats <https://doi.org/10.1007/s12015-021-10156-4>/Published.
58. Fazekasova H, Lechler R, Langford K, Lombardi G. 2011. Placenta-derived MSCs are partially immunogenic and less immunomodulatory than bone marrow-derived MSCs. *J Tissue Eng Regen Med* 5:684–694.
59. Calle A, Gutiérrez-Reinoso MÁ, Re M, Blanco J, De la Fuente J, Monguió-Tortajada M, Borràs FE, Yáñez-Mó M, Ramírez MÁ. 2021. Bovine peripheral blood MSCs chemotax towards inflammation and embryo implantation stimuli. *J Cell Physiol* 236:1054–1067.
60. Karaoz E, Aksoy A, Ayhan S, Sarıboycu AE, Kaymaz F, Kasap M. 2009. Characterization of mesenchymal stem cells from rat bone marrow: Ultrastructural properties, differentiation potential and immunophenotypic markers. *Histochem Cell Biol* 132:533–546.
61. Karussis D, Kassis I, Kurkalli BGS, Slavin S. 2008. Immunomodulation and neuroprotection with mesenchymal bone marrow stem cells (MSCs): A proposed treatment for multiple sclerosis and other neuroimmunological/neurodegenerative diseases. *J Neurol Sci* 265:131–135.
62. Jones E, McGonagle D. 2008. Human bone marrow mesenchymal stem cells in vivo. *Rheumatology* <https://doi.org/10.1093/rheumatology/kem206>.
63. Boxall SA, Jones E. 2012. Markers for characterization of bone marrow multipotential stromal cells. *Stem Cells Int* <https://doi.org/10.1155/2012/975871>.
64. Lv FJ, Tuan RS, Cheung KMC, Leung VYL. 2014. Concise review: The surface markers and identity of human mesenchymal stem cells. *Stem Cells*. Wiley-Blackwell <https://doi.org/10.1002/stem.1681>.
65. Li CY, Wu XY, Tong JB, Yang XX, Zhao JL, Zheng QF, Zhao G Bin, Ma ZJ. 2015. Comparative analysis of human mesenchymal stem cells from bone marrow and adipose tissue under xeno-free conditions for cell therapy. *Stem Cell Res Ther* 6.
66. Raquel Taléns-Visconti ABRJVMFCJVMJG-L. 2006. Hepatogenic differentiation of human mesenchymal stem cells from adipose tissue in comparison with bone marrow mesenchymal stem cells. *World J Gastroenterol* 12:5834–5845.
67. Penny J, Harris P, Shakesheff K, Mobasher A. 2012. The biology of equine mesenchymal stem cells: phenotypic characterization, cell surface markers and multilineage differentiation *Frontiers in Bioscience*.
68. Ranera B, Lyahyai J, Romero A, Vázquez FJ, Remacha AR, Bernal ML, Zaragoza P, Rodellar C, Martín-Burriel I. 2011. Immunophenotype and gene expression profiles of cell surface markers of mesenchymal stem cells derived from equine bone marrow and adipose tissue. *Vet Immunol Immunopathol* 144:147–154.
69. Kusindarta DL, Wihadmadyatami H. 2021. Conditioned medium derived from bovine umbilical mesenchymal stem cells as an alternative source of cell-free therapy. *Vet World*. *Veterinary World* <https://doi.org/10.14202/vetworld.2021.2588-2595>.
70. Yan L, Wu X. 2020. Exosomes produced from 3D cultures of umbilical cord mesenchymal stem cells in a hollow-fiber bioreactor show improved osteochondral regeneration activity. *Cell Biol Toxicol* 36:165–178.
71. Han Y, Chai J, Sun T, Li D, Tao R. 2011. Differentiation of human umbilical cord mesenchymal stem cells into dermal fibroblasts in vitro. *Biochem Biophys Res Commun* 413:561–565.
72. Gargett CE, Schwab KE, Deane JA. 2016. Endometrial stem/progenitor cells: The first 10 years. *Hum Reprod Update*. Oxford University Press <https://doi.org/10.1093/humupd/dmv051>.
73. Darzi S, Werkmeister JA, Deane JA, Gargett CE. 2016. Identification and Characterization

- of Human Endometrial Mesenchymal Stem/Stromal Cells and Their Potential for Cellular Therapy. *Stem Cells Transl Med* 5:1127–1132.
74. Schwab KE, Hutchinson P, Gargett CE. 2008. Identification of surface markers for prospective isolation of human endometrial stromal colony-forming cells. *Hum Reprod* 23:934–943.
  75. Castrechini NM, Murthi P, Gude NM, Erwich JJHM, Gronthos S, Zannettino A, Brennecke SP, Kalionis B. 2010. Mesenchymal stem cells in human placental chorionic villi reside in a vascular Niche. *Placenta* 31:203–212.
  76. Abumaree MH, Al Jumah MA, Kalionis B, Jawdat D, Al Khaldi A, Abomaray FM, Fatani AS, Chamley LW, Knawy BA. 2013. Human Placental Mesenchymal Stem Cells (pMSCs) Play a Role as Immune Suppressive Cells by Shifting Macrophage Differentiation from Inflammatory M1 to Anti-inflammatory M2 Macrophages. *Stem Cell Rev Reports* 9:620–641.
  77. Vellasamy S. 2012. Isolation and characterisation of mesenchymal stem cells derived from human placenta tissue. *World J Stem Cells* 4:53.
  78. Portmann-Lanz CB, Schoeberlein A, Huber A, Sager R, Malek A, Holzgreve W, Surbek D V. 2006. Placental mesenchymal stem cells as potential autologous graft for pre- and perinatal neuroregeneration, p. 664–673. *In American Journal of Obstetrics and Gynecology*.
  79. Malek A. 2012. Human placental stem cells: Biomedical potential and clinical relevance Placental tissue-derived mesenchymal stromal cells for the therapy of perinatal brain injury View project Stem Cell Sheet Engineering View project Article in *Journal of Stem Cells*.
  80. Zhou Y, Zhou Z, Zhang W, Hu X, Wei H, Peng J, Jiang S. 2015. SIRT1 inhibits adipogenesis and promotes myogenic differentiation in C3H10T1/2 pluripotent cells by regulating Wnt signaling. *Cell Biosci* 5.
  81. James AW. 2013. Review of Signaling Pathways Governing MSC Osteogenic and Adipogenic Differentiation. *Scientifica (Cairo)* 2013:1–17.
  82. Barry F, Boynton RE, Liu B, Murphy JM. 2001. Chondrogenic differentiation of mesenchymal stem cells from bone marrow: Differentiation-dependent gene expression of matrix components. *Exp Cell Res* 268:189–200.
  83. Sekiya I, Larson BL, Vuoristo JT, Cui JG, Prockop DJ. 2004. Adipogenic Differentiation of Human Adult Stem Cells from Bone Marrow Stroma (MSCs). *J Bone Miner Res* 19:256–264.
  84. Scott MA, Nguyen VT, Levi B, James AW. 2011. Current methods of adipogenic differentiation of mesenchymal stem cells. *Stem Cells Dev* 20:1793–1804.
  85. Mastroiannopoulos NP, Antoniou AA, Koutsoulidou A, Uney JB, Phylactou LA. 2013. Twist reverses muscle cell differentiation through transcriptional down-regulation of myogenin. *Biosci Rep* 33.
  86. Xu Y, Li Z, Li X, Fan Z, Liu Z, Xie X, Guan J. 2015. Regulating myogenic differentiation of mesenchymal stem cells using thermosensitive hydrogels. *Acta Biomater* 26:23–33.
  87. Gang EJ, Jeong JA, Hong H, Hwang SH, Kim W, Yang H, Ahn C, Han H, Kim H. Skeletal Myogenic Differentiation of Mesenchymal Stem Cells Isolated from Human Umbilical Cord Blood.
  88. Nakatsuka R, Nozaki T, Uemura Y, Matsuoka Y, Sasaki Y, Shinohara M, Ohura K, Sonoda Y. 2010. 5-Aza-2'-deoxycytidine treatment induces skeletal myogenic differentiation of mouse dental pulp stem cells. *Arch Oral Biol* 55:350–357.
  89. Rowlands AS, George PA, Cooper-White JJ. 2008. Directing osteogenic and myogenic differentiation of MSCs: interplay of stiffness and adhesive ligand presentation. *Am J Physiol Cell Physiol* 295:1037–1044.
  90. Almalki SG, Agrawal DK. 2016. Key transcription factors in the differentiation of mesenchymal stem cells. *Differentiation*. Elsevier Ltd <https://doi.org/10.1016/j.diff.2016.02.005>.
  91. Han X, Fan Z. 2021. MicroRNAs Regulation in Osteogenic Differentiation of Mesenchymal Stem Cells. *Front Dent Med* 2.
  92. Rutkovskiy A, Stenslkken K-O, Vaage IJ. 2016. Osteoblast Differentiation at a Glance. *Med Sci Monit Basic Res* 22:95–106.



93. Thiagarajan L, Abu-Awwad HADM, Dixon JE. 2017. Osteogenic Programming of Human Mesenchymal Stem Cells with Highly Efficient Intracellular Delivery of RUNX2. *Stem Cells Transl Med* 6:2146–2159.
94. Schinke T, Karsenty G. 1999. Characterization of *Osf1*, an Osteoblast-specific Transcription Factor Binding to a Critical cis-acting Element in the Mouse Osteocalcin Promoters\*.
95. Liu TM, Lee EH. 2013. Transcriptional regulatory cascades in Runx2-dependent bone development. *Tissue Eng - Part B Rev* <https://doi.org/10.1089/ten.teb.2012.0527>.
96. Xu J, Li Z, Hou Y, Fang W. 2015. Review Article Potential mechanisms underlying the Runx2 induced osteogenesis of bone marrow mesenchymal stem cells *Am J Transl Res*.
97. Sankovski E, Karro K, Sepp M, Kurg R, Ustav M, Abroi A. 2015. Characterization of the nuclear matrix targeting sequence (NMTS) of the *bpv1* E8/E2 protein — the shortest known NMTS. *Nucleus* 6:289–300.
98. Lefebvre V, Dvir-Ginzberg M. 2017. SOX9 and the many facets of its regulation in the chondrocyte lineage. *Connect Tissue Res*. Taylor and Francis Ltd <https://doi.org/10.1080/03008207.2016.1183667>.
99. Cai R, Nakamoto T, Kawazoe N, Chen G. 2015. Influence of stepwise chondrogenesis-mimicking 3D extracellular matrix on chondrogenic differentiation of mesenchymal stem cells. *Biomaterials* 52:199–207.
100. Li Q, Gao Z, Chen Y, Guan MX. 2017. The role of mitochondria in osteogenic, adipogenic and chondrogenic differentiation of mesenchymal stem cells. *Protein Cell*. Higher Education Press <https://doi.org/10.1007/s13238-017-0385-7>.
101. Eslaminejad MB, Fani N, Shahhoseini M. 2013. Epigenetic Regulation of Osteogenic and Chondrogenic Differentiation of Mesenchymal Stem Cells in Culture. *CELL J* 15:1–10.
102. Griffin M, Hindocha S, Khan WS. 2012. Chondrogenic Differentiation of Adult MSCs *Current Stem Cell Research & Therapy*.
103. Iijima K, Otsuka H. 2020. Cell scaffolds for bone tissue engineering. *Bioengineering* 7:1–11.
104. Wang L, Zhu L xin, Wang Z, Lou A ju, Yang Y xi, Guo Y, Liu S, Zhang C, Zhang Z, Hu H sheng, Yang B, Zhang P, Ouyang H wei, Zhang Z yong. 2018. Development of a centrally vascularized tissue engineering bone graft with the unique core-shell composite structure for large femoral bone defect treatment. *Biomaterials* 175:44–60.
105. Perez JR, Kouroupis D, Li DJ, Best TM, Kaplan L, Correa D. 2018. Tissue Engineering and Cell-Based Therapies for Fractures and Bone Defects. *Front Bioeng Biotechnol*. *Frontiers Media S.A.* <https://doi.org/10.3389/fbioe.2018.00105>.
106. Zhou J, Lin H, Fang T, Li X, Dai W, Uemura T, Dong J. 2010. The repair of large segmental bone defects in the rabbit with vascularized tissue engineered bone. *Biomaterials* 31:1171–1179.
107. Salvadè A, Mina P Della, Gaddi D, Gatto F, Villa A, Bigoni M, Perseghin P, Serafini M, Zatti G, Biondi A, Biagi E. 2010. Characterization of Platelet Lysate Cultured Mesenchymal Stromal Cells and Their Potential Use in Tissue-Engineered Osteogenic Devices for the Treatment of Bone Defects. *Tissue Eng Part C Methods* 2:201–214.
108. Marcacci M, Kon E, Moukhachev V, Lavroukov A, Kutepov S, Quarto R, Mastrogiacomo M, Cancedda R. 2007. Stem cells associated with macroporous bioceramics for long bone repair: 6- To 7-year outcome of a pilot clinical study. *Tissue Eng* 13:947–955.
109. Zamora-Sequeira R, Ardao I, Starbird R, García-González CA. 2018. Conductive nanostructured materials based on poly-(3,4-ethylenedioxythiophene) (PEDOT) and starch/k-carrageenan for biomedical applications. *Carbohydr Polym* 189:304–312.
110. Chu CC, Hsing CH, Shieh JP, Chien CC, Ho CM, Wang JJ. 2014. The cellular mechanisms of the antiemetic action of dexamethasone and related glucocorticoids against vomiting. *Eur J Pharmacol* <https://doi.org/10.1016/j.ejphar.2013.10.008>.
111. Wadhwa R, Lagenaur CF, Cui XT. 2006. Electrochemically controlled release of dexamethasone from conducting polymer polypyrrole coated electrode. *J Control Release* 110:531–541.
112. Hamidouche Z, Haÿ E, Vaudin P, Charbord P, Schüle R, Marie PJ, Fromigué O. 2008. FHL2 mediates dexamethasone-induced mesenchymal cell differentiation into osteoblasts

- by activating Wnt/ $\beta$ -catenin signaling-dependent Runx2 expression. *FASEB J* 22:3813–3822.
113. Hu H, Li Z, Lu M, Yun X, Li W, Liu C, Guo A. 2018. Osteoactivin inhibits dexamethasone-induced osteoporosis through up-regulating integrin  $\beta$ 1 and activate ERK pathway. *Biomed Pharmacother* 105:66–72.
  114. Hong D, Chen HX, Xue Y, Li DM, Wan XC, Ge R, Li JC. 2009. Osteoblastogenic effects of dexamethasone through upregulation of TAZ expression in rat mesenchymal stem cells. *J Steroid Biochem Mol Biol* 116:86–92.
  115. Wang Z, Zhang T, Xie S, Liu X, Li H, Linhardt RJ, Chi L. 2018. Sequencing the oligosaccharide pool in the low molecular weight heparin dalteparin with offline HPLC and ESI–MS/MS. *Carbohydr Polym* 183:81–90.
  116. Mangrum JB, Mehta AY, Alabbas AB, Desai UR, Hawkrigde AM. 2017. Comparative analysis of INLIGHT™-labeled enzymatically depolymerized heparin by reverse-phase chromatography and high-performance mass spectrometry. *Anal Bioanal Chem* 409:499–509.
  117. Alvarado-Hidalgo F, Ramírez-Sánchez K, Starbird-Perez R. 2020. Smart porous multi-stimulus polysaccharide-based biomaterials for tissue engineering. *Molecules*. MDPI AG <https://doi.org/10.3390/molecules25225286>.
  118. Zhang W, Zhao B, He Z, Zhao X, Wang H, Yang S, Wu H, Cao Y. 2013. High-efficiency ITO-free polymer solar cells using highly conductive PEDOT:PSS/surfactant bilayer transparent anodes. *Energy Environ Sci* 6:1956.
  119. Barsan MM, Ghica ME, Brett CMA. 2015. Electrochemical sensors and biosensors based on redox polymer/carbon nanotube modified electrodes: A review. *Anal Chim Acta* 881:1–23.
  120. Moroni L, de Wijn JR, van Blitterswijk CA. 2008. Integrating novel technologies to fabricate smart scaffolds. *J Biomater Sci Polym Ed* 19:543–572.
  121. Starbird R, García-González CA, Smirnova I, Krautschneider WH, Bauhofer W. 2014. Synthesis of an organic conductive porous material using starch aerogels as template for chronic invasive electrodes. *Mater Sci Eng C* 37:177–183.
  122. Bendrea A-D, Cianga L, Cianga I. 2011. Review paper: Progress in the Field of Conducting Polymers for Tissue Engineering Applications. *J Biomater Appl* 26:3–84.
  123. Hernandez-Suarez P, Ramirez K, Alvarado F, Avendano E, Starbird R. 2019. Electrochemical characterization of poly(3,4-ethylenedioxythiophene)/ $\kappa$ -carrageenan as a biocompatible conductive coat for biologic applications. *MRS Commun* 9:218–223.
  124. Hotchkiss KM, Reddy GB, Hyzy SL, Schwartz Z, Boyan BD, Olivares-Navarrete R. 2016. Titanium surface characteristics, including topography and wettability, alter macrophage activation. *Acta Biomater* 31:425–434.
  125. Krukiewicz K. 2018. Tailorable drug capacity of dexamethasone-loaded conducting polymer matrix. *IOP Conf Ser Mater Sci Eng* 369:012002.
  126. Löffler S, Seyock S, Nybom R, Jacobson GB, Richter-Dahlfors A. 2016. Electrochemically triggered release of acetylcholine from scCO<sub>2</sub> impregnated conductive polymer films evokes intracellular Ca<sup>2+</sup> signaling in neurotypic SH-SY5Y cells. *J Control Release* 243:283–290.
  127. Boehler C, Kleber C, Martini N, Xie Y, Dryg I, Stieglitz T, Hofmann UG, Asplund M. 2017. Actively controlled release of Dexamethasone from neural microelectrodes in a chronic in vivo study. *Biomaterials* 129:176–187.
  128. Balint R, Cassidy NJ, Cartmell SH. 2014. Conductive polymers: Towards a smart biomaterial for tissue engineering. *Acta Biomater* 10:2341–2353.
  129. Alshammary B, Walsh FC, Herrasti P, Ponce de Leon C. 2016. Electrodeposited conductive polymers for controlled drug release: polypyrrole. *J Solid State Electrochem* 20:839–859.
  130. Krukiewicz K, Chudy M, Gregg S, Biggs MJPP. 2019. The Synergistic Effects of Gold Particles and Dexamethasone on the Electrochemical and Biological Performance of PEDOT Neural Interfaces. *Polymers (Basel)* 11:67.
  131. Alizadeh N, Shamaeli E. 2014. Electrochemically controlled release of anticancer drug methotrexate using nanostructured polypyrrole modified with cetylpyridinium: Release

- kinetics investigation. *Electrochim Acta* 130:488–496.
132. Svirskis D, Sharma M, Yu Y, Garg S. 2013. Electrically switchable polypyrrole film for the tunable release of progesterone. *Ther Deliv* 4:307–313.
  133. Kleber C, Lienkamp K, Rhe J, Asplund M. 2019. Electrochemically Controlled Drug Release from a Conducting Polymer Hydrogel (PDMAAp/PEDOT) for Local Therapy and Bioelectronics. *Adv Healthc Mater* 8:1801488.
  134. Leprince L, Dogimont A, Magnin D, Demoustier-Champagne S. 2010. Dexamethasone electrically controlled release from polypyrrole-coated nanostructured electrodes. *J Mater Sci Mater Med* 21:925–930.
  135. Stevenson G, Moulton SE, Innis PC, Wallace GG. 2010. Polyterthiophene as an electrostimulated controlled drug release material of therapeutic levels of dexamethasone. *Synth Met* 160:1107–1114.
  136. Qu J, Liang Y, Shi M, Guo B, Gao Y, Yin Z. 2019. Biocompatible conductive hydrogels based on dextran and aniline trimer as electro-responsive drug delivery system for localized drug release. *Int J Biol Macromol* 140:255–264.
  137. Qu J, Zhao X, Ma PX, Guo B. 2018. Injectable antibacterial conductive hydrogels with dual response to an electric field and pH for localized “smart” drug release. *Acta Biomater* 72:55–69.
  138. Lpez-Iglesias C, Barros J, Ardao I, Monteiro FJ, Alvarez-Lorenzo C, Gmez-Amoza JL, Garca-Gonzlez CA. 2019. Vancomycin-loaded chitosan aerogel particles for chronic wound applications. *Carbohydr Polym* 204:223–231.
  139. Garca-Gonzlez CAA, Smirnova I. 2013. Use of supercritical fluid technology for the production of tailor-made aerogel particles for delivery systems. *J Supercrit Fluids* 79:152–158.
  140. Franco P, De Marco I. 2020. Supercritical CO<sub>2</sub> adsorption of non-steroidal anti-inflammatory drugs into biopolymer aerogels. *J CO<sub>2</sub> Util* 36:40–53.
  141. Goimil L, Braga MEM, Dias AMA, Gmez-Amoza JL, Concheiro A, Alvarez-Lorenzo C, de Sousa HC, Garca-Gonzlez CA. 2017. Supercritical processing of starch aerogels and aerogel-loaded poly( $\epsilon$ -caprolactone) scaffolds for sustained release of ketoprofen for bone regeneration. *J CO<sub>2</sub> Util* 18:237–249.
  142. De Marco I, Reverchon E. 2017. Starch aerogel loaded with poorly water-soluble vitamins through supercritical CO<sub>2</sub> adsorption. *Chem Eng Res Des* 119:221–230.
  143. Garca-Gonzlez CA, Uy JJ, Alnaief M, Smirnova I. 2012. Preparation of tailor-made starch-based aerogel microspheres by the emulsion-gelation method. *Carbohydr Polym* 88:1378–1386.
  144. Betz M, Garca-Gonzlez CA, Subrahmanyam RP, Smirnova I, Kulozik U. 2012. Preparation of novel whey protein-based aerogels as drug carriers for life science applications. *J Supercrit Fluids* 72:111–119.
  145. Kormsmeier RW, Gurny R, Doelker E, Buri P, Peppas NA. 1983. Mechanisms of solute release from porous hydrophilic polymers. *Int J Pharm* 15:25–35.
  146. Santoro M, Shah SR, Walker JL, Mikos AG. 2016. Poly(lactic acid) nanofibrous scaffolds for tissue engineering. *Adv Drug Deliv Rev* 107:206–212.
  147. Stratton S, Shelke NB, Hoshino K, Rudraiah S, Kumbar SG. 2016. Bioactive polymeric scaffolds for tissue engineering. *Bioact Mater* 1:93–108.
  148. Jo H, Sim M, Kim S, Yang S, Yoo Y, Park J-H, Yoon TH, Kim M-G, Lee JY. 2017. Electrically conductive graphene/polyacrylamide hydrogels produced by mild chemical reduction for enhanced myoblast growth and differentiation. *Acta Biomater* 48:100–109.
  149. Theocharis AD, Skandalis SS, Gialeli C, Karamanos NK. 2016. Extracellular matrix structure. *Adv Drug Deliv Rev* 97:4–27.
  150. P. J, J. F. 2011. Composite Scaffolds for Orthopaedic Regenerative Medicine *Advances in Composite Materials for Medicine and Nanotechnology*. InTech.
  151. Garca-Gonzlez CA, Concheiro A, Alvarez-Lorenzo C. 2015. Processing of Materials for Regenerative Medicine Using Supercritical Fluid Technology. *Bioconjug Chem* 26:1159–1171.
  152. Viswanathan P, Ondeck MG, Chirasatitsin S, Ngamkham K, Reilly GC, Engler AJ, Battaglia G. 2015. 3D surface topology guides stem cell adhesion and differentiation. *Biomaterials*

- 52:140–147.
153. Chen H, Zhong J, Wang J, HUang R, Qiao X, Wang H, Tan Z. 2019. Enhanced growth and differentiation of myoblast cells grown on E-jet 3D printed platforms. *Int J Nanomedicine* Volume 14:937–950.
  154. Uygun BE, Stojisic SE, Matthew HWT. 2009. Effects of Immobilized Glycosaminoglycans on the Proliferation and Differentiation of Mesenchymal Stem Cells. *Tissue Eng Part A* 15:3499–3512.
  155. Seto SP, Casas ME, Temenoff JS. 2012. Differentiation of mesenchymal stem cells in heparin-containing hydrogels via coculture with osteoblasts. *Cell Tissue Res* 347:589–601.
  156. Benoit DSW, Durney AR, Anseth KS. 2007. The effect of heparin-functionalized PEG hydrogels on three-dimensional human mesenchymal stem cell osteogenic differentiation. *Biomaterials* 28:66–77.
  157. Paez-Mayorga J, Capuani S, Farina M, Lotito ML, Niles JA, Salazar HF, Rhudy J, Esnaola L, Chua CYX, Taraballi F, Corradetti B, Shelton KA, Nehete PN, Nichols JE, Grattoni A. 2020. Enhanced In Vivo Vascularization of 3D-Printed Cell Encapsulation Device Using Platelet-Rich Plasma and Mesenchymal Stem Cells. *Adv Healthc Mater* 9.
  158. Farina M, Chua CYX, Ballerini A, Thekkedath U, Alexander JF, Rhudy JR, Torchio G, Fraga D, Pathak RR, Villanueva M, Shin CS, Niles JA, Sesana R, Demarchi D, Sikora AG, Acharya GS, Gaber AO, Nichols JE, Grattoni A. 2018. Transcutaneously refillable, 3D-printed biopolymeric encapsulation system for the transplantation of endocrine cells. *Biomaterials* 177:125–138.
  159. Erdem A, Darabi MA, Nasiri R, Sangabathuni S, Ertas YN, Alem H, Hosseini V, Shamloo A, Nasr AS, Ahadian S, Dokmeci MR, Khademhosseini A, Ashammakhi N. 2020. 3D Bioprinting of Oxygenated Cell-Laden Gelatin Methacryloyl Constructs. *Adv Healthc Mater* 9.
  160. Blakney AK, Swartzlander MD, Bryant SJ. 2012. Student award winner in the undergraduate category for the society of biomaterials 9th World Biomaterials Congress, Chengdu, China, June 1-5, 2012: The effects of substrate stiffness on the in vitro activation of macrophages and in vivo host response to poly(ethylene glycol)-based hydrogels. *J Biomed Mater Res - Part A* 100 A:1375–1386.
  161. Aznar-Cervantes S, Pagán A, Martínez JG, Bernabeu-Esclapez A, Otero TF, Meseguer-Olmo L, Paredes JI, Cenis JL. 2017. Electrospun silk fibroin scaffolds coated with reduced graphene promote neurite outgrowth of PC-12 cells under electrical stimulation. *Mater Sci Eng C* 79:315–325.
  162. Montero-Rodríguez JJ, Ramirez-Sanchez K, Valladares-Castrillo G, Avendano-Soto ED, Starbird-Perez R. 2020. Design and Simulation of Flexible Thin-Film Electrodes for Cell Culture Stimulation. 2020 IEEE Lat Am Electron Devices Conf.
  163. Ramírez-Sánchez K, Alvarado-Hidalgo F, Zamora-Sequeira R, Sáenz-Arce G, Rojas-Carrillo O, Avedaño-Soto E, Ruppert C, Mena-Torres F, Starbird-Pérez R. 2019. Biosensor based on the directly enzyme immobilization into a gold nanotriangles/conductive polymer biocompatible coat for electrochemical detection of Chlorpyrifos in water. *Med DEVICES SENSORS* 2.
  164. Ricardo Starbird, Wolfgang Bauhofer, Mario Meza-Cuevas, Wolfgang H. Krautschneider. 2012. Effect of experimental factors on the properties of PEDOT-NaPSSgalvanostatically deposited from an aqueous micellar media for invasive electrodes. 5th 2012 Biomed Eng Int Conf IEEE 1–5.
  165. Gómez-Ordóñez E, Rupérez P. 2011. FTIR-ATR spectroscopy as a tool for polysaccharide identification in edible brown and red seaweeds. *Food Hydrocoll* 25:1514–1520.
  166. Konermann L. 2017. Addressing a Common Misconception: Ammonium Acetate as Neutral pH “Buffer” for Native Electrospray Mass Spectrometry. *J Am Soc Mass Spectrom* 28:1827–1835.
  167. Zamora-Sequeira R, Alvarado-Hidalgo F, Robles-Chaves D, Sáenz-Arce G, Avendano-Soto ED, Sánchez-Kopper A, Starbird-Perez R. 2019. Electrochemical characterization of mancozeb degradation for wastewater treatment using a sensor based on poly (3,4-ethylenedioxythiophene) (PEDOT) modified with carbon nanotubes and gold nanoparticles. *Polymers (Basel)* 11.

168. Santos-Rosales V, Alvarez-Rivera G, Hillgärtner M, Cifuentes A, Itskov M, García-González CA, Rege A. 2020. Stability Studies of Starch Aerogel Formulations for Biomedical Applications. *Biomacromolecules* 21:5336–5344.
169. Ceylan S, Göktürk D, Demir D, Damla Özdemir M, Bölgen N. 2018. Comparison of additive effects on the PVA/starch cryogels: Synthesis, characterization, cytotoxicity, and genotoxicity studies. *Int J Polym Mater Polym Biomater* 67:855–864.
170. Yuan P, Qiu X, Liu T, Tian R, Bai Y, Liu S, Chen X, Jin Y. 2020. Substrate-independent polymer coating with stimuli-responsive dexamethasone release for on-demand fibrosis inhibition. *J Mater Chem B* 8:7777–7784.
171. Yu A, Shi H, Liu H, Bao Z, Dai M, Lin D, Lin D, Xu X, Li X, Wang Y. 2020. Mucoadhesive dexamethasone-glycol chitosan nanoparticles for ophthalmic drug delivery. *Int J Pharm* 575.
172. Thangprasert A, Tansakul C, Thuaksubun N, Meesane J. 2019. Mimicked hybrid hydrogel based on gelatin/PVA for tissue engineering in subchondral bone interface for osteoarthritis surgery. *Mater Des* 183.
173. Luo X, Gu X, Li L. 2018. Development of a simple and efficient method of harvesting and lysing adherent mammalian cells for chemical isotope labeling LC-MS-based cellular metabolomics. *Anal Chim Acta* 1037:97–106.
174. Karlsson M, Pålsgård E, Wilshaw PR, Di Silvio L. 2003. Initial in vitro interaction of osteoblasts with nano-porous alumina. *Biomaterials* 24:3039–3046.
175. Tsiridis E, Bhalla A, Ali Z, Gurav N, Heliotis M, Deb S, DiSilvio L. 2006. Enhancing the osteoinductive properties of hydroxyapatite by the addition of human mesenchymal stem cells, and recombinant human osteogenic protein-1 (BMP-7) in vitro. *Injury* 37.
176. Sethi S, Radio NM, Kotlarczyk MP, Chen CT, Wei YH, Jockers R, Witt-Enderby PA. 2010. Determination of the minimal melatonin exposure required to induce osteoblast differentiation from human mesenchymal stem cells and these effects on downstream signaling pathways. *J Pineal Res* 49:222–238.
177. Sun H, Wu C, Dai K, Chang J, Tang T. 2006. Proliferation and osteoblastic differentiation of human bone marrow-derived stromal cells on akermanite-bioactive ceramics. *Biomaterials* 27:5651–5657.
178. Loebel C, Czekanska EM, Bruderer M, Salzmann G, Alini M, Stoddart MJ. 2015. In vitro osteogenic potential of human mesenchymal stem cells is predicted by Runx2/Sox9 ratio. *Tissue Eng - Part A* 21:115–123.
179. Hunter RJ. 1981. *Zeta Potential in Colloid Science: Principles and Applications*, 1st ed. Academic Press.
180. Lowry G V., Hill RJ, Harper S, Rawle AF, Hendren CO, Klaessig F, Nobbmann U, Sayre P, Rumble J. 2016. Guidance to improve the scientific value of zeta-potential measurements in nanoEHS. *Environ Sci Nano* 3:953–965.
181. Ali H, Kalashnikova I, White MA, Sherman M, Rytting E. 2013. Preparation, characterization, and transport of dexamethasone-loaded polymeric nanoparticles across a human placental in vitro model. *Int J Pharm* 454:149–157.
182. Pargaonkar N, Lvov YM, Li N, Steenekamp JH, de Villiers MM. 2005. Controlled Release of Dexamethasone from Microcapsules Produced by Polyelectrolyte Layer-by-Layer Nanoassembly. *Pharm Res* 22:826–835.
183. Sagbas S, Butun S, Sahiner N. 2012. Modifiable chemically crosslinked poli( $\kappa$ -carrageenan) particles. *Carbohydr Polym* 87:2718–2724.
184. Antonov YA, Zhuravleva IL, Cardinaels R, Moldenaers P. 2018. Macromolecular complexes of lysozyme with kappa carrageenan. *Food Hydrocoll* 74:227–238.
185. Zhang Z, Grijpma DW, Feijen J. 2006. Poly(trimethylene carbonate) and monomethoxy poly(ethylene glycol)-block-poly(trimethylene carbonate) nanoparticles for the controlled release of dexamethasone. *J Control Release* 111:263–270.
186. Walsh FC, Ponce de Leon C. 2014. A review of the electrodeposition of metal matrix composite coatings by inclusion of particles in a metal layer: an established and diversifying technology. *Trans IMF* 92:83–98.
187. Deligianni DD, Katsala ND, Koutsoukos PG, Missirlis YF. 2000. Effect of surface roughness of hydroxyapatite on human bone marrow cell adhesion, proliferation,

- differentiation and detachment strength. *Biomaterials* 22:87–96.
188. Kokkinos PA, Koutsoukos PG, Deligianni DD. 2012. Detachment strength of human osteoblasts cultured on hydroxyapatite with various surface roughness. Contribution of integrin subunits. *J Mater Sci Mater Med* 23:1489–1498.
  189. Tran-Van F, Garreau S, Louarn G, Froyer G, Chevrot C. 2001. Fully undoped and soluble oligo(3,4-ethylenedioxythiophene)s: spectroscopic study and electrochemical characterization. *J Mater Chem* 11:1378–1382.
  190. Martins A, Duarte ARC, Faria S, Marques AP, Reis RL, Neves NM. 2010. Osteogenic induction of hBMSCs by electrospun scaffolds with dexamethasone release functionality. *Biomaterials* 31:5875–5885.
  191. Bredas JL, Street GB. 1985. Polarons, bipolarons, and solitons in conducting polymers. *Acc Chem Res* 18:309–315.
  192. Ritger PL, Peppas NA. 1987. A simple equation for description of solute release II. Fickian and anomalous release from swellable devices. *J Control Release* 5:37–42.
  193. Thomas D, Nair V V., Latha MS, Thomas KK. 2019. Theoretical and experimental studies on theophylline release from hydrophilic alginate nanoparticles. *Futur J Pharm Sci* 5:2.
  194. Siepmann J, Peppas NA. 2011. Higuchi equation: Derivation, applications, use and misuse. *Int J Pharm* 418:6–12.
  195. Spataro L, Dilgen J, Retterer S, Spence AJ, Isaacson M, Turner JN, Shain W. 2005. Dexamethasone treatment reduces astroglia responses to inserted neuroprosthetic devices in rat neocortex. *Exp Neurol* 194:289–300.
  196. Zhao S, Malfait WJ, Guerrero-Alburquerque N, Koebel MM, Nyström G. 2018. Biopolymer Aerogels and Foams: Chemistry, Properties, and Applications. *Angew Chemie - Int Ed. Wiley-VCH Verlag* <https://doi.org/10.1002/anie.201709014>.
  197. Baudron V, Gurikov P, Smirnova I, Whitehouse S. 2019. Porous starch materials via supercritical-and freeze-drying. *Gels* 5.
  198. Ge J, Guo L, Wang S, Zhang Y, Cai T, Zhao RCHH, Wu Y. 2014. The Size of Mesenchymal Stem Cells is a Significant Cause of Vascular Obstructions and Stroke. *Stem Cell Rev Reports* 10:295–303.
  199. Krueger TEGG, Thorek DLJJ, Denmeade SR, Isaacs JT, Brennen WN. 2018. Concise Review: Mesenchymal Stem Cell-Based Drug Delivery: The Good, the Bad, the Ugly, and the Promise. *Stem Cells Transl Med* 7:651–663.
  200. Kim H-WWH-EE, Knowles JC, Kim H-WWH-EE. 2004. Hydroxyapatite/poly( $\epsilon$ -caprolactone) composite coatings on hydroxyapatite porous bone scaffold for drug delivery. *Biomaterials* 25:1279–1287.
  201. Ecaterina Stela DCAGMVDADSC. 2023. Fabrication of self-antibacterial chitosan/oxidized starch polyelectrolyte complex sponges for controlled delivery of curcumin. *Food Hydrocoll* 135:108147.
  202. Apopei Loghin DF, Biliuta G, Coseri S, Dragan ES. 2017. Preparation and characterization of oxidized starch/poly(N,N-dimethylaminoethyl methacrylate) semi-IPN cryogels and in vitro controlled release evaluation of indomethacin. *Int J Biol Macromol* 96:589–599.
  203. Edgar KJ, Marks JA. 2020. Green hydrogels based on starch: Preparation methods for biomedical applications, p. 173–196. *In ACS Symposium Series. American Chemical Society*.
  204. Çetin K, Alkan H, Bereli N, Denizli A. 2017. Molecularly imprinted cryogel as a pH-responsive delivery system for doxorubicin. *J Macromol Sci Part A Pure Appl Chem* 54:502–508.
  205. Bakhshpour M, Idil N, Perçin I, Denizli A. 2019. Biomedical applications of polymeric cryogels. *Appl Sci. MDPI AG* <https://doi.org/10.3390/app9030553>.
  206. Kovermann N, Basoli V, Della Bella E, Alini M, Lischer C, Schmal H, Kubosch E, Stoddart M. 2019. BMP2 and TGF- $\beta$  Cooperate Differently during Synovial-Derived Stem-Cell Chondrogenesis in a Dexamethasone-Dependent Manner. *Cells* 8:636.
  207. Panek M, Antunović M, Pribolšan L, Ivković A, Gotić M, Vukasović A, Mihalić KC, Pušić M, Jurkin T, Marijanović I. 2019. Bone tissue engineering in a perfusion bioreactor using dexamethasone-loaded peptide hydrogel. *Materials (Basel)* 16.
  208. Yehuda R, Halligan SL, Grossman R, Golier JA, Wong C. 2002. The Cortisol and

- Glucocorticoid Receptor Response to Low Dose Dexamethasone Administration in Aging Combat Veterans and Holocaust Survivors with and without Posttraumatic Stress Disorder *Biol Psychiatry*.
209. Wang Y, Han L, Diao T, Jing Y, Wang L, Zheng H, Ma X, Qi J, Yu L. 2018. A comparison of systemic and local dexamethasone administration: From perilymph/cochlea concentration to cochlear distribution. *Hear Res* 370:1–10.
  210. Weijtens O, Schoemaker RC, Cohen AF, Romijn FPHTM, Lentjes EGWM, Van Meurs JC. 1998. Dexamethasone Concentration in Vitreous and Serum After Oral Administration.
  211. Sinulingga K, Sirait M, Siregar N, Doloksaribu ME. 2021. Investigation of Antibacterial Activity and Cell Viability of Ag/Mg and Ag/Zn Co-doped Hydroxyapatite Derived from Natural Limestone. *ACS Omega* 6:34185–34191.
  212. De-Deus G, Canabarro A, Alves GG, Marins JR, Linhares ABR, Granjeiro JM. 2012. Cytocompatibility of the ready-to-use bioceramic putty repair cement iRoot BP Plus with primary human osteoblasts. *Int Endod J* 45:508–513.
  213. Farsalinos KE, Romagna G, Alliffranchini E, Ripamonti E, Bocchietto E, Todeschi S, Tsiapras D, Kyrzopoulos S, Voudris V. 2013. Comparison of the cytotoxic potential of cigarette smoke and electronic cigarette vapour extract on cultured myocardial cells. *Int J Environ Res Public Health* 10:5146–5162.
  214. Das P, Maity PP, Ganguly S, Ghosh S, Baral J, Bose M, Choudhary S, Gangopadhyay S, Dhara S, Das AK, Banerjee S, Das NC. 2019. Biocompatible carbon dots derived from κ-carrageenan and phenyl boronic acid for dual modality sensing platform of sugar and its anti-diabetic drug release behavior. *Int J Biol Macromol* 132:316–329.
  215. Bhushan P, Umasankar Y, Hutcheson JD, Bhansali S. 2019. Toxicity assessment of wearable wound sensor constituents on keratinocytes. *Toxicol Vitro* 58:170–177.
  216. Narayanan KB, Kim HD, Han SS. 2020. Biocompatibility and hemocompatibility of hydrothermally derived reduced graphene oxide using soluble starch as a reducing agent. *Colloids Surfaces B Biointerfaces* 185.
  217. Noè C, Tonda-Turo C, Chiappone A, Sangermano M, Hakkarainen M. 2020. Light processable starch hydrogels. *Polymers (Basel)* 12:1359.
  218. Madruga LYC, Sabino RM, Santos ECG, Popat KC, Balaban R de C, Kipper MJ. 2020. Carboxymethyl-kappa-carrageenan: A study of biocompatibility, antioxidant and antibacterial activities. *Int J Biol Macromol* 152:483–491.
  219. Bagri LP, Saini RK, Kumar Bajpai A, Choubey R. 2019. Silver hydroxyapatite reinforced poly(vinyl alcohol)—starch cryogel nanocomposites and study of biodegradation, compressive strength and antibacterial activity. *Polym Eng Sci* 59:254–263.
  220. Alhuthali S, Kotidis P, Kontoravdi C. 2021. Osmolality effects on cho cell growth, cell volume, antibody productivity and glycosylation. *Int J Mol Sci* 22.
  221. Van Dijk B, Potier E, Ito K. 2011. Culturing bovine nucleus pulposus explants by balancing medium osmolarity. *Tissue Eng - Part C Methods* 17:1089–1096.
  222. Solazzo M, Krukiewicz K, Zhussupbekova A, Fleischer K, Biggs MJ, Monaghan MG. 2019. PEDOT:PSS interfaces stabilised using a PEGylated crosslinker yield improved conductivity and biocompatibility. *J Mater Chem B* 7:4811–4820.
  223. Guex AG, Puetzer JL, Armgarth A, Littmann E, Stavrinidou E, Giannelis EP, Malliaras GG, Stevens MM. 2017. Highly porous scaffolds of PEDOT:PSS for bone tissue engineering. *Acta Biomater* 62:91–101.
  224. Babaie A, Bakhshandeh B, Abedi A, Mohammadnejad J, Shabani I, Ardeshtyrlajimi A, Reza Moosavi S, Amini J, Tayebi L. 2020. Synergistic effects of conductive PVA/PEDOT electrospun scaffolds and electrical stimulation for more effective neural tissue engineering. *Eur Polym J* 140.
  225. Boroojeni FR, Mashayekhan S, Abbaszadeh H-A. 2019. The Controlled Release of Dexamethasone Sodium Phosphate from Bioactive Electrospun PCL/Gelatin Nanofiber Scaffold *Iranian Journal of Pharmaceutical Research*.
  226. Rossi L, Castro M, D’Orto F, Damonte G, Serafini S, Bigi L, Panzani I, Novelli G, Dallapiccola B, Panunzi S, Di Carlo P, Bella S, Magnani M. 2004. Low doses of dexamethasone constantly delivered by autologous erythrocytes slow the progression of lung disease in cystic fibrosis patients. *Blood Cells, Mol Dis* 33:57–63.

227. Bossa F, Annese V, Valvano MR, Latiano A, Martino G, Rossi L, Magnani M, Palmieri O, Serafini S, Damonte G, De Santo E, Andriulli A. 2013. Erythrocytes-mediated delivery of dexamethasone 21-phosphate in steroid-dependent ulcerative colitis: A randomized, double-blind sham-controlled study. *Inflamm Bowel Dis* 19:1872–1879.
228. Coker SA, Szczepiorkowski ZM, Siegel AH, Ferrari A, Mambrini G, Anand R, Hartman RD, Benatti L, Dumont LJ. 2018. A Study of the Pharmacokinetic Properties and the In Vivo Kinetics of Erythrocytes Loaded With Dexamethasone Sodium Phosphate in Healthy Volunteers. *Transfus Med Rev*. W.B. Saunders <https://doi.org/10.1016/j.tmr.2017.09.001>.
229. Keeler GD, Durdik JM, Stenken JA. 2015. Localized delivery of dexamethasone-21-phosphate via microdialysis implants in rat induces M(GC) macrophage polarization and alters CCL2 concentrations. *Acta Biomater* 12:11–20.
230. Sadeghi F, Vahednia E, Naderi Meshkin H, Kerachian MA. 2020. The effect of adrenocorticotrophic hormone on alpha-2-macroglobulin in osteoblasts derived from human mesenchymal stem cells. *J Cell Mol Med* 24:4784–4790.
231. Ghensi P, Cucchi A, Bonaccorso A, Ferroni L, Gardin C, Mortellaro C, Zavan B. 2019. In vitro effect of bromelain on the regenerative properties of mesenchymal stem cells. *J Craniofac Surg* 30:1064–1067.
232. Kang ES, Kim DS, Suhito IR, Lee W, Song I, Kim TH. 2018. Two-dimensional material-based bionano platforms to control mesenchymal stem cell differentiation. *Biomater Res*. BioMed Central Ltd. <https://doi.org/10.1186/s40824-018-0120-3>.
233. Patel KD, Mahapatra C, Jin GZ, Singh RK, Kim HW. 2015. Biocompatible Mesoporous Nanotubular Structured Surface to Control Cell Behaviors and Deliver Bioactive Molecules. *ACS Appl Mater Interfaces* 7:26850–26859.
234. Sun H, Zhang L, Xia W, Chen L, Xu Z, Zhang W. 2016. Fabrication of graphene oxide-modified chitosan for controlled release of dexamethasone phosphate. *Appl Phys A Mater Sci Process* 122.
235. Vieira S, da Silva Morais A, Garet E, Silva-Correia J, Reis RL, González-Fernández Á, Miguel Oliveira J. 2019. Self-mineralizing Ca-enriched methacrylated gellan gum beads for bone tissue engineering. *Acta Biomater* 93:74–85.
236. Bispo DSC, Jesus CSH, Marques IMC, Romek KM, Oliveira MB, Mano JF, Gil AM. 2021. Metabolomic Applications in Stem Cell Research: a Review. *Stem Cell Rev Reports*. Springer <https://doi.org/10.1007/s12015-021-10193-z>.
237. Jäger M, Fischer J, Dohrn W, Li X, Ayers DC, Czibere A, Prall WC, Lensing-Höhn S, Krauspe R. 2008. Dexamethasone modulates BMP-2 effects on mesenchymal stem cells in vitro. *J Orthop Res* 26:1440–1448.
238. Joung YK, Bae JW, Park KD. 2008. Controlled release of heparin-binding growth factors using heparin-containing particulate systems for tissue regeneration. *Expert Opin Drug Deliv* <https://doi.org/10.1517/17425240802431811>.
239. Rice JJ, Martino MM, De Laporte L, Tortelli F, Briquez PS, Hubbell JA. 2013. Engineering the Regenerative Microenvironment with Biomaterials. *Adv Healthc Mater*. Wiley-VCH Verlag <https://doi.org/10.1002/adhm.201200197>.
240. Eswarakumar VP, Lax I, Schlessinger J. 2005. Cellular signaling by fibroblast growth factor receptors. *Cytokine Growth Factor Rev* 16:139–149.
241. Mathews S, Mathew SA, Gupta PK, Bhonde R, Totey S. 2014. Glycosaminoglycans enhance osteoblast differentiation of bone marrow derived human mesenchymal stem cells. *J Tissue Eng Regen Med* 8:143–152.
242. Chevallier N, Anagnostou F, Zilber S, Bodivit G, Maurin S, Barrault A, Bierling P, Hernigou P, Layrolle P, Rouard H. 2010. Osteoblastic differentiation of human mesenchymal stem cells with platelet lysate. *Biomaterials* 31:270–278.
243. Manaster J, Chezar J, Shurtz-Swirski R, Shapiro G, Tendler Y, Kristal B, Shasha SM, Sela S. Heparin induces apoptosis in human peripheral blood neutrophils.
244. Si W, Kang Q, Luu HH, Park JK, Luo Q, Song W-X, Jiang W, Luo X, Li X, Yin H, Montag AG, Haydon RC, He T-C. 2006. Ccn1/Cyr61 Is Regulated by the Canonical Wnt Signal and Plays an Important Role in Wnt3A-Induced Osteoblast Differentiation of Mesenchymal Stem Cells. *Mol Cell Biol* 26:2955–2964.
245. Colombres M, Henríquez JP, Reig GF, Scheu J, Calderón R, Alvarez A, Brandan E,



- Inestrosa NC. 2008. Heparin activates Wnt signaling for neuronal morphogenesis. *J Cell Physiol* 216:805–815.
246. Nillesen STM, Geutjes PJ, Wismans R, Schalkwijk J, Daamen WF, van Kuppevelt TH. 2007. Increased angiogenesis and blood vessel maturation in acellular collagen-heparin scaffolds containing both FGF2 and VEGF. *Biomaterials* 28:1123–1131.
  247. Lu Q, Zhang S, Hu K, Feng Q, Cao C, Cui F. 2007. Cytocompatibility and blood compatibility of multifunctional fibroin/collagen/heparin scaffolds. *Biomaterials* 28:2306–2313.
  248. Ho YC, Mi FL, Sung HW, Kuo PL. 2009. Heparin-functionalized chitosan-alginate scaffolds for controlled release of growth factor. *Int J Pharm* 376:69–75.
  249. Sasaguri K, Jiang H, Chen J. 1998. The effect of altered functional forces on the expression of bone-matrix proteins in developing mouse mandibular condyle. *Arch Oral Biol* 43:83–92.
  250. Boutin A, Neumann S, Gershengorn MC. 2016. Multiple transduction pathways mediate thyrotropin receptor signaling in preosteoblast-like cells. *Endocrinology* 157:2173–2181.
  251. Sun M, Huang K, Luo X, Li H. 2021. Templated Three-Dimensional Engineered Bone Matrix as a Model for Breast Cancer Osteolytic Bone Metastasis Process. *Int J Nanomedicine* 16:8391–8403.
  252. Coelho MJ, Fernandes MH. 2000. Human bone cell cultures in biocompatibility testing. Part II: effect of ascorbic acid, glycerophosphate and dexamethasone on osteoblastic differentiation. *Biomaterials*.
  253. Jaiswal N, Haynesworth SE, Caplan AI, Bruder SP. Osteogenic Differentiation of Purified, Culture-Expanded Human Mesenchymal Stem Cells In Vitro.
  254. Oh Y, Ahn CB, Je JY. 2020. Ark shell protein-derived bioactive peptides promote osteoblastic differentiation through upregulation of the canonical Wnt/ $\beta$ -catenin signaling in human bone marrow-derived mesenchymal stem cells. *J Food Biochem* 44.
  255. Kim HS, Lee JH, Mandakhbayar N, Jin GZ, Kim SJ, Yoon JY, Jo S Bin, Park JH, Singh RK, Jang JH, Shin US, Knowles JC, Kim HW. 2021. Therapeutic tissue regenerative nanohybrids self-assembled from bioactive inorganic core / chitosan shell nanounits. *Biomaterials* 274.
  256. Chen Y, Li J, Kawazoe N, Chen G. 2017. Preparation of dexamethasone-loaded calcium phosphate nanoparticles for the osteogenic differentiation of human mesenchymal stem cells. *J Mater Chem B* 5:6801–6810.
  257. El-Fiqi A, Kim JH, Kim HW. 2015. Osteoinductive fibrous scaffolds of biopolymer/mesoporous bioactive glass nanocarriers with excellent bioactivity and long-term delivery of osteogenic drug. *ACS Appl Mater Interfaces* 7:1140–1152.
  258. Pettersen E, Shah FA, Ortiz-Catalan M. 2021. Enhancing osteoblast survival through pulsed electrical stimulation and implications for osseointegration. *Sci Rep* 11.
  259. Yamada M, Tanemura K, Okada S, Iwanami A, Nakamura M, Mizuno H, Ozawa M, Ohyama-Goto R, Kitamura N, Kawano M, Tan-Takeuchi K, Ohtsuka C, Miyawaki A, Takashima A, Ogawa M, Toyama Y, Okano H, Kondo T. 2007. Electrical Stimulation Modulates Fate Determination of Differentiating Embryonic Stem Cells. *Stem Cells* 25:562–570.
  260. Hsiao YS, Kuo CW, Chen P. 2013. Multifunctional graphene-pedot microelectrodes for on-chip manipulation of human mesenchymal stem cells. *Adv Funct Mater* 23:4649–4656.
  261. Thiruvikraman G, Lee PS, Hess R, Haenchen V, Basu B, Scharnweber D. 2015. Interplay of Substrate Conductivity, Cellular Microenvironment, and Pulsatile Electrical Stimulation toward Osteogenesis of Human Mesenchymal Stem Cells in Vitro. *ACS Appl Mater Interfaces* 7:23015–23028.
  262. Zhang Y, Li M, Gao L, Duan K, Wang J, Weng J, Feng B. 2016. Effect of dexamethasone,  $\beta$ -glycerophosphate, OGP and BMP2 in TiO<sub>2</sub> nanotubes on differentiation of MSCs. *Mater Technol* 31:603–612.
  263. Shin H, Temenoff JS, Bowden GC, Zygourakis K, Farach-Carson MC, Yaszemski MJ, Mikos AG. 2005. Osteogenic differentiation of rat bone marrow stromal cells cultured on Arg-Gly-Asp modified hydrogels without dexamethasone and  $\beta$ -glycerol phosphate. *Biomaterials* 26:3645–3654.

264. Si J, Wang C, Zhang D, Wang B, Hou W, Zhou Y. 2020. Osteopontin in Bone Metabolism and Bone Diseases. *Med Sci Monit.* International Scientific Information, Inc. <https://doi.org/10.12659/MSM.919159>.
265. Chen Q, Shou P, Zhang L, Xu C, Zheng C, Han Y, Li W, Huang Y, Zhang X, Shao C, Roberts AI, Rabson AB, Ren G, Zhang Y, Wang Y, Denhardt DT, Shi Y. 2014. An osteopontin-integrin interaction plays a critical role in directing adipogenesis and osteogenesis by mesenchymal stem cells. *Stem Cells* 32:327–337.

## 18 Annexes

### Annex 1. Code used for the configuration of the electrode stimulator

```

#include <SPI.h>

//Use direct port write for additional speed over DigitalWrite
#define SS0 (1 << 4) //Slave Select 0 PORTB
#define SS0PORT &PORTB

#define SS1 (1 << 6) //Slave Select 1 PORTH
#define SS1PORT &PORTH

#define SS2 (1 << 5) //Slave Select 2 PORTH
#define SS2PORT &PORTH

#define SS3 (1 << 4) //Slave Select 2 PORTH
#define SS3PORT &PORTH

//Pins needed for Soft SPI
#define MOSI 11
#define CLK 13

int i;

void setup() {
  // set the slaveSelectPin as an output:

  pinMode (MOSI,OUTPUT);
  pinMode (CLK,OUTPUT);
  pinMode (10, OUTPUT);
  pinMode (11, OUTPUT);
  i=0;
}

void loop() {

  if (ciclos > 0){

    // Onda ciclovoltametria (-0.6 V hasta + 1 V):
    for(i=1912;i<2275;i++) {
      writeMCP492x((int)( i ),SS0,SS0PORT);
      delay(stepTime);
    }
    for(i=2275;i>1912;i--) {
      writeMCP492x((int)( i ),SS0,SS0PORT);
      delay(stepTime);
    }
  }
}

```

```

    ciclos--;
}
else{
    // poner la salida en cero:
    writeMCP492x((int)( 2048 ),SS0,SS0PORT);
}
}

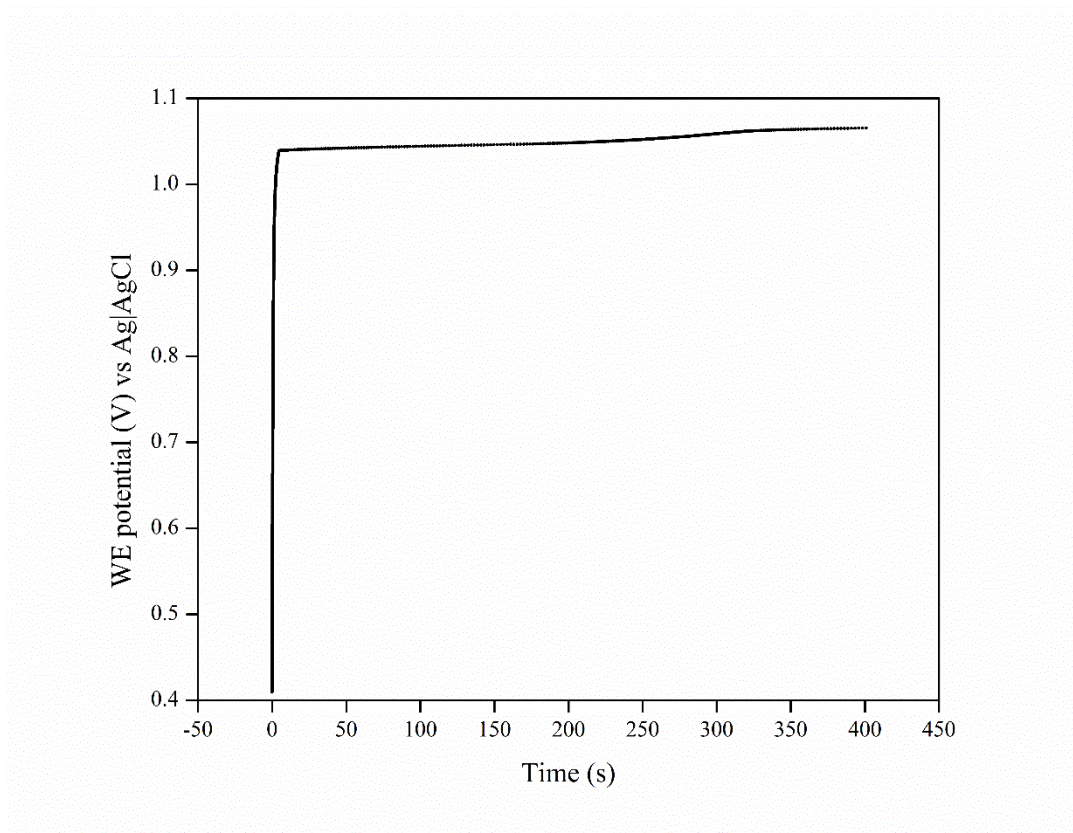
//Method to write to the DAC
void writeMCP492x(uint16_t data,uint8_t ss,volatile uint8_t* slave_port) {
    // Take the top 4 bits of config and the top 4 valid bits (data is actually a 12 bit number) and or
    // them together
    uint8_t top_msg = (0x30 & 0xF0) | (0x0F & (data >> 8));

    // Take the bottom octet of data
    uint8_t lower_msg = (data & 0x00FF);

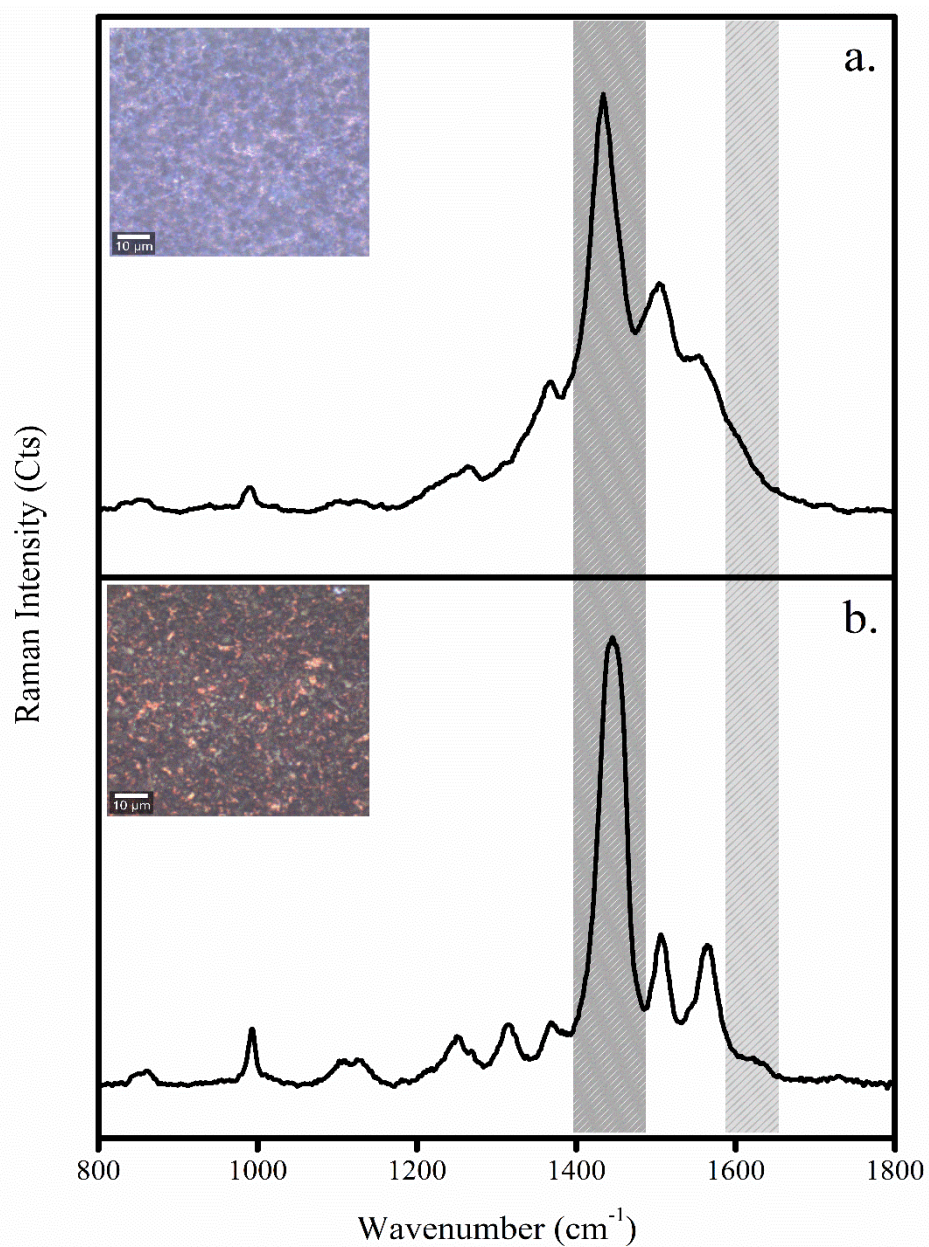
    // Select our DAC
    *slave_port &= ~ss;
    // Send first 8 bits
    shiftOut(MOSI,CLK,MSBFIRST,top_msg);
    // Send second 8 bits
    shiftOut(MOSI,CLK,MSBFIRST,lower_msg);
    *slave_port |= ss;
}

```

**Annex 2.** Galvanostatic curve of the electro-polymerization process from an EDOT/ $\kappa$ C/Dex dispersion onto a bare gold electrode.



**Figure 1:** Galvanostatic curve of the electro-polymerization process from an EDOT/ $\kappa$ C/Dex dispersion onto a bare gold electrode using a constant current of 102.45 microamperes.

**Annex 3.** Raman spectra of the PEDOT/ $\kappa$ C/Dex coating.

**Figure 1.** Raman spectra of the PEDOT/ $\kappa$ C/Dex coating (a) before dexamethasone release process (inset: PEDOT/ $\kappa$ C/Dex electrode surface) and (b) after 160 release cycles (inset: PEDOT/ $\kappa$ C/Dex electrode surface). The signals at 1435 cm<sup>-1</sup> and 1625 cm<sup>-1</sup> were used to identify PEDOT and  $\kappa$ C/Dex, respectively.

**Annex 4.**  $\mu$ -Raman spectral measurement of the dexamethasone 21-phosphate disodium salt.

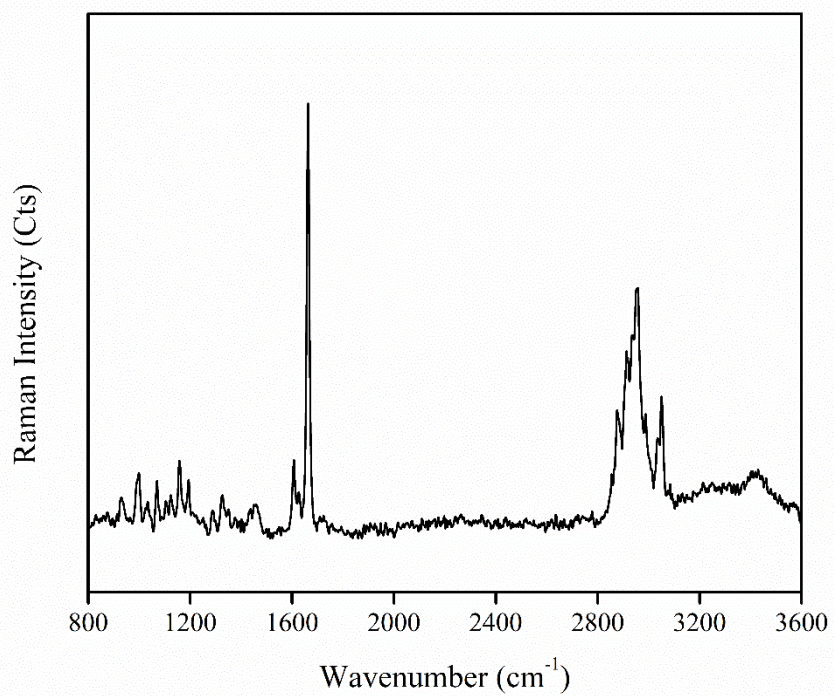


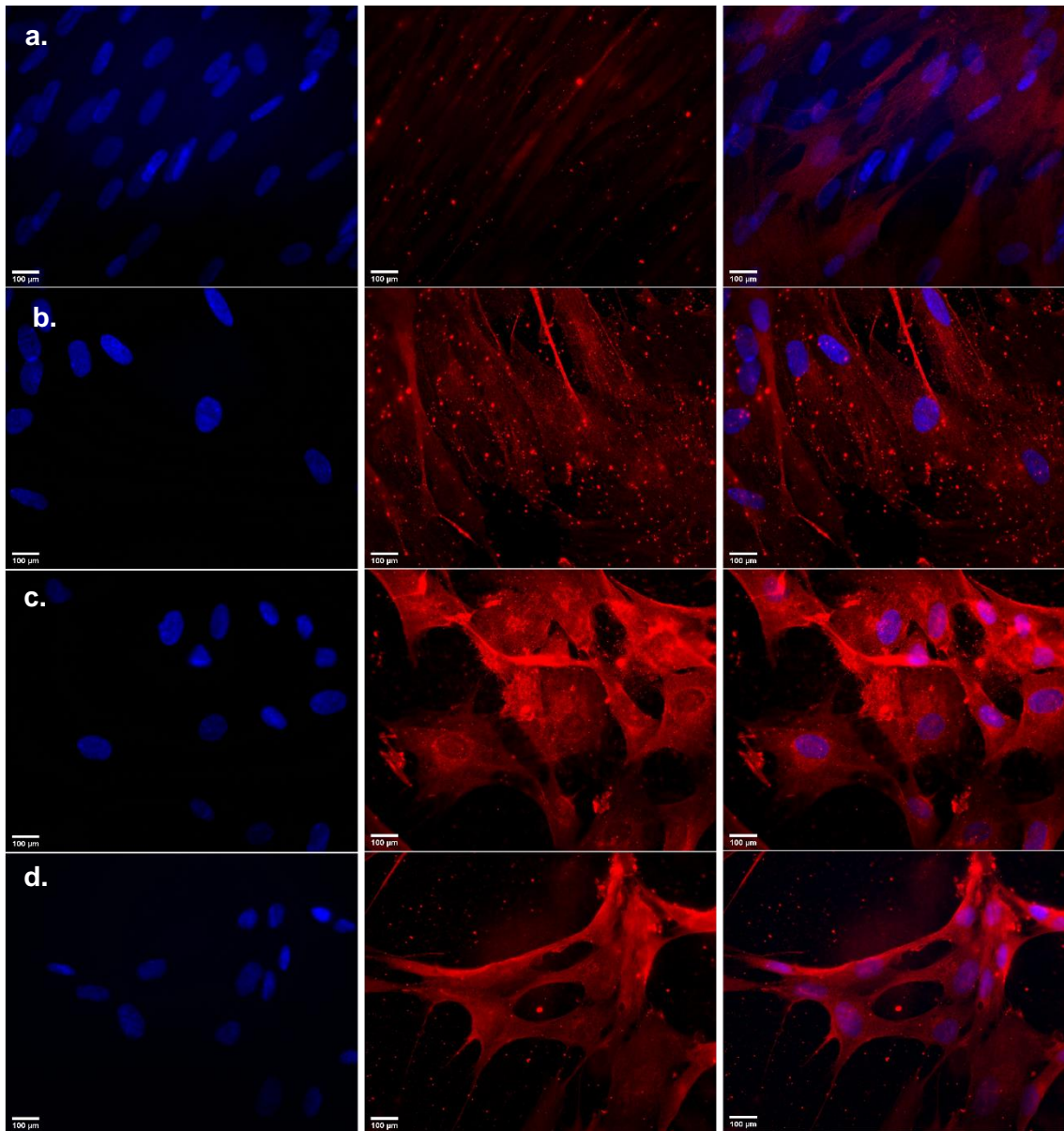
**Figure 1:**  $\mu$ -Raman spectral measurement of the dexamethasone 21-phosphate disodium salt.

**Annex 5.** RNA concentration values.

<b>Sample</b>	<b>Time</b>	<b>RNA (ng/<math>\mu</math>L)</b>	<b>Abs 260/280</b>	<b>Abs 260/230</b>
C-	7d	9.200	2.120	0.160
C-	7d	12.400	2.110	0.120
C-	14d	8.724	2.172	0.068
C-	14d	11.211	2.078	0.079
Dex	7d	12.300	2.240	0.300
Dex	7d	12.000	2.090	0.290
Dex	14d	17.932	2.041	0.253
Dex	14d	7.697	2.032	0.801
Dx	7d	10.060	2.130	0.100
Dx	7d	8.700	2.300	0.060
Dx	14d	29.387	2.122	0.136
Dx	14d	28.956	2.023	0.661
Cryogel	7d	8.800	2.040	0.070
Cryogel	7d	8.800	2.320	0.040
Cryogel	14d	14.050	2.011	0.646
Cryogel	14d	8.691	2.061	0.046
Electrode	7d	10.800	2.100	0.160
Electrode	7d	9.200	1.930	0.050
Electrode	14d	20.533	2.064	0.493
Electrode	14d	17.517	2.062	1.176



**Annex 6.** Immunofluorescence analysis of hMSCs using anti-ALPL antibody after biochemical stimulation induced by dexamethasone 21-phosphate and heparin: a. Negative control, b. Dex 100 nM + Hep 0.5 UI·mL<sup>-1</sup>, c. 25 mg Dex 0.00005% cryogel + Hep 0.5 UI·mL<sup>-1</sup>, and d. electrode + Hep 0.5 UI·mL<sup>-1</sup>.



## Annex 7. Paper 1. Design and simulation of flexible thin-film electrodes for cell culture stimulation

2020 IEEE Latin America Electron Devices Conference (LAEDC)  
San José, Costa Rica, February 25-28, 2020

# Design and Simulation of Flexible Thin-Film Electrodes for Cell Culture Stimulation

Montero-Rodríguez, Juan J., *Member, IEEE*; Ramirez-Sánchez, Karla; Valladares-Castrillo, Gerardo; Avendano-Soto, Esteban D. and Starbird-Pérez, Ricardo

**Abstract**— This document reviews the design and fabrication process of electrodes in Costa Rica, to be use in electric cell-substrate stimulations and electrochemical impedance sensing up to 10 kHz. The effect of the electrode design (through electrode sensor area and passivation coating) on electrode was simulated and experimentally evaluated using electrochemical impedance spectroscopy (EIS) measurements. The high charge points in the electrode were minimize by passivation after the simulation. It was observed that the passivated area has an impedance contribution by minimizing parasite currents. The optimized design of electrode reported in this work will make it possible to probe the cell growth, adhesion and biological cell layers by reducing measurement artifacts and improving the quality of data. The self-made flexible electrodes may allow being use in cell culture studies and to measure in real-time the cellular properties during the in vitro study and by chemical modifications may be used in the charge molecules control release.

**Index Terms**—biosensor, computer simulation, finite-element method, impedance spectroscopy.

### I. INTRODUCTION

The design and fabrication of electrodes for sensing has increase their applications especially in the biomedical field [1], [2]. Biomedical applications, including cell culture studies by electrical stimulation and sensing is a remarkable and challenging field regarding the electrode properties [3]. The consideration of costs, mechanical, thermal and chemical stability and high electrical conductivity along with uniform current distribution are mandatory in the electrode design [4]. New materials, coating technology, electrode manufacture, computational simulation of electrochemical systems and new applications in medical science including electrochemical processes, provide several tools to be considered in the design of electrodes for specific applications.

Submitted on November 1<sup>st</sup>, 2019. This work was financially supported by the Costa Rica Institute of Technology (ITCR) and FEES funding (08-2018) (CONARE), the Vicrectoria de Investigación from Instituto Tecnológico de Costa Rica and Universidad de Costa Rica.

Juan J. Montero-Rodríguez is with the Instituto Tecnológico de Costa Rica, Escuela de Ingeniería Electrónica, Cartago 30102, Costa Rica (e-mail: jmontero@tec.ac.cr).

Karla Ramirez-Sánchez is with the Centro de Investigación y de Servicios Químicos y Microbiológicos (CEQIATEC), Instituto Tecnológico de Costa Rica, Escuela de Química, Cartago 30102, Costa Rica (e-mail: kararimr@tec.ac.cr).

The materials for electrodes have been changed in recently times, including conductive polymers [5]-[7] and ceramics, such diamond [8] and electrically conductive metal suboxides [9]. The introduction of nanostructured surfaces with their high active area is strategies to be apply during the fabrication of nanostructured electrodes [6], [10], [11]. Moreover, flexible and stretchable electrodes are part of the new generation of intelligent electronics [12], [13]. The use of interdigitated electrodes has important applications in the detection, quantification and characterization of biomolecules, microorganisms, nanostructures and chemical traces in aqueous solutions. Electrochemical characterization techniques, such as electrochemical impedance spectroscopy (EIS) is used to study these systems [14], [15]. Meanwhile, the electric field (EF) stimulation has a direct role in cellular morphology and physiology, and it may elicit different cellular responses [16]. The direct effects depend mainly of the type of signal applied, as well as the amplitude and frequency of the electric potential or current applied and the type of cell studied.

Through computational simulation of biological systems, the interactions among all biochemical processes in a cell are theoretically feasible, but limited by the lack of quantitative data [17]. During the measurement and stimulation on living organisms, it is essential to understand the mechanisms involved in the generation of the signals to involved in the measurement [18]. Therefore, the simulation of those systems tends to be complex and required experimental data to be improved.

In this work, we present the simulation and real data of self-made electrodes to be use in electric cell-substrate stimulations and electrochemical impedance sensing. The collected results confirmed that the simulation allow to evaluate the effect of the

Gerardo Valladares-Castillo is with the Instituto Tecnológico de Costa Rica, Escuela de Ingeniería en Materiales, Cartago 30102, Costa Rica (e-mail: gerzaval08@gmail.com).

Esteban D. Avendano-Soto is with the Departamento de Física, Centro de Investigación en Ciencia e Ingeniería de Materiales (CICIMA), Universidad de Costa Rica, San Pedro 11501, Costa Rica (esteban.avendanosoto@ucr.ac.cr).

Ricardo Starbird-Pérez is with the Centro de Investigación y de Servicios Químicos y Microbiológicos (CEQIATEC), Instituto Tecnológico de Costa Rica, Escuela de Química, Cartago 30102, Costa Rica (e-mail: rstarbird@tec.ac.cr).

electrical signal measurements. Therefore, systems that are more complex may be studied in the future by means of computational tools, in order to understand and describe biological systems.

## II. MATERIALS AND METHODS

### A. Electrode Fabrication and Characterization

The electrochemical impedance spectroscopy (EIS) measurements and electrical stimulation were prepared on 12.5  $\mu\text{m}$  thick polyimide film (Kapton®, DuPont™) substrates (American DuraFilm, Holliston, MA, USA) with gold (Au) 99.99 % pure (Goodfellow Corporation, Coraopolis, PA 15108-9302, USA) in an high vacuum chamber). In brief, a coating thickness of  $42.0 \pm 0.4$  nm of gold was deposited in order to avoid the use of a buffer layer to improve adherence and reduce delamination. The coating was deposited by means of electron beam evaporation with a base pressure of the order of  $2.2 \times 10^{-6}$  Torr, typical deposition rates of  $0.38 \pm 0.03$  nm/s were used. The electrodes were passivated and etched by photolithography methods using a S1805™ photoresist (Microposit, Philadelphia, USA). The photoresist was hard baked to impart stability and inertness to the polymer. S1805 photoresist was used as the 500 nm-thick coating. Finally, the connections were made using Flexible Flat Cable (FFC) connectors (Mouser Electronics, Mansfield, Texas, USA).

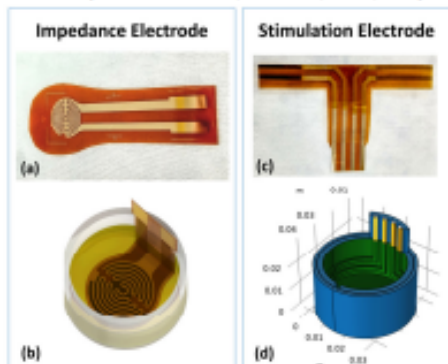


Fig. 1. Gold electrodes fabricated over a polyimide substrate: electrode (a) is used for growing the cells directly on the top, electrode (c) is designed to apply an electric field from side to side. Metallic contacts are connected using a flex cable connector (not shown). Three-dimensional models (b) and (d) of the electrodes to be placed in a 3 cm diameter cell culture well.

### B. Impedance Spectroscopy Measurements

Electrochemical impedance spectroscopy (EIS) measurements for electrodes were performed with an alternating sinusoidal signal of 50 mV amplitude at open circuit potential in a potentiostat (AUTOLAB, model: PGSTAT-302, Utrecht, Netherlands) combined with a FRA32M module.

Impedance spectra were collected by scanning the frequency range from 1 to 10 000 Hz. Interdigitated coated electrodes (see the inset of Fig. 1a) were used as the working and counter electrodes, while an Ag|AgCl (in 3 M KCl) electrode was used as the reference electrode. The Kramers–Kronig test was performed using the software NOVA v2.1.4 (Utrecht, Netherlands).

### C. Finite-Element Method Simulation

The electrode analysis system is modeled using the COMSOL® (COMSOL Inc., Burlington, Massachusetts, USA) Multiphysics package, a software designed to simulate any physical process. The simulations are performed using the Secondary Current Distribution physics. The COMSOL simulations considers a gold (Au) electrode structure with overall dimensions of 3 cm  $\times$  3 cm in an electrolytic (potassium chloride) media.

## III. RESULTS AND DISCUSSION

The patterned gold electrodes showed mechanical and electrical stability during the application. The electrodes may be coated with different materials, in order to improve the electrochemical response during sensing.

### A. Impedance Spectroscopy Measurements

The experimental Bode plots for the impedance electrode (see Fig. 1a) are shown in Fig. 2a and Fig. 2b. It should be noted that the impedance at low frequencies is high, approximately 10 k $\Omega$  for 1 Hz, mainly due to the double-layer capacitance. The data is in agreement with previous reports [19], [20].

### B. Simulation of Impedance Electrodes

The electrode of Fig. 1c was simulated with an excitation signal of 50 mV. The simulated Bode plots are shown in Fig. 2c and Fig. 2d. As expected, the impedance is high at 1 Hz and decreases with the frequency, illustrating the effect of the double-layer capacitance [15]. These Bode plots exhibit a frequency response similar as that of Fig. 2a and Fig. 2b, which indicates that the Finite-Element Method (FEM) is a powerful technique that may be used to replicate experimental results and could be useful for the design of optimized electrode geometries with high accuracy.

Fig. 2e shows that the current density at the interdigitated electrode surface is low and homogeneous, which are electrical characteristics desired for the EIS sensors. The expected increase in current density at the connecting bridges shows an opportunity to improve electrode performance at higher frequencies. Fig. 2f shows the electrolyte current density at the surface of the electrode.

This model based on the material conductivity is a practical option to understand electrical characteristics derived from electrode geometries. The simulation results are consistent with the measurements performed in the previous section.

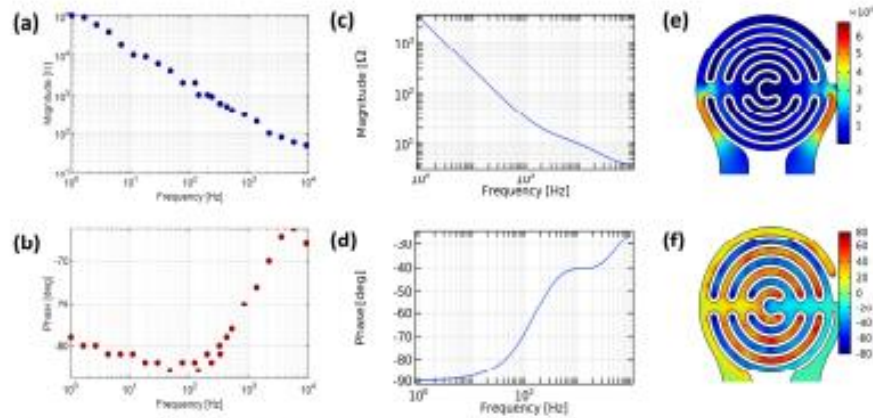


Fig. 2. Impedance electrode real data (a) Bode plot (magnitude) of the impedance and (b) Phase of the impedance vs. frequency. (c) Bode plot (magnitude) impedance and (d) Bode plot (phase) of the simulated electrode. (e) Simulation of the electrode current density norm [ $\mu\text{A}/\text{mm}^2$ ] and (f) electrolyte current density [ $\mu\text{A}/\text{mm}^2$ ].

### C. Simulation of Stimulation Electrodes

The electrode of Fig. 1c is simulated using the same signal of 50 mV and considering the same electrolyte. Fig. 3a shows the current density of the electrode, where it may be seen that the current density decreases with the length of the electrode.

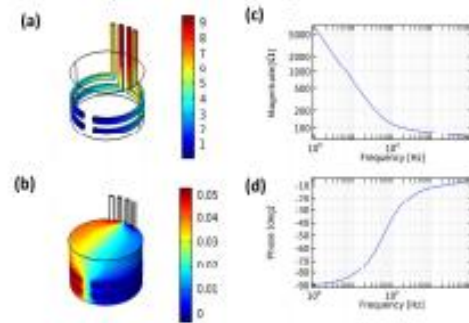


Fig. 3. Stimulation electrode (a) current density [ $\mu\text{A}/\text{mm}^2$ ] and (b) electrolyte potential [V], showing a uniform field distribution. (c) Bode plot (magnitude) and (d) Bode plot (phase) of the simulated electrode impedance.

The electrolyte potential distribution is shown on Fig. 3b, where it is observed that the electric field reaches the complete volume of the well. This allows stimulation of cell cultures that may grow at the bottom of the experiment setup, placed on a standard cell substrate. With our configuration, it is possible to

achieve electrical stimulation of biological tissue, that may lead to differentiation and maturation of cells [21]–[23].

The Bode plots for magnitude and phase for the stimulation electrode are presented in Fig. 3c and Fig. 3d, respectively.

### IV. CONCLUSION

Simulation by FEM allowed to confirm adequate properties from the interdigitated electrode geometry. The simulated impedance matches the measurements performed using KCl solutions. Due to a charge density selection error, the polymer film was compressed by the MFC, which lead to a change in exposed electrode areas preventing the comparison of macro and MFE system's sensitivity. The self-made flexible electrodes may allow being use in cell culture studies and to measure in real-time the cellular properties during the *in vitro* study and by chemical modifications may be used in the charge molecules control release.

### V. ACKNOWLEDGMENTS

This work was financially supported by the Costa Rica Institute of Technology (ITCR) and FEES funding (08-2018) (CONARE), the Vicerrectoria de Investigación from Instituto Tecnológico de Costa Rica and Universidad de Costa Rica. We would like to thank to Jorge I. Sandoval-Sandoval for his help in the electrode design.

2020 IEEE Latin America Electron Devices Conference (LAEDC)  
San José, Costa Rica, February 25-28, 2020

#### VI. REFERENCES

- [1] R. Akmal and R. N. Salama, "Physical Sensors for Biomedical Applications," in *Proceedings of IEEE Sensors*, 2018, vol. 2018-October.
- [2] D. T. Price, A. R. A. Ralman, and S. Bhanoli, "Design rule for optimization of microelectrodes used in electric cell-substrate impedance sensing (ECIS)," *Biomater. Bioelectron.*, vol. 24, no. 7, pp. 2071–2076, 2009.
- [3] D. A. Wagenaar, J. Pinz, and S. M. Potter, "Effective parameters for stimulation of dissociated cultures using multi-electrode arrays," *J. Neurosci. Methods*, vol. 138, no. 1–2, pp. 23–37, 2004.
- [4] F. C. Walsh, L. F. Arenas, and C. Ponce de León, "Developments in electrode design: structure, decoration and applications of electrodes for electrochemical technology," *Journal of Chemical Technology and Biotechnology*, vol. 93, no. 11, pp. 3073–3090, 2018.
- [5] R. Starbird, W. Buehler, M. Mera-Cuevas, and W. H. Krautschneider, "Effect of experimental factors on the properties of PEDOT-NaPSS galvanostatically deposited from an aqueous micellar media for invasive electrodes," in *Feb 2012 Biomedical Engineering International Conference, BMECON 2012*, 2012.
- [6] R. Zamora, F. Maciá-Meléndez, H. Phillips, L. A. Alvarado-Marchana, and R. Starbird, "Development of Poly(3,4-ethylenedioxythiophene)(PEDOT)/carbon nanotube electrodes for electrochemical detection of Manganese in water," *Int. J. Electrochem. Sci.*, vol. 13, no. 2, pp. 1931–1944, 2018.
- [7] R. Zamora-Sosa et al., "Electrochemical Characterization of Manganese Degradation for Wastewater Treatment Using a Sensor Based on Poly(3,4-ethylenedioxythiophene)(PEDOT) Modified with Carbon Nanotubes and Gold Nanoparticles," *Polymer (Bareil)*, vol. 11, no. 9, p. 1449, 2019.
- [8] N. Spitzaru, B. V. Sarada, E. Popa, D. A. Tryk, and A. Fujishima, "Voltammetric determination of L-cysteine at conductive diamond electrodes," *Anal. Chem.*, vol. 73, no. 3, pp. 514–519, 2001.
- [9] S. Sircusano, V. Baglio, C. D'Ursi, V. Antonacci, and A. S. Arico, "Preparation and characterization of titanium suboxides as conductive supports of IrO<sub>2</sub> electrocatalysts for application in SPE electrolyzers," *Electrochim. Acta*, vol. 54, no. 26, pp. 6292–6299, 2009.
- [10] R. Zamora-Sosa, I. Arias, R. Starbird, and C. A. Garcia-González, "Conductive nanostructured materials based on poly(3,4-ethylenedioxythiophene) (PEDOT) and starch/carrageenan for biomedical applications," *Carbohydr. Polym.*, vol. 189, pp. 304–312, 2018.
- [11] K. Ramírez-Sánchez et al., "Biosensor based on the directly enzyme immobilization into a gold nanotriangles/conductive polymer biocompatible coat for electrochemical detection of Clopprylin in water," *Med. DEVICES SENSORS*, 2019.
- [12] S. Huang, Y. Liu, Y. Zhao, Z. Ren, and C. F. Guo, "Flexible Electronics: Stretchable Electrodes and Their Future," *Advanced Functional Materials*, vol. 29, no. 6, 2019.
- [13] D. Vilela, A. Romo, and S. Sánchez, "Flexible sensors for biomedical technology," *Lab Chip*, vol. 16, no. 3, pp. 402–408, 2016.
- [14] A. Laita, *Electrochemical impedance spectroscopy and its applications*, vol. 9781461489. 2014.
- [15] E. Barsukov and J. R. Macdonald, *Impedance Spectroscopy: Theory, Experiment, and Applications*, 2005.
- [16] T. Taghian, D. A. Narmoneva, and A. B. Kogan, "Modulation of cell function by electric field: A high-resolution analysis," *J. R. Soc. Interface*, vol. 12, no. 107, 2015.
- [17] S. Spolton et al., "Towards human cell stimulation," in *Lecture Notes in Computer Science (including subseries Lecture Notes in Artificial Intelligence and Lecture Notes in Bioinformatics)*, vol. 11400, 2019, pp. 221–249.
- [18] V. L. D. S. N. Brito, "Introduction to Biomedical Variables Transducing," in *Principles of Measurement and Transduction of Biomedical Variables*, 2015, pp. 1–24.
- [19] R. Starbird and W. Buehler, "Effect of experimental factors on the properties of PEDOT-NaPSS galvanostatically deposited from an aqueous micellar media for invasive electrodes," *Biomater.*, 2012.
- [20] R. Starbird, C. A. Garcia-González, I. Sznimova, W. H. Krautschneider, and W. Buehler, "Synthesis of an organic conductive porous material using starch aerogels as template for chronic invasive electrodes," *Mater. Sci. Eng. C*, vol. 57, pp. 177–183, 2014.
- [21] M. L. P. Langshan, K. J. M. Boonen, K. V. Rosaria-Chuk, D. W. J. van der Schaaf, M. J. Post, and F. P. T. Baaijens, "Advanced maturation by electrical stimulation: Differences in response between C2C12 and primary muscle progenitor cells," *J. Tissue Eng. Regen. Med.*, vol. 5, no. 7, pp. 529–539, Jul. 2011.
- [22] H. Kondo et al., "Movement of cultured myotube with electrical stimulation," in *WASCI 2008 - The 12th World Multi-Conference on Systemics, Cybernetics and Informatics, Jointly with the 14th International Conference on Information System Analysis and Synthesis, ISAS 2008 - Proc.*, 2008, vol. 2, pp. 104–109.
- [23] L. Liu, C. Zhang, W. Wang, N. Xi, and Y. Wang, "Regulation of C2C12 differentiation and control of the beating dynamics of contractile cells for a muscle-driven bio-inspired crawler by electrical stimulation," *Soft Robot.*, vol. 5, no. 6, pp. 748–760, 2018.

## Annex 8. Paper 2. Polysaccharide $\kappa$ -Carrageenan as Doping Agent in Conductive Coatings for Electrochemical Controlled Release of Dexamethasone at Therapeutic Doses.



Article

### Polysaccharide $\kappa$ -Carrageenan as Doping Agent in Conductive Coatings for Electrochemical Controlled Release of Dexamethasone at Therapeutic Doses

Karla Ramírez Sánchez <sup>1,2,\*</sup>, Aura Ledezma-Espinoza <sup>1</sup>, Andrés Sánchez-Kopper <sup>1</sup>, Esteban Avendaño-Soto <sup>3,4</sup>, Mónica Prado <sup>2</sup> and Ricardo Starbird Pérez <sup>1,\*</sup>

<sup>1</sup> Centro de Investigación y de Servicios Químicos y Microbiológicos (CEQIATEC), School of Chemistry, Instituto Tecnológico de Costa Rica, 159-7050 Cartago, Costa Rica; aledezma@itcr.ac.cr (A.L.-E.); ansanchez@itcr.ac.cr (A.S.-K.)

<sup>2</sup> Centro de Investigación en Enfermedades Tropicales (CIET), Faculty of Microbiology, Universidad de Costa Rica, 11501-2060 San José, Costa Rica; monica.pradoperras@ucr.ac.cr

<sup>3</sup> Centro de Investigación en Ciencia e Ingeniería de Materiales (CICIMA), Universidad de Costa Rica, 11501-2060 San José, Costa Rica; esteban.avendanoso@ucr.ac.cr

<sup>4</sup> School of Physics, Universidad de Costa Rica, 11501-2060 San José, Costa Rica

\* Correspondence: karamirez@itcr.ac.cr (K.R.S.); rstarbird@itcr.ac.cr (R.S.P.); Tel.: +506-25502731 (R.S.P.)

Academic Editor: Mitsuhiro Ebura

Received: 13 April 2020; Accepted: 30 April 2020; Published: 3 May 2020



**Abstract:** Smart conductive materials are developed in regenerative medicine to promote a controlled release profile of charged bioactive agents in the vicinity of implants. The incorporation and the active electrochemical release of the charged compounds into the organic conductive coating is achieved due to its intrinsic electrical properties. The anti-inflammatory drug dexamethasone was added during the polymerization, and its subsequent release at therapeutic doses was reached by electrical stimulation. In this work, a Poly (3,4-ethylenedioxythiophene):  $\kappa$ -carrageenan: dexamethasone film was prepared, and  $\kappa$ -carrageenan was incorporated to keep the electrochemical and physical stability of the electroactive matrix. The presence of  $\kappa$ -carrageenan and dexamethasone in the conductive film was confirmed by  $\mu$ -Raman spectroscopy and their effect in the topographic was studied using profilometry. The dexamethasone release process was evaluated by cyclic voltammetry and High-Resolution mass spectrometry. In conclusion,  $\kappa$ -carrageenan as a doping agent improves the electrical properties of the conductive layer allowing the release of dexamethasone at therapeutic levels by electrochemical stimulation, providing a stable system to be used in organic bioelectronics systems.

**Keywords:** polysaccharide;  $\kappa$ -carrageenan; dexamethasone; electrochemical active deliver system; doping agent; charged molecule; conductive polymers

#### 1. Introduction

Conductive polymers are a new generation of smart materials extensively used in organic bioelectronics, mostly in the development of neural implants, biosensors, and active controlled release systems [1–4]. Poly (3,4-ethylenedioxythiophene) (PEDOT) is a conductive polymer synthesized from 3,4-ethylenedioxythiophene (EDOT), used as a coating in diverse types of sensors due to its biocompatibility, conductivity, processing versatility, and stability [5,6]. Moreover, PEDOT is reported as a promising material for the immobilization of enzymes and other biologically active molecules [2,7,8]. The incorporation of charged molecules into the PEDOT backbone is described through an electrostatic mechanism due to the formation of charge carriers and the doping process during the electropolymerization process [9]. The subsequent release of the charged compounds was

reported to be dependent on the polymer thickness and charge applied during the electrochemical stimulus [10–13].

Diverse implants and scaffolds are developed in regenerative medicine to serve as extracellular matrices for cell colonization [14–16]. Many of them are loaded with bioactive agents to improve the therapeutic efficacy and safety of the drugs, playing important roles in treatment of several chronic diseases, damaged tissues, and providing a potential stimulation of different types of cells [17–19].

Although diverse engineering groups established different types of implants for a broad range of applications, those implants can elicit body responses involving inflammatory processes, which may result in the formation of glial scars due to neural devices specifically [12,13,20,21]. One strategy to avoid immune responses consists of releasing an anti-inflammatory biomolecule (i.e., dexamethasone) in the vicinity of the implant [11,13,22,23]. Dexamethasone (Dx) is a synthetic glucocorticoid that reduces inflammation in the central nervous system, acting through glucocorticoid receptors found in most neurons and glial cells. Due to being locally delivered, the specificity and efficiency of dexamethasone means that only small amounts of the drug are required [13,22,24–28].

$\kappa$ -Carrageenan ( $\kappa$ C) is a sulfonated polysaccharide recently used in aqueous micellar dispersions for the polymerization of EDOT, since it provides an appropriate environment for the monomer dispersion while acting as a doping agent in the conductive layer [29–31]. According to the previous work, the electrochemical properties of PEDOT are retained when  $\kappa$ C is used as a doping agent [29,30], avoiding a potential delamination during the reduction-oxidation process needed during the active delivering process. Biocompatibility of PEDOT: $\kappa$ C composite has been demonstrated in previous studies [2,29].

In this work, we induce the loading of dexamethasone phosphate during the deposition of the electroactive composite onto a bare gold electrode by changing the amount of drug in the dispersion prior the polymerization.  $\kappa$ C was incorporated to maintain the electrochemical stability and biocompatibility of the PEDOT matrix and the subsequent drug release using electrical stimulation. The presence of  $\kappa$ C and Dx inside the conductive film was confirmed by  $\mu$ -Raman spectroscopy and their effect in the topography was studied using profilometry. Dexamethasone release was evaluated by cyclic voltammetry and High-Resolution (HR) mass spectrometry. Therapeutic doses of dexamethasone were achieved during the electrical stimulation of the bioelectronic device.

## 2. Results and Discussion

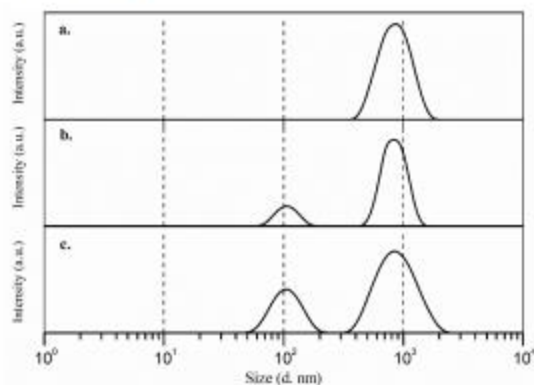
### 2.1. Evaluation of the Stability and Size of the Dispersion Systems

The dispersions used to electrodeposit the monomer and the Dx on the electrode were evaluated by their  $\zeta$ -potential values and particle size distribution in order to determine its stability in aqueous medium.  $\zeta$ -potential data was obtained for the six prepared dispersions, and they are shown in Table 1. It is possible to observe that EDOT: $\kappa$ C:Dx has an appropriate stability ( $-48.70$  mV), which is dominated for the  $\kappa$ C micellar system ( $-43.30$  mV). Values of  $\zeta$ -potential over  $-30$  mV are considered stable assuming that an electrostatic charge is the main stabilization mechanism and the colloidal system is in the range of hundreds [32,33]. The anionic nature of the  $\kappa$ C and Dx avoids aggregation due to the negative values obtained in the  $\zeta$ -potential analysis, which are comparable with previously reported results for these molecules [30,34,35]. A stable dispersion prevents aggregation or deposition of the particles that carried the monomer during the electrochemical deposition. Additionally, the stable system may allow a homogeneous dispersion of  $\kappa$ C and dexamethasone in the electrodeposited film as seen by Raman spectroscopy.

**Table 1.**  $\zeta$ -potential values of dispersions used in the fixation of the drug on the electrode.

System	$\zeta$ -potential (mV)	SD (mV)
Dx	-69.40	1.14
$\kappa$ C	-43.30	3.31
$\kappa$ C:Dx	-42.63	1.67
EDOT:Dx	70.83	1.09
$\kappa$ C:EDOT	-48.46	1.70
EDOT: $\kappa$ C:Dx	-48.70	1.21

Particle size measurements of the main three dispersions were performed to determine the dimension of their aggregates after the sonication process. Figure 1a shows the size distribution for the  $\kappa$ C 0.2% w/v solution, it is possible to observe a single population for the surfactant. Some authors have reported previously that  $\kappa$ C solutions are polydisperse (two or more populations), because it increases the gel behavior due to its polysaccharide nature [36,37]. Nevertheless, they emphasized that the main signal for the  $\kappa$ C aggregates has an average size in the range of 800 to 1000 nm [37], which agrees with our results. The intensive sonication process before the measures and the low concentration of  $\kappa$ C used in the analysis may explain why only one population were observed in the  $\kappa$ C size distribution, similar to a previous report [30].

**Figure 1.** Size distribution (d, nm) of (a)  $\kappa$ C; (b)  $\kappa$ C:Dx; and (c) EDOT: $\kappa$ C:Dx dispersions, measured by dynamic light scattering (DLS) method.

On the other hand, once the Dx was added to the dispersion, a polydisperse behavior was found in the  $\kappa$ C:Dx system and two populations were detected (Figure 1b,c). Desamethasone solutions are characterized by a single population with a particle size average of 100 nm [38] and was consistent with our results. Eventually, it is possible to observe that the stability of the system has remained when the monomer was added (Figure 1c). The stability of the dispersions depends mainly on the used surfactant and it has an important influence in the physical and electrochemical properties of the electrodeposited films [39].



## 2.2. Analysis of the Topography and Composition of PEDOT:αC:Dx Coating by $\mu$ -Raman Spectroscopy and Profilometry Methods

The PEDOT:αC:Dx composite was obtained from a EDOT:αC:Dx dispersion by electrochemical deposition under galvanostatic conditions (Figure S1), as it was established in a previous work [2,30]. Then, the topography of the PEDOT:αC:Dx coating was characterized before ( $S_a$ :  $0.270 \pm 0.005 \mu\text{m}$ , surface area:  $1361 \text{ mm}^2$ , negative volume  $0.1562 \text{ mm}^3$ , and volume  $1.695 \text{ mm}^3$ ) and after ( $S_b$ :  $0.250 \pm 0.005 \mu\text{m}$ , surface area:  $1337 \text{ mm}^2$ , negative volume  $0.1707 \text{ mm}^3$ , and volume  $1.690 \text{ mm}^3$ ) releasing the Dx from the conductive coating. The roughness data of both surfaces did not show significant differences between them (see Figure 2a,b). The volume ratio between peaks and valleys describes the symmetry in the surface topography. A negative value is indicative of more distinct valleys and positive of more distinct peaks about the average plane. Our samples were dominated by peaks and low negative volume (around ten times) and those values are consistent with a previous report for PEDOT:αC coatings [30]. It is suggested that rough surfaces in comparison with smooth surfaces improve cell attachment due to the formation of specific surface-cell contacts by increasing the expression of different integrins subunits [40,41]. Although, diverse authors have reported that surface roughness values higher than  $0.5 \mu\text{m}$  are desirable to ensure the maximum attachment and proliferation of cells, large rough surfaces also stimulate more anti-inflammatory responses because the activation of M2 macrophages and the subsequent release of anti-inflammatory cytokines [42]. The PEDOT:αC:Dx surface roughness value and the lack of their significative variation during the delivery of dexamethasone may indicate the reliability of electroactive composite for cell culture studies, since no additional mechanism may be seemed due to the topography changes.

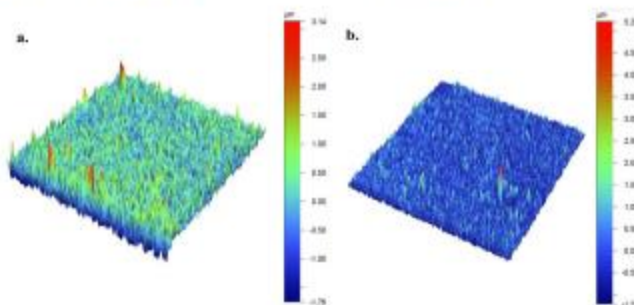


**Figure 2.** Profilometry images obtained for PEDOT:αC:Dx films (a) before and (b) after 160 cycles of cyclic voltammetry in a 0.10 M ammonium acetate solution.

The qualitative composition of the conductive film was determined using confocal  $\mu$ -Raman spectroscopy before (Figure 3a,c) and after (Figure 3b,d) 160 sweeps of electrical stimulation in a  $4 \mu\text{m}^2$  area and  $5 \mu\text{m}$  depth inside the composite. The analysis was performed in order to determine the presence of PEDOT, dexamethasone, and  $\alpha$ -carrageenan inside the electroactive composite. The signal was obtained and plotted in a 2D image that allows the association of the signal (counts) to the presence of the corresponding functional groups for each component.

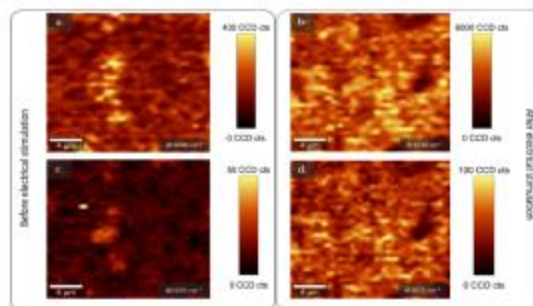


**Figure 3.** 2D confocal Raman map of the  $1430\text{ cm}^{-1}$  band (a) before release process and (b) after 160 release cycles. Raman mapping of the  $1625\text{ cm}^{-1}$  band intensity (c) before release process and (d) after 160 release cycles at  $0.5\text{ }\mu\text{m}$  depth inside the conductive layer. The yellow areas are related to the presence of PEDOT and  $\kappa\text{C/Dx}$ , respectively.

PEDOT shows a strong signal in the spectral range of  $1421\text{--}1442\text{ cm}^{-1}$ , associated to the thiophene symmetric  $C_a - C_b$  stretching [2,30,43] and its oxidation state. The corresponding signal was obtained from the composite before and after 160 cycles of electrical stimulation (Figure S2) and it was mapped at  $1430 \pm 25\text{ cm}^{-1}$  (Figure 3a,b), where bright yellow dots corresponded to presence of PEDOT. A homogeneous distribution of the conductive polymer was detected in both samples.

Additionally, a relative intense band at  $1625 \pm 30\text{ cm}^{-1}$  was detected, corroborating the qualitative existence of Dx and  $\kappa\text{C}$  in the conductive film (Figure 3c,d). This signal, in the 2D, is distributed through the conductive matrix. The result is similar to previous studies [13,26], which reported the characteristic spectral signals of dexamethasone in the ranges of  $3200\text{--}3500\text{ cm}^{-1}$ ,  $2850\text{--}3000\text{ cm}^{-1}$ , and near to  $1650\text{ cm}^{-1}$ , as is verified in Figure S3, corresponding to hydroxyl, methyl, and carbonyl groups, respectively. Dexamethasone and  $\kappa\text{C}$  act as doping agents, so there is a consistent association of the respective signal for both molecules and the PEDOT band. The identification of the band at  $1625\text{ cm}^{-1}$  overlapping with PEDOT signal, confirmed the presence of the doping agent before and even after electrochemical stimulation, as is shown in Figure S2a,b, respectively. Adding  $\kappa\text{C}$  in the formulation provides a proper doping agent during the release of the Dx, reducing the degradation by overoxidation and eventually delamination as is shown in Figure S4 [30].

### 2.3. Dexamethasone Release Experiments from the PEDOT: $\kappa\text{C/Dx}$ Coating

Drug loading into the conducting polymers films is based on the fact that these kinds of polymers are electrically oxidized during the polymerization processes, generating charge carriers [9,44,45]. The doping agent (e.g., Dx and  $\kappa\text{C}$ ) is incorporated to the oxidized polymer [46] to maintain charge neutrality. In this work, dexamethasone 21 phosphate and  $\kappa\text{C}$  are used as doping agents, the presence of sulfate and phosphate groups imparts negative charges in the polysaccharide and the drug, respectively.

The electrochemical controlled release studies from PEDOT: $\kappa\text{C/Dx}$  coating were performed within a potential range of  $-600$  to  $1000\text{ mV}$  to evaluate intrinsic redox processes of the film [13,35,45]. Figure 4 shows the characteristic oxidation and reduction potential signal ranges at  $0$  to  $500\text{ mV}$  and  $-100$  to  $-400\text{ mV}$ , respectively, after a different number of voltammetry scans. According to some authors, the voltammetric behavior of dexamethasone shows a reduction signal at the potential of  $-350\text{ mV}$  [13,45], which indicates the release of the drug from a stimulated electrode. The corresponding CV signals are shown in Figure 4, this signal gradually decreased according to the sweep

number, disappearing completely after 160 cycles of electrical stimulation. Electrochemical reduction of a conducting polymer results in the migration of small doping molecules from the conducting composite to maintain the electro neutrality of the matrix [44,46]. Thus, the application of alternating positive and negative potentials during cyclic voltammetry analysis caused the release of the Dx from the PEDOT coating.

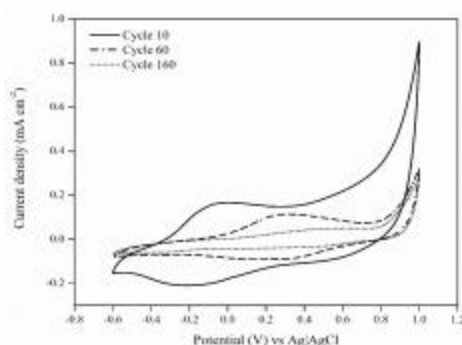


**Figure 4.** Cyclic voltammograms for the PEDOT:αC:Dx recorded at  $25 \text{ mV s}^{-1}$  after 10, 60, and 160 cycles of electrical stimulation in ammonium acetate 0.10 M.

Spontaneous release of the dopant from the PEDOT structure is an instant process, but the Dx release is slow, since it is driven by diffusion from the inner film to the surface. αC is a large molecule, this type of dopant is more attached into the polymer coating and it is not leached out during the electrical stimulation, granting to the polymer greater electrochemical stability [13,46,47], as confirmed by Raman spectroscopy.

The release profile of the Dx was investigated under passive conditions (unstimulated) and active electrical stimulation using an ammonium acetate 0.10 M solution as supporting electrolyte. The surface area of the electrode is associated with promoting larger amounts of passive drug release according to the second Fick's law of diffusion [48,49], yet, in our case, the electrode surface and total area are maintained virtually constant. The quantification of Dx from the PEDOT:αC:Dx modified electrodes was achieved using HR-mass spectrometry (Figure 5).

The active release profile was performed with a total of 76 CV sweeps in five release events, taking around 300 min to be completed. Accordingly, the passive release profile from unstimulated electrodes were evaluated over the same period of 300 min.

Figure 5a shows the passive release profile of Dx as a function of square root of time according to the Higuchi model for the drug release from a polymer film [27,50], where pure Fickian diffusion is the dominant phenomena [48]. The low diffusion value, in the beginning of the process, may depend on the slow penetration of supportive electrolyte into the polymeric film [49]. The pattern changed after 80 min and a higher diffusion value reflects the diffusivity of the passive Dx release process. The three systems (1 mM, 5 mM, and 10 mM) showed analogous Fickian diffusion behavior.

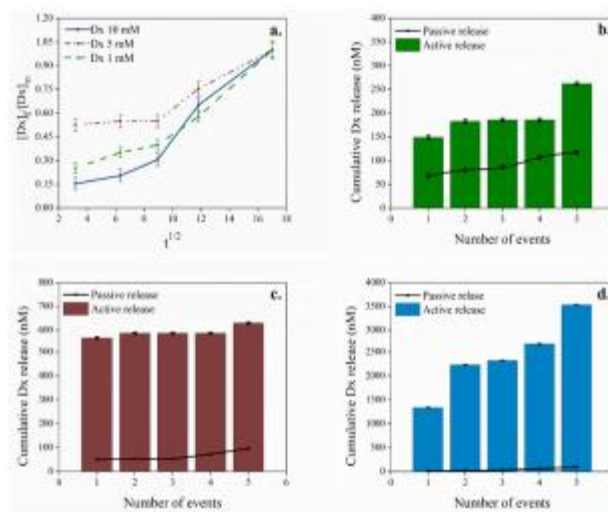


**Figure 5.** (a) The passive release profile of Dx as a function of square root of time, over 300 min from unstimulated electrodes. The active electrically controlled delivery process by stimulation events (columns) compared to the passive release profile (line) using: (b) 1 mM, (c) 5 mM, and (d) 10 mM of Dx in the initial formulation.

On the other hand, Figure 5b–d showed a remarkable dependency of the released Dx concentration during the electrical stimulated events (bars) compared to a passive unstimulated electrode (line). Some authors have studied controlled drug release systems using conductive polymers such as polypyrrole and PEDOT, where the anionic molecule is used as doping agent and their subsequent release is mainly determined via diffusion [11,13,44,45,51]. Nevertheless, for a controllable release system, it is desirable to have a high active release and low diffusion relationship [11,12], as shown by our system (see Figure 5). For instance, the initial concentration of 10 mM released in the passive process ca. 2% of the delivered Dx in stimulated process. This is probably associated with the use of  $\alpha$ C as second doping in the matrix, which grants the film stability and integrity during stimulation cycles [30,46].

The therapeutic dosages of Dx in mesenchymal stem cell cultures are effective at levels of 100–1000 nM to promote their differentiation to osteoblast or in order to be used during anti-inflammatory treatment [52–54]. In this work, the accumulative concentration of the released Dx using 1 mM and 5 mM initial formulations (Figure 5b,c) were 300 nM ( $0.66 \mu\text{g cm}^{-2}$ ) and 600 nM ( $1.60 \mu\text{g cm}^{-2}$ ), respectively. Even though, these values are at therapeutically relevant levels, they are in part determined by the Dx amount release via diffusion.

Instead, when 10 mM of the drug was poured in the initial formulation, a total of 3700 nM ( $8.89 \mu\text{g cm}^{-2}$ ) of cumulative Dx was detected. This concentration range far in excess of the quantity of dexamethasone released from similar systems using an identical initial concentration of the drug for the coating preparation, for which values are even lower than  $5.03 \mu\text{g cm}^{-2}$  [11,12,51]. Such concentrations

surpass the amount of the drug needed in cell cultures and it is not recommended to apply in biological systems. Nonetheless, using a specific electrochemical stimulation profile may be allowed to provide an adequate quantity of the drug for different biological applications.

### 3. Materials and Methods

#### 3.1. Materials

Monomer 3,4-ethylenedioxythiophene (EDOT, 97.0% purity),  $\kappa$ -carrageenan ( $\kappa$ C, ACS reagent), potassium chloride (KCl, >99.0% purity), dexamethasone 21-phosphate disodium salt (Dx, 98.0% purity), ammonium acetate ( $\text{NH}_4\text{CH}_2\text{CO}_2$ , 98.0% purity), ultrapure water MS quality, and MS methanol were purchased from Sigma Aldrich (San José, Costa Rica). All chemical reagents were used without further purification.

#### 3.2. Synthesis and Preparation of the Modified PEDOT: $\kappa$ C:Dx Electrode

Electrodes ( $20.49 \pm 0.02 \text{ mm}^2$ ) were fabricated by the deposition of gold on a polyimide substrate (see Figure S4) and they were passivated using a shadow mask to leave a specific exposed area to the electrode [55]. Prior to the polymer deposition, all electrodes were electrochemically cleaned applying cyclic voltammetry (CV) sweeps from a range of  $-600$  to  $900 \text{ mV}$  with  $100 \text{ mV s}^{-1}$  scan rate, in KCl  $0.2 \text{ M}$  [56], using an Autolab Potentiostat supplied by Metrohm (PGSTAT-302N, AUTOLAB, Utrecht, The Netherlands).

The surfactant dispersion was prepared according to a previous work [30], briefly:  $\kappa$ C ( $0.2\% \text{ w/v}$ ) and KCl ( $0.2 \text{ M}$ ) were added to deionized water previously heated at  $50 \text{ }^\circ\text{C}$ . The samples were sonicated using  $140 \text{ Joules}$  in a Sonifier Q500 (Q700, Ultrasonic Corporation, Danbury, CT, USA), before and after adding the monomer EDOT ( $10 \text{ mM}$ ) and Dx at three different concentrations:  $1 \text{ mM}$ ,  $5 \text{ mM}$ , and  $10 \text{ mM}$ .

The solution was electropolymerized on the electrode surface using galvanostatic conditions in the Autolab Potentiostat. The gold electrode (see Figure S4) is used as working electrode, platinum as counter electrode, and Ag/AgCl ( $\text{KCl } 3.0 \text{ M}$ ) works as reference electrode. The electrical polymerization was carried out with a constant current of  $102.45 \text{ microamperes}$  (current density:  $0.5 \text{ mA cm}^{-2}$ ) using a potential limit of  $1400 \text{ mV}$  during  $360 \text{ s}$  (ca.  $180 \text{ mC cm}^{-2}$  of charge density). Following the PEDOT: $\kappa$ C:Dx deposition, the electrodes were intensively rinsed with deionized water and stored at  $4 \text{ }^\circ\text{C}$  before their use.

#### 3.3. Evaluation of the Stability and Size of the Dispersion Systems

The characterization of the particle size and  $\zeta$ -potential was performed using six dispersions, prepared in deionized water, namely: (1)  $\kappa$ C  $0.2\% \text{ w/v}$ ; (2) Dx  $10 \text{ mM}$ ; (3) EDOT  $10 \text{ mM}$ : $\kappa$ C  $0.2\% \text{ w/v}$ ; (4) EDOT  $10 \text{ mM}$ :Dx  $10 \text{ mM}$ ; (5)  $\kappa$ C  $0.2\% \text{ w/v}$ :Dx  $10 \text{ mM}$ ; and (6) EDOT  $10 \text{ mM}$ : $\kappa$ C  $0.2\% \text{ w/v}$ :Dx  $10 \text{ mM}$ . Measurements were performed in a Zetasizer instrument (Nano ZS, Malvern Analytical Ltd., Worcestershire, UK) at  $25 \text{ }^\circ\text{C}$  and  $173^\circ$  angle. All the measurements were done by triplicate. Finally, dispersions were sonicated using a high-power ultrasonic bath (Bransonic<sup>®</sup>, Merck corporation, San José, Costa Rica) for  $6 \text{ min}$  to promote their homogenization. Two more formulations of EDOT: $\kappa$ C:Dx were prepared to reach lower dexamethasone concentrations into the conductive layer.

#### 3.4. Analysis of the Topography and Composition of PEDOT: $\kappa$ C:Dx Coating by Profilometry and $\mu$ -Raman Spectroscopy Methods

The electrode topography was studied by profilometry analysis (Bruker, model: Dektak TX Advance, AZ, USA) and the arithmetical mean roughness of the surface ( $S_a$ ) was calculated to describe the topography of the materials by using a  $2 \text{ }\mu\text{m}$  tip radius and a force of  $1 \text{ mg}$  in a  $300 \times 300 \text{ }\mu\text{m}^2$  and a scan area rate of  $2.5 \text{ }\mu\text{m s}^{-1}$ .

Raman spectroscopy analysis was carried out using a confocal  $\mu$ -Raman microscope (Alpha300 R WITec, GmbH, Ulm, Germany) with a 532nm excitation laser, exposure time of 0.5 s, and 105 accumulations. The Raman stack scan was obtained using an integration time of 4 s in  $4 \mu\text{m}^2$  of area, 200 measurements per line were recorded for a total of 20 lines in each stack. Oversampling was used to improve the image quality, which was done in case of the cross-sectional scan. The scan depth was fixed at  $5 \mu\text{m}$  and a total of 10 stack scans were achieved. The intensity of the relative wavenumber at  $1435 \text{ cm}^{-1}$  and  $1625 \text{ cm}^{-1}$  were extracted from each acquired spectrum, corresponding to PEDOT [2] and Ds/cC [44,57], respectively and plotted as 2D image. The intensity counts are related to the presence of the functional group and it is presented as bright yellow areas.

### 3.5. Dexamethasone Release Experiments from the PEDOT:cC:Ds Film

The Ds release from the modified electrode was carried out in a continuous flow cell using cyclic voltammetry (CV) sweeps with a three electrodes system (PEDOT:cC:Ds, Ag|AgCl and a gold film as working, reference, and counter electrodes, respectively). The active release of the drug was performed in 1 mL of fresh ammonium acetate solution (0.10 M) pH 7.2 [38], by scanning of CV from  $-600$  to  $1000 \text{ mV}$  with a  $25 \text{ mV s}^{-1}$  scan rate, over a period of 300 min (5 samples total) at room temperature.

The second release event, without electrical stimulation, was performed in order to analyze and to quantify the passive drug release process. For the experiment, 1.0 mL of 0.10 M ammonium acetate was injected through the cell containing the electrodes, a total of five samples were collected during 300 min of analysis.

Dexamethasone phosphate concentration, in the samples for the active and passive release events, was determined using a Xevo G2-XS quadrupole time of flight (Q-tof) mass spectrometer (Waters Corporation, Wilmslow, UK) coupled with an Acquity UPLC H-Class. For the analysis, a  $10\text{-}\mu\text{L}$  injection of the sample was separated with an Acquity UPLC<sup>®</sup> C18 column ( $2.1 \text{ mm} \times 50.0 \text{ mm}$ ). The mobile phase consisted of a solution of water:formic acid 0.05% v/v and methanol:formic acid 0.05% v/v and they were supplied under not isocratic conditions with a constant flow of  $0.3 \text{ mL min}^{-1}$  (Table S1).

The mass spectrometer was configured according to the parameters in a previous work [39], with the modifications shown in supplementary information S1. Quantification was carried out using Multiple Reaction Monitoring (MRM) acquisition method with the optimized transition of  $471.1584 \text{ m/z}$  for the precursor ion and  $78.9585 \text{ m/z}$  for the product ion, with a collision energy of  $35 \text{ eV}$ . Concentration in each sample was calculated using the Software MassLynx<sup>™</sup> (V4.1, Waters Corporation, Wilmslow, UK) and an external calibration curve between 0.5 ppb to 5000 ppb of dexamethasone phosphate ( $R^2 = 0.9965$ ).

## 4. Conclusions

We have successfully delivered therapeutic doses of dexamethasone by an electroactive controlled system, adjusting the initial formulation and the electrical stimulated events. Moreover, using  $\kappa$ -carrageenan as dispersant during the polymerization and as a doping agent in the composite, we avoided delamination and changes in the film roughness. The chemical composition inside the conductive film was confirmed by 2D Raman and electrochemical signal in the cyclic voltammetry analysis. Concentrations of dexamethasone in the range of 100 to 1000 nM were obtained using a lower amount of dexamethasone in the initial formulation. Those concentrations are recommended to induce differentiation in mesenchymal cell cultures and in anti-inflammatory responses. Therefore, an adequate formulation along with a proper active electrochemical stimulation profile allowed the delivery of therapeutic doses of charged molecules without significant changes in our film roughness. Our approach may be useful in the development of diverse strategies and implant systems in the regenerative medicine field.

**Supplementary Materials:** The following is available online, Figure S1: Galvanostatic curve of the electro-polymerization process from an EDOT:xC-Ds dispersion onto a bare gold electrode. Figure S2: Raman spectra of the PEDOT:xC-Ds coating (a.) before dexamethasone release process (Inset: PEDOT:xC-Ds electrode surface) and (b.) after 160 release cycles (Inset: PEDOT:xC-Ds electrode surface). Figure S3:  $\mu$ -Raman spectral measurement of the dexamethasone 21-phosphate disodium salt. Figure S4: Deposited PEDOT:xC-Ds electrode after 160 cycles of electrical stimulation (left) and gold electrode without passivation as reference (right). Table S1: Gradient elution method for the mobile phase using during dexamethasone analysis. Solvents were water, 0.05% formic acid (A) and methanol: 0.05% formic acid (B), and S1: Configuration of the mass spectrometer during dexamethasone quantification.

**Author Contributions:** Conceptualization, K.R.S.; M.P. and R.S.P.; methodology, K.R.S.; A.L.-E.; A.S.-K.; E.A.-S. and R.S.P.; software, K.R.S.; A.L.-E.; A.S.-K.; E.A.-S. and R.S.P.; validation, K.R.S.; A.L.-E.; A.S.-K. and R.S.P.; formal analysis, R.S.P.; investigation, K.R.S. and R.S.P.; resources, E.A.-S. and R.S.P.; data curation, K.R.S.; A.L.-E. and A.S.-K.; writing—original draft preparation, K.R.S. and R.S.P.; writing—review and editing, K.R.S.; A.L.-E.; A.S.-K.; E.A.-S.; M.P. and R.S.P.; visualization, K.R.S. and R.S.P.; supervision, M.P. and R.S.P.; project administration, K.R.S. and R.S.P.; funding acquisition, E.A.-S. and R.S.P. All authors have read and agree to the published version of the manuscript.

**Funding:** This research was funded by Costa Rica Institute of Technology (ITCR), project number: 5402-1360-4401.

**Acknowledgments:** Costa Rica Institute of Technology (ITCR), project number: 5402-1360-4401. Part of this work was carried out in the frame of the COST-Action “Advanced Engineering of Aerogels for Environment and Life Sciences” (AERoGELS, ref. CA18125) funded by the European Commission. The authors would like to thank to Steven Hidalgo and Jazmin Umaha for their participation in the electrode fabrication process. RGSF-RIP.

**Conflicts of Interest:** The authors declare no conflict of interest.

## References

- Ozkan, B.C.; Soganci, T.; Turhan, H.; Ak, M. Investigation of rGO and chitosan effects on optical and electrical properties of the conductive polymers for advanced applications. *Electrochim. Acta* **2019**, *295*, 1044–1051. [\[CrossRef\]](#)
- Ramirez-Sanchez, K.; Alvarado-Hidalgo, F.; Zamora-Sepaeira, R.; Sáenz-Aroca, G.; Rojas-Carrillo, O.; Acosta-Soto, E.; Ruappert, C.; Mena-Torres, F.; Starbird-Pérez, R. Biosensor based on the directly enzyme immobilization into a gold nanotriangles/conductive polymer biocompatible coat for electrochemical detection of Chlorpyrifos in water. *Med. Devices Sens.* **2019**, *2*, 1–18.
- Mantione, D.; del Agua, I.; Sanchez-Sanchez, A.; Mecerreyes, D. Poly(3,4-ethylenedioxythiophene) (PEDOT) derivatives: Innovative conductive polymers for bioelectronics. *Polymers (Basel)* **2017**, *9*, 354. [\[CrossRef\]](#) [\[PubMed\]](#)
- Ghorbani Zamani, F.; Moulahoum, H.; Ak, M.; Odaci Demirkol, D.; Timur, S. Current trends in the development of conducting polymers-based biosensors. *TrAC Trends Anal. Chem.* **2019**, *118*, 264–276. [\[CrossRef\]](#)
- Khan, S.; Ul-Islam, M.; Ullah, M.W.; Israr, M.; Jang, J.H.; Park, J.K. Nano-gold assisted highly conducting and biocompatible bacterial cellulose-PEDOT/PSS films for biology-device interface applications. *Int. J. Biol. Macromol.* **2018**, *107*, 865–873. [\[CrossRef\]](#)
- Lu, B.; Yue, H.; Lin, S.; Jian, N.; Qu, K.; Xu, J.; Zhao, X. Pure PEDOT/PSS hydrogels. *Nat. Commun.* **2019**, *10*, 1–10. [\[CrossRef\]](#)
- Kabouah, M.; Behary, N.; Cayla, A.; Mutel, B.; Guan, J.; Nierstrasz, V. Influence of remote plasma on PEDOT/PSS-coated carbon felt for improved activity of glucose oxidase. *J. Appl. Polym. Sci.* **2020**, *137*, 1–11. [\[CrossRef\]](#)
- Luo, S.C.; Ali, E.M.; Tamsil, N.C.; Yu, H.H.; Gao, S.; Kantechev, E.A.B.; Ying, J.Y. Poly(3,4-ethylenedioxythiophene) (PEDOT) nanobiointerface: Thin, ultrasoft, and functionalized PEDOT films with in vitro and in vivo biocompatibility. *Langmuir* **2008**, *24*, 8071–8077. [\[CrossRef\]](#)
- Starbird, R.; Bauhofer, W.; Meza-Cuevas, M.; Krautchnneider, W.H. Effect of experimental factors on the properties of PEDOT-NaPSS galvanostatically deposited from an aqueous micellar media for invasive electrodes. In Proceedings of the 5th 2012 Biomedical Engineering International Conference, Ubon Ratchathani, Thailand, 5–7 December 2012; pp. 1–5.
- Li, Y.; Neuh, K.G.; Kang, E.T. Controlled release of heparin from polypyrrole-poly(vinylalcohol) assembly by electrical stimulation. *J. Biomed. Mater. Res. Part A* **2005**, *72*, 171–180. [\[CrossRef\]](#)

11. Boshler, C.; Oberbauer, F.; Asplund, M. Tuning drug delivery from conducting polymer films for accurately controlled release of charged molecules. *J. Control. Release* **2019**, *304*, 173–180. [\[CrossRef\]](#)
12. Boshler, C.; Kleber, C.; Martini, N.; Xie, Y.; Drey, I.; Stieglitz, T.; Hofmann, U.G.; Asplund, M. Actively controlled release of dexamethasone from neural microelectrodes in a chronic in vivo study. *Biomaterials* **2017**, *129*, 176–187. [\[CrossRef\]](#) [\[PubMed\]](#)
13. Wadhwa, R.; Lageraur, C.F.; Cui, X.T. Electrochemically controlled release of dexamethasone from conducting polymer polypyrrole coated electrode. *J. Control. Release* **2006**, *110*, 531–541. [\[CrossRef\]](#) [\[PubMed\]](#)
14. Wang, W.; Yeung, K.W.K. Bone grafts and biomaterials substitutes for bone defect repair: A review. *Biomater. Mater.* **2017**, *2*, 224–247. [\[CrossRef\]](#) [\[PubMed\]](#)
15. Wang, Z.; Zhang, T.; Xie, S.; Liu, X.; Li, H.; Linhardt, R.J.; Chi, L. Sequencing the oligosaccharide pool in the low molecular weight heparin dalteparin with offline HPLC and ESI-MS/MS. *Carbohydr. Polym.* **2018**, *183*, 81–90. [\[CrossRef\]](#) [\[PubMed\]](#)
16. Mao, A.S.; Mooney, D.J. Regenerative medicine: Current therapies and future directions. *Proc. Natl. Acad. Sci. USA* **2015**, *112*, 14452–14459. [\[CrossRef\]](#)
17. Benoit, D.S.W.; Durney, A.R.; Anseth, K.S. The effect of heparin-functionalized PEG hydrogels on three-dimensional human mesenchymal stem cell osteogenic differentiation. *Biomaterials* **2007**, *28*, 66–77. [\[CrossRef\]](#)
18. He, Q.; Shi, J. Mesoporous silica nanoparticle based nano drug delivery systems: Synthesis, controlled drug release and delivery, pharmacokinetics and biocompatibility. *J. Mater. Chem.* **2011**, *21*, 5845–5855. [\[CrossRef\]](#)
19. Kumar, C.S.S.R.; Mohammad, F. Magnetic nanomaterials for hyperthermia-based therapy and controlled drug delivery. *Adv. Drug Deliv. Rev.* **2011**, *63*, 789–808. [\[CrossRef\]](#)
20. Vishwakarma, A.; Bhisie, N.S.; Evangelista, M.B.; Roswanka, J.; Dokmeci, M.R.; Ghaemmaghami, A.M.; Vrana, N.E.; Khademhosseini, A. Engineering immunomodulatory biomaterials to tune the inflammatory response. *Trends Biotechnol.* **2016**, *34*, 470–482. [\[CrossRef\]](#)
21. Thuvanon, P.T.; Nair, A.M.; Shen, J.; Lotfi, P.; Ko, C.Y.; Tang, L. The effect of incorporation of SDF-1 $\alpha$  into PLGA scaffolds on stem cell recruitment and the inflammatory response. *Biomaterials* **2010**, *31*, 3997–4008. [\[CrossRef\]](#)
22. Goimil, L.; Jaeger, P.; Ardau, I.; Gómez-Amoza, J.L.; Corcheiro, A.; Alvarez-Lorenzo, C.; Garcia-González, C.A. Preparation and stability of dexamethasone-loaded polymeric scaffolds for bone regeneration processed by compressed CO<sub>2</sub> foaming. *J. CO<sub>2</sub> Util.* **2018**, *24*, 89–98. [\[CrossRef\]](#)
23. Costa, P.F.; Puga, A.M.; Diaz-Gomez, L.; Corcheiro, A.; Busch, D.H.; Alvarez-Lorenzo, C. Additive manufacturing of scaffolds with dexamethasone controlled release for enhanced bone regeneration. *Int. J. Pharm.* **2015**, *496*, 541–550. [\[CrossRef\]](#) [\[PubMed\]](#)
24. Langerbach, F.; Handsche, J. Effects of dexamethasone, ascorbic acid and  $\beta$ -glycerophosphate on the osteogenic differentiation of stem cells in vitro. *Stem Cell Res. Ther.* **2013**, *4*, 423–430. [\[CrossRef\]](#) [\[PubMed\]](#)
25. Helledie, T.; Dombrowski, C.; Rai, B.; Lim, Z.X.H.; Hin, L.L.H.; Rider, D.A.; Stein, G.S.; Hong, W.; van Wijnen, A.J.; Hui, J.H.; et al. Heparan sulfate enhances the self-renewal and therapeutic potential of mesenchymal stem cells from human adult bone marrow. *Stem Cells Dev.* **2012**, *21*, 1897–1910. [\[CrossRef\]](#) [\[PubMed\]](#)
26. Martins, A.; Duarte, A.R.C.; Faria, S.; Marques, A.P.; Reis, R.L.; Neves, N.M. Osteogenic induction of hBMSCs by electrospun scaffolds with dexamethasone release functionality. *Biomaterials* **2010**, *31*, 5875–5885. [\[CrossRef\]](#) [\[PubMed\]](#)
27. Goimil, L.; Santos-Rosales, V.; Delgado, A.; Évora, C.; Reyes, R.; Lozano-Pérez, A.A.; Azenar-Cervantes, S.D.; Cernis, J.L.; Gómez-Amoza, J.L.; Corcheiro, A.; et al. SeCO<sub>2</sub>-foamed silk fibroin aerogel/poly( $\epsilon$ -caprolactone) scaffolds containing dexamethasone for bone regeneration. *J. CO<sub>2</sub> Util.* **2019**, *31*, 51–64. [\[CrossRef\]](#)
28. Chu, C.C.; Hsiang, C.H.; Shieh, J.P.; Chien, C.C.; Ho, C.M.; Wang, J.J. The cellular mechanisms of the antiemetic action of dexamethasone and related glucocorticoids against vomiting. *Eur. J. Pharmacol.* **2014**, *722*, 48–54. [\[CrossRef\]](#)
29. Zamora-Sequeira, R.; Ardau, I.; Starbird, R.; Garcia-González, C.A. Conductive nanostructured materials based on poly-(3,4-ethylenedioxythiophene) (PEDOT) and starch/carrageenan for biomedical applications. *Carbohydr. Polym.* **2018**, *188*, 304–312. [\[CrossRef\]](#)



30. Hernández-Suarez, P.; Ramirez, K.; Alvarado, F.; Avendaño, E.; Starbird, R. Electrochemical characterization of poly(3,4-ethylenedioxythiophene)/ $\kappa$ -carrageenan as a biocompatible conductive coat for biologic applications. *MRS Commun.* **2018**, *1*, 6. [[CrossRef](#)]
31. Pourjavadi, A.; Harzaendi, A.M.; Hossainzadeh, H. Modified carrageenan 3. Synthesis of a novel polysaccharide-based superabsorbent hydrogel via graft copolymerization of acrylic acid onto kappa-carrageenan in air. *Eur. Polym. J.* **2004**, *40*, 1363–1370. [[CrossRef](#)]
32. Hunter, R. *Zeta Potential in Colloid Science: Principles and Applications*; Academic Press: Cambridge, MA, USA, 2013; pp. 6–7.
33. Lowry, G.V.; Hill, R.J.; Harper, S.; Rawle, A.F.; Hendren, C.O.; Klaessig, F.; Nöbbmann, U.; Saye, P.; Rumble, J. Guidance to improve the scientific value of zeta-potential measurements in nanoEHS. *Environ. Sci. Nano* **2016**, *3*, 953–965. [[CrossRef](#)]
34. Ali, H.; Kalashnikova, I.; White, M.A.; Sherman, M.; Rytting, E. Preparation, characterization, and transport of dexamethasone-loaded polymeric nanoparticles across a human placental in vitro model. *Int. J. Pharm.* **2013**, *454*, 149–157. [[CrossRef](#)]
35. Pargaonkar, N.; Lvov, Y.M.; Li, N.; Stoerckamp, J.H.; De Villiers, M.M. Controlled release of dexamethasone from microcapsules produced by polyelectrolyte layer-by-layer nanoassembly. *Pharm. Res.* **2005**, *22*, 826–835. [[CrossRef](#)]
36. Saghas, S.; Butun, S.; Sahiner, N. Modifiable chemically crosslinked poly( $\kappa$ -carrageenan) particles. *Carbohydr. Polym.* **2012**, *87*, 2718–2724. [[CrossRef](#)]
37. Antonov, Y.A.; Zhuravleva, I.L.; Cardinaels, R.; Moldenaers, P. Macromolecular complexes of lysozyme with kappa carrageenan. *Food Hydrocoll.* **2018**, *74*, 227–238. [[CrossRef](#)]
38. Zhang, Z.; Griegens, D.W.; Feijen, J. Poly(trimethylene carbonate) and monomethoxy poly(ethylene glycol)-block-poly(trimethylene carbonate) nanoparticles for the controlled release of dexamethasone. *J. Control. Release* **2006**, *111*, 263–270. [[CrossRef](#)]
39. Walsh, F.C.; Ponce De Leon, C. A review of the electrodeposition of metal matrix composite coatings by inclusion of particles in a metal layer: An established and diversifying technology. *Trans. Inst. Met. Finish.* **2014**, *92*, 83–98. [[CrossRef](#)]
40. Deligianni, D.D.; Katsala, N.D.; Koutsoukos, P.G.; Missiridis, Y.F. Effect of surface roughness of hydroxyapatite on human bone marrow cell adhesion, proliferation, differentiation and detachment strength. *Biomaterials* **2000**, *22*, 87–96. [[CrossRef](#)]
41. Kokkinos, P.A.; Koutsoukos, P.G.; Deligianni, D.D. Detachment strength of human osteoblasts cultured on hydroxyapatite with various surface roughness. Contribution of integrin subunits. *J. Mater. Sci. Mater. Med.* **2012**, *23*, 1489–1498. [[CrossRef](#)]
42. Hotchkiss, K.M.; Reddy, G.B.; Hyzy, S.L.; Schwartz, Z.; Boyan, B.D.; Olivares-Navarrete, R. Titanium surface characteristics, including topography and wettability, alter macrophage activation. *Acta Biomater.* **2016**, *31*, 425–434. [[CrossRef](#)]
43. Tran-Van, F.; Garmou, S.; Lasaun, G.; Froyet, G.; Chevrot, C. Fully undoped and soluble oligo(3,4-ethylenedioxythiophene)s: Spectroscopic study and electrochemical characterization. *J. Mater. Chem.* **2001**, *11*, 1378–1382. [[CrossRef](#)]
44. Stevenson, G.; Moulton, S.E.; Irwin, P.C.; Wallace, G.G. Poly(terthiophene) as an electrostimulated controlled drug release material of therapeutic levels of dexamethasone. *Synth. Met.* **2010**, *160*, 1107–1114. [[CrossRef](#)]
45. Leprince, L.; Dogimont, A.; Magnin, D.; Demoustier-Champagne, S. Dexamethasone electrically controlled release from polypyrrole-coated nanostructured electrodes. *J. Mater. Sci. Mater. Med.* **2010**, *21*, 925–930. [[CrossRef](#)]
46. Ballint, R.; Cassidy, N.J.; Cartmell, S.H. Conductive polymers: Towards a smart biomaterial for tissue engineering. *Acta Biomater.* **2014**, *10*, 2341–2353. [[CrossRef](#)]
47. Bredas, J.; Stroet, B. Polarons, bipolarons, and solitons in conducting polymers. *Acc. Chem. Res.* **1985**, *18*, 309–315. [[CrossRef](#)]
48. Ritger, P.L.; Peppas, N.A. A simple equation for description of solute release II. Fickian and anomalous release from swellable devices. *J. Control. Release* **1987**, *5*, 37–42. [[CrossRef](#)]
49. Thomas, D.; Nair, V.V.; Latha, M.S.; Thomas, K.K. Theoretical and experimental studies on theophylline release from hydrophilic alginate nanoparticles. *Futur. J. Pharm. Sci.* **2019**, *5*, 2. [[CrossRef](#)]

50. Siepmann, J.; Pappas, N.A. Higuchi equation: Derivation, applications, use and misuse. *Int. J. Pharm.* **2011**, *418*, 6–12. [[CrossRef](#)]
51. Kleber, C.; Lienkamp, K.; Rühe, J.; Asplund, M. Electrochemically controlled drug release from a conducting polymer hydrogel (PDMAAp/PEDOT) for local therapy and bioelectronics. *Adv. Health. Mater.* **2019**, *8*, 1–11. [[CrossRef](#)]
52. Hong, D.; Chen, H.X.; Xue, Y.; Li, D.M.; Wan, X.C.; Ge, R.; Li, J.C. Osteoblastogenic effects of dexamethasone through upregulation of TAZ expression in rat mesenchymal stem cells. *J. Steroid Biochem. Mol. Biol.* **2009**, *116*, 86–92. [[CrossRef](#)]
53. Simann, M.; Schneider, V.; Le Blanc, S.; Dötterweich, J.; Zeh, V.; Krug, M.; Jakob, F.; Schilling, T.; Schütze, N. Heparin affects human bone marrow stromal cell fate: Promoting osteogenic and reducing adipogenic differentiation and conversion. *Bone* **2015**, *78*, 102–113. [[CrossRef](#)] [[PubMed](#)]
54. Spatano, L.; Dilgen, J.; Rethere, S.; Spence, A.; Isaacson, M.; Turner, J.N.; Shain, W. Dexamethasone treatment reduces astroglia responses to inserted neuroprosthetic devices in rat neocortex. *Exp. Neurol.* **2005**, *194*, 289–300. [[CrossRef](#)] [[PubMed](#)]
55. Muntero-Rodríguez, J.J.; Ramírez-Sánchez, K.; Valladares-Castrillo, G.; Avendaño-Soto, E.D.; Starbird-Pérez, R. Design and simulation of flexible thin-film electrodes for cell culture stimulation. In Proceedings of the 2020 Latin American Electron Devices Conference (LAEDC), San José, Costa Rica, 25–28 February 2020.
56. Wakkad, E.; Shams, D. The Anodic oxidation of metals at very low current density. Part V\*. *J. Chem. Soc.* **1946**, *1*, 3098–3102.
57. Gómez-Ordóñez, E.; Rupérez, P. FTIR-ATR spectroscopy as a tool for polysaccharide identification in edible brown and red seaweeds. *Food Hydrocoll.* **2011**, *25*, 1514–1520. [[CrossRef](#)]
58. Konermann, L. Addressing a common misconception: Ammonium acetate as neutral pH “buffer” for native electrospray mass spectrometry. *J. Am. Soc. Mass Spectrom.* **2017**, *28*, 1827–1835. [[CrossRef](#)] [[PubMed](#)]
59. Zamora-Sequeira, R.; Alvarado-Hidalgo, F.; Robles-Chaves, D.; Saiz-Ara, G.; Avendaño-Soto, E.; Sánchez-Kooper, A.; Starbird-Pérez, R. Degradation for wastewater treatment using a sensor based on poly (3, 4-ethylenedioxythiophene)(PEDOT) modified with carbon nanotubes and gold nanoparticles. *Polymers (Basel)* **2019**, *11*, 1449. [[CrossRef](#)]

**Sample Availability:** Samples of the compounds are not available from the authors.



© 2020 by the authors. Licensee MDPI, Basel, Switzerland. This article is an open access article distributed under the terms and conditions of the Creative Commons Attribution (CC BY) license (<http://creativecommons.org/licenses/by/4.0/>).

## Annex 9. Paper 3. Smart Porous Multi-Stimulus Polysaccharide-Based Biomaterials for Tissue Engineering



Review

### Smart Porous Multi-Stimulus Polysaccharide-Based Biomaterials for Tissue Engineering

Fernando Alvarado-Hidalgo <sup>1,2,\*,†</sup>, Karla Ramírez-Sánchez <sup>1,3,\*,†</sup> and Ricardo Starbird-Pérez <sup>1,\*,†</sup>

<sup>1</sup> Centro de Investigación en Servicios Químicos y Microbiológicos, CEQUATEC, Escuela de Química, Instituto Tecnológico de Costa Rica, Cartago 159-7050, Costa Rica

<sup>2</sup> Master Program in Medical Devices Engineering, Instituto Tecnológico de Costa Rica, Cartago 159-7050, Costa Rica

<sup>3</sup> Centro de Investigación en Enfermedades Tropicales, CIET, Facultad de Microbiología, Universidad de Costa Rica, San José 11501-2060, Costa Rica

\* Correspondence: f.alvarado@itcr.ac.cr (F.A.-H.); karamirez@itcr.ac.cr (K.R.-S.); rstarbird@itcr.ac.cr (R.S.-P); Tel.: +506-2550-27-31 (R.S.-P)

† These authors contributed equally to this work.

Academic Editor: T. Joan Daou

Received: 2 October 2020; Accepted: 5 November 2020; Published: 13 November 2020



**Abstract:** Recently, tissue engineering and regenerative medicine studies have evaluated smart biomaterials as implantable scaffolds and their interaction with cells for biomedical applications. Porous materials have been used in tissue engineering as synthetic extracellular matrices, promoting the attachment and migration of host cells to induce the in vitro regeneration of different tissues. Biomimetic 3D scaffold systems allow control over biophysical and biochemical cues, modulating the extracellular environment through mechanical, electrical, and biochemical stimulation of cells, driving their molecular reprogramming. In this review, first we outline the main advantages of using polysaccharides as raw materials for porous scaffolds, as well as the most common processing pathways to obtain the adequate textural properties, allowing the integration and attachment of cells. The second approach focuses on the tunable characteristics of the synthetic matrix, emphasizing the effect of their mechanical properties and the modification with conducting polymers in the cell response. The use and influence of polysaccharide-based porous materials as drug delivery systems for biochemical stimulation of cells is also described. Overall, engineered biomaterials are proposed as an effective strategy to improve in vitro tissue regeneration and future research directions of modified polysaccharide-based materials in the biomedical field are suggested.

**Keywords:** biomaterials; porous materials; biomimetic; multi-stimulation; tissue engineering; conductive polymers

#### 1. Introduction

The number of publications related to the tissue engineering field has increased dramatically in recent years, referring to the potential regenerative methods and strategies for almost every tissue and organ of the human body. Progress has been reached by the integration of interdisciplinary research from cell biology, biomaterial sciences, and medical fields [1]. Specifically, tissue engineering involves the design and synthesis of three-dimensional (3D) matrices from biomaterials to provide a structural framework and to facilitate the attachment and migration of host cells, inducing a successful in vitro and in vivo regeneration of tissues [2–4]. Biomimetic 3D scaffolds may allow the control and application of a multi-stimulus to cells, including mechanical, electrical, and biochemical stimulations, in order to trigger specific responses, such as cell differentiation and tissue repair [5–8].

Tissue regeneration is naturally mediated by molecular processes, which direct gene expression to control renewal, restoration, and cell proliferation [9]. Nevertheless, normal regeneration is affected by aging, diseases, or accidents [10,11]. Thus, the increasing incidence of skin, muscle, and bone disorders, suffered by many people around the world, has prompted a critical need to develop engineered strategies to improve the replacement and regeneration of biological materials [11–13]. While many repair techniques have been proposed over recent decades, most of the surgical interventions have been directed toward the treatment of clinical symptoms but none have successfully repaired damaged tissues [14]. Consequently, in recent years, tissue engineering and regenerative medicine studies are focused on using the regenerative abilities of cells, in combination with engineered biomaterials, to create implantable scaffolds for tissue regeneration and repair [1,10].

Porous materials from polysaccharides have been used as extracellular matrices (ECM) in tissue engineering in order to generate diverse types of cell lineages, promoting regeneration [15,16], for instance, in stem cells [17], osteoblasts [18], skeletal muscle cells [19], and endothelial cells [20]. In the biomedical field, aerogels from different sources have found applications as implantable devices, dressings for wound healing, synthetic bone grafts, carriers for different drugs, biosensing, and biomedical imaging [6,21].

Since they were first fabricated in 1932, aerogels have become the subject of great interest for different application fields [22]. Most common aerogel sources are from inorganic or petrochemical-based materials, such as those used to produce silica and graphene aerogels [23,24]. Recently, large efforts have been dedicated to produce aerogels using polysaccharides as raw materials. Relating them with inorganic starting materials and those derived from fossil oil, natural polysaccharides are more sustainable, green, non-toxic [25], biodegradable [26] and they have more abundant natural sources [27]. Several examples of engineering porous materials from polysaccharides have been developed. Starch and alginate aerogels [28,29], starch microspheres [30], and cellulose nanowhiskers [31] are among the different examples found in the literature. From a basic science perspective, the capacity to modulate the biomaterial properties to convey unique material characteristics allows their application in different fields, with biomedical being the most important, from our point of view.

Numerous strategies have been reported to obtain polysaccharide-based aerogels to guide functional restoration to the site of injury. Control of the size and porosity in the scaffold mediates cellular infiltration [32] and facilitates the transport of nutrients [33], oxygen [34], and waste products [35]. Porosity also regulates the vascularization by angiogenesis and cell attachment [30,36]. Mechanical properties of biomaterials, such as stiffness, structure, and topography, are also considered during ECM synthesis, mainly because they can alter the local tissue microenvironments through intracellular and intercellular signaling [7,9,37]. Besides, one of the most relevant applications of polysaccharide-based aerogels is the capability of releasing drugs as controlled delivery systems. The synthetic scaffold acts as a carrier for drug molecules, in order to release them specifically to target cells or tissues and improve their differentiation and regeneration [6,38,39]. Specifically, the combination of polysaccharide-based porous materials with biomolecules is known as a polymer bioconjugate and is a novel strategy used for the fixation of amino acids, nucleic acids, peptides, and carbohydrates to different polymers, in order to improve their application as therapeutics [40]. Alternatively, conductive polymers have been proposed in combination with aerogels as a system for electrical stimulation of cells and tissues in regenerative medicine [5,41].

Our review summarizes the current status of smart 3D scaffold systems based on polysaccharides regarding their production, properties, and potential applications in the biomedical field. Although these topics have been extensively reviewed in the past, our approach will focus on the potential development of biomimetic 3D scaffold systems including the physical, mechanical, electrical, and biochemical properties of modified polysaccharide-based aerogels and cryogels. Moreover, novel research directions of these smart materials, including strategies for the impregnation of drugs and their subsequent release from porous materials, and modification with conductive polymers were covered to be applied in the biomedical field.

## 2. Overview: Polysaccharide-Based Porous Materials

Aerogels are solid, lightweight, and high specific surface area materials with interconnected networks of particles obtained from a wet gel during a process where their liquid phase is removed and replaced with gas without the collapsing of the solid structure [6,22].

Through time, aerogels have been obtained by structuring both organic and inorganic materials. Silica [24,42,43], silica/pre-polymerized vinyl trimethoxy silane (VTMS) composites [44], and graphene-based aerogels [23,45] are among the most used inorganic materials reported for aerogel production. However, despite several relevant features found for inorganic aerogels, biopolymer-based aerogels have been the object of much research lately due to their mechanical properties [46], non-toxicity [25], and biocompatibility [21], all desirable properties in systems to be used in biomedical field [47].

Polysaccharide-based aerogels were reported first by Kistler [22], using cellulose, nitrocellulose, gelatin, agar, and egg albumin. More recent research has reported the obtention of aerogels from polysaccharides such as chitosan [48], chitosan/alginate [49], cellulose [50], starch [13,30,51–53], starch/*s*-carrageenan (*s*C) [53], and pectin [27].

Considering that polysaccharides possess abundant natural sources from which they can be obtained [27], along with renewability and non-toxicity, they are excellent raw material candidates for aerogel processing regarding circular economy principles, relying on renewable raw material or energy sources [25,54].

### 2.1. Processing Strategies for Polysaccharide-Based Aerogels

Diverse strategies have been used to obtain polysaccharide-based aerogels. The sol-gel method is commonly reported as an initial step in the processing pathways for organic or inorganic materials [28]. In the sol-gel process, a hydrogel formation is induced by crosslinking of the base material. Once the hydrogel is formed, it is necessary to select the drying method to be used; materials obtained from supercritical drying are commonly known as aerogels, whereas materials dried by freeze drying (lyophilization) are known as cryogels [21]. Figure 1 illustrates the scheme for supercritical drying and freeze drying, the most widely used methods in processing porous materials [21].

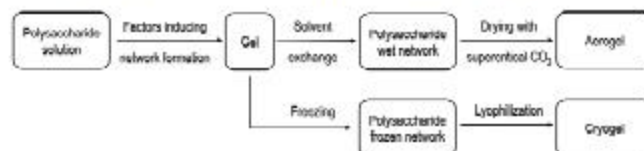


**Figure 1.** Pathway for porous materials produced by supercritical drying as well as freeze drying. Modified from [55] under Creative Commons attribution license.

#### 2.1.1. Processing Using Supercritical Fluid Technology

The usage of supercritical fluid technology allows the material design with different composition, morphology, porosity, and linear architecture [56]. In addition, processing with supercritical fluids (SCFs) leads to a solvent-free end-product with high purity. This environmentally friendly feature has been noted by other studies. In fact, SCFs have been regarded as “the green solvents for the future” since they compress different ecological benefits, an emphasis is made on their low energy consumption [21,57].

Carbon dioxide ( $\text{CO}_2$ ) is the most widely used supercritical fluid, in part due to the mild operating conditions, 7.38 MPa and 304 K [56]. Supercritical drying (SCD) avoids the formation of the vapor–liquid interface that occurs upon solvent evaporation. When evaporation of the solvent occurs, the capillary pressure gradient on the pore walls may reach up to 100–200 MPa [28]. Aerogels processed

by means of SCD tend to show a mesoporous structure (pores of a 2–50 nm diameter) and thus require a templating technique for inducing the formation of macropores [56]. Finally, SCF technology has been applied not only to obtain porous materials but also as a strategy for the sterilization of polymeric scaffolds from aerogels [13].

### 2.1.2. Cryogels Obtained by Freeze Drying

Freeze drying (FD), or lyophilization, is a drying process in which the solvent or the medium of suspension is crystallized at low temperatures and is thereafter sublimated from the solid state directly into the vapor state [58]. It is reported as a simple, environmentally friendly and economic technique for producing highly porous cryogels with reduced shrinkage [21].

Significant advantages of using FD during cryogel synthesis are that the whole conversion of raw materials and the recycling of water without pollution or volatile organic compounds problems are achieved [59]. High safety derived from its straightforward operation is an important feature that has been remarked in the literature [27]. Nevertheless, one important drawback reported for freeze drying is that the process takes several hours to be completed [23]. In addition, freeze-dried materials tend to have larger macroporosity (pores >50 nm diameter) than SCD-processed materials [21].

Freeze drying requires freezing the hydrogels, transforming all the liquid that fills the interconnected 3D structure, to solid. Then, at low pressures, the sublimation of the solid solvent is promoted, avoiding the formation of the vapor–liquid interface [51,59]. The morphology of the porous structure is determined by the nucleation and ice crystal growth process of the gel solution [27], producing cryogel pores due to sublimation of the ice crystals [60]. Large ice crystals are obtained with low nucleation rates; this is reached by using small subcooling temperatures, as close to the equilibrium state as possible, between solution and ice crystals (0 °C) [58].

Two important steps are found for the crystallization process: nucleation and ice crystal growth [27]. Since pores are formed due to the sublimation of the ice crystals [60], the crystal morphology has a direct effect on the final pore morphology of the cryogel. The crystal morphology can be related to the freezing or pre-freezing conditions (temperature and rate), additives, suspended solids [60], or the initial material concentration [27]. In addition, increasing the pressure at the freezing phase can shorten the cooling time and form small regular ice crystals [27].

Direct comparison between the porous materials obtained by SCD or by FD results in an important specific surface area decrement for the freeze-dried cryogels [51]. However, cryogels have shown porosity values equal to or higher than SCD aerogels, with an important macropore fraction that may be suitable for different applications where macroporosity is required. See detailed information in Table 1.

**Table 1.** Properties reported in different research studies for porous materials from biopolymers.

Raw Material	Fabrication Method	Specific Surface Area (m <sup>2</sup> /g)	Porosity (%)	Reference
Corn starch	scCO <sub>2</sub>	130–183	80–89	[31]
	scCO <sub>2</sub>	102–274	N.R.	[61]
	scCO <sub>2</sub>	221–234	85–90	[62]
	scCO <sub>2</sub>	79–87	N.R.	[32]
	scCO <sub>2</sub>	183–197	61–73	[33]
	FD	0.6–7.7	>80	[33]
	scCO <sub>2</sub>	223–247	87	[33]
	scCO <sub>2</sub>	313–362	N.R.	[63]
	scCO <sub>2</sub>	254	N.R.	[64]
Wheat starch	scCO <sub>2</sub>	370	N.R.	[65]
	scCO <sub>2</sub>	52.6–57.9	N.R.	[66]
Pea starch	scCO <sub>2</sub>	34.7–60.9	91–95	[66]
	scCO <sub>2</sub>	204–230	84–92	[62]
Potato starch	scCO <sub>2</sub>	221	N.R.	[64]
	scCO <sub>2</sub>	42–70	N.R.	[67]
Starch/κ-carrageenan	scCO <sub>2</sub>	85–86	N.R.	[64]
	scCO <sub>2</sub>	194–231	78–85	[33]
κ-carrageenan	scCO <sub>2</sub>	< 230	N.R.	[68]
Chitosan	scCO <sub>2</sub>	>250	>96	[48]
Cellulose	scCO <sub>2</sub>	287–303	92–96	[36]
	FD	297	96.4	[36]
	scCO <sub>2</sub>	20–246	91–99	[69]
Alginate/chitosan	scCO <sub>2</sub>	127.4–192.3	N.R.	[49]
Alginate composites	scCO <sub>2</sub>	200–800	N.R.	[70]
Whey protein isolate	scCO <sub>2</sub>	14–447	N.R.	[71]
	FD	<5	N.R.	[71]
Poly (ε-caprolactone)	scCO <sub>2</sub>	N.R.	54–56.8	[72]

N.R.: Not reported; scCO<sub>2</sub>: Supercritical CO<sub>2</sub>; FD: Freeze Drying.

### 3. Polysaccharide-Based Porous Materials for Tissue Engineering

In recent years, tissue engineering and regenerative medicine studies have been based on the combination of specific types of cells and 3D porous scaffolds to induce a successful *in vitro* regeneration of diverse tissues [2–4].

The main efforts on engineered ECM in the biomedical field have been focused on the use and stimulation of pluripotent stem cells, which are special cells that have the ability to perpetuate themselves through a mechanism of self-renewal and to generate diverse types of cells through differentiation processes [15–17]. Nevertheless, osteoblasts [18], skeletal muscle cells [18], and endothelial cells [20] have been also studied.

#### 3.1. Polysaccharide-Based Porous Materials as Extracellular Matrices

An extracellular matrix is an organized network composed by a mixture of cellular and non-cellular components. It plays an important role in tissue and organ morphogenesis, cell function, and structure maintenance. The biochemical and mechanical stimulus that cells receive from the matrix influences their growth, migration, differentiation, survival, and homeostasis [73].

Aerogels, as porous 3D matrices, possess a nanostructure that is able to mimic the extracellular matrix of the natural tissue, providing a favorable environment for the regeneration of tissues and organs [6,74]. Coupled with high porosity, low densities, and high inner surface areas, porous materials can provide appropriate morphology engineering, opening the possibility for their application as synthetic scaffolds for tissue engineering [32].

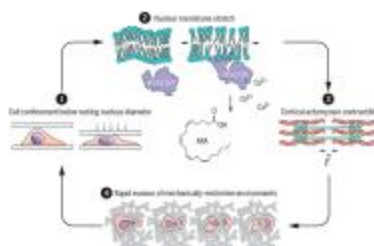
A scaffold acts as a template for new tissue formation [75] and its 3D structure guides the proliferation and colonization of cells, promoting tissue growth [56]. An ideal synthetic ECM should

exhibit a highly open and uniform porosity, over 80%, with micro- and mesopores that enable cell attachment and macropores for proper vascularization [56]. The configuration of the scaffold topology is critical in controlling cellular function, it should match the endogenous topology of the cell membrane in order to enhance signaling and function [56].

Nowadays, regenerative medicine is focused on the evaluation of novel skeletal muscle regeneration strategies, which involve the prefabrication of muscle tissues *in vitro* by differentiation and maturing of muscle precursor cells on a scaffold, providing the required environment for myogenic differentiation of the cultured cells [76]. Researchers are studying the incorporation of products obtained from cellular metabolism in synthetic ECMs. These materials are mainly constituted of glycosaminoglycans, a group of polysaccharides that can modulate cell activity by mimicking aspects of the *in vivo* extracellular environment, providing important roles in cell signaling, proliferation, and differentiation through their ability to interact with ECM proteins and growth factors [77–81]. Hyaluronic acid, heparan sulfate, and heparin are the most used glycosaminoglycans in synthetic ECMs, mainly to direct the differentiation on mesenchymal stem cells (MSC) [82,83].

The synthesis of alginate hydrogels for platelet-rich plasma encapsulation as a coating for polylactic acid porous devices is another strategy used to improve cellular responses on synthetic ECM, the hydrogel system allows for better cellular integration and influences the vascularization into the membrane after skin implantation of the device, and the access to nutrients and growth factors was also improved with the engineered hydrogel. Platelet-rich plasma hydrogels could also support oxygenation of cells, avoiding hypoxia immediately post-transplantation [84,85]. In a similar study, calcium peroxide (CPO) was used during the synthesis of a gelatin methacryloyl bioprinted scaffold to achieve improved cellular oxygenation and increase fibroblast viability under hypoxia conditions [86].

The spatial arrangement, porosity, biocompatibility, and proper scale of the ECM are some of the most important features that must be adjusted for use in nervous tissue, skin, bone, and muscle [76]. Nevertheless, several other factors, such as mechanical properties and chemical modification of scaffolds, significantly influence cellular behavior [5,87]. For example, recent studies have shown that the cell nucleus works as a fast mechanical respondent in cell contractility events because of the three-dimensional extracellular matrix restriction environment, inducing deformation and the movement of cells through the activation of cytosolic phospholipase A<sub>2</sub> and arachidonic acid, which regulate myosin activity [88,89] (Figure 2).



**Figure 2.** Schematic representation of nuclear deformation and stretching of the nuclear envelope after cell compression (1), which cause calcium release, phospholipase A<sub>2</sub> activation, and arachidonic acid production (2), for the regulation of actomyosin (3) and the increasing of cell migratory capacity through the 3D matrix (4). Reproduced from [89] under Science Copyright Clearance Center (CCC) license.



### 3.2. Influence of the Mechanical Properties of the Scaffold in Cells and Tissues Behavior

The main goal of tissue engineering and regenerative medicine is to create strategies for replacing defective tissue. The use of polymeric scaffolds as extracellular matrices tries to mimic the *in vivo* host conditions to restore or improve the regeneration of damaged tissues. An extracellular matrix requires not only pore size control to induce cell adhesion and the ingress of nutrients and oxygen but also the incorporation of signal molecules, such as growth and differentiation factors, as well as a proper matrix architecture and mechanical properties to keep the implanted cells alive [46,90–94].

The mechanical characteristics of a scaffold for *in vitro* or *in vivo* cell studies may ultimately impact how the hosted tissue responds to the scaffold [87]. In this regard, the architecture, chemistry, topography, and physical properties of the employed scaffold as an ECM influence the structure and function of the surrounding tissue. Cells are constantly subjected to physical forces from their microenvironment. Mechanical properties of the porous materials are indispensable to determine the viability of a tissue and play a crucial role in cellular phenotype and homeostasis [95]. There are several types of cells that respond to a mechanical stimulus. The mechanoresponsive cells include chondrocytes [88], cardiomyocytes [94], osteoblasts [96], muscle cells [97], endothelial cells [98], stem cells [7], and other tissue connective cells.

Atomic force microscopy (AFM) analysis, magnetic resonance elastography (MRE), shear rheometry, micropipette aspiration, and microindentation are some techniques commonly used to determine systematic cell responses, induced by mechanical properties of scaffold [95]. These methods cause the compression, bending, twisting, and stretching of the scaffold [99–101], inducing specific cellular responses.

Cells may sense physical cues, such as osmotic pressure, shear force, and compression loading, as well as architecture, rigidity, and other several properties of the ECM, through a process known as mechanotransduction [95]. Thus, mechanotransduction corresponds to the cell capacity to transform a mechanical stimulus into biochemical signals. There are surface proteins in cell membranes which detect a force differential and then amplify and propagate this mechanical signal to elicit a change in cell behavior [37,95].

Compression and shear stress, caused by the synthetic ECM in a cell culture, transfer mechanical stimulation to the cells and enhance their biochemical signaling. The upregulation of gene expression and the changes in cellular metabolism during mechanical stimulation are regulated by mechanically sensitive surface receptors on cell membranes. There are several proteins related with the mechanotransduction to biochemical events, integrins, specifically  $\beta 1$  and  $\alpha 5 \beta 1$  integrins, are the best proteins studied so far [37].

Scaffold stiffness has been shown to have a significant impact on numerous cells and their fate, such as cell adhesion, cytoskeleton rearrangement, cell migration, stem cell differentiation, and muscle cell contractility [87]. The stiffness of an ECM in 2D cell cultures may influence the differentiation pattern of a same cell type; it has been reported that a soft matrix (0.1–1 kPa) promotes neurogenic differentiation, matrices with a medium stiffness (8–17 kPa) promote myogenic differentiation, and matrices with high stiffness (25–40 kPa) promote the osteogenic differentiation of mesenchymal stem cells [9]. Several authors have reported that the stiffness of a synthetic ECM induces mechanical stimulation of cells and the subsequent expression of cellular differentiation markers [93], tissue organization [97], causes the synthesis of extracellular matrix components [93], changes cell morphology, and improves their adhesion to synthetic scaffolds [93,98]. Additionally, the positive inotropic and chronotropic responses to both ion concentration (i.e., calcium,  $Ca^{2+}$ ) and temperature after mechanical stimulation of cardiomyocytes are also reported [94].

Complexity of the mechanotransduction induced by integrins is multifaceted as the proteins can form 24 possible functional distinct dimers and each dimer forms diverse complexes with multiple intracellular adaptor proteins to dictate the interplay between biochemical and cytoskeletal elements to determine their contribution to cellular mechanoresponses [37,95]. Nevertheless, it is well known that efficient force transfer and associated cytoskeleton changes are correlated with

focal adhesion formation, as defined by the recruitment of talin, vinculin, and  $\alpha$ -actinin to the stimulated integrin; these focal adhesion proteins form the molecular bridge that physically interlinks integrins with actin microfilaments [9,92,102].

Cytoskeletal changes caused by mechanical stimulation of cells are influenced by several biochemical pathways. It has been reported that maturation of focal adhesions causes activation of focal adhesion kinase (FAK); the scaffold protein, associated with adhesion plaque, triggered the Rho-associated protein kinase cascade (ROCK), which enhanced cellular tension through engagement of actomyosin contractility [95,103]. ROCK protein involves several downstream signals, including extracellular signal-regulated kinases (ERKs) and the hippo pathway, which is related with yes-associated protein 1 (YAP1); both biochemical pathways translocate some activated proteins to the nucleus and associated with transcriptional factors to regulate cell proliferation, tissue growth, and differentiation, as well as cell migration [89,104,105]. The chronic cellular tension reinforces these downstream signaling pathways to potentiate the production of ECM and ECM remodeling proteins that stiffen the local microenvironment and reinforce mechanosignaling [95].

Experiments related with the mechanical stimulation of cells have been carried out since 1938, when Glücksmann studied endosteal cells from embryonic chick tibiae [106]. Cells were grown on substrates of explanted intercostal muscle, to which pairs of neighboring ribs were left attached [106]. After several days, cells were compressed when the ribs were drawn near toward one another as the muscle tissue degenerated. Table 2 summarizes the main strategies to induce mechanical stimulation of synthetic ECM and their effect in cultured cells.

The study of mechanical properties of extracellular matrices is important to ensure resistance of cultivated cells to *in vivo* stress where the matrix is used to replace damaged tissue [110,111]. Cellular responses depend on the magnitude and duration of the stimulus and high pressures may cause damage to the cell membrane and nucleus, followed by inflammatory reactions due to tissue breakdown *in vivo* [101]. Additionally, stiffness, roughness, and viscoelasticity are important in directing the immune response of cells. There are several T cell receptors that act as mechanical sensors, enabling the T cells to discriminate between a wide range of stiffness found in the body and respond accordingly [9]. Thus, hydrogels with higher stiffness stimulate the production of both pro- and anti-inflammatory cytokines, in contrast with low stiffness hydrogels, where the inflammatory response is suppressed and results in an overall lower foreign-body reaction *in vivo* [9]. The effect of the substrate mechanical properties on the *in vitro* response of macrophages has been also studied using poly(ethylene glycol) hydrogels (PEG) [87]. Results showed that stiffness did not impact the macrophage attachment; nevertheless, it elicited differences in their morphology.

The mechanical characteristics of scaffolds can be adjusted using adequate dynamic biomaterials in order to create matrices with an appropriate stiffness to direct specific cellular responses. Mechanical properties of synthetic scaffolds are also used to design stimulation protocols to induce the controlled release of responsive drugs potentially used for tissue regeneration.

### 3.3. Polysaccharide-Based Porous Materials as Scaffolds for Electrical Stimulation of Cells

Another research field of interest is focused on the preparation of electrical systems to induce specific cellular responses. Diverse tissues (e.g., nerve, muscle, and glandular) make use of endogenous electric fields (EF) to transmit electrical signals. The endogenously-generated EF exists in both the cytoplasm and extracellular space [112]. Ionic currents and EFs in living cells play critical roles in important biological processes as they generate electromotive force, maintain a required electric potential, and allow some cellular functions [113,114]. These bioelectric signals are generated by gap junctional connections and ion channels or pumps moving ions, mainly potassium ( $K^+$ ) and chloride ( $Cl^-$ ), across the membrane [113,115], and the regulation in cellular physiology is induced by pH gradients, specific ion flows, and changes in transmembrane potential [116].

**Table 2.** Used methods to induce mechanical stimulation of cells in synthetic extracellular matrices (ECM).

Raw Material	Mechanical Test	Result	Reference
Gelatin/hydroxyapatite cryogel	Compressive mechanical stimulation of cryogels for 34 days in a bioreactor containing 150 mL of cultured medium at 30% compression strain.	Mesenchymal stem cells were attached to the scaffold and a higher extent of osteogenic differentiation was obtained after compression.	[7]
Self-assembled peptide hydrogel (arginine, leucine, aspartic acid, and alanine)	The hydrogel containing cells was placed into a hand-scrutinized stretch device for 120 h.	Smooth muscle cells resulting in a tight adhesion in the porous structure and a linear cell proliferation rate were reported.	[64]
Poly(lactic-co-glycolic acid) fiber coated with polypyrrole	The electrical stimulation of the matrix induced their volume modification, causing changes in the mechanical strain.	The direct dual electrical and mechanical stimulation of the pluripotent stem cells cultured in the scaffold caused a faster expression of cardiac myocytes genes, important for myocardial regeneration.	[107]
Collagen matrix reinforced with rings of electrospun silk fibroin mat	Dynamic stimulation with pulsatile or laminar flow. Pulsatile flow was induced with a gear pump which supply a steady flow (75 mL/min) in series with a pulsatile manifold. Laminar flow test carried out of steady flow of 75 mL/min.	Chondrogenic differentiation of MSCs was observed in the presence of chondrogenic supplements in laminar flow cultures. Pulsatile flow resulted in preferential cellular orientation, as dictated by dynamic circumferential strain, and induced MSC contractile phenotype expression.	[108]
Silicon tubes with inner surfaces modified with collagen type I solutions	Cells cultured on collagen-coated silicon tubes were exposed for 24 hours to the shear stress created when culture medium passes through the tube.	Mechanical stimulation caused by shear stress on adipose-derived mesenchymal stem cells depicted significantly higher gene expression of osteoblast and adipogenic lineages. Moreover, mechanical stimulus induced endothelial differentiation after the addition of VEGF on cultured medium.	[8]
Microcracked hydroxyapatite substrates	Bending the top surface of the cracked substrate in a piezoelectric actuator using a force of 50 N at 5 Hz for 150 s.	Piezoelectricity caused by mechanical stimulation on a hydroxyapatite substrate induced apoptotic responses on osteoblasts and osteocytes. Apoptosis was followed by proliferation of the cells adjacent to the crack, better attachment on the substrate, and an increased expression of osteocyte markers.	[109]

Currently, exogenous electrical stimulation of cells is a widely used method to improve their biological functions. Many authors have reported the use of nerve [117], bone [118], muscle [119], and neural stem cells [120], because their extensively recognized piezoelectric characteristics make them attractive for research on the role of exogenous electrical stimulation.

Coupling of an electromagnetic field with a live cell can occur via field interaction with charged molecules and proteins in the cell membrane [114]. The application of an electrical stimulus to induce cellular responses depends mainly on the level and nature of the electric potential or current applied, the frequency of the stimulus, and the type of cell studied [115]. It is reported that the application of the EF in a culture medium affects the migration [121], orientation [122], proliferation, and differentiation of cells [123,124]. Nevertheless, in most cases, it is used specifically to revive damaged or disabled tissues in the neuromuscular system as well as to accelerate the healing of injured musculoskeletal tissues, such as bone, ligament, and articular cartilage [132].

In this regard, biomaterials may receive considerable attention for their influence on cellular behaviors, ability to mimic biological functions, and, more recently, as electronic conductive systems with a potential use as tissue engineering scaffolds [5,125].

Some electroactive materials, such as conductive polymers (CPs) (e.g., poly(3,4-ethylenedioxythiophene) (PEDOT)), which are a special class of polymeric materials that present electric and ionic conductivity, are currently being studied in combination with aerogels or cryogels as a promising field in regenerative

medicine (Figure 3). Nevertheless, in the past, research studies have extensively used this kind of polymer to create organic conductive interfaces, neuroprosthetic devices, neural probes, and controlled drug-delivery systems [5,41,126].

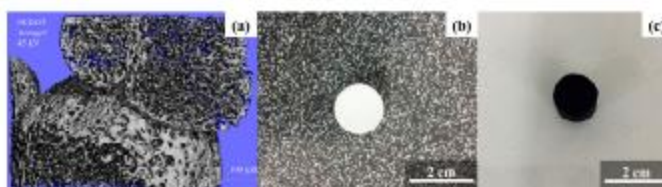


**Figure 3.** Porous material microtomography (micro-CT) image (a) and aerogel images before (b) and after conductive polymer (i.e., poly(3,4-ethylenedioxythiophene) (PEDOT)) modification (c). Reproduced from [52,53] under Elsevier Copyright Clearance Center (CCC) licenses.

Conductive polymers can be structured with porous systems using different techniques [127–129]. Starch and starch/ $\kappa$ -carrageenan aerogels have been used as templates for the obtention of nanoporous conductive materials [52,53]. In the biomedical field, conductive nanoporous materials have been applied not only as physical support but also as a medium to provide electrical stimulation of a cell culture. Electrical stimulation in neural cells has shown great potential for function restoring and wound healing [130].

On the other hand, the incorporation of anionic drugs and  $\kappa$ -carrageenan on the structure of starch porous materials is particularly interesting since both compounds may act as dopant agents for the conductive matrix, as it was shown recently [39,53,131]. Dexamethasone, a well-known glucocorticoid anionic drug, has recently been the object of research from an electrochemical point of view, regarding its doping properties on conductive matrices [132] and for its ability to be released by electrochemical stimulation from a PEDOT/ $\kappa$ -carrageenan film [39]. The above opens the possibility to create scaffolds from conductive porous materials and the incorporation of specific drugs in their structure to be applied as stimulation systems in tissue engineering.

#### 3.4. Polysaccharide-Based Porous Materials as Drug-Delivery Systems

One of the main approaches and most relevant applications of biopolymer-based aerogels is their use as drug-delivery systems [6,38]. The application of these materials as controlled drug-release matrices has gained interest in the last years due to aerogel properties, such as its high surface area, high porosity, and biocompatibility [38]. Aerogels can act as a carrier for bioactive compounds, showing high loading capacity, enhanced stability upon storage, and accelerated drug release, if required [48]. Along with the high loading capacity, biopolymer-based aerogels also show an improved dissolution rate of poorly water-soluble drugs [6].

The biocompatibility of natural polymers along with the outstanding performance of aerogels as carriers for active compounds, such as drugs, have promoted the systems as scaffolds in body implants to accelerate tissue formation by providing a suitable porous structure that promotes cell colonization [62,133]. Diverse authors have also studied the incorporation of drugs and growth factors to promote the attachment, proliferation, and differentiation of cells, in order to provide both substitutes for damaged tissues and therapeutic schemes that reduce post-implantation inflammation and infections [12,133–135].

Controllable drug-release systems may be categorized as mechanical methods, which are mainly in vivo implantable pump delivery systems built from biocompatible nanomaterials [136,137], and as polymeric drug delivery systems. The last one makes use of biopolymers, in which the

delivery of drugs is mainly dominated via diffusion and recently by electrochemical methods [137]. Hence, the incorporation of drugs within these kinds of porous scaffolds has been studied previously for osteogenic differentiation, bone repair activity, and the stimulation of neural tissues [126,133].

#### 3.4.1. Diffusive Phenomena on the Controlled Release of Drugs on Polysaccharide-Based Aerogels

Different methods for drug impregnation or loading can be found in literature regarding porous materials from polysaccharides. Supercritical technology employing  $scCO_2$  has been defined as the most innovative technique for producing polymer/drug composite systems for pharmaceutical applications [138]. By means of supercritical fluid technology, the impregnation of aerogel particles with drugs such as ketoprofen was achieved [62]. This process consists of placing aerogel particles and ketoprofen in a closed autoclave under agitation; the ketoprofen was dissolved in  $scCO_2$  and adsorbed in the aerogel matrix [62]. The same procedure was reproduced for obtaining poly( $\epsilon$ -Caprolactone) (PCL) scaffolds loaded with ketoprofen [72] and for alginate-based aerogel microparticles for mucosal drug delivery [38]. In addition, maize starch aerogels and calcium alginate aerogels were impregnated with different non-steroidal anti-inflammatory drugs, such as nimesulide, ketoprofen, and diclofenac sodium [138].

Supercritical  $CO_2$  was also applied in the impregnation of starch and sodium alginate aerogels with five different active compounds, namely loratadine, ibuprofen, rifabutin, dihydroquercetin, and artemisinin, showing enhanced releasing times as well as double bioavailability in some drug-aerogel systems [139]. In addition, this research concludes that the affinity between the aerogel and the active substance must be high so that the active compound loading will be high enough to provide an increase in the dissolution rate and bioavailability [139].

Another method for loading aerogel particles was reported by mixing the active compound (Vancomycin) with a chitosan solution in different weight ratios, thus obtaining vancomycin-loaded chitosan aerogel particles, which are proposed as a system for fast local administration of the antibiotic for wound dressings [48]. A similar procedure was performed by [67], where mesoporous starch aerogels were loaded with celecoxib by adsorption during the solvent exchange steps.

Three steps are considered for the diffusion model: first, the film diffusion; the second step is the slowest, thus controlling the kinetics of the phenomenon, and it is called intraparticle diffusion; finally, the last step is the adsorbate release on adsorbent active sites [140]. Several works have been published regarding the release of drugs by means of diffusion phenomena [38,48,62,71,72,139,141]. The first mechanism when a drug-loaded polymeric material meets an aqueous solution is the filling of the pores near the surface; then, drug diffusion is initiated by the dissolution of the solute in the water-filled pores and the continuous diffusion in water [142]. Through time, the polymeric network starts swelling, inducing several structural changes that are affected by the cross-linking density and the degree of crystallinity of the 3D network. From the swelling of the polymer, a new diffusion starts through the swelled polymer structure [142]. By analyzing the release profile of drugs, conclusions can be obtained on whether the kinetics follow a Fickian or non-Fickian diffusion profile [143,144].

Innovative drug delivery systems are not only studied to improve cellular responses in different tissues but as a strategy that develops platforms and nano-scale devices for selective delivery of therapeutic small drug molecules to the cells or tissues of interest, for the maintenance of appropriate doses, and to improve individual therapy. To meet this demand, many drugs have been reformulated in new drug delivery systems to provide enhanced efficiency and more beneficial therapies [136,137].

#### 3.4.2. Controlled Drug Release by Electrical Stimulation Employing Conductive Porous Materials

In order to prevent the negative effects resulting from exposure to high dosages of drugs, local electronically-controlled release of pharmaceutical compounds from implantable devices appears as a promising option [145]. Drugs anchored inside the conductive materials have been reported using supercritical technology and electropolymerization [126,146].

Electrochemical methods involve the use of conductive polymers, which are electrochemically oxidized during the polymerization processes, generating charge carriers, and, thus, allowing ionic drugs' impregnation based on electrostatic interactions [147]. There are two main electrochemical methods to induce the immobilization of drugs. In the first one, an ionic drug (preferably anionic) acts as a doping agent and its anchoring proceeds simultaneously with the process of matrix formation, commonly named one-step immobilization or *in situ* immobilization [146,148,149]. Drug fixation is the result of the ion-exchange processes during polymer oxidation. Ionic drugs can serve as counter-ions for the positively charged centers in the growing polymer chain [149]. Anti-cancer drugs, anti-inflammatory compounds, and hormones have been fixed on conductive materials using one-step immobilization, mainly for the development of neural devices [150–152].

The second method corresponds to the two-step or *ex situ* immobilization. The incorporation of the drug is carried out after the synthesis of the matrix, through ion exchange processes taking place at their surface. First, the polymer film is synthesized from a solution consisting of the monomer and a small ionic molecule as doping agent, without the drug. The obtained film is later reduced and oxidized by an electrical stimulus [148,149]. Reduction induces the removal of the dopant from the film; meanwhile, the drug, which acts as the second doping agent, is incorporated during the process of matrix oxidation [149]. This approach allows to prevent the interference of drugs during the growth of polymer matrix and their subsequent release does not have much impact on their physicochemical properties [148,149].

Related with the above, some strategies of drug fixation on conductive polymers using two different doping agents have been reported [39,149,153]. The anti-inflammatory drugs dexamethasone and  $\kappa$ -carrageenan were anchored simultaneously during PEDOT film formation, using *in situ* immobilization. After film oxidation,  $\kappa$ C was maintained on the matrix, granting the film greater stability and integrity even after drug release [39].

Drug delivery is caused by electrochemical stimulation of the conductive matrix, which induces the oxidation and/or reduction of the film. By applying a negative potential, the polymeric matrix is reduced and the cationic charge of the polymer backbone is neutralized, causing the release of the anionic drug by electrostatic mechanisms [148]. In a similar procedure, applying negative and positive cyclic potentials induces the reduction and oxidation of the polymeric film, respectively; meanwhile, the matrix experiences expansion and contraction, which force the release of the drug. Although cyclic stimulation allows a greater amount of drug release in comparison with other methods, some authors have reported that the application of the stimulus may cause delamination, cracks, and breakdowns of the matrix, mainly in one-step immobilization systems [126,154,155].

The controlled release of drugs using electrical stimulation from conductive polymer films [39,126,151] opens the door for a different approach regarding the application of polysaccharide aerogels on drug delivery. Since these materials can be coated with an electrically conductive material while incorporating active compounds, these composites may be used in the controlled release of bioactive molecules by electrical stimulation [156,157]. These biochemical release systems are the main focus of several research groups and further investigations should follow this path in order to promote smart scaffolds that merge mechanical, electrical, and biochemical stimulation processes, mimicking the *in vivo* ECM conditions, in order to promote specific cell behavior, as shown in Figure 4.

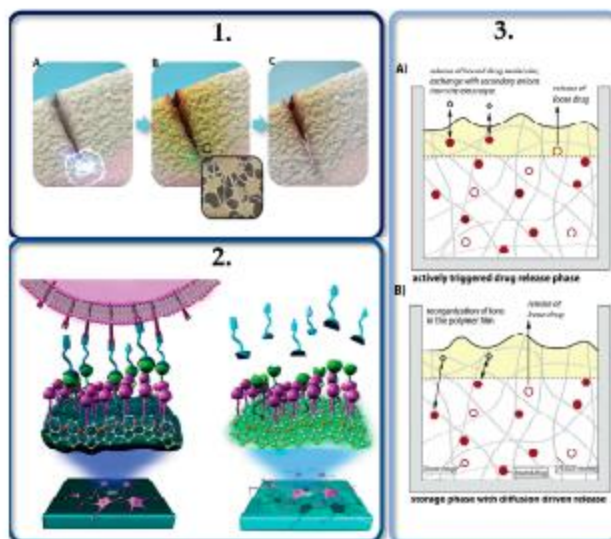


**Figure 4.** (1) Fluxoelectricity induced by mechanical stimulation (A) plays an important role in bone repair and remodeling by inducing osteoblasts migration (B) and mineralization (C). Reproduced from [109] under Creative Commons Attribution License. (2) Electrical communication and redox-triggered interaction between neurons and (PEDOT) matrices functionalized with hydroquinone electroswitches and phosphorylcholine zwitterions. (3) Schematic representation of the active drug-delivery triggered by an electrical stimulus (A) and passive drug-release induced by diffusion processes from a conductive polymeric matrix (B). Reproduced from [151,158] under Elsevier Copyright Clearance Center (CCC) licenses.

#### 4. Conclusions

The current status of biomimetic scaffold systems based on polysaccharides has been reviewed regarding multi-stimulation, mechanical, electrical, and biochemical, in order to trigger specific responses in cells during growth and differentiation, specifically in the biomedical field. Some details of their production and properties have been summarized, including modification with conductive polymers and strategies for controlled drug release from porous materials, such as aerogels. Therefore, future studies of modified polysaccharide-based aerogels for tissue engineering could consider promoting physical, mechanical, electrical, and biochemical multi-stimulation with the aim to mimic *in vivo* conditions.

**Author Contributions:** Conceptualization, F.A.-H. and K.R.-S.; methodology, F.A.-H. and K.R.-S.; validation, F.A.-H., K.R.-S. and R.S.-P.; formal analysis, F.A.-H., K.R.-S. and R.S.-P.; investigation, F.A.-H., K.R.-S. and R.S.-P.; resources, R.S.-P.; data curation, F.A.-H., K.R.-S. and R.S.-P.; writing, original draft preparation, F.A.-H. and K.R.-S.; writing, review and editing, F.A.-H., K.R.-S. and R.S.-P.; visualization, F.A.-H., K.R.-S. and R.S.-P.; supervision, R.S.-P.; project administration R.S.-P.; funding acquisition, R.S.-P. All authors have read and agreed to the published version of the manuscript.

**Funding:** This research was funded by Vicerrectoría de Investigación from Instituto Tecnológico de Costa Rica (VIE-ITCR), grant number 5402-1360-4401 and the Ministerio de Ciencia, Tecnología y Telecomunicaciones de Costa Rica (MICTT), grant number FI-038B-19.

**Acknowledgments:** The authors would like to thank the Centro de Investigación y Extensión en Materiales (CIEMTEC) and the Centro de Investigación en Biotecnología (CIB) from Instituto Tecnológico de Costa Rica. Aerogels COST action (CA18125). F.A.-H would like to thank Carlos A. García-González for his mentoring on aerogel processing and characterization.

**Conflicts of Interest:** The authors declare no conflict of interest.

## References

- Dhandayuthapani, B.; Yoshida, Y.; Maekawa, T.; Kumar, D.S. Polymeric scaffolds in tissue engineering application: A review. *Int. J. Polym. Sci.* **2011**, *2011*, 200602. [\[CrossRef\]](#)
- Stratton, S.; Shelke, N.B.; Hoshino, K.; Rudraiah, S.; Kumbhar, S.G. Bioactive polymeric scaffolds for tissue engineering. *Biomater. Mater.* **2016**, *1*, 93–108. [\[CrossRef\]](#) [\[PubMed\]](#)
- Santoro, M.; Shah, S.R.; Walker, J.L.; Mikos, A.G. Poly(lactic acid) nanofibrous scaffolds for tissue engineering. *Adv. Drug Deliv. Rev.* **2016**, *107*, 206–212. [\[CrossRef\]](#) [\[PubMed\]](#)
- Jo, H.; Sim, M.; Kim, S.; Yang, S.; Yoo, Y.; Park, J.-H.; Yoon, T.H.; Kim, M.-G.; Lee, J.Y. Electrically conductive graphene/polyacrylamide hydrogels produced by mild chemical reduction for enhanced myoblast growth and differentiation. *Acta Biomater.* **2017**, *48*, 100–109. [\[CrossRef\]](#) [\[PubMed\]](#)
- Aznar-Cervantes, S.; Pagan, A.; Martínez, J.G.; Bernabeu-Escápez, A.; Otero, T.F.; Meseguer-Olmo, L.; Paredes, J.L.; Cerdas, J.L. Electrospun silk fibroin scaffolds coated with reduced graphene promote neurite outgrowth of PC-12 cells under electrical stimulation. *Mater. Sci. Eng. C* **2017**, *79*, 315–325. [\[CrossRef\]](#) [\[PubMed\]](#)
- García-González, C.A.; Budtova, T.; Durães, L.; Erkey, C.; Del Gaudio, P.; Gurikov, P.; Koebel, M.; Liebrner, F.; Neagu, M.; Svirimova, I. An opinion paper on aerogels for biomedical and environmental applications. *Molecules* **2019**, *24*, 1815. [\[CrossRef\]](#) [\[PubMed\]](#)
- Shalimon, K.T.; Liao, H.; Kuo, C.; Wong, C.; Li, C.; Mini, P.A.; Chen, J. Rational design of gelatin/nanohydroxyapatite cryogel scaffolds for bone regeneration by introducing chemical and physical cues to enhance osteogenesis of bone marrow mesenchymal stem cells. *Mater. Sci. Eng. C* **2019**, *104*, 109855. [\[CrossRef\]](#)
- Afanasekau, D.; Kalinina, D.; Lyakhovetskii, V.; Tondera, C.; Gersky, O.; Moosavi, S.; Pavlova, N.; Merkul'yeva, N.; Kaluzoff, A.V.; Mineev, I.R.; et al. Rapid prototyping of soft bioelectronic implants for use as neuromuscular interfaces. *Nat. Biomat. Eng.* **2020**, *4*, 1010–1022. [\[CrossRef\]](#) [\[PubMed\]](#)
- Gaharwar, A.K.; Singh, I.; Khademhosseini, A. Engineered biomaterials for in situ tissue regeneration. *Nat. Rev. Mater.* **2020**, *5*, 686–705. [\[CrossRef\]](#)
- Jahromi, M.; Razavi, S.; Bakhtian, A. The advances in nerve tissue engineering: From fabrication of nerve conduit to in vivo nerve regeneration assays. *J. Tissue Eng. Regen. Med.* **2019**, *13*, 2077–2100. [\[CrossRef\]](#)
- Lin, H.; Sohn, J.; Shen, H.; Langhans, M.T.; Tuan, R.S. Bone marrow mesenchymal stem cells: Aging and tissue engineering applications to enhance bone healing. *Biomaterials* **2019**, *203*, 96–110. [\[CrossRef\]](#)
- Paun, I.A.; Zamfirescu, M.; Luculescu, C.R.; Acasandrei, A.M.; Mustaciano, C.C.; Mihailescu, M.; Diniescu, M. Electrically responsive microsensors for controllable delivery of dexamethasone in bone tissue engineering. *Appl. Surf. Sci.* **2017**, *392*, 321–331. [\[CrossRef\]](#)
- Santos-Ruales, V.; Ardau, I.; Alvarez-Lorenzo, C.; Ribeiro, N.; Oliveira, A.L.; García-González, C.A. Sterile and dual-porous aerogels scaffolds obtained through a multistep supercritical CO<sub>2</sub>-based approach. *Molecules* **2019**, *24*, 871. [\[CrossRef\]](#) [\[PubMed\]](#)
- Francis Suh, J.K.; Matthew, H.W.T. Application of chitosan-based polysaccharide biomaterials in cartilage tissue engineering: A review. *Biomaterials* **2000**, *21*, 2589–2598. [\[CrossRef\]](#)
- Hamidouche, Z.; Hay, E.; Vaudin, P.; Charbord, P.; Schüle, R.; Marie, P.J.; Fromiguet, O. FHL2 mediates dexamethasone-induced mesenchymal cell differentiation into osteoblasts by activating Wnt/ $\beta$ -catenin signaling-dependent Runx2 expression. *FASEB J.* **2008**, *22*, 3813–3822. [\[CrossRef\]](#) [\[PubMed\]](#)
- Reya, T.; Morrison, S.J.; Clarke, M.; Weissman, I. Stem cells, cancer, and cancer stem cells. *Nature* **2001**, *414*, 105–111. [\[CrossRef\]](#)



17. Sammons, J.; Ahmed, N.; Hassan, H.T. The role of BMP-6, IL-6, and BMP-4 in mesenchymal stem cell-dependent bone development: Effects on osteoblastic differentiation induced by parathyroid hormone and vitamin D3. *Stem Cells Dev.* **2004**, *280*, 273–280. [\[CrossRef\]](#)
18. Wojak-Cwik, I.M.; Rumian, L.; Krok-Borkowicz, M.; Hoss, R.; Bernhardt, R.; Dobrzyński, P.; Möller, S.; Schabeltrauch, M.; Hintze, V.; Scharnweber, D.; et al. Synergistic effect of bimodal pore distribution and artificial extracellular matrices in polymeric scaffolds on osteogenic differentiation of human mesenchymal stem cells. *Mater. Sci. Eng. C* **2019**, *97*, 12–22. [\[CrossRef\]](#) [\[PubMed\]](#)
19. Cheema, U.; Yang, S.Y.; Madera, V.; Goldspink, G.G.; Brown, R.A. 3-D in vitro model of early skeletal muscle development. *Cell Motil. Cytoskelet.* **2003**, *54*, 226–236. [\[CrossRef\]](#)
20. He, H.; Sofman, M.; Wang, A.J.S.; Ahrens, C.C.; Wang, W.; Griffith, L.G.; Hammond, P.T. Engineering helical modular polypeptide-based hydrogels as synthetic extracellular matrices for cell culture. *Biomacromolecules* **2020**, *21*, 566–580. [\[CrossRef\]](#)
21. El-Naggar, M.E.; Othman, S.I.; Allam, A.A.; Morsy, O.M. Synthesis, drying process and medical application of polysaccharide-based aerogels. *Int. J. Biol. Macromol.* **2020**, *145*, 1115–1128. [\[CrossRef\]](#)
22. Kistler, S.S. Coherent expanded aerogels. *J. Phys. Chem.* **1992**, *36*, 52–64. [\[CrossRef\]](#)
23. Korkmaz, S.; Kariper, A. Graphene and graphene oxide based aerogels: Synthesis, characteristics and supercapacitor applications. *J. Energy Storage* **2020**, *27*, 101038. [\[CrossRef\]](#)
24. Shewale, P.M.; Rao, A.V.; Gurav, J.L.; Rao, A.P. Synthesis and characterization of low density and hydrophobic silica aerogels dried at ambient pressure using sodium silicate precursor. *J. Porous Mater.* **2009**, *16*, 101–108. [\[CrossRef\]](#)
25. Zhu, F. Starch based aerogels: Production, properties and applications. *Trends Food Sci. Technol.* **2019**, *89*, 1–10. [\[CrossRef\]](#)
26. Ulery, B.D.; Nair, L.S.; Laurencin, C.T. Biomedical applications of biodegradable polymers. *J. Polym. Sci. Part B Polym. Phys.* **2011**, *49*, 832–864. [\[CrossRef\]](#)
27. Wang, Y.; Su, Y.; Wang, W.; Fang, Y.; Rifat, S.B.; Jiang, F. The advances of polysaccharide-based aerogels: Preparation and potential application. *Carbohydr. Polym.* **2019**, *226*, 115242. [\[CrossRef\]](#)
28. Garcia-González, C.A.; Alnaif, M.; Smirnova, I. Polysaccharide-based aerogels-promising biodegradable carriers for drug delivery systems. *Carbohydr. Polym.* **2011**, *86*, 1425–1438. [\[CrossRef\]](#)
29. Martins, M.; Barros, A.A.; Quraishi, S.; Gurikov, P.; Raman, S.P.; Smirnova, I.; Duarte, A.R.C.; Reis, R.L. Preparation of macroporous alginate-based aerogels for biomedical applications. *J. Supercrit. Fluids* **2015**, *106*, 152–159. [\[CrossRef\]](#)
30. Garcia-González, C.A.; Jin, M.; Gerth, J.; Alvarez-Lorenzo, C.; Smirnova, I. Polysaccharide-based aerogel microspheres for oral drug delivery. *Carbohydr. Polym.* **2015**, *117*, 797–806. [\[CrossRef\]](#)
31. Rosa, M.F.; Medeiros, E.S.; Malmonge, J.A.; Grogorski, K.S.; Wood, D.F.; Mattoso, L.H.C.; Glenn, G.; Orts, W.J.; Imam, S.H. Cellulose nanowhiskers from coconut husk fibers: Effect of preparation conditions on their thermal and morphological behavior. *Carbohydr. Polym.* **2010**, *81*, 83–92. [\[CrossRef\]](#)
32. Sussman, E.M.; Halpin, M.C.; Mosher, J.; Moon, R.T.; Ratner, B.D. Porous implants modulate healing and induce shifts in local macrophage polarization in the foreign body reaction. *Ann. Biomed. Eng.* **2014**, *42*, 1508–1516. [\[CrossRef\]](#)
33. Loh, Q.; Choong, C. Three-dimensional scaffolds for tissue engineering applications: Role of porosity and pore size. *Tissue Eng. Part B Rev.* **2013**, *19*, 485–502. [\[CrossRef\]](#)
34. Takahashi, Y.; Tabata, Y. Effect of the fiber diameter and porosity of non-woven PET fabrics on the osteogenic differentiation of mesenchymal stem cells. *J. Biomat. Sci. Polym. Ed.* **2012**, *15*, 37–41. [\[CrossRef\]](#) [\[PubMed\]](#)
35. Pramanik, S.; Pingguan-Murphy, B.; Abu Osman, N.A. Progress of key strategies in development of electrospun scaffolds. *Bone tissue. Sci. Technol. Adv. Mater.* **2012**, *13*, 43002. [\[CrossRef\]](#) [\[PubMed\]](#)
36. Viswanathan, P.; Orudek, M.G.; Chirasatitsin, S.; Ngamkham, K.; Reilly, G.C.; Engler, A.J.; Battaglia, G. 3D surface topology guides stem cell adhesion and differentiation. *Biomaterials* **2015**, *52*, 140–147. [\[CrossRef\]](#)
37. Shuaib, A.; Motan, D.; Bhattacharya, P.; McNabb, A.; Skerry, T.M.; Lacroix, D. Heterogeneity in the mechanical properties of integrins determines mechanotransduction dynamics in bone osteoblasts. *Sci. Rep.* **2019**, *9*, 13113. [\[CrossRef\]](#)
38. Gonçalves, V.S.S.; Gurikov, P.; Poje, J.; Matias, A.A.; Heinrich, S.; Duarte, C.M.M.; Smirnova, I. Alginate-based hybrid aerogel microparticles for mucosal drug delivery. *Eur. J. Pharm. Biopharm.* **2016**, *107*, 160–170. [\[CrossRef\]](#)

39. Ramirez-Sanchez, K.; Ledezma-Espinoza, A.; Sanchez-Kopper, A.; Avendaño-Soto, E.; Prado, M.; Starbird Perez, R. Polysaccharide *s*-carrageenan as doping agent in conductive coatings for electrochemical controlled release of dexamethasone at therapeutic doses. *Molecules* **2020**, *25*, 2139. [[CrossRef](#)]
40. Chen, C.; Yuen, D.; Ng, W.; Weil, T. Progress in polymer science polymer bioconjugates: Modern design concepts toward precision hybrid materials. *Prog. Polym. Sci.* **2020**, *105*, 101241. [[CrossRef](#)]
41. Pires, F.; Ferreira, Q.; Rodrigues, C.A.V.; Margado, J.; Ferreira, F.C. Neural stem cell differentiation by electrical stimulation using a cross-linked PEDOT substrate: Expanding the use of biocompatible conjugated conductive polymers for neural tissue engineering. *BBA-Gen. Subj.* **2015**, *1850*, 1158–1168. [[CrossRef](#)] [[PubMed](#)]
42. Smirnova, I.; Mamic, J.; Arlt, W. Adsorption of drugs on silica aerogels. *Langmuir* **2003**, *19*, 8521–8525. [[CrossRef](#)]
43. Durães, L.; Hajej, M.; Vazda, J.P.; Lamy-Mendes, A.; Portugal, A. Exploring the versatile surface chemistry of silica aerogels for multipurpose application. *MRS Adv.* **2017**, *2*, 3511–3519. [[CrossRef](#)]
44. Rezaei, S.; Jalali, A.; Zolali, A.M.; Alshrah, M.; Karamikamkar, S.; Park, C.B. Robust, ultra-insulative and transparent polyethylene-based hybrid silica aerogel with a novel non-particulate structure. *J. Colloid Interface Sci.* **2019**, *548*, 206–216. [[CrossRef](#)]
45. Zaogler, C.; Wolf, A.; Liu, W.; Herrmann, A.K.; Gaponik, N.; Eychmüller, A. Modern inorganic aerogels. *Angew. Chem. Int. Ed.* **2017**, *56*, 13200–13221. [[CrossRef](#)]
46. Nagai, Y.; Yokoi, H.; Kaitera, K.; Naruse, K. The mechanical stimulation of cells in 3D culture within a self-assembling peptide hydrogel. *Biomaterials* **2012**, *33*, 1044–1051. [[CrossRef](#)]
47. Garcia-González, C.A.; Canenza, E.; Zeng, M.; Smirnova, I.; Roig, A. Design of biocompatible magnetic pectin aerogel monoliths and microspheres. *RSC Adv.* **2012**, *2*, 9816–9823. [[CrossRef](#)]
48. López-Iglesias, C.; Barros, J.; Andao, I.; Monteiro, F.J.; Alvarez-Lorenzo, C.; Gómez-Amoza, J.L.; Garcia-González, C.A. Vancomycin-loaded chitosan aerogel particles for chronic wound applications. *Carbohydr. Polym.* **2019**, *204*, 223–231. [[CrossRef](#)]
49. Baldino, L.; Cardea, S.; Scognamiglio, M.; Reverchon, E. A new tool to produce alginate-based aerogels for medical applications, by supercritical gel drying. *J. Supercrit. Fluids* **2019**, *146*, 152–158. [[CrossRef](#)]
50. Ganesan, K.; Demstedt, A.; Barowski, A.; Ratke, L. Design of aerogels, cryogels and xerogels of cellulose with hierarchical porous structures. *Mater. Des.* **2016**, *92*, 345–355. [[CrossRef](#)]
51. Baudron, V.; Gurikov, P.; Smirnova, I.; Whitehouse, S. Porous starch materials via supercritical-and freeze-drying. *Gels* **2019**, *5*, 12. [[CrossRef](#)]
52. Starbird, R.; Garcia-González, C.A.; Smirnova, I.; Knautschneider, W.H.; Bauhofer, W. Synthesis of an organic conductive porous material using starch aerogels as template for chronic invasive electrodes. *Mater. Sci. Eng. C* **2014**, *37*, 177–183. [[CrossRef](#)]
53. Zamora-Sequeira, R.; Andao, I.; Starbird, R.; Garcia-González, C.A. Conductive nanostructured materials based on poly-(3,4-ethylenedioxythiophene) (PEDOT) and starch/*s*-carrageenan for biomedical applications. *Carbohydr. Polym.* **2018**, *189*, 304–312. [[CrossRef](#)] [[PubMed](#)]
54. Avramidou, S.; Barabas, S.G.; Tian, Y.; Psotikopoulos, E.N. Circular economy—A challenge and an opportunity for Process Systems Engineering. *Comput. Chem. Eng.* **2020**, *133*, 106629. [[CrossRef](#)]
55. Ganesan, K.; Budnova, T.; Ratke, L.; Gurikov, P.; Baudron, V.; Preibisch, I.; Niemeyer, P.; Smirnova, I.; Milow, B. Review on the production of polysaccharide aerogel particles. *Materials* **2018**, *11*, 2144. [[CrossRef](#)]
56. Garcia-González, C.A.; Concheiro, A.; Alvarez-Lorenzo, C. Processing of materials for regenerative medicine using supercritical fluid technology. *Bioconjug. Chem.* **2015**, *26*, 1159–1171. [[CrossRef](#)]
57. Knez, Ž.; Partić, M.; Čit, D.; Novak, Z.; Knez Hršić, M. Are supercritical fluids solvents for the future? *Chem. Eng. Process. Process Intensif.* **2019**, *141*, 107532. [[CrossRef](#)]
58. Wilhelm Ostjen, G. *Freeze Drying*; Wiley-VCH Verlag GmbH & Co. KGaA: Weinheim, Germany, 1999; ISBN 3-527-29571-2.
59. Liao, W.; Zhao, H.B.; Liu, Z.; Xu, S.; Wang, Y.Z. On controlling aerogel microstructure by freeze casting. *Compos. Part B Eng.* **2019**, *173*, 107036. [[CrossRef](#)]
60. Ni, X.; Ke, F.; Xiao, M.; Wu, K.; Kuang, Y.; Corke, H.; Jiang, F. The control of ice crystal growth and effect on porous structure of konjac glucomannan-based aerogels. *Int. J. Biol. Macromol.* **2016**, *92*, 1130–1135. [[CrossRef](#)]

61. García-gonzález, C.A.; Camino-rey, M.C.; Alnaief, M.; Zetzl, C.; Smirnova, I. Supercritical drying of aerogels using CO<sub>2</sub>: Effect of extraction time on the end material textural properties. *J. Supercrit. Fluids* **2012**, *66*, 297–306. [\[CrossRef\]](#)
62. García-González, C.A.; Smirnova, I. Use of supercritical fluid technology for the production of tailor-made aerogel particles for delivery systems. *J. Supercrit. Fluids* **2013**, *79*, 152–158. [\[CrossRef\]](#)
63. Kamar, J.A.; Eller, F.J.; Felker, F.C.; Jackson, A.; Fanta, G.F. Starch aerogel beads obtained from inclusion complexes prepared from high amylose starch and sodium palmitate. *Green Chem.* **2014**, *16*, 1921–1930. [\[CrossRef\]](#)
64. Deusil, L.; Bardl, R.; Vorweg, W.; Budtova, T. Starch aerogels: A member of the family of thermal super-insulating materials. *Biomacromolecules* **2017**, *18*, 4232–4239. [\[CrossRef\]](#)
65. Zhang, Y.; Zhu, J.; Ren, H.; Bi, Y.; Shi, X.; Wang, B.; Zhang, L. A novel starch-enhanced melamine-formaldehyde aerogel with low volume shrinkage and high toughness. *J. Polym. Mater.* **2017**, *24*, 1303–1307. [\[CrossRef\]](#)
66. Ubeyitogullari, A.; Brahma, S.; Rose, D.J.; Ciftci, O. In vitro digestibility of nanoporous wheat starch aerogels. *J. Agric. Food Chem.* **2018**, *66*, 9490–9497. [\[CrossRef\]](#)
67. Mohammadi, A.; Moghaddas, J. Mesoporous tablet-shaped potato starch aerogels for loading and release of the poorly water-soluble drug celecoxib. *Chin. J. Chem. Eng.* **2020**, *28*, 1778–1787. [\[CrossRef\]](#)
68. Ganesan, K.; Ratka, L. Facile preparation of monolithic  $\alpha$ -carrageenan aerogels. *Soft Matter* **2014**, *10*, 3218–3224. [\[CrossRef\]](#)
69. Nedelec, J.-M.; Pincher, N.; Strauß, C.; Carbajal, L.; Kasper, C.; Rosenau, T.; Fischhuber, D.; Lieber, F. Preparation and reinforcement of dual-porous biocompatible cellulose scaffolds for tissue engineering. *Macromol. Mater. Eng.* **2013**, *300*, 911–924.
70. Raman, S.P.; Garikav, P.; Smirnova, I. Hybrid alginate based aerogels by carbon dioxide induced gelation: Novel technique for multiple applications. *J. Supercrit. Fluids* **2015**, *106*, 23–33. [\[CrossRef\]](#)
71. Betz, M.; García-González, C.A.; Subrahmanyam, R.P.; Smirnova, I.; Kulczik, U. Preparation of novel whey protein-based aerogels as drug carriers for life science applications. *J. Supercrit. Fluids* **2012**, *72*, 111–119. [\[CrossRef\]](#)
72. Goimil, L.; Braga, M.E.M.; Dias, A.M.A.; Gómez-Amoza, J.L.; Corchero, A.; Alvarez-Lorenzo, C.; De Sousa, H.C.; García-González, C.A. Supercritical processing of starch aerogels and aerogel-loaded poly( $\epsilon$ -caprolactone) scaffolds for sustained release of ketoprofen for bone regeneration. *J. CO<sub>2</sub> Util.* **2017**, *18*, 237–249. [\[CrossRef\]](#)
73. Theocharis, A.D.; Skandalis, S.S.; Gianneli, C.; Karamanos, N.K. Extracellular matrix structure. *Adv. Drug Deliv. Rev.* **2016**, *97*, 4–27. [\[CrossRef\]](#)
74. Brien, F.J.O. Biomaterials & scaffolds every day thousands of surgical procedures are performed to replace. *Mater. Today* **2011**, *14*, 88–95.
75. Gleason, J.P.; Brien, F.J.O. Composite scaffolds for orthopaedic regenerative medicine. In *Advances in Composite Materials for Medicine and Nanotechnology*; InTech Open Access: Rijeka, Croatia, 2011; Volume 10, pp. 39–59.
76. Chen, H.; Zhong, J.; Wang, J.; Huang, R.; Qiao, X.; Wang, H.; Tan, Z. Enhanced growth and differentiation of myoblast cells grown on E-jet 3D printed platforms. *Int. J. Nanomed.* **2019**, *14*, 937–950. [\[CrossRef\]](#)
77. Miroslaw, L.; Capila, I.; Kaundinya, G. Mass spectrometric methods for the analysis of heparin and heparan sulfate. *Glycosaminoglycans Methods Mol. Biol.* **2014**, *1229*, 119–128.
78. Park, J.S.; Lim, H.J.; Yi, S.W.; Park, K.H. Stem cell differentiation-related protein-loaded PLGA microspheres as a novel platform micro-typed scaffold for chondrogenesis. *Biomater. Mater.* **2016**, *11*, 5503. [\[CrossRef\]](#)
79. Simans, M.; Schneider, V.; Le Blanc, S.; Dotterweich, J.; Zehe, V.; Krug, M.; Jakob, F.; Schilling, T.; Schütze, N. Heparin affects human bone marrow stromal cell fate: Promoting osteogenic and reducing adipogenic differentiation and conversion. *Bone* **2015**, *78*, 102–113. [\[CrossRef\]](#) [\[PubMed\]](#)
80. Selakyyikirim, K. Recent advances in glycosaminoglycan analysis by various mass spectrometry techniques. *Anal. Bioanal. Chem.* **2019**, *411*, 3731–3741. [\[CrossRef\]](#)
81. Uygun, B.E.; Stojich, S.E.; Matthew, H.W.T. Effects of immobilized glycosaminoglycans on the proliferation and differentiation of mesenchymal stem cells. *Tissue Eng. Part A* **2009**, *15*, 3499–3512. [\[CrossRef\]](#)
82. Benoit, D.S.W.; Durney, A.R.; Anseth, K.S. The effect of heparin-functionalized PEG hydrogels on three-dimensional human mesenchymal stem cell osteogenic differentiation. *Biomaterials* **2007**, *28*, 66–77. [\[CrossRef\]](#)

83. Seto, S.P.; Casas, M.E.; Temeroff, J.S. Differentiation of mesenchymal stem cells in heparin-containing hydrogels via coculture with osteoblasts. *Cell Tissue Res.* **2012**, *347*, 589–601. [[CrossRef](#)]
84. Farina, M.; Chua, C.Y.X.; Ballerini, A.; Thekkedath, U.; Alexander, J.F.; Rhudy, J.R.; Torchio, G.; Fraga, D.; Pathak, R.R.; Villanueva, M.; et al. Transcutaneously refillable, 3D-printed biopolymeric encapsulation system for the transplantation of endocrine cells. *Biomaterials* **2018**, *177*, 125–138. [[CrossRef](#)] [[PubMed](#)]
85. Paez-Mayorga, J.; Capuani, S.; Farina, M.; Lofito, M.L.; Niles, J.A.; Salazar, H.F.; Rhudy, J.; Esmola, L.; Chua, C.Y.X.; Taraballi, F.; et al. Enhanced in vivo vascularization of 3D-printed cell encapsulation device using platelet-rich plasma and mesenchymal stem cells. *Adv. Healthc. Mater.* **2020**, *2000670*, 1–11. [[CrossRef](#)]
86. Erdem, A.; Darabi, M.A.; Nasiri, R.; Sangabathani, S.; Ertas, Y.N.; Alem, H.; Hosseini, V.; Shamloo, A.; Nasr, A.S.; Ahadian, S.; et al. 3D bioprinting of oxygenated cell-laden gelatin methacryloyl constructs. *Adv. Healthc. Mater.* **2020**, *9*, e1901794. [[CrossRef](#)]
87. Blakney, A.K.; Swartzlander, M.D.; Bryant, S.J. The effects of substrate stiffness on the in vitro activation of macrophages and in vivo host response to poly (ethylene glycol)-based hydrogels. *Sci. Biomater.* **2012**, *100*, 1375–1386.
88. Venturini, V.; Pezano, F.; Frederic, C.; Hakkinen, H.-M.; Jimenez-delgado, S.; Colomer-cosell, M.; Marm, M.; Tolosa-ramon, Q.; Paz-lópez, S.; Valverde, M.A.; et al. The nucleus maintains shape changes for cellular proprioception to control dynamic cell behavior. *Science* **2020**, *370*, 2644. [[CrossRef](#)]
89. Lomakin, A.; Cattin, C.; Cuvellier, D.; Alraies, Z.; Molina, M.; Nader, G.P.; Srivastava, N.; Saez, P.; Garcia-Arcos, J.M.; Zhilnyak, I.Y.; et al. The nucleus acts as a ruler tailoring cell responses to spatial constraints. *Science* **2020**, *370*, 2894. [[CrossRef](#)]
90. Faby, N.; Alini, M.; Stoddart, M.J. Mechanical stimulation of mesenchymal stem cells: Implications for cartilage tissue engineering. *J. Orthop. Res.* **2018**, *36*, 52–63. [[CrossRef](#)]
91. Mao, A.S.; Mooney, D.J. Regenerative medicine: Current therapies and future directions. *Proc. Natl. Acad. Sci. USA* **2015**, *112*, 14452–14459. [[CrossRef](#)]
92. Pedersen, J.; Swartz, M. Mechanobiology in the third dimension. *Ann. Biomed. Eng.* **2005**, *33*, 1469–1490. [[CrossRef](#)] [[PubMed](#)]
93. Terraciano, V.; Hwang, N.; Moroni, L.; Park, H.B.; Zhang, Z.; Mizrahi, J.; Seiktar, D.; Elisseeff, J. Differential response of adult and embryonic mesenchymal progenitor cells to mechanical compression in hydrogels. *Stem Cells* **2007**, *25*, 2730–2738. [[CrossRef](#)]
94. Zhang, W.; Kong, C.W.; Tong, M.H.; Chooi, W.H.; Huang, N.; Li, R.A.; Chan, B.P. Maturation of human embryonic stem cell-derived cardiomyocytes (hESC-CMs) in 3D collagen matrix: Effects of niche cell supplementation and mechanical stimulation. *Acta Biomater.* **2017**, *49*, 204–217. [[CrossRef](#)]
95. Barnes, J.M.; Prybyla, L.; Weaver, V.M. Tissue mechanics regulate brain development, homeostasis and disease. *J. Cell Sci.* **2017**, *130*, 71–82. [[CrossRef](#)]
96. Liu, C.; Cui, X.; Ackermann, T.M.; Flamini, V.; Chen, W.; Castillo, A.B. Osteoblast-derived paracrine factors regulate angiogenesis in response to mechanical stimulation. *Integr. Biol.* **2016**, *8*, 785–794. [[CrossRef](#)]
97. Bono, N.; Pezzoli, D.; Lavesque, L.; Loy, C.; Candiani, G.; Fiore, G.B.; Mantovani, D. Unraveling the role of mechanical stimulation on smooth muscle cells: A comparative study between 2D and 3D models. *Biotecnol. Bioeng.* **2016**, *113*, 2254–2263. [[CrossRef](#)]
98. Hasanzadeh, E.; Amosbediny, G.; Haghighipour, N.; Gholami, N.; Mohammadrezaei, J.; Shejari, S.; Salehi-Nik, N. The stability evaluation of mesenchymal stem cells differentiation toward endothelial cells by chemical and mechanical stimulation. *Vitr. Cell. Dev. Biol.—Annu.* **2017**, *53*, 818–826. [[CrossRef](#)]
99. Gault, B.M.; Mu, D.J. Mechanical stimulation of piezol receptors depends on extracellular matrix proteins and directionality of force. *News Lett.* **2017**, *17*, 2064–2072. [[CrossRef](#)]
100. Godau, B. Determining the Effect of Structure and Function on 3D Bioprinted Hydrogel Scaffolds for Applications in Tissue Engineering. Bachelor's Thesis, University of Victoria, Victoria, BC, Canada, 2019.
101. Peeters, E.A.G. Monitoring the biomechanical response of individual cells under compression: A new compression device. *Mat. Sci. Eng. Comput.* **2003**, *41*, 498–503. [[CrossRef](#)]
102. Wang, N.; Butler, J.P.; Ingber, D.E. Mechanotransduction across the cell surface and through the cytoskeleton. *Science* **1993**, *260*, 1124–1128. [[CrossRef](#)] [[PubMed](#)]

123. Bajaj, P.; Bobby, R.; Millet, L.; Wei, C.; Zorlutuna, P.; Bao, G.; Bashir, R. Patterning the differentiation of C2C12 skeletal myoblasts. *Integr. Biol.* **2011**, *3*, 897–909. [\[CrossRef\]](#)
124. Guo, W.; Zhang, X.; Yu, X.; Wang, S.; Qiu, J.; Tang, W.; Li, L.; Liu, H.; Wang, Z.L. Self-powered electrical stimulation for enhancing neural differentiation of mesenchymal stem cells on graphene-Poly(3,4-ethylenedioxythiophene) hybrid microfibers. *ACS Nano* **2016**, *10*, 5086–5095. [\[CrossRef\]](#)
125. Wang, J.; Tian, L.; Chen, N.; Ramakrishna, S.; Mo, X. The cellular response of nerve cells on poly-L-lysine coated PLGA-MWCNTs aligned nanofibers under electrical stimulation. *Mater. Sci. Eng. C* **2018**, *91*, 715–726. [\[CrossRef\]](#)
126. Boehler, C.; Kleber, C.; Martini, N.; Xie, Y.; Dryg, I.; Stieglitz, T.; Hofmann, U.G.; Asplund, M. Actively controlled release of Dexamethasone from neural microelectrodes in a chronic *in vivo* study. *Biomaterials* **2017**, *129*, 176–187. [\[CrossRef\]](#)
127. Hao, H.B.; Yuan, L.; Fu, Z.B.; Wang, C.Y.; Yang, X.; Zhu, J.; Qu, J.; Chen, H.; Schiraldi, D. Biomass-based mechanically-strong and electrically-conductive polymer aerogels and their application for supercapacitors. *ACS Appl. Mater. Interfaces* **2016**, *8*, 9917–9924.
128. You, I.; Jeung, U. Electromechanical decoupling by porous aerogel conducting polymer. *Mater* **2019**, *1*, 24–25. [\[CrossRef\]](#)
129. Zhang, X.; Chang, D.; Liu, J.; Luo, Y. Conducting polymer aerogels from supercritical CO<sub>2</sub> drying PEDOT-PSS hydrogels. *J. Mater. Chem.* **2010**, *20*, 5080–5085. [\[CrossRef\]](#)
130. Bertucci, C.; Koppes, R.; Dumont, C.; Koppes, A. Neural responses to electrical stimulation in 2D and 3D *in vitro* environments. *Brain Res. Bull.* **2019**, *152*, 265–284. [\[CrossRef\]](#)
131. Hernández-Suarez, P.; Ramirez, K.; Alvarado, F.; Avendaño, E.; Starbied, R. Electrochemical characterization of poly(3,4-ethylenedioxythiophene)/ $\alpha$ -carrageenan as a biocompatible conductive coat for biologic applications. *MRS Commun.* **2018**, *9*, 218–223. [\[CrossRef\]](#)
132. Ryan, E.M.; Besslin, C.B. Formation of polypyrrole with dexamethasone as a dopant: Its cation and anion exchange properties. *J. Electroanal. Chem.* **2018**, *824*, 188–194. [\[CrossRef\]](#)
133. Gimil, L.; Santos-Rosales, V.; Delgado, A.; Évora, C.; Reyes, R.; Lozano-Pérez, A.A.; Amar-Cervantes, S.D.; Cenís, J.L.; Gómez-Amoza, J.L.; Concheiro, A.; et al. SeCO<sub>2</sub>-foamed silk fibrin aerogel/poly( $\epsilon$ -caprolactone) scaffolds containing dexamethasone for bone regeneration. *J. CO<sub>2</sub> Util.* **2019**, *31*, 51–64. [\[CrossRef\]](#)
134. Costa, P.F.; Puga, A.M.; Diaz-Gomez, L.; Concheiro, A.; Busch, D.H.; Alvarez-Lorenzo, C. Additive manufacturing of scaffolds with dexamethasone controlled release for enhanced bone regeneration. *Int. J. Pharm.* **2015**, *496*, 541–550. [\[CrossRef\]](#)
135. Liu, Q.; Cen, L.; Zhou, H.; Yin, S.; Liu, G.; Liu, W.; Cao, Y.; Cui, L. The role of the extracellular signal-related kinase signaling pathway in osteogenic differentiation of human adipose-derived stem cells and in adipogenic transition initiated by dexamethasone. *Tissue Eng. Part A* **2009**, *15*, 3487–3497. [\[CrossRef\]](#) [\[PubMed\]](#)
136. Danckwerts, M.; Fassihi, A. Implantable controlled release drug delivery system: A review. *Drug Del. Inf. Pharm.* **1991**, *7*, 1465–1502. [\[CrossRef\]](#)
137. Ding, C.; Li, Z. A review of drug release mechanisms from nanocarrier systems. *Mater. Sci. Eng. C* **2017**, *76*, 1440–1453. [\[CrossRef\]](#)
138. Franco, P.; Marco, I. De supercritical CO<sub>2</sub> adsorption of non-steroidal anti-inflammatory drugs into biopolymer aerogels. *J. CO<sub>2</sub> Util.* **2020**, *36*, 40–53. [\[CrossRef\]](#)
139. Lovskaya, D.D.; Lebedev, A.E.; Menshutina, N.V. Aerogels as drug delivery systems: *In vitro* and *in vivo* evaluations. *J. Supercrit. Fluids* **2015**, *106*, 5–11. [\[CrossRef\]](#)
140. De Marco, I.; Reverchon, E. Starch aerogel loaded with poorly water-soluble vitamins through supercritical CO<sub>2</sub> adsorption. *Chem. Eng. Res. Des.* **2017**, *119*, 221–230. [\[CrossRef\]](#)
141. Garcia-González, C.A.; Uy, J.J.; Alnaief, M.; Smirnova, I. Preparation of tailor-made starch-based aerogel microspheres by the emulsion-gelation method. *Carbohydr. Polym.* **2012**, *88*, 1378–1386. [\[CrossRef\]](#)
142. Korsmeyer, R.W.; Gurny, R.; Doellker, E.; Buri, P.; Peppas, N.A. Mechanisms of solute release from porous hydrophilic polymers. *Int. J. Pharm.* **1983**, *15*, 25–35. [\[CrossRef\]](#)
143. Ritger, P.L.; Peppas, N.A. A simple equation for description of solute release II. Fickian and anomalous release from swellable devices. *J. Control. Release* **1987**, *5*, 37–42. [\[CrossRef\]](#)
144. Ritger, P.L.; Peppas, N.A. A simple equation for description of solute release I. Fickian and non-fickian release from non-swelling devices in the form of slabs, spheres, cylinders or discs. *J. Control. Release* **1987**, *5*, 23–36. [\[CrossRef\]](#)

145. Krukiewicz, K. Tailorable drug capacity of dexamethasone-loaded conducting polymer matrix. *JOP Conf. Ser. Mater. Sci. Eng.* **2018**, *369*, 12202. [[CrossRef](#)]
146. Löffler, S.; Seyock, S.; Nybom, R.; Jacobson, G.B.; Richter-Dahlborg, A. Electrochemically triggered release of acetylcholine from  $\text{scCO}_2$  impregnated conductive polymer films evokes intracellular  $\text{Ca}^{2+}$  signaling in neurotypic SH-SY5Y cells. *J. Control. Release* **2016**, *243*, 283–290. [[CrossRef](#)]
147. Balint, R.; Cassidy, N.J.; Cartmell, S.H. Conductive polymers: Towards a smart biomaterial for tissue engineering. *Acta Biomater.* **2014**, *10*, 2341–2353. [[CrossRef](#)]
148. Alshammary, B.; Walsh, F.C.; Herrasti, P.; Ponco de Leon, C. Electrodeposited conductive polymers for controlled drug release: Polypyrrole. *J. Solid State Electrochem.* **2016**, *20*, 839–859. [[CrossRef](#)]
149. Krukiewicz, K.; Gniazdowska, B.; Jamsz, T.; Herman, A.P.; Bonco, S.; Turczyn, R. Effect of immobilization and release of ciprofloxacin and quercetin on electrochemical properties of poly(3,4-ethylenedioxythiophene) matrix. *Synth. Met.* **2019**, *249*, 52–62. [[CrossRef](#)]
150. Alizadeh, N.; Shamsadi, E. Electrochemically controlled release of anticancer drug methotrexate using nanostructured polypyrrole modified with cetylpyridinium: Release kinetics investigation. *Electrochim. Acta* **2014**, *130*, 488–496. [[CrossRef](#)]
151. Boehler, C.; Oberbauer, F.; Asphand, M. Tuning drug delivery from conducting polymer films for accurately controlled release of charged molecules. *J. Control. Release* **2019**, *304*, 173–180. [[CrossRef](#)]
152. Swieskis, D.; Sharma, M.; Yu, Y.; Garg, S. Electrically switchable polypyrrole film for the tunable release of progesterone. *Ther. Deliv.* **2013**, *4*, 307–313. [[CrossRef](#)]
153. Kim, B.D.; Richardson-burns, S.M.; Hendricks, J.L.; Siquera, C.; Martin, D.C. Effect of immobilized nerve growth factor on conductive polymers: Electrical properties and cellular response. *Adv. Funct. Mater.* **2007**, *17*, 79–86. [[CrossRef](#)]
154. Leprince, L.; Dogimont, A.; Magnin, D.; Demoustier-Champagne, S. Dexamethasone electrically controlled release from polypyrrole-coated nanostructured electrodes. *J. Mater. Sci. Mater. Med.* **2010**, *21*, 925–930. [[CrossRef](#)]
155. Stevenson, G.; Moulton, S.E.; Ibris, P.C.; Wallace, G.G. Polyterthiophene as an electrostimulated controlled drug release material of therapeutic levels of dexamethasone. *Synth. Met.* **2010**, *160*, 1107–1114. [[CrossRef](#)]
156. Qu, J.; Liang, Y.; Shi, M.; Guo, B.; Gao, Y.; Yin, Z. Biocompatible conductive hydrogels based on dextran and aniline trimer as electro-responsive drug delivery system for localized drug release. *Int. J. Biol. Macromol.* **2019**, *140*, 255–264. [[CrossRef](#)]
157. Qu, J.; Zhao, X.; Ma, P.X.; Gao, B. Injectable antibacterial conductive hydrogels with dual response to an electric field and pH for localized “smart” drug release. *Acta Biomater.* **2018**, *72*, 55–69. [[CrossRef](#)]
158. Lin, H.; Zhu, B.; Wu, Y.; Sekino, J.; Nakao, A.; Luo, S. Dynamic poly(3,4-ethylenedioxythiophene)s integrate low impedance with redox-switchable biofunction. *Adv. Funct. Mater.* **2018**, *28*, 1703890. [[CrossRef](#)]

**Publisher's Note:** MDPI stays neutral with regard to jurisdictional claims in published maps and institutional affiliations.



© 2020 by the authors. Licensee MDPI, Basel, Switzerland. This article is an open access article distributed under the terms and conditions of the Creative Commons Attribution (CC BY) license (<http://creativecommons.org/licenses/by/4.0/>).